Pattern Formation in a Neural Field Model

A thesis presented in partial fulfillment of the
requirements for the degree of

Doctor of Philosophy
in
Mathematics

at Massey University, Auckland, New Zealand.

Amanda Jane Elvin

2008

Note: This thesis differs slightly from that submitted for examination in that it includes four additional references and some minor spelling and grammatical changes.

Abstract

In this thesis I study the effects of gap junctions on pattern formation in a neural field model for working memory. I review known results for the base model (the "Amari model"), then see how the results change for the "gap junction model".

I find steady states of both models analytically and numerically, using lateral inhibition with a step firing rate function, and a decaying oscillatory coupling function with a smooth firing rate function. Steady states are homoclinic orbits to the fixed point at the origin. I also use a method of piecewise construction of solutions by deriving an ordinary differential equation from the partial integro-differential formulation of the model. Solutions are found numerically using AUTO and my own continuation code in MATLAB. Given an appropriate level of threshold, as the firing rate function steepens, the solution curve becomes discontinuous and stable homoclinic orbits no longer exist in a region of parameter space. These results have not been described previously in the literature.

Taking a phase space approach, the Amari model is written as a four-dimensional, reversible Hamiltonian system. I develop a numerical technique for finding both symmetric and asymmetric homoclinic orbits. I discover a small separate solution curve that causes the main curve to break as the firing rate function steepens and show there is a global bifurcation. The small curve and the global bifurcation have not been reported previously in the literature. Through the use of travelling fronts and construction of an Evans function, I show the existence of stable heteroclinic orbits.

I also find asymmetric steady state solutions using other numerical techniques. Various methods of determining the stability of solutions are presented, including a method of eigenvalue analysis that I develop. I then find both stable and transient Turing structures in one and two spatial dimensions, as well as a Type-I intermittency. To my knowledge, this is the first time transient Turing structures have been found in a neural field model. In the Appendix, I outline numerical integration schemes, the pseudo-arclength continuation method, and introduce the software package AUTO used throughout the thesis.

Acknowledgements

All the work in this thesis is believed to be original except where explicit reference is made in the text to other authors. This thesis is my own work except for the following contributions: the conjugate system in Chapter 5, Section 5.4 is due to Robert McLachlan; Carlo Laing developed the shooting method in Chapter 6, Section 6.4 and I modified the method in numerical implementation so that minimisation techniques would work; and in Chapter 8, Section 8.2, Carlo Laing carried out the bifurcation analysis using Fourier series, created Figure 8.9 and suggested intermittency as the cause of transient solutions.

I have had a very enjoyable postgraduate experience at Massey University with supportive and encouraging supervisors. Firstly, I would like to thank my supervisor, Dr Carlo Laing. He has been an enthusiastic and patient supervisor who was always keen to discuss ideas and made the subject come alive. I thank my second supervisor, Professor Mick Roberts, for his invaluable input and his humour. Mick's confidence always boosted me. I would also like to express my appreciation to Professor Robert McLachlan who was very generous with his time, showing me a different approach to my work which allowed me to understand some initially perplexing results.

Many other people have also contributed to my thesis and I thank them: Robert McKibbin, Graeme Wake, Alona Ben-Tal and Winston Sweatman for their encouragement and assistance; Vivien Kirk for her interest, advice and discussions about dynamical systems theory; Bart Oldeman, my very patient AUTO genius; Bruce van Brunt for his friendship and guidance; Matt Perlmutter and Barbara Holland for their interest; and while in Canada, Axel Hutt for discussions on Turing instabilities and neural modelling, and Frances Skinner for her advice.

My fellow students Ratneesh Suri, Qing Zhang, Dion O'Neale, Sharleen Harper, Sena Galkadowite, Joanne Mann and Gang (John) Xie have provided a great sense of community. I am also very grateful to Freda Mickisch for her support and for smoothing the way.

I thank my parents, Robert and Marilyn, my brother and sister, Matthew and Victoria, and Maddie, who from a very young age was my captive audience of choice for presentation practice, for their love and support. I also wish to thank my uncle, Dr Donal Forsyth, for the inspiration. Others I thank are Deb Moran for being there, Robyn Tearle for the music, David Schwarz for his innovative perspective, Miraz Jordan for all things Apple, Lisa Williams for the movies, Carolyn Anderson, David Morgan and Jan Suckling for their friendship and support, and Shaneen Moloney for helping make everything possible.

I am grateful to Massey University for the Vice-Chancellor's scholarship funding, and to the Institute of Information and Mathematical Sciences and the Centre for Mathematical Biology for other financial support. I also thank the New Zealand Mathematical Society and the Royal Society of New Zealand for providing financial support for research-related travel.

Contents

List of Figures

List of Tables

Chapter 1

Introduction

1.1 Neurons and working memory

The brain consists of around a hundred billion neurons, or brain cells, connected in an incredibly complex network. Neurons are specialised cells found in the brain and spinal cord of the human body. Neurons communicate with each other by electrical signals. In certain situations, such as when we are remembering something, making a decision, or having an epileptic seizure, large groups of neurons in the brain send nerve impulses at the same time. We are interested in the patterns formed by the neural activity.

The fundamental task of a neuron is to receive, transform and send electrical signals. There are many different types of neurons, but they have some common features. A typical neuron consists of four parts: a *cell body* or *soma*, branches of *dendrites*, an *axon* and presynaptic *terminals* at the end of the axon. See Figure 1.1 for a schematic of a neuron. Depending upon the type of nerve cell, an axon can be from 1mm to 1 meter long. The length of the axon means that connections can be formed between neighbouring neurons or over long distances, creating the nonlocal coupling that is a characteristic of the brain. A neuron typically has a resting state of approximately -70mV as measured against the zero potential level of the extracellular space. The resting voltage or *resting membrane potential* arises through ion balance concentrations on both sides of the cell membrane. The dendrites on a neuron receive electrical stimulus currents from the nerve terminals of other neurons and deliver the current down to the *axon hillock* in the soma. In the soma, the combined currents are integrated to produce a change in the internal voltage, or potential, of the cell. Depolarisation (hyperpolarisation) is a shift of the membrane potential to a less (more) negative value and affects voltage-gated channels in the cell membrane. A synapse is the term used to describe the region of connection between two

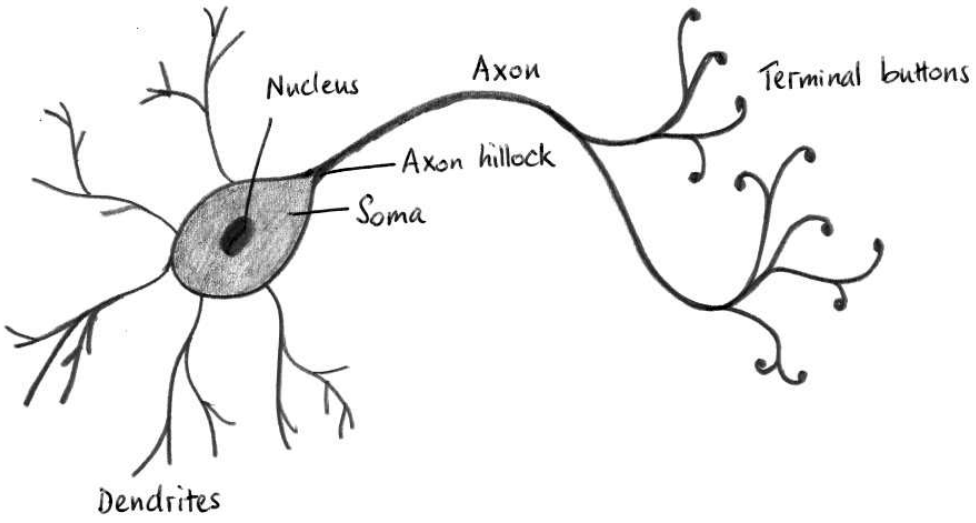

Figure 1.1: Schematic of a neuron showing the main parts of the cell.

neurons. Synapses can be either excitatory or inhibitory. We now describe an excitatory synapse.

If the change in the membrane potential is not very large, the neuron's potential is subthreshold. The voltage change then propagates passively and decays exponentially as it travels a short distance along the axon. If the potential of the neuron is sufficient to clear a threshold, a travelling wave of electrical excitation called an *action potential* is triggered by a sudden depolarisation of the cell membrane. The action potential is actively propagated along the axon away from the soma to the terminal branches of the neuron at a speed of up to 100m/s. The active conductance properties of the axon enable the action potential to maintain its electrical pulse without weakening as it travels along the axon. In cells connected via a chemical synapse, there is a gap between the axon of the presynaptic neuron and the dendrite of the postsynaptic neuron. This gap is known as the synaptic cleft and is about 20-40nm wide. When the action potential arrives at the terminal buttons of the axon, the signal is transmitted across the synaptic cleft to the postsynaptic neuron via chemical neurotransmitters, causing a synaptic delay. At an excitatory synapse, the chemical transmission of the signal causes an excitatory postsynaptic potential, or EPSP, in the postsynaptic cell through rapid depolarisation of the membrane potential. An inhibitory synapse creates an inhibitory postsynaptic potential, or IPSP, through rapid hyperpolarisation of the cell membrane. A schematic of a chemical synapse is shown in Figure 1.2.

Communication between neurons is through either chemical synapses or electrical

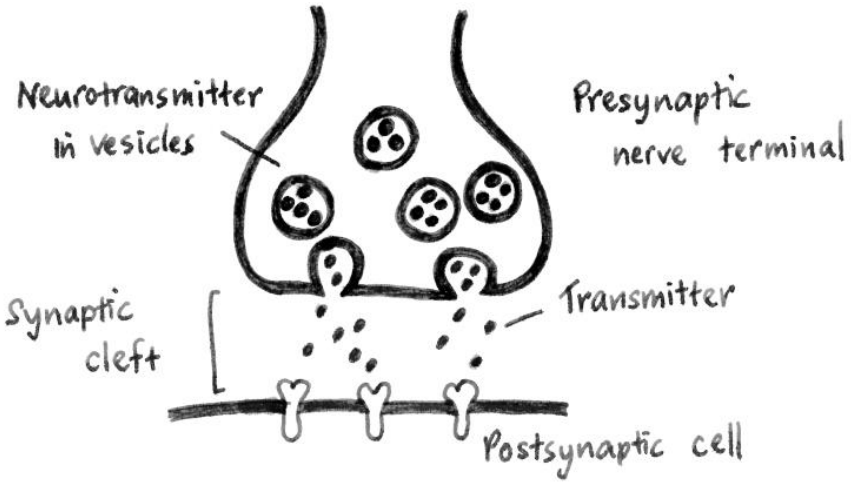

Figure 1.2: Schematic of a chemical synapse.

synapses, with chemical synapses being the most common form of synapse in the brain. A single neuron can support both chemical and electrical transmission. Unlike the chemical transmission of a chemical synapse, electrical synapses permit the direct passing of electrical signal from one cell to another. One type of electrical synapse is a gap junction, a form of direct, low-resistance connection between two neurons. The gap between the neurons joined by a gap junction is approximately $2-4$nm and is much smaller than the gap at a chemical synapse. Gap junctions are formed by an assembly of connexons in each cell that are aligned across the gap. Connexons are made of proteins forming aqueous channels between the cytoplasms of adjacent cells and can be open or closed, hence gap junctions are dynamic structures [76]. See Figure 1.3 for a schematic of a gap junction. The main drawing shows the connexons in two neurons creating a gap junction. The connexons can be open or closed as seen in the diagram in the top right. The diagram on the bottom right shows three neurons connected via gap junctions. Current flows across the membranes of all electrically coupled cells at the same time, creating a diffusive-type effect between surrounding cells as the electrical charge spreads and causes the voltage of these cells to become similar.

Electrically mediated synaptic transmission offers several advantages over chemical synaptic transmission [6, 57]. Firstly, the electrically mediated mechanism can cause very rapid transmission of neural signals. Unlike the chemical synapse, there is no synaptic delay and the presynaptic potential does not need to reach the threshold to produce a response in the postsynaptic cell. It is more difficult for electrically coupled cells to fire action potentials as they require a larger synaptic current to depolarise them to

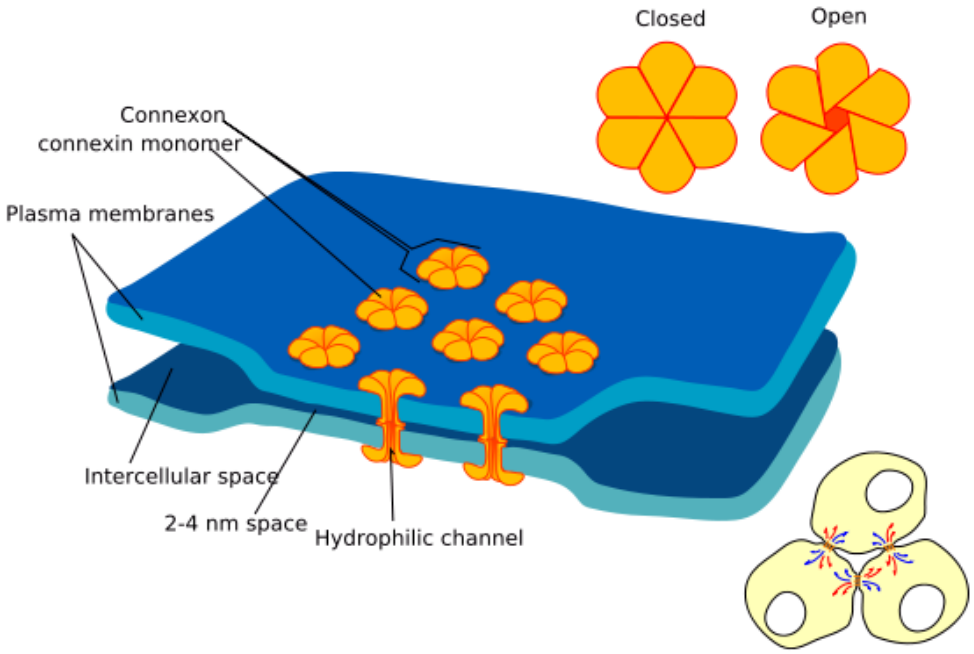

Figure 1.3: Schematic of a gap junction connecting two neurons. Connexons both open and closed (top right); three neurons connected by gap junctions (bottom right). Public domain image created by Mariana Ruiz Villarreal *(http://neuroendokrinologie.de/index.html).*

threshold. Once the threshold is surpassed, however, electrically coupled cells tend to fire synchronously as active Na^+ currents generated in one cell are rapidly transmitted to the other cells. Secondly, electrical transmission can be more reliable as it cannot be blocked by neurotoxins. Thirdly, gap junctions can allow synchronisation of large groups of neurons which can be critical in faciliating rapid reflexes such as escape reactions. The speed advantage of electrical over chemical synapses is less important in mammals than in cold blooded animals, as the higher mammalian body temperature reduces the delay of the chemical synapse [6]. Bennett [5, 6] provides interesting reading on gap junctions and also notes that electrical transmission can occur slowly, if required.

Gap junctions have been previously recognised for their critical role in synchrony, however, their role in seizures is becoming clearer as abnormal synchronisation of neuronal discharges is seen as critical. Temporal lobe epilepsy disturbs the normal electrical function of the brain and causes seizures. Temporal lobe epilepsy is not always successfully treated with medication and another form of treatment is surgery to remove the hippocampus. This type of surgery, however, may form further abnormal cell coupling and research is underway to create a less invasive and more successful treatment [78]. Traub *et al.* [96] proposed that electrical coupling between principal neurons, such as via axonal gap junc-

tions, could be the mechanism behind very fast oscillations in the seizure-prone brain, and perhaps also the normal brain. Very fast oscillations were seen in children before seizure onset and the oscillations were seen as a possible cause of seizure initiation. In slice experiments, runs of very fast oscillations were seen when chemical synapses were blocked. Traub *et al.* suggested gap junction blockers (GJBs) used to treat ulcer disease could have anticonvulsant potential. Velazquez and Carlen [101] examined the role of gap junctions in seizures and firing synchrony from experiments with gap junction communication (GJC). Through pharmacological manipulations of electrical coupling, it was found that GJC played a vital role in a range of neuronal network activities. Velazquez and Carlen saw the development of tools to change GJC as important in determining the role of gap junctions in seizures. The role of gap junctions in seizure generation and propagation was later investigated by Nilsen *et al.* [77] through the use of GJBs. GJBs were found to be effective in suppressing seizures in rats where tetanus toxin was used to induce a chronic epilepsy focus in the cortex.

In areas of the brain where epileptic events are common, researchers at the University of Auckland,[1] New Zealand, have recently discovered there is a high incidence of gap junctions [33, 103]. It is possible that these gap junctions are responsible for the abnormal waves occurring during an epileptic seizure. Astrocytes are glial cells in the brain that maintain normal brain physiology, playing a role in the repair process within the brain and providing nutrients to the nervous tissue. Astrocytes are extensively coupled by gap junctions and can be damaged by epileptic seizures. Fonseca *et al.* [33] found that in the presence of severe trauma, the electrical coupling between astrocytes can be responsible for a further spreading of the damaged area.

We are interested in including gap junctions in a mathematical model of working memory. Working memory, a heavily studied area in neuroscience, relies upon the temporary storage of information to carry out complex cognitive tasks such as planning, decision making and information retrieval [3, 44, 104]. The prefrontal cortex is vital for controlling working memory [24] and is the area of highest cognitive processing within the brain. Experiments with animals have shown persistent activity in cortical neurons when the animal is performing memory tasks [37]. Spatially localised areas of neurons are thought to fire during recall and their activity would form spatial patterns. These groups of neurons then cease firing upon completion of the memory task. The spatial patterns formed by neural activity can be persistent and self-sustaining, requiring no external stimulus.

[1] Personal communication with Profs C.R. Green and L.F.B. Nicholson, University of Auckland.

Neural field models have been used to study pattern formation in working memory for more than thirty years. The development of neural field models of firing rate activity has been an enormous help in understanding the dynamics seen in brain slice preparations. In this thesis, we are interested in mathematically modelling the effect of gap junctions on pattern formation in working memory. The cortex is most realistically modelled as a two-dimensional, continuous structure. Given that the number of neurons in a small piece of the cortex is immense, it is not feasible to model every neuron in the cortex. The neural dynamics of a continuum model are a more appropriate form of modelling than a discrete model [39]. Therefore we take the continuum limit and study neural networks where space is continuous and macroscopic state variables are mean firing rates. Continuum models are also nonlinear to reflect the nonlocal coupling and firing characteristics of neurons. There has been a tremendous amount of work within the area of mathematical neuroscience. Given that the field is so immense, we briefly discuss some of the literature most relevant to the work in this thesis.

1.2 The literature

Spatially localised solutions

In modelling working memory, we are interested in persistent states of localised excitation. In particular, neural field models with local excitation and distal inhibition can support spatially localised areas of high activity. Local excitation and distal inhibition is known as lateral inhibition. The lateral connectivity is a function of distance only. Lateral inhibition is represented by coupling functions of local excitation and distal inhibition that are symmetric, peaked at the origin, and integrable. See the right plot of Figure 1.4 for an example of lateral inhibition.

In 1973, using a two population, one spatial dimension continuum model of cortical and thalamic nervous tissue with lateral inhibition, Wilson and Cowan [105] found stable, spatially localised "bump"-like patterns of activity. The model was extended by Amari in 1977 [1]. Amari developed a neural rate model to study pattern formation in lateral-inhibition type homogeneous neural fields comprised of a single-layer of neurons in a one-dimensional domain. The single population model uses a partial integro-differential equation

$$\frac{\partial u(x,t)}{\partial t} = -u(x,t) + \int_{-\infty}^{\infty} w(x-y) f(u(y,t))\, dy + s(x,t) + h. \tag{1.1}$$

Here, u is the average voltage, or activity level, of a neuronal population at spatial

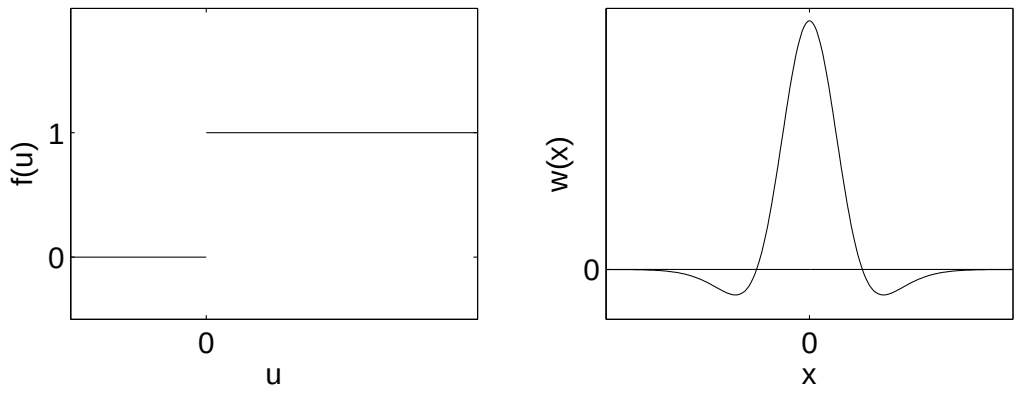

Figure 1.4: Left: The Heaviside firing rate function of Equation (1.2). Right: A Mexican hat coupling function as an example of lateral inhibition.

position x and time t. In Equation (1.1), $s(x,t)$ is a variable external input with spatial structure and h is a constant external input. The function $w(x)$ is the distance-dependent strength of connectivity between neuronal elements and is sometimes referred to as the kernel of the model. The kernel is symmetric, that is, $w(x) = w(|x|)$. The model is translationally invariant. Lateral inhibition is considered an appropriate approximation to a two population model of excitatory and inhibitory neurons where the inhibition is linear and very fast [27]. In Equation (1.1), $w(x)$ is a Mexican hat coupling function. The Mexican hat coupling function is an example of lateral inhibition and has one positive zero in $(0,\infty)$. See the right plot in Figure 1.4. The function $f(u)$ is the synaptic firing rate which depends upon the level of activity u relative to a threshold θ, say. For simplicity, a threshold of 0 is assumed and $f(u)$ is the Heaviside function $\Theta(u)$:

$$f(u) = \Theta(u) = \begin{cases} 1, & \text{if } u > 0 \\ 0, & \text{if } u < 0. \end{cases} \tag{1.2}$$

The Heaviside firing rate function in Equation (1.2) determines that neurons fire at their maximal rate as soon as they reach the threshold $u = 0$, that is, they saturate immediately. If threshold is not reached, the neuron does not fire (see the left plot in Figure 1.4).

Amari [1] found single spatially localised regions of high activity ("bumps") and studied the existence and stability properties of stationary solutions (equilibrium persistent activity). Ermentrout refers to a bump as a standing pulse [27]. Single-bump steady state solutions are believed to be the analogue of short-term memory [27] and there has been much mathematical modelling in this area. Amari defines the region of excitation for a given distribution $u(x)$ to be

$$R(u) = \{x | u(x) > 0\}.$$

"Localised excitation" is defined as a finite, continuous region of excitation such that $R(u) = (x_1, x_2)$, where x_1, x_2 are finite. We refer to this as a single-bump solution. N-bump solutions refer to a solution with $N > 1$ disjoint, finite connected intervals of excitation. Solutions of Equation (1.1) are translationally invariant, hence if $u(x)$ is a solution, $u(x-a)$ is also, for all a. Amari proved that with lateral inhibition, Equation (1.1) has zero, one or two single–bump, time independent solutions. He used linear stability analysis to find the stability of solutions. The analysis shows that where two single-bump solutions can co-exist, the larger, wider bump is stable and the smaller, lower bump is unstable. We present the analysis in Chapter 7. Amari identified a parameter regime of bistability where a stable bump solution coexists with a stable uniform steady state.

Stationary single bump solutions can also be found when the restriction of a Heaviside firing rate function is relaxed. Kishimoto and Amari [61] showed that bump solutions can exist where a smooth sigmoidal firing rate function is used. Using a nonsaturating piecewise linear firing rate function, Guo and Chow studied the existence [48] and stability [49] of stationary solutions in a one-dimensional neural field model on a homogeneous domain with lateral inhibition. The firing rate function is of the form

$$f(u) = [\alpha(u - \theta) + \beta]\,\Theta(u - \theta) \tag{1.3}$$

where θ is the firing threshold. See Figure 1.5 for a schematic of this function. If $u < \theta$, the neuron does not fire. Once u reaches θ, the neuron immediately begins to fire at the rate β. As the stimulus is increased, the rate of firing increases without limit. Guo and Chow [48] showed that an existence condition for single-bump solutions can be reduced to the solution of an algebraic system. The use of the firing rate function in Equation (1.3) permitted three or more single-bump solutions to coexist, as well as "dimple"-bump and two-bump solutions. A "dimple"-bump is a single-bump where the second spatial derivative is positive at the bump centre (a nonconvex dimple). If two stationary single-bump solutions coexist, the larger one is stable and the smaller one unstable, as in Amari's work [1]. The larger bump also exhibits bistability with the uniform zero steady state. Dimple bumps have the same stability as the larger single-bump solutions and two-bump solutions are always unstable.

There has been substantial work using Amari-like models to model the patterns made by the activity in cortical neurons in working or short-term memory. This work includes studying multiple bumps; travelling waves and fronts; stationary and oscillatory bifurcations; including spike-frequency adaptation; space-dependent delays; examining two-population models (an inhibitory population and an excitatory population); two

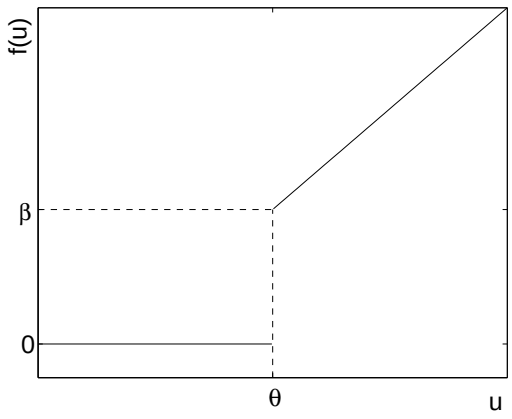

Figure 1.5: Example of a nonsaturating piecewise linear firing rate function, $f(u)$, from Equation (1.3) with threshold θ.

spatial dimensional models; spatially periodic patterns; and spiral waves. This list is not exhaustive. In Amari-like models, many different combinations of delay and adaptation have been used, with one or two populations in one or two spatial dimensions. A model may be written in travelling coordinates to find travelling fronts, waves or bumps. Stability of solutions can be found using various techniques. We explore some of these later in the thesis. Both Coombes [14] and Ermentrout [27] have reviewed many of the various approaches used over the past thirty or so years to model the formation of spatial patterns in persistent neural activity. We briefly review some of these here.

Laing and Troy [69] studied the Amari model in Equation (1.1). For a one-dimensional domain with Heaviside firing rate function and lateral inhibition, they derived existence and stability criteria for equal-width two-bump steady states. They found that families of two-bump solutions are unstable. By using a coupling function with three positive zeros, they found that both stable and unstable two-bump steady states could co-exist. It was found numerically that both single and two-bump stable solutions can co-exist in two spatial dimensions. This implies that stable N-bump solutions for $N > 1$ require a coupling function with more than one positive zero.

Motivated by labelling studies showing that spatially approximate periodic stripes are formed by coupled groups of neurons in the prefrontal cortex [50], Laing *et al.* [70] extended the work of Amari. They allowed a decaying oscillatory form of coupling between neurons using the function

$$w(x) = e^{-b|x|}(b\sin(|x|) + \cos(x)). \tag{1.4}$$

The parameter $b \in \mathbb{R}^+$ governs the rate at which oscillations decay with distance. The constant external stimulus h was removed from the Amari model in Equation (1.1) and a

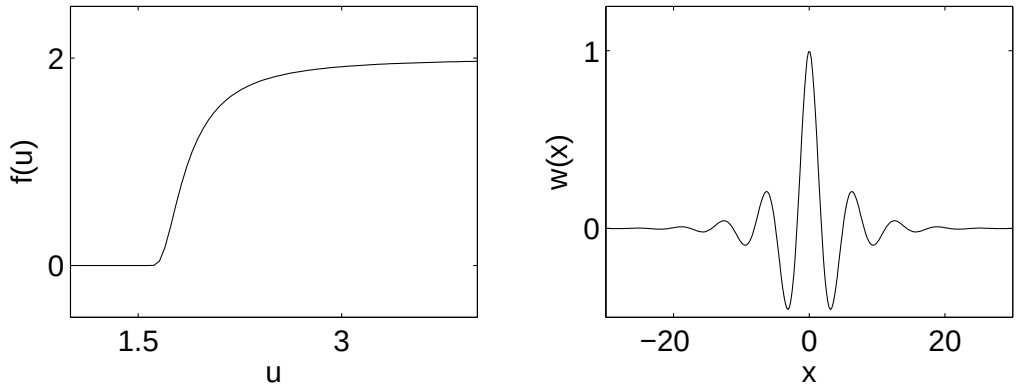

Figure 1.6: Left: Smooth firing rate function in Equation (1.5) with steepness parameter $r = 0.095$ and threshold $\theta = 1.5$. Right: Decaying oscillatory coupling function in Equation (1.4) with decay parameter $b = 0.25$.

threshold, $\theta \in \mathbb{R}^+$, included within the firing rate function instead. Rather than the all or nothing firing rate characteristics of a Heaviside firing rate function, the following smooth firing rate function was used

$$f(u) = 2e^{-r/(u-\theta)^2}\Theta(u-\theta), \tag{1.5}$$

where $r \in \mathbb{R}^+$ is a steepness parameter. The function models neurons firing once threshold is reached and tending to a maximal firing rate limit as the stimulus is increased. The partial integro-differential equation (PIDE) model is

$$\frac{\partial u(x,t)}{\partial t} = -u(x,t) + \int_{-\infty}^{\infty} w(x-y)f(u(y,t))\,dy. \tag{1.6}$$

See Figure 1.6 for Equations (1.4)–(1.5). The form of the model in Equation (1.6) is the form we study in this thesis.

The relaxation of the restrictions Amari placed upon neural coupling and firing permitted both single- and multiple-bump solutions. Multiple-bump solutions are referred to as N-bump solutions. Solutions are homoclinic orbits to the origin. A homoclinic orbit is a trajectory of the flow of the system which joins a fixed point to itself as x moves to $+\infty$ and $-\infty$. Importantly, given the specific choice of $w(x)$ in the given form of the model in Equation (1.6), the use of a smooth firing rate function allows the derivation of a fourth-order ordinary differential equation, solutions of which are also steady states of the PIDE model. The order of the ODE is kernel dependent. This ODE can be expressed as a four-dimensional reversible Hamiltonian system. Numerical methods are required to find solutions of Equation (1.6) given the nonlinearity of the firing rate function when $r > 0$. When $r = 0$, twice the Heaviside function is recovered.

Single-bump solutions are also seen in two population (two layer) models. Pinto and Ermentrout [82] studied a two population Amari–type model in a one spatial dimension domain

$$\frac{\partial u}{\partial t} = -u + \int_{-\infty}^{\infty} w_{ee}(x-y)P_e\left(u(y,t)-\theta\right)\,dy - \int_{-\infty}^{\infty} w_{ie}(x-y)P_i\left(v(y,t)-\theta\right)\,dy \quad (1.7)$$

$$\tau\frac{\partial v}{\partial t} = -v + \int_{-\infty}^{\infty} w_{ei}(x-y)P_e\left(u(y,t)-\theta\right)\,dy. \quad (1.8)$$

Equations (1.7)-(1.8) model a population of excitatory neurons (e) and a population of inhibitory neurons (i) where u and v are the average neural activity of each population respectively. Single-bump steady states of Equations (1.7)–(1.8) were constructed using singular perturbation analysis. Only one single-bump solution was found. A linear bump-width analysis was used to determine the stability of solutions when P_e is the Heaviside function and P_i is the identity.

With instantaneous inhibition ($\tau = 0$), P_e the Heaviside function in Equation (1.2) and P_i the identity, we can solve for v in Equation (1.8) and substitute into Equation (1.7) to obtain

$$\frac{\partial u}{\partial t} = -u + (w_{ee} - w_{ie} \otimes w_{ei}) \otimes \Theta(u-\theta). \quad (1.9)$$

The symbol $\otimes$ represents a spatial convolution. As $w_{ee} - w_{ie} \otimes w_{ei}$ is a coupling function, Equation (1.9) is an Amari–type model. Solution stability agrees with Amari's in that both a wide, stable single-bump steady state and a narrow, unstable single-bump steady state are found. For realistic inhibitory dynamics we set $\tau > 0$ and find that the wide pulse becomes unstable through a Hopf bifurcation. Pinto and Ermentrout showed this change of stability through a similar argument to Amari's stability analysis and also through analysis of the linearised system. Pinto and Ermentrout's [82] model has been extended in further work where bumps that are stable for fast inhibition become stable breathers (bump solutions with width periodically changing as a function of time) through a Hopf bifurcation at a critical relative inhibition time [7].

Travelling waves

Travelling fronts and bumps have been observed in slice preparations [45, 87, 106]. In cortical tissue, metabolic processes can modulate neuronal response through a type of spike-frequency adaptation [73]. There has been much modelling of travelling waves in one-dimensional models. By incorporating delays and adaptation, complexity can be added to the models. Spike-frequency adaptation can lead to the generation of bump solutions for network connectivity that would usually only support travelling fronts [14]. Delays that

depend upon axonal distance are modelled using a finite axonal propagation velocity. A synaptic rate constant can be used to model relative synaptic speed differences between excitatory and inhibitory populations. An example of this approach is the inclusion of the parameter τ in Equation (1.8).

Travelling and standing waves have been found in a model with adaptation and lateral inhibition [21]. Linear recovery has also been modelled [11, 110]. See [8, 15, 16, 54] for some examples of modelling with delay. Different types of delay and adaptation can be included in the same model. An example of this is the modelling of axo-dendritic synaptic processing, finite axonal propagation velocity and spike-frequency adaptation in a single population, one-dimensional model [15] where a simple model of spike-frequency adaptation was shown to change travelling wave solutions from fronts to bumps. Adaptation was included in the two population, one spatial dimension model of Pinto and Ermentrout [81]

$$\frac{\partial u(x,t)}{\partial t} = -u(x,t) + \int_{-\infty}^{\infty} w(x-y)P\left(u(y,t)-\theta\right)\,dy - v(x,t) \tag{1.10}$$

$$\frac{1}{\epsilon}\frac{\partial v(x,t)}{\partial t} = -\beta v(x,t) + u(x,t), \qquad \epsilon \ll 1. \tag{1.11}$$

The negative feedback term, v, is included in the synaptic coupling. The parameter β determines the strength of the negative feedback, P is the firing rate function and w the coupling function. The speed and stability of travelling waves was calculated. It is not necessary to demand that $\epsilon \ll 1$ as the linearity of the equation means that it does not have to be studied in the singular limit.

More recently, Evans functions have been applied to neural field models, particularly with a Heaviside firing rate function, where they can be useful in analysing the bifurcation structure of travelling waves. Evans [30] originally defined the Evans function when developing a stability theorem about Hodgkin-Huxley type excitable nerve axon equations. Evans functions are an analytic function of the eigenvalues of the linearised operator and are used to locate the essential spectrum of this operator. The zeros of an Evans function correspond to the eigenvalues and the order of the zero is the algebraic multiplicity of the eigenvalue.

An Evans function approach was used by Coombes and Owen [16]. With space-dependent delay and Heaviside firing function in a scalar integral field model, a formula for the speed of a travelling front was found. The model was written in the integral form

$$u(x,t) = \int_{-\infty}^{\infty}\int_{0}^{\infty} w(y)\eta(s)f\left(u(x-y,t-s-|y|/v)\right)\,ds\,dy \tag{1.12}$$

where v is the velocity of action potential propagation and $\eta(t)$ models synaptic processing

($\eta(t) = 0$ for $t < 0$). When $\eta(t) = e^{-t}$ and $v \to \infty$, Equation (1.12) is the integro-differential form of Equation (1.6). By rewriting Equation (1.12) in moving coordinates, $\xi = x - ct$, and linearising about a travelling front, an Evans function was defined. The Evans function was used to find the stability of travelling waves.

Recently, Kapitula *et al.* [58] constructed Evans functions for a general class of nonlocal eigenvalue problems. Sandstede [88] constructed Evans functions for a class of nonlocal neuronal networks using the approach of Kapitula *et al.* [58], showing this is the same as the independent construction of Coombes and Owen [16]. Evans function analysis has been used to show that with spike-frequency adaptation in a one-dimensional Amari–type model with lateral inhibition, bump steady states can give rise to breathers (bump solutions with width periodically changing as a function of time) and travelling waves [17]. Evans functions have also been used to find the stability of travelling pulses with a slow recovery variable [83]. Other applications include a one-dimensional model with distributed axonal transmission speeds and nonlocal feedback delay distributions [2] and a two population model with axonal propagation velocities and synaptic rate constants [66].

Turing patterns

In 1952, Alan Turing [97] modelled pattern formation in a simple chemical reaction-diffusion system to account for morphogenesis. His idea was that a stable uniform steady state could give rise to spatially inhomogeneous patterns through diffusion-driven instability. This type of spatio-temporal pattern formation is known as a Turing instability. Murray [75] discusses spatio-temporal pattern formation in biological and chemical systems in depth, using Fourier mode analysis to determine the wavenumber of the unstable mode. In spatio-temporal pattern formation, the unstable mode initally grows exponentially with time and establishes a spatial pattern. Fourier mode analysis is used extensively in the study of spatio-temporal dynamics in neural field models.

Turing instabilities have been found in single population models with dendritic delay [8], with axonal delay and spike-frequency adaptation [102], and in both one and two population models [21, 85]. In a model for intracortical activity based upon the Amari model with synaptic rate constants and finite axonal propagation velocities, Hutt *et al.* [53] found that local excitation and lateral inhibition enabled static periodic patterns (Turing patterns). Local inhibition and lateral excitation enabled oscillatory (Hopf) instabilities. Waves could only occur where their activity propagation velocity was below a certain threshold. A two population model was studied in [107].

Recently, Turing structures have also been analysed in several two-dimensional models. Steyn-Ross *et al.* [94] studied a continuum model of a noise-driven cortex with gap junction connections between inhibitory neurons. Using a linear stability analysis and numerical simulation, they found that Turing structures form when the diffusive coupling between gap junctions is large. Coombes *et al.* [18] also studied another continuum model with space-dependent axonal delays where amplitude equations were developed as well as a Turing analysis.

Homogeneous domains are not always assumed. Turing instabilities have also been found with heterogeneous connections in a model of the primary visual cortex [9] and in neural systems [55].

Two dimensional models

In the mammalian neocortex, there is strong vertical coupling between laminar layers of connectivity patterns. Hence, the cortex is more realistically modelled as a two-dimensional layered sheet rather than as a one-dimensional system. In this kind of planar neural field model, there is near instantaneous vertical propagation from the coupling between layers [14, 27]. The same patterns seen in one dimension are also seen in two dimensions. There are also many other interesting patterns.

Pattern formation in visual hallucinations has been modelled using two-dimensional neural field models [29]. Turing instabilities have also been found in two dimensional models [18, 94]. Spiral waves are seen in two-dimensional media in biological and chemical systems [59]. Once initiated, rotating spiral waves are self-sustainable. Stable spiral waves have been reported in rat neocortical slices and a computational model was developed that predicted many of the experimental results [51]. Spatial inhomogeneity in two-dimensional integral neural fields can give rise to oscillatory bumps through a Hopf bifurcation. The oscillatory bumps can act as a pulse generator and periodically generate travelling bump solutions [84].

We briefly outline the construction of a two-dimensional system using polar coordinates [79]. Writing the Amari–type model in Equation (1.6) in a purely integral framework we have

$$u = \eta \star w \otimes f \circ u \tag{1.13}$$

where $\otimes$ is the spatial convolution, $\star$ is the temporal convolution

$$(\eta \star f)(x,t) = \int_0^t \eta(s) f(x, t-s)\, ds \tag{1.14}$$

and $\eta(t) = e^{-t}\Theta(t)$ is the Green's function of the linear differential operator $\mathcal{L} = 1 + \partial_t$. The two dimensional generalisation of Equation (1.13) is

$$u(\mathbf{r},t) = \int_{\mathbb{R}^2}\int_0^\infty w(|\mathbf{r}-\mathbf{r}'|)\eta(s) f\left(u(\mathbf{r}',t-s)\right)\, ds\, d\mathbf{r}' \tag{1.15}$$

where $u = u(\mathbf{r},t)$, $\mathbf{r} = (r,\theta)$ $(r \in \mathbb{R}^+, \theta \in [0,2\pi], t \in \mathbb{R}^+)$. Time independent solutions satisfy

$$q(\mathbf{r}) = \int_{\mathbb{R}^2} w(|\mathbf{r}-\mathbf{r}'|) f\left(q(\mathbf{r})\right)\, d\mathbf{r}'. \tag{1.16}$$

Linearising about the time independent solution in $u(\mathbf{r},t) = q(\mathbf{r}) + u(\mathbf{r})e^{\lambda t}$ and retaining first order terms, Equation (1.15) becomes

$$u(\mathbf{r}) = \int_{\mathbb{R}^2}\int_0^\infty w(|\mathbf{r}-\mathbf{r}'|)\eta(s) f'\left(q(\mathbf{r})\right) e^{-\lambda s}\, ds\, d\mathbf{r}'. \tag{1.17}$$

Given certain choices of coupling function and firing rate function, the solution of the eigenvalue problem in Equation (1.17) can be used to find an Evans function. The Evans function can then be used to determine the discrete spectrum and hence the stability of the solutions. One example is the work of Owen *et al.* [79], where Evans functions were used to predict both the point of instability and the number of spots a bump solution would split into under variation of the firing threshold. A general stability argument (valid for smooth firing rates) was used to predict the onset of rotating waves. Complexity was added to the model through the inclusion of spike-frequency adaptation. Numerical simulations then showed that structures without rotational symmetry, particularly multi-bumps, could lose stability to angular perturbations and form a rotating wave.

There are many other examples of two dimensional work in the literature. These include the analytical study of plane waves and circular rings, and the numerical study of spiral waves [62], circular solutions [31] and nonradially symmetric breathers [32]. In a two dimensional extension of the model of Pinto and Ermentrout [81], rotating spiral waves on a circular domain have been studied [65]. PDE methods have also been developed to calculate the stability of circularly symmetric solutions with respect to symmetry-breaking perturbations via the numerical solution of an eigenvalue problem [68].

We now conclude our review of some of the literature and look at an approach to modelling gap junctions in a continuum model.

1.3 Derivation of the gap junction model

In this section, we derive a first approximation to modelling gap junctions in a neural field model. The role of gap junctions in synchrony is known [95] and gap junctions are

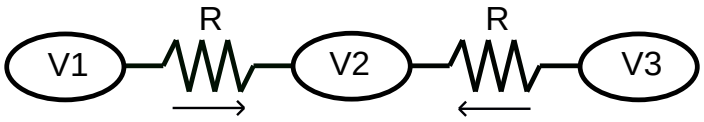

Figure 1.7: Connection of two resistors in a circuit.

often seen in inhibitory networks [36, 38, 40]. Examples of modelling of gap junctions in inhibitory networks with discrete models are seen in [64, 89]. Excitatory networks have also been studied using discrete models. Ermentrout [28] showed that gap junctions destroy persistent states. By assuming a sparsely gap junction-coupled network of excitable cells, Lewis and Rinzel [72] found spontaneous oscillatory activity could be generated. However, there has been little previous work in modelling gap junctions in a continuum model.

The experimental evidence presented by Fukuda *et al.* [36] showing that dense and far-ranging networks can be formed through dendritic gap junctions also provides motivation for a continuum model. A continuum approach has been previously used by researchers at the University of Waikato, New Zealand to develop a physics-based model of general anaesthesia [91, 92, 93]. These researchers then developed a continuum model where both chemical synaptic connectivity and gap junction coupling between inhibitory cells is included [94]. We now develop a continuum model of gap junction coupling using an Amari–type model.

Gap junctions, or electrical synapses, connect neurons with a resistive–like connection. This type of connection creates a diffusive-type effect between surrounding cells as the electrical charge spreads and has the effect of causing the voltage of these cells to become similar. In a voltage model, where V_i is the voltage of the i^{th} neuron and w_{ij} is the strength of the gap junction coupling between the i^{th} and j^{th} neurons, and ignoring other currents, we have an equation for the change in voltage of each neuron i $(i = 1, \ldots, N)$ of

$$\frac{dV_i}{dt} = \sum_{j=1}^{N} w_{ij}(V_j - V_i). \tag{1.18}$$

We must determine an appropriate way of modelling electrical coupling over a continuous domain rather than a discrete one. A gap junction connection between two cells obeys Ohm's law, where the current flow between the two cells is proportional to the voltage difference of the two cells. Thus

$$I = \frac{\Delta V}{R} \tag{1.19}$$

where I is the current, ΔV is the difference in voltage and R is the resistance. Thus gap

junctions act as resistors in a circuit.

Consider the connection of neurons via resistors. See Figure 1.7 for a schematic of two resistors connecting three neurons. Assume we have N neurons connected by resistors in series. Again, let i be the index of a neuron for $i = 1, \dots N$ and let V_i be the voltage or potential of the i^{th} neuron at time t. Let Δx be the distance between each neuron. We evaluate the current coming into neuron i due to the voltage differences at time t as follows:

$$\begin{aligned}\frac{(V_{i+1}-V_i)}{R}+\frac{(V_{i-1}-V_i)}{R} &= \frac{(\Delta x)^2}{R}\frac{(V_{i+1}-2V_i+V_{i-1})}{(\Delta x)^2}\\ &= \frac{(\Delta x)^2}{R}\nabla^2 V_i \\ &= \kappa^2\,\nabla^2 V_i\end{aligned} \tag{1.20}$$

where $\kappa^2 = (\Delta x)^2/R$ and $\nabla^2 V_i$ is the finite difference approximation of the second spatial derivative of V_i. Therefore, evaluation of a series of resistors in a circuit results in the finite difference approximation of the second spatial derivative of V.

We thus add $\partial^2 u/\partial x^2$ to Equation (1.6) to include the effect of gap junctions[2] and obtain

$$\frac{\partial u(x,t)}{\partial t} = \kappa^2\frac{\partial^2 u}{\partial x^2} - u(x,t) + \int_{-\infty}^{\infty} w(x-y)f(u(y,t))\,dy. \tag{1.21}$$

The strength of the term modelling gap junctions is given by the positive coefficient κ^2. We refer to Equation (1.21) as the "gap junction" model. Equation (1.6) is recovered when we set $\kappa^2 = 0$.

In this thesis, we refer to the model of [70] in Equation (1.6) as the "Amari" model. We study both the Amari model and the gap junction model in this thesis. Our interest is in seeing how including a term to model gap junctions in Equation (1.6) changes the solutions found in the literature. As discussed earlier, gap junctions are dynamic structures. We consider only a static model in the thesis, however dynamical models have been used to model gap junctions previously [4].

1.4 Thesis outline

The outline of the remainder of the thesis is as follows:

- In Chapter 2 we investigate analytical solutions of the two models. In general, the nonlinearity of the model means that steady states of the model can only be inves-

[2] Although we derived a term to model the effect of gap junctions, this term could also be used to model other types of diffusive processes.

tigated numerically. However, by placing assumptions upon the firing rate function, analytical solutions are possible. Using a lateral-inhibition coupling function with Heaviside firing rate function, as used by Amari, we review previously published results for the Amari model. First, we find spatially uniform steady states, then analytic single-bump steady state solutions using the integral expression for steady states. Lastly, we use a method of piecewise construction of steady state solutions by deriving a fourth-order ODE from the PIDE. These methods are then applied to the gap junction model. We find that as the strength of the term modelling gap junctions increases, the threshold must drop for single-bump solutions to be sustained.

- In Chapter 3 we use the decaying oscillatory coupling function and smooth firing rate function of [70] with both the Amari model and the gap junction model. This permits multiple-bump solutions. Numerical methods must be used to find solutions given the nonlinearity of the model. We rely upon formulation of the partial integro-differential equation as an ordinary differential equation representing steady states to facilitate numerical analysis. Steady state solutions are homoclinic orbits to a zero fixed point of the ODE, therefore we use HomCont in AUTO to find bifurcation curves. We also use our own code for the pseudo-arclength method to find solutions. We review some results from [70], then see how solutions change for the gap junction model. It is found that as the firing rate function steepens for a range of firing threshold, the solution curve becomes discontinuous. These results have not been previously described in the literature. We use phase space analysis to investigate this phenomenon further in Chapter 5.

- In Chapter 4 we apply the method of piecewise construction of steady states from Chapter 2 to the Amari model with the decaying oscillatory coupling function. This is done for both a shifted Heaviside firing rate function and a piecewise linear firing rate function. In each case, discontinuity in the solution curve depends upon the level of the firing threshold and the steepness of the firing rate function, as in Chapter 3. We then extend the analysis to the gap junction model and find similar behaviour.

- In Chapter 5, we take a phase space approach and write the Amari model as a four-dimensional, reversible Hamiltonian system. We develop a numerical technique that reduces the problem of finding single-bump symmetric and asymmetric homoclinic orbits to finding the zeros of a real scalar function. We find symmetric homoclinic orbits to the zero fixed point of the Hamiltonian system. For certain areas of

parameter space, a separate disconnected solution curve can be found within the larger solution curve. The separate solution curve has not been previously described in the literature. For certain levels of firing threshold, as the firing rate function steepens, the small solution curve eventually touches the main curve. The main solution curve breaks as the firing rate function continues to steepen. This explains the phenomenon seen in Chapter 3 and 4. Therefore, for a certain steepness of firing rate function, stable homoclinic orbits do not exist in a region of parameter space. This has not been previously described in the literature.

We look for homoclinic orbits to other fixed points of the system using level set analysis with three different firing rate functions. We show that there is a global bifurcation where the stable and unstable manifolds of the zero fixed point and a positive fixed point collide for an appropriate level of threshold when the firing rate function is sufficiently steep. For a step firing rate function, we find a system symmetry which allows derivation of a bifurcation curve for homoclinic orbits to the positive steady state. Using travelling fronts, we show there is a heteroclinic orbit between the zero fixed point and the positive fixed point at these bifurcation points. We also briefly discuss future work on travelling fronts in the area of discontinuity in the solution curves.

- In Chapter 6 we discuss four different numerical techniques that may be used to find asymmetric steady state solutions. One of the techniques is a shooting method we develop that utilises the Hamiltonian structure of the system. We successfully find one- and two-bump asymmetric solutions in a region of parameter space.

- In Chapter 7 we present five different approaches to determining the stability of solutions. With each method, we first review its application to the Amari model, then apply it to the gap junction model. We use both the Mexican hat coupling function and the decaying oscillatory coupling function, where possible. The first three methods have been previously presented in the literature and require a step firing rate function. First, we discuss the linear stability analysis of Amari. Second, we apply the linearised stability analysis of Pinto and Ermentrout [81]. Third, we follow Coombes and Owen [16] and use Evans functions to find the isolated eigenvalues of travelling fronts. We then develop an eigenvalue analysis of the full, time-dependent model with the smooth firing rate function. Finally, we discuss how the method of numerical integration can be used to indicate solution stability.

Throughout the thesis, we indicate solution stability where appropriate and refer the reader to Chapter 7 for the methodology.

- In Chapter 8 we study the formation of spatially periodic patterns (Turing patterns) through spatially heterogeneous perturbations of a uniform steady state. We apply the analytical stability analysis of Hutt *et al.* [53] to both the Amari model and the gap junction model. Using the decaying oscillatory coupling function, we find that the Turing structures become transient and exhibit Type-I intermittency as we vary the coupling parameter. To our knowlege, this is the first time transient Turing structures have been found in a one-dimensional neural field model. We then extend the Turing instability analysis to the Amari model in two dimensions. The behaviour is similar to that of the one-dimensional model.

Chapter 2

Finding steady states analytically

2.1 Introduction

In this chapter we study the one-dimensional single population neural field model discussed in the rest of the thesis. We find steady state solutions of the model using analytical methods.

We restrict the work in this chapter to the existence of spatially uniform steady states and single-bump steady states. We note that the model is capable of different types of pattern formation such as N-bump solutions and travelling waves, as discussed in the previous chapter. We study these types of solution in later chapters.

We study the one-dimensional neural field model of the 1977 work of Amari [1]

$$\tau \frac{\partial u(x,t)}{\partial t} = -u(x,t) + \int_{-\infty}^{\infty} w(x-y) f(u(y,t))\, dy + h + s(x,t) \tag{2.1}$$

where $u(x,t)$ is the average membrane potential of the neural element at position $x \in (-\infty, \infty)$ in the neural field at time $t \geq 0$, $s(x,t)$ is an inhomogeneous input and h is a constant external input. This assumes a spatially homogeneous and isotropic domain. The model in Equation (2.1) also assumes an infinitely fast propagation velocity of action potentials along axons, therefore there is no temporal delay in synaptic coupling.

Amari studied the existence and stability properties of single-bump steady state solutions of the model in Equation (2.1) in the absence of inhomogeneous input ($s(x,t) = 0$) with lateral-inhibition and a Heaviside firing rate function.

We modify Equation (2.1) by removing the term h and including instead a firing threshold in the firing rate function. The function f is not the same as before. We set all external stimuli to be zero and the synaptic rate constant to be $\tau = 1$ to obtain

$$\frac{\partial u(x,t)}{\partial t} = -u(x,t) + \int_{-\infty}^{\infty} w(x-y) f(u(y,t))\, dy. \tag{2.2}$$

This type of model has been studied extensively in modelling short term memory and working memory [69, 70], visual hallucinations [10, 29], motion perception and robotic navigation [41].

Laing *et al.* [70] reviewed the existence and stability results obtained by Amari [1]. They then extended the analysis of the original model in Equation (2.1) and applied it to the modified form of the model in Equation (2.2). We use this modified model also. In this thesis, we refer to Equation (2.2) as the "Amari model". By restricting the firing rate function $f(u)$ to be the shifted Heaviside function, $\Theta(u-\theta)$, with threshold θ such that

$$f(u) = \Theta(u-\theta) = \begin{cases} 1, & \text{if } u \geq \theta \\ 0, & \text{if } u < \theta, \end{cases} \tag{2.3}$$

we can find steady state solutions of Equation (2.2) analytically. In the step firing rate function in Equation (2.3), a neuron fires at its maximum rate if $u \geq \theta$ or not at all if $u < \theta$ (see Figure 2.1). When the threshold is $\theta = 0$, the function in Equation (2.3) is the Heaviside function.

We review the general properties of lateral-inhibition outlined by Amari [1]:

1. $w(x)$ is symmetric, that is, $w(-x) = w(x)$ for all $x \in \mathbb{R}$;
2. there exists a unique, finite, positive $x = x_0$ such that $w(x) > 0$ on the interval $(-x_0, x_0)$ where $w(-x_0) = w(x_0) = 0$;
3. there exists a unique, finite, positive $x_{min} > x_0$ such that $w(x)$ is decreasing on the interval $(0, x_{min})$ and increasing on the interval $(-x_{min}, 0)$;
4. $w(x) < 0$ on $(-\infty, -x_0) \cup (x_0, \infty)$; and,
5. $w(x)$ is both continuous and integrable on $\mathbb{R}$.

Lateral inhibition produces excitatory connections for close neural elements and inhibitory connections for neural elements separated by a distance greater than x_0. In this chapter we use the "Mexican hat"-type coupling function

$$w(x) = Ke^{-k|x|} - Me^{-m|x|} \tag{2.4}$$

where $K > M > 0$ and $k > m > 0$ ($K, M, k, m \in \mathbb{R}^+$). The coupling function satisfies the properties listed above. The parameter values of $K = 3.5, M = 3, k = 1.8, m = 1.52$ from [70] are used for the numerical work in this chapter (see Figure 2.1).

Gertsner and Kistler [39] studied stationary patterns of neuronal activity in spatially structured networks with a sigmoidal firing rate function, lateral-inhibition and external

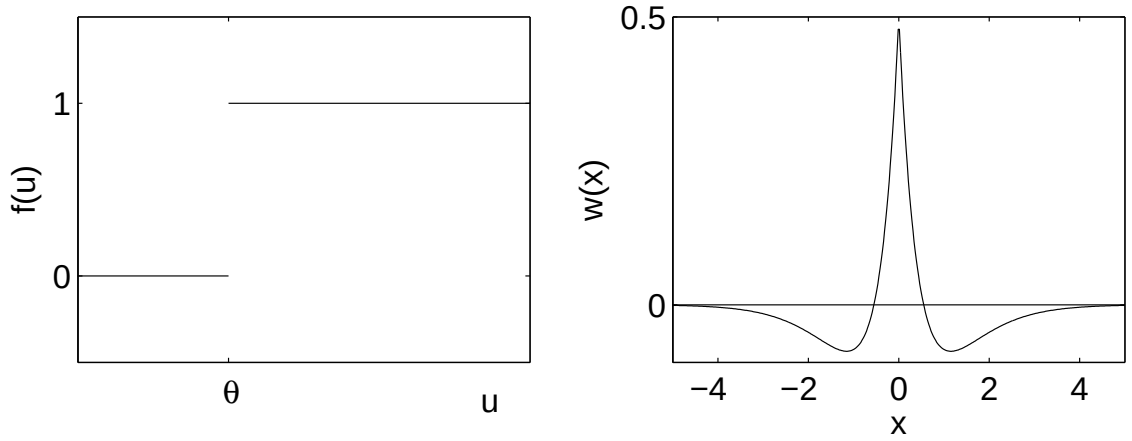

Figure 2.1: Left: Shifted Heaviside firing rate function of Equation (2.3) with threshold θ. Right: Mexican hat coupling function of Equation (2.4) with parameter values $K = 3.5, M = 3, k = 1.8, m = 1.52$.

input. They studied spatially homogeneous, stationary solutions and found that there could be up to three of these, depending upon the strength of the external input. They used linear stability analysis to determine stability with respect to spatially homogeneous perturbations. However, they pointed out that even though standard stability analysis may show stability, the spatially uniform steady state may be unstable to spatial perturbations. We will return to this in a later chapter exploring Turing structures in our neural model, Chapter 8. In the present chapter we investigate spatially homogeneous solutions.

In her PhD thesis, Guo [47] studied the existence and stability of stationary bump solutions in the Amari model with lateral inhibition and a non-saturating piecewise linear firing rate function. Guo stated that this particular firing rate function was chosen as it was seen as more biophysically relevant than a Heaviside firing rate function, given that cortical neurons exhibiting persistent activity usually fire well below their maximum rate.

Using the approach of [70], Guo derived a fourth-order ODE, satisfied by stationary solutions of the Amari model, by applying Fourier transforms in space. Guo constructed single-bump, steady state solutions using a piecewise differential equation framework where the stationary bump was represented with above-threshold functions and below-threshold functions. This piecewise differential equation method is another technique that can be used to find steady state solutions analytically. We use the piecewise differential equation method in this chapter to find single-bump solutions of both the Amari and gap junction models with lateral inhibition and the shifted Heaviside firing rate function. The method is discussed further in Chapter 4 where we relax the restrictions on the coupling function

and the firing rate function, then apply bifurcation analysis.

The outline of the present chapter is as follows. The next section reviews some known results for the Amari model using lateral inhibition and a shifted Heaviside firing rate function. We take a similar approach to [39, 47] and start by reviewing spatially uniform solutions of Equation (2.2). Amari studied the existence of single-bump solutions, therefore we review the existence criteria for single-bump steady state solutions, using the integral expression for steady states. We construct piecewise single-bump steady state solutions using the method of [47], although we use different coupling parameters to those used by [47].

We then turn to our gap junction model from Chapter 1 of

$$\frac{\partial u(x,t)}{\partial t} = \kappa^2 \frac{\partial^2 u}{\partial x^2} - u(x,t) + \int_{-\infty}^{\infty} w(x-y) f(u(y,t))\, dy. \tag{2.5}$$

Our interest lies in seeing how the inclusion of the extra term modelling gap junctions changes the steady state solutions of the Amari model. We find spatially uniform solutions, then use Green's functions to find single-bump steady state solutions. Lastly, we again construct piecewise single-bump steady state solutions, by deriving a sixth-order ODE, solutions of which are stationary solutions of the model in Equation (2.5).

The stability calculations for all spatially localised steady state solutions in this chapter are given in Chapter 7 where several different approaches from the literature are applied to the Amari model and then to the gap junction model. The results are quoted in the present chapter where appropriate.

2.2 Amari model

A steady state or stationary solution of the Amari model in Equation (2.2) satisfies the equation

$$u(x) = \int_{-\infty}^{\infty} w(x-y) f(u(y))\, dy. \tag{2.6}$$

Solutions of Equation (2.6) are defined on an infinite domain. When we use numerical methods to find solutions, for example, numerical integration, continuation or construction of a solution from an explicit function, we must use a finite domain. We choose a sufficiently large domain size that boundaries are unlikely to have any significant effect on spatially localised solutions. Without spatial structure in the solution, Equation (2.6) easily simplifies to provide homogeneous steady state solutions. When we permit spatial structure in the solution, we define a width parameter for the above-threshold region. We

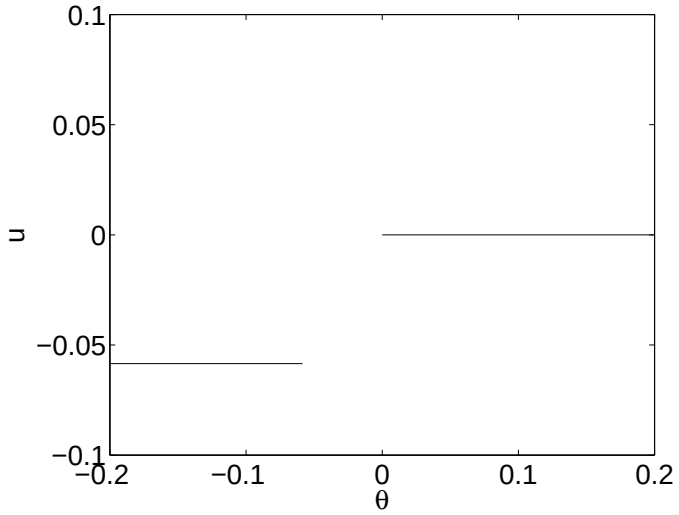

Figure 2.2: Spatially uniform steady states of Equation (2.2) with the shifted Heaviside firing rate function in Equation (2.3) and the coupling function in Equation (2.4) with parameter values as in Figure 2.1. Threshold is at θ. These are stable solutions.

solve for single-bump solutions explicitly, by evaluating the convolution on the righthand side of Equation (2.6).

Spatially uniform steady states

We first look for spatially uniform steady state solutions of the model. Let u^* denote a spatially uniform steady state. With no spatial structure in the solution and assuming $f(u)$ is the shifted Heaviside function in Equation (2.3), Equation (2.6) becomes the scalar equation

$$u^* = Jf(u^*) \tag{2.7}$$

where

$$J = \int_{-\infty}^{\infty} w(x)\,dx = 2\left(\frac{K}{k} - \frac{M}{m}\right). \tag{2.8}$$

Hence, $u^* = 2\big(K/k - M/m\big)$ for $\theta < 2\big(K/k - M/m\big)$ and $u^* = 0$ for $\theta > 0$, with no solutions for $2\big(K/k - M/m\big) < \theta < 0$. See Figure 2.2. Let $u = u^* + v$ where v is a spatially uniform perturbation. Using linear stability analysis,

$$\frac{dv}{dt} = v\big(Jf'(u^*) - 1\big).$$

Then u^* is stable to spatially uniform perturbations if $Jf'(u^*) < 1$.

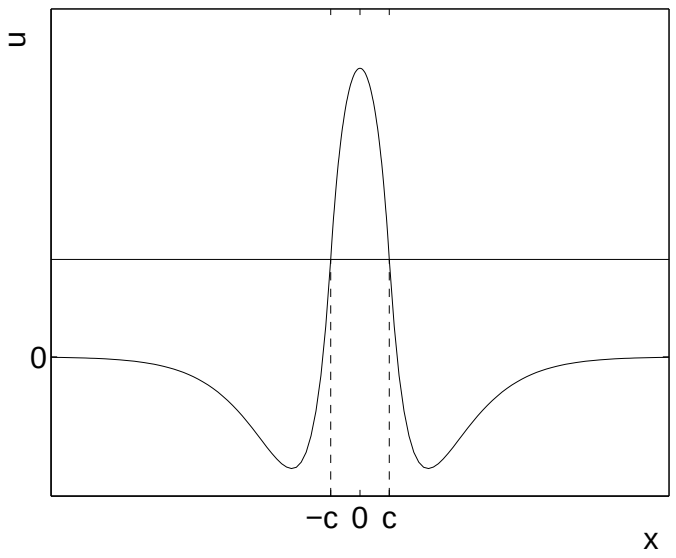

Figure 2.3: Structure of symmetric single-bump solution centered at $x = 0$ with width $2c$ and threshold θ given by the horizontal line.

Single-bump steady states

Consider a stationary solution of the form of a single bump of width $2c$ where $c > 0$, such that $u(c) = u(-c) = \theta$, $u(x) \geq \theta$ for $|x| < c$ and $u(x) < \theta$ for $|x| > c$. See Figure 2.3 for a schematic. With $f(u)$ as in Equation (2.3), Equation (2.6) reduces to

$$u(x) = \int_{-c}^{c} w(x-y)\,dy. \tag{2.9}$$

Using $w(x)$ from Equation (2.4), Equation (2.9) becomes

$$\begin{aligned} u(x) &= \int_{-c}^{c} (Ke^{-k|x-y|} - Me^{-m|x-y|})\,dy \\ &= \int_{x-c}^{x+c} (Ke^{-k|z|} - Me^{-m|z|})\,dz. \end{aligned} \tag{2.10}$$

Evaluating this, the expression for a single-bump steady state solution of width $2c$ of the Amari model in Equation (2.2) is

$$u(x) = \begin{cases} \dfrac{K}{k}\left(e^{k(x+c)} - e^{k(x-c)}\right) - \dfrac{M}{m}\left(e^{m(x+c)} - e^{m(x-c)}\right), & \text{if } x < -c \\ \dfrac{K}{k}\left(2 - e^{k(x-c)} - e^{-k(x+c)}\right) - \dfrac{M}{m}\left(2 - e^{m(x-c)} - e^{-m(x+c)}\right), & \text{if } -c < x < c \\ \dfrac{K}{k}\left(e^{-k(x-c)} - e^{-k(x+c)}\right) - \dfrac{M}{m}\left(e^{-m(x-c)} - e^{-m(x+c)}\right), & \text{if } c < x. \end{cases} \tag{2.11}$$

Evaluating the self-consistency condition of $u(c) = \theta$ in Equation (2.11), we obtain a

nonlinear equation in c, the bump half-width, of

$$\frac{K}{k}(1-e^{-2kc})-\frac{M}{m}(1-e^{-2mc})-\theta=0. \tag{2.12}$$

This is a special case of a more general existence result that has been derived before [1, 47, 70]. Amari [1] derived an existence condition for the model in Equation (2.1), where there is no threshold, but there is a constant external input, h. The same approach can be applied to our model in Equation (2.2). We briefly discuss the derivation of the existence condition here.

In the analysis of single-bump solutions, Amari [1] uses the notation

$$W(x)=\int_0^x w(y)\,dy. \tag{2.13}$$

If Equation (2.2) has a single-bump solution with region of excitation $R(u)=(-c,c)$ then

$$u(x)=\int_{-c}^{c} w(x-y)\,dy=W(x+c)-W(x-c). \tag{2.14}$$

When $x=c$, $u(c)=\theta$ and as $W(0)=0$, Equation (2.14) becomes

$$W(2c)=\theta. \tag{2.15}$$

Equation (2.15) can have zero, one or two positive solutions, depending upon W and the value of the threshold. The number of solutions of Equation (2.15) is equal to the number of single-bump solutions of Equation (2.2). We use Equation (2.13) to construct $W(x)$ for the coupling function in Equation (2.4). For $\theta=0.07$, there are two values, $a1$ and $a2$, that satisfy Equation (2.15). Hence there are two single-bump steady state solutions for these parameter values. See Figure 2.4 for a schematic.

To demonstrate the existence condition in Equation (2.12), we choose a particular value of $\theta=0.07$. Using Newton's method [60], solutions of Equation (2.12) are $c=0.0989716$ and $c=0.5691795$. From the function defined in Equation (2.11), we present the full solution, $u(x)$, over a finite domain for these two specific values of c in Figure 2.5, with a horizontal line at $u=\theta$. The smaller, narrower solution is unstable and the taller, wider solution is stable (see Chapter 7 for the stability analysis).

Piecewise construction of steady states

In this section we introduce the method of constructing piecewise single-bump steady state solutions of the Amari model in [47]. Guo [47] reviewed the Amari model with a shifted Heaviside firing rate function. We do the same in this section, using the parameter values

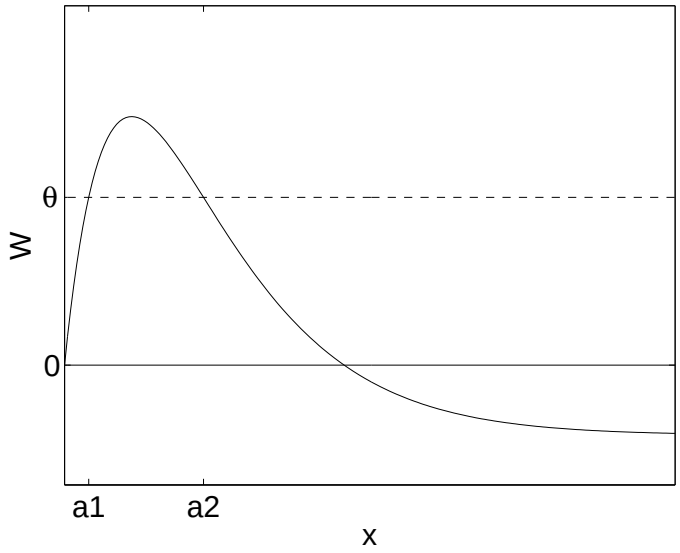

Figure 2.4: Threshold given by θ and $W(x)$ from Equation (2.13). There are two single-bump steady state solutions of widths $2c = a1$ and $2c = a2$, where $W(x) = \theta$.

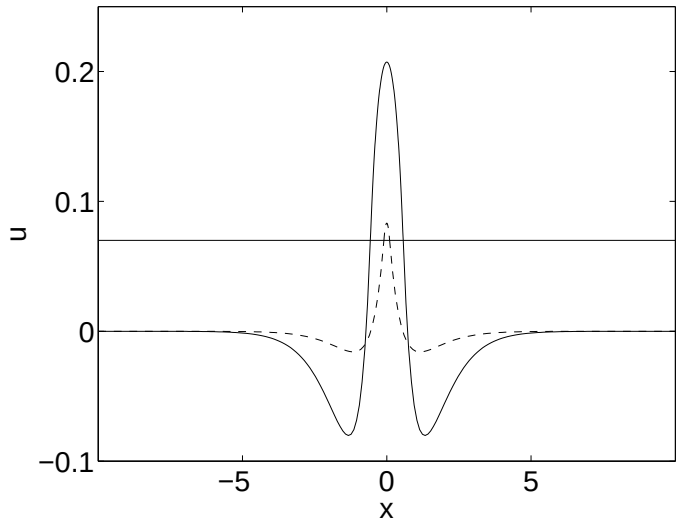

Figure 2.5: Two single-bump steady state solutions to the Amari model in Equation (2.2) with step firing rate function ($\theta = 0.07$) and lateral inhibition (parameter values of Figure 2.1). Solid line: stable solution; dashed line: unstable solution.

of the previous section. We look for symmetric single-bump solutions centred at $x = 0$. Only one half of the bump is constructed ($x \geq 0$) as the change of variables $x \to -x$ can be used to find the solution for $x < 0$.

A fourth-order piecewise ODE in u is derived from Equation (2.6) by using Fourier transforms in space. For a step firing rate function, the ODE can be written as two linear differential equations – a nonhomogeneous ODE for an above-threshold region and a homogeneous ODE for a below-threshold region. At the threshold, we have matching conditions on u and its derivatives to obtain a smooth and continuous function on $\mathbb{R}$. Given the assumption of a single-bump solution, there is the boundary condition

$$\lim_{x \to \pm\infty} (u, u', u'', u''') \to (0, 0, 0, 0). \tag{2.16}$$

All derivatives are with respect to space. We choose a threshold $\theta > 0$. A single-bump solution of Equation (2.6) with width $2c$ satisfies

$$u(x) \begin{cases} > \theta, & \text{if } |x| < c \\ = \theta, & \text{if } x = -c \text{ or } x = c \\ < \theta, & \text{if } c < |x| \end{cases} \tag{2.17}$$

and Equation (2.16).

Derivation of the ODE

The continuous Fourier transform is valid when used on compactly bounded smooth functions. We can therefore use Fourier transforms to derive an ordinary differential equation from Equation (2.6) if we assume the firing rate function, $f(u)$, is a continuous function. We then take the limit of the steepness of $f(u)$ as tending to infinity and obtain the Heaviside function. Thus we can use the Fourier transform

$$F[p](\alpha) = \int_{-\infty}^{\infty} p(x) e^{-i\alpha x} \, dx \tag{2.18}$$

where $p \in L^1(\mathbb{R})$ and $\alpha \in \mathbb{R}$ is the transform variable. The inverse Fourier transform is

$$p(x) = \frac{1}{2\pi} \int_{-\infty}^{\infty} F[p](\alpha) e^{i\alpha x} \, d\alpha. \tag{2.19}$$

We apply the Fourier transform to Equation (2.6) to obtain

$$F[u] = F[w] F[f(u)]. \tag{2.20}$$

We note that a convolution in space becomes a multiplication in frequency space under the application of the Fourier transform. The Fourier transform of $w(x)$ in Equation (2.4) is

$$F[w] = 2\left[\frac{km^2K - k^2mM + (kK - mM)\alpha^2}{k^2m^2 + (k^2 + m^2)\alpha^2 + \alpha^4}\right]. \tag{2.21}$$

We substitute for $F[w]$ in Equation (2.20) and multiply both sides by the denominator of the right hand side to obtain

$$(k^2m^2+(k^2+m^2)\alpha^2+\alpha^4)F[u]-2\left(km^2K - k^2mM + (kK - mM)\alpha^2\right)F[f(u)] = 0. \tag{2.22}$$

Use of the Fourier transform identities

$$F[u^{(iv)}] = \alpha^4 F[u] \text{ and } F[-u''] = \alpha^2 F[u] \tag{2.23}$$

gives

$$F[u^{(iv)}-(k^2+m^2)u''+k^2m^2u] = 2(km^2K-k^2mM)F[f(u)]+2(kK-mM)F[f''(u)]. \tag{2.24}$$

A fourth-order ODE is obtained through the application of inverse Fourier transforms to Equation (2.24)

$$u^{(iv)} - (k^2 + m^2)u'' + k^2m^2u = 2km(mK - kM)f(u) - 2(kK - mM)f''(u(x)). \tag{2.25}$$

If u is a solution of the ODE in Equation (2.25) and satisfies Equation (2.16) then Equations (2.20) – (2.24) are satisfied. We claim that u is a solution of Equation (2.6). Hence the problem of finding single-bump solutions of Equation (2.6) is reduced to finding single-bump solutions of the ODE in Equation (2.25). We now use the ODE to find steady state solutions of Equation (2.2).

Construction of solutions

To find symmetric single-bump steady state solutions of width $2c$, with a step firing rate function, we find u for $x \in \mathbb{R}_0^+$ only. We decompose u into two functions, u_T and u_L, such that $u_T(x) > \theta$ and $u_L(x) < \theta$. See Figure 2.6 for a schematic. Then $u_T(c) = u_L(c) = \theta$ and

$$u(x) = \begin{cases} u_T, & 0 \le x < c \\ u_L, & c < x. \end{cases} \tag{2.26}$$

The ODE in Equation (2.25) can be written as two linear differential equations

$$u_T'''' - (k^2 + m^2)u_T'' + k^2m^2u_T = 2km(mK - kM), \quad \text{for } 0 \le x < c \tag{2.27}$$

$$u_L'''' - (k^2 + m^2)u_L'' + k^2m^2u_L = 0, \quad \text{for } c < x. \tag{2.28}$$

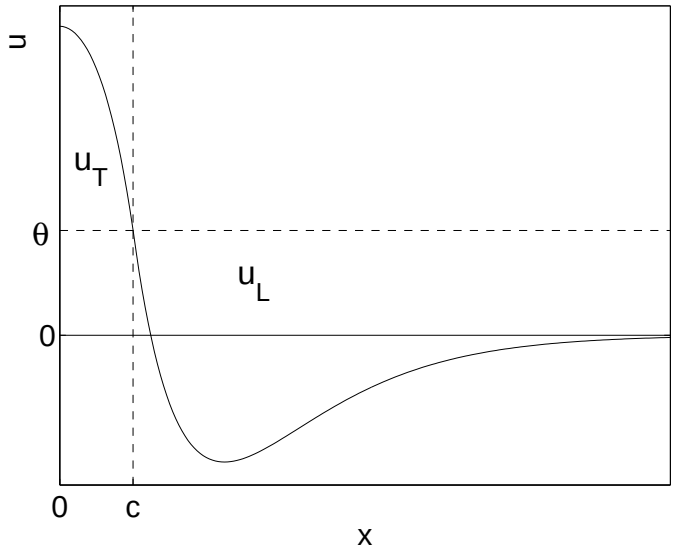

Figure 2.6: Piecewise construction of a single-bump solution for $x \in \mathbb{R}_0^+$ with a step firing rate function, horizontal line at $u = \theta$, above threshold function u_T and below threshold function u_L.

Solutions of u_T must satisfy the nonhomogeneous ODE in Equation (2.27) on the interval $0 \leq x < c$. Solutions are of the form

$$u_T(x) = C_1(e^{kx} + e^{-kx}) + C_2(e^{mx} + e^{-mx}) + \frac{2(mK - kM)}{km}, \qquad (C_1, C_2 \in \mathbb{R}). \quad (2.29)$$

Solutions of u_L must satisfy the homogeneous ODE in Equation (2.28) for $c < x$. They must also satisfy the boundary condition

$$\lim_{x \to \infty} u_L \to 0. \quad (2.30)$$

Thus, solutions are of the form

$$u_L(x) = C_3 e^{-kx} + C_4 e^{-mx}, \qquad (C_3, C_4 \in \mathbb{R}). \quad (2.31)$$

The functions u_T and u_L, and their first three derivatives, must satisfy the matching conditions

$$u_T(c) = u_L(c) = \theta \quad (2.32)$$

$$u_T^{'}(c) = u_L^{'}(c) \quad (2.33)$$

$$u_T^{''}(c) = u_L^{''}(c) - 2(kK - mM) \quad (2.34)$$

$$u_T^{'''}(c) = u_L^{'''}(c) \quad (2.35)$$

The first two matching conditions are a result of the continuity of u and $u^{'}$. Note that $u^{''}$ has a discontinuity at $x = c$ as there is a jump in $u^{''}(c)$ given the shifted Heaviside firing rate function.

Evaluation of Equations (2.32)–(2.35) gives the system of equations

$$C_1(e^{kc}+e^{-kc})+C_2(e^{mc}+e^{-mc})+\frac{2(mK-kM)}{km}=C_3e^{-kc}+C_4e^{-mc} \tag{2.36}$$

$$kC_1(e^{kc}-e^{-kc})+mC_2(e^{mc}-e^{-mc})=-kC_3e^{-kc}-mC_4e^{-mc} \tag{2.37}$$

$$k^2C_1(e^{kc}+e^{-kc})+m^2C_2(e^{mc}+e^{-mc})=k^2C_3e^{-kc}+m^2C_4e^{-mc}-2(kK-mM) \tag{2.38}$$

$$k^3C_1(e^{kc}-e^{-kc})+m^3C_2(e^{mc}-e^{-mc})=-k^3C_3e^{-kc}-m^3C_4e^{-mc}. \tag{2.39}$$

Equations (2.32)–(2.35) can be solved in terms of c for given parameter values of K, M, k, m:

$$C_1=-\frac{K}{k}e^{kc} \tag{2.40}$$

$$C_2=\frac{M}{m}e^{mc} \tag{2.41}$$

$$C_3=\frac{K}{k}(e^{kc}-e^{-kc}) \tag{2.42}$$

$$C_4=-\frac{M}{m}(e^{mc}-e^{-mc}). \tag{2.43}$$

Substituting for C_1, C_2, C_3, C_4 from Equations (2.40)–(2.43) into the formulas for u_T and u_L in Equations (2.29) and (2.31) respectively gives

$$u_T(x)=-\frac{K}{k}(e^{k(x+c)}+e^{-k(x-c)})+\frac{M}{m}(e^{m(x+c)}+e^{-m(x-c)})+\frac{2(mK-kM)}{km} \tag{2.44}$$

$$u_L(x)=\frac{K}{k}(e^{-k(x-c)}-e^{-k(x+c)})-\frac{M}{m}(e^{-m(x-c)}-e^{-m(x+c)}). \tag{2.45}$$

Setting $x=c$ in Equation (2.45) and evaluating $u(c)=\theta$, the existence condition for a single-bump solution is

$$\frac{K}{k}(1-e^{-2kc})-\frac{M}{m}(1-e^{-2mc})-\theta=0. \tag{2.46}$$

This is the same as the existence condition in Equation (2.12) in Section 2.2. A change of variables of $x\to -x$ in Equation (2.26) permits construction of the other half of the solution for $x\in(-\infty,0]$. Therefore, Equation (2.26) defines a single-bump steady state solution of the Amari model in Equation (2.2) for $x\in\mathbb{R}_0^+$ with lateral inhibition and step firing rate function.

This completes our review of some results of the Amari model that can be found analytically. We now apply these analytical techniques to the gap junction model and see how solutions differ from those found in this section for the Amari model.

2.3 Gap junction model

Steady state solutions of the gap junction model in Equation (2.5) satisfy the equation

$$u(x) = \kappa^2 \frac{d^2u}{dx^2} + \int_{-\infty}^{\infty} w(x-y) f(u(y))\, dy. \tag{2.47}$$

It is more difficult to find single-bump solutions when the term $\dfrac{d^2u}{dx^2}$ is included. To find single-bump solutions of Equation (2.47), we use Green's functions.

Spatially uniform steady states

We first find spatially uniform solutions of the gap junction model in Equation (2.47). Without spatial structure in the solution, the second spatial derivative in Equation (2.47) is always zero. The model reverts to the Amari model and Equation (2.47) reduces to Equation (2.6). Therefore, uniform steady states of the gap junction model are the same as those of the Amari model, $u = 2\big(K/k - M/m\big)$ for $\theta < 2\big(K/k - M/m\big)$ and $u = 0$ for $\theta > 0$, as seen previously in Figure 2.2.

Single-bump steady states

Using Green's functions [90], we solve Equation (2.47) to find single-bump steady states of the gap junction model. Green's functions can be used to solve nonhomogeneous n^{th}-order linear differential equations of the form

$$\mathcal{L}u(x) = H(x) \tag{2.48}$$

over $\mathbb{R}$ with n suitable boundary conditions. $\mathcal{L}$ is a linear differential operator acting upon u over the domain $\mathbb{R}$ and $H(x)$ is a continuous function. A Green's function, $G(x,\xi)$, of $\mathcal{L}$ is any solution of

$$\mathcal{L}G(x,\xi) = \delta(x-\xi), \qquad x \in \mathbb{R} \tag{2.49}$$

satisfying the boundary conditions. If such a function G can be found for the operator $\mathcal{L}$, then we can multiply both sides of Equation (2.49) by $H(\xi)$ and integrate to obtain

$$\int_{\mathbb{R}} \mathcal{L}G(x,\xi)H(\xi)\, d\xi = \int_{\mathbb{R}} \delta(x-\xi)H(\xi)\, d\xi. \tag{2.50}$$

Thus, from Equations (2.48) and (2.50) we have

$$\mathcal{L}u(x) = \int_{\mathbb{R}} \mathcal{L}G(x,\xi)H(\xi)\, d\xi \tag{2.51}$$

$$= \mathcal{L}\int_{\mathbb{R}} G(x,\xi)H(\xi)\, d\xi \tag{2.52}$$

since the differential operator $\mathcal{L}$ acts only on the variable x, not on the integration variable ξ. Equation (2.52) implies the solution of Equation (2.48)

$$u(x) = \int_{\mathbb{R}} G(x,\xi)H(\xi)\,d\xi. \tag{2.53}$$

This results from the linearity of the operator $\mathcal{L}$ and relies upon being able to find the Green's function, $G(x,\xi)$. We remark that not every operator $\mathcal{L}$ has a Green's function.

To summarise, the function $G(x,\xi)$ must satisfy the following conditions for $\xi \in \mathbb{R}$ where $\mathcal{L}$ is an n^{th} order linear differential operator:

1. $\mathcal{L}G(x,\xi) = \delta(x-\xi)$

2. n boundary conditions

3. Continuity conditions $G(\xi^+,\xi) = G(\xi^-,\xi)$ and

$$\frac{\partial^j G}{\partial x^j}\Big|_{x=\xi^+} = \frac{\partial^j G}{\partial x^j}\Big|_{x=\xi^-}$$

   for $j = 1,\ldots,n-2$

4. Jump discontinuity condition

$$\left[\frac{\partial^{(n-1)} G}{\partial x^{(n-1)}}\right]_{x=\xi^-}^{x=\xi^+} = \frac{1}{v(\xi)}$$

   where $v(x)$ is the coefficient of the highest order derivative in $\mathcal{L}u$.

We now find single-bump steady state solutions of the model in Equation (2.5) using Green's functions. We look for a single stationary bump of width $2c$ ($c > 0$) satisfying Equation (2.47), where $u(-c) = u(c) = \theta$, as before. So

$$u(x) = \kappa^2 \frac{d^2u}{dx^2} + \int_{-c}^{c} w(x-y)f(u(y))\,dy. \tag{2.54}$$

To find $u(x)$, we first find a solution to the homogeneous equation

$$u - \kappa^2 \frac{d^2u}{dx^2} = 0. \tag{2.55}$$

We do this by determining the Green's function of the linear differential operator $\mathcal{L}$, where

$$\mathcal{L} = 1 - \kappa^2 \frac{d^2}{dx^2}. \tag{2.56}$$

This is the function G satisfying

$$G - \kappa^2 \frac{d^2G}{dx^2} = \delta(x-\xi). \tag{2.57}$$

Evaluation of Equation (2.57) gives

$$G(x,\xi) = \begin{cases} c_1 e^{-x/\kappa} + c_2 e^{x/\kappa}, & \text{for } \xi < x \\ c_3 e^{-x/\kappa} + c_4 e^{x/\kappa}, & \text{for } x < \xi \end{cases} \tag{2.58}$$

where c_1–c_4 are constants. By applying boundary conditions

$$\lim_{x\to\pm\infty} G(x,\xi) = 0, \tag{2.59}$$

we obtain

$$G(x,\xi) = \begin{cases} c_1 e^{-x/\kappa}, & \text{for } \xi < x \\ c_4 e^{x/\kappa}, & \text{for } x < \xi. \end{cases} \tag{2.60}$$

The Green's function must also satisfy a discontinuity condition in the first derivative of

$$\lim_{x\to\xi^+} \frac{\partial G}{\partial x} - \lim_{x\to\xi^-} \frac{\partial G}{\partial x} = -\frac{1}{\kappa^2}, \tag{2.61}$$

which means that

$$c_4 = \frac{e^{-\xi/\kappa}}{\kappa} - c_1 e^{-2\xi/\kappa}. \tag{2.62}$$

Finally, the function must be continuous, that is, $G(\xi^+,\xi) = G(\xi^-,\xi)$, giving

$$c_1 = \frac{e^{\xi/\kappa}}{2\kappa}, \quad c_4 = \frac{e^{-\xi/\kappa}}{2\kappa}. \tag{2.63}$$

Hence, the Green's function, G, which satisfies Equation (2.57) and the boundary conditions $\lim_{x\to\pm\infty} G(x,\xi) = 0$, is the function

$$G(x,\xi) = \begin{cases} \dfrac{e^{-(x-\xi)/\kappa}}{2\kappa}, & \text{for } \xi < x \\ \\ \dfrac{e^{(x-\xi)/\kappa}}{2\kappa}, & \text{for } x < \xi. \end{cases} \tag{2.64}$$

The solution of Equation (2.54) is

$$u(x) = \int_{-\infty}^{\infty} G(x,\xi) H(\xi)\, d\xi \tag{2.65}$$

where

$$H(x) = \int_{-\infty}^{\infty} w(x-y) f(u(y))\, dy. \tag{2.66}$$

Since we assume $u > \theta$ for $|x| < c$,

$$H(x) = \int_{-c}^{c} w(x-y)\, dy. \tag{2.67}$$

We substitute the expression for $H(x)$ in Equation (2.67) into Equation (2.65) to obtain the explicit steady state single-bump solution to Equation (2.47) of

$$u(x) = \begin{cases} \dfrac{K}{k(k^2\kappa^2-1)}\left[e^{k(x-c)} - e^{k(x+c)} + k^2\kappa^2\left(e^{(x+c)/\kappa} - e^{(x-c)/\kappa}\right)\right] \\ \quad -\dfrac{M}{m(m^2\kappa^2-1)}\left[e^{m(x-c)} - e^{m(x+c)} + m^2\kappa^2\left(e^{(x+c)/\kappa} - e^{(x-c)/\kappa}\right)\right], \\ \qquad\qquad \text{for } x < -c \\ \\ \dfrac{K}{k(k^2\kappa^2-1)}\left[+e^{k(x-c)} + e^{-k(x+c)} - k^2\kappa^2\left(e^{(x-c)/\kappa} + e^{-(x+c)/\kappa}\right)\right] \\ \quad -\dfrac{M}{m(m^2\kappa^2-1)}\left[+e^{m(x-c)} + e^{-m(x+c)} - m^2\kappa^2\left(e^{(x-c)/\kappa} + e^{-(x+c)/\kappa}\right)\right] \\ \quad +\dfrac{2(mK-kM)}{km}, \qquad\qquad \text{for } -c < x < c \\ \\ \dfrac{K}{k(k^2\kappa^2-1)}\left[e^{-k(x+c)} - e^{-k(x-c)} + k^2\kappa^2\left(e^{-(x-c)/\kappa} - e^{-(x+c)/\kappa}\right)\right] \\ \quad -\dfrac{M}{m(m^2\kappa^2-1)}\left[e^{-m(x+c)} - e^{-m(x-c)} + m^2\kappa^2\left(e^{-(x-c)/\kappa} - e^{-(x+c)/\kappa}\right)\right], \\ \qquad\qquad \text{for } c < x \end{cases} \tag{2.68}$$

We now find the existence criterion for single-bump solutions. Setting $u(c) = \theta$ in Equation (2.68), we obtain the nonlinear equation

$$\frac{K}{k(k^2\kappa^2-1)}\left[e^{-2kc} - 1 + k^2\kappa^2(1-e^{-2c/\kappa})\right] - \frac{M}{m(m^2\kappa^2-1)}\left[e^{-2mc} - 1 + m^2\kappa^2(1-e^{-2c/\kappa})\right] = \theta. \tag{2.69}$$

Note that when $\kappa^2 = 0$, Equation (2.69) reduces to the existence condition for single-bump steady states of the Amari model in Equation (2.12). Again, we choose $\theta = 0.07$. We use Newton's method [60] to solve for c in Equation (2.69) for $\kappa^2 = 0.05, 0.10$ and find

$$\kappa^2 = 0.05: \quad c = 0.55373355 \text{ and } c = 0.17302904 \tag{2.70}$$

$$\kappa^2 = 0.10: \quad c = 0.51147893 \text{ and } c = 0.23901298 \tag{2.71}$$

We construct the specific solutions for these values of (κ^2, c) from Equation (2.68) over a finite domain (see Figure 2.7). The top plot shows the solutions for $\kappa^2 = 0.05$ and the bottom plot the solutions for $\kappa^2 = 0.10$. Once again, there are two solutions for each value of κ^2. The smaller bump solution is unstable and the taller bump solution stable (see Chapter 7 for the stability analysis). We expect that once κ^2 exceeds an upper limit, single-bump solutions cease to exist as increasing κ^2 causes the maximum to decrease and eventually move downward through the threshold.

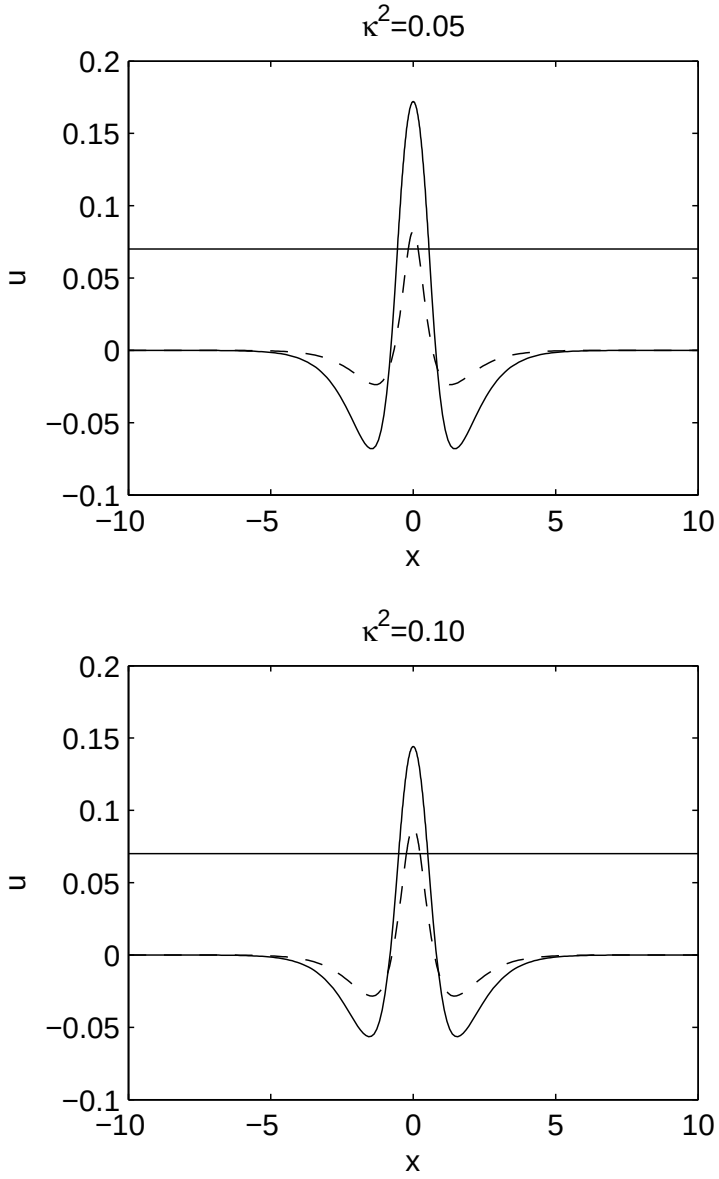

Figure 2.7: Single-bump steady states for $\kappa^2 = 0.05$ (top), $\kappa^2 = 0.10$ (bottom) in the gap junction model of Equation (2.68) with coupling function (2.4) (with parameter values as in Figure 2.1) and step firing rate function with $\theta = 0.07$ (horizontal line). Solid line: stable solution; dashed line: unstable solution.

We are interested in the relationship between the threshold θ, the bump half-width c, and the parameter κ^2. By fixing κ^2 or θ in Equation (2.69) and continuing solutions we obtain Figure 2.8. The top plot shows c as a function of θ for various values of κ^2. The dashed line shows the curve for the model with no gap junctions, that is, $\kappa^2 = 0$. These are solutions of the Amari model. The curves to the left of the dotted curve are for progressively larger values of κ^2: $0.025, 0.05, 0.75, 2.0$. It can be seen that as θ increases, the maximum value of κ^2 for which a bump can exist decreases.

The bottom plot gives the bump half-width c as a function of κ^2 for various values of the threshold, $\theta : 0.025, 0.05, 0.07$ from right to left. When $\kappa^2 = 0$ we have the Amari model. The two values of c where the curve for $\theta = 0.07$ meets the y-axis agree with the values of c we found in the previous section for the Amari model. It is evident that higher thresholds result in a narrower bump width for the stable solution than that of lower thresholds. As κ^2 grows, the threshold must be decreased to sustain single-bump solutions.

Piecewise construction of steady states

In this section we apply the method of piecewise construction of single-bump steady states to the gap junction model. We look for symmetric single-bump solutions centred at $x = 0$. As in Section 2.2, only one half of the bump is constructed ($x \geq 0$).

We use Fourier transforms in space to derive a sixth-order ODE. Again, for a step firing rate function, the ODE can be written as two linear differential equations – a non-homogeneous ODE for an above-threshold region and a homogeneous ODE for a below-threshold region. At the threshold, we have matching conditions on u and its derivatives to obtain a smooth and continuous function on $\mathbb{R}$. Given the assumption of a single-bump solution, we require $(u, u', u'', u''', u^{(iv)}, u^{(v)}) \to (0, 0, 0, 0, 0, 0)$ as $x \to \infty$.

We choose a threshold $\theta > 0$. A single-bump steady state solution of Equation (2.47) with width $2c$ satisfies

$$u(x) \begin{cases} > \theta, & \text{if } |x| < c \\ = \theta, & \text{if } x = -c \text{ or } x = c \\ < \theta, & \text{if } c < |x| \end{cases} \tag{2.72}$$

and

$$\lim_{x \to \pm\infty} (u, u', u'', u''', u^{(iv)}, u^{(v)}) \to (0, 0, 0, 0, 0, 0). \tag{2.73}$$

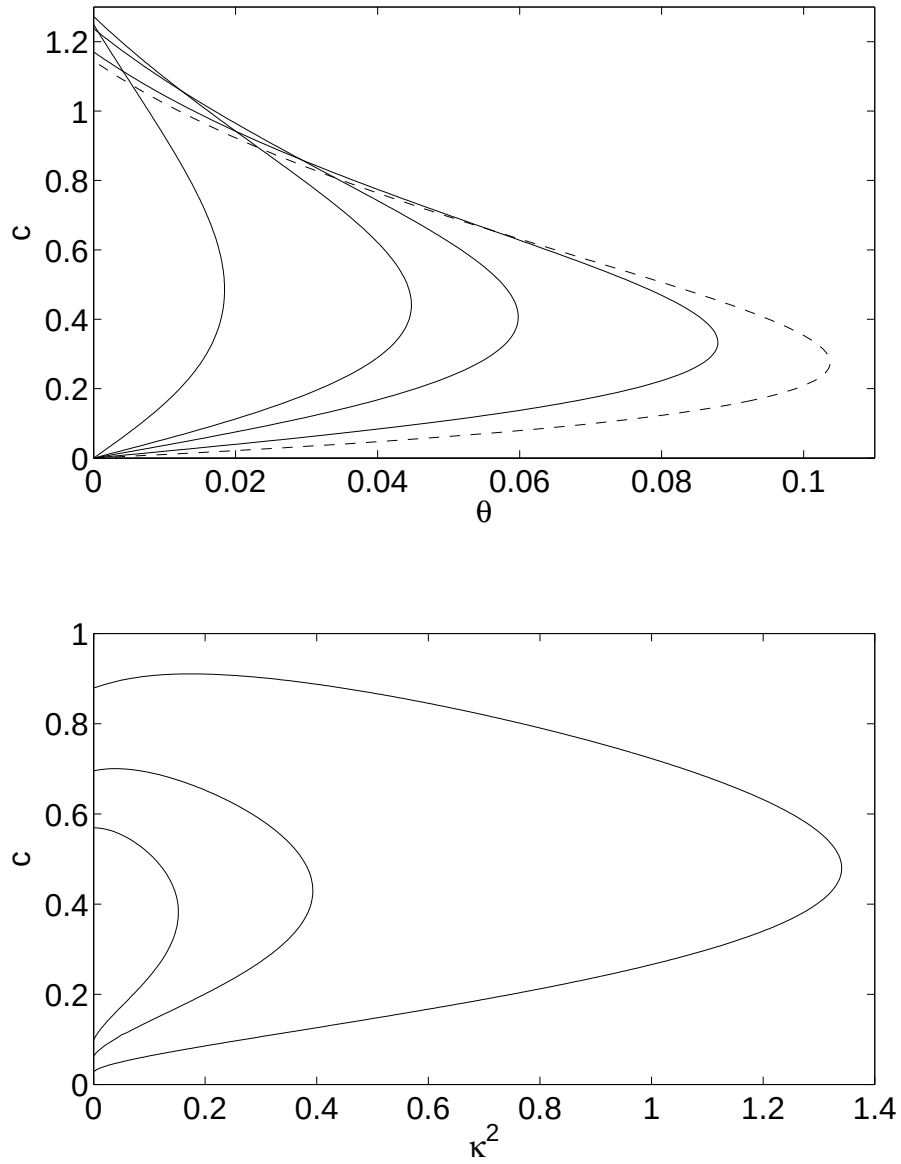

Figure 2.8: Single-bump steady states of the gap junction model in Equation (2.5) with firing rate function in Equation (2.3) and coupling function in Equation (2.4) with parameter values as in Figure 2.1. Top: Bump half-width c as a function of threshold θ with $\kappa^2 = 0$ (dotted line), $0.05, 0.25, 0.5, 2.0$ (right to left). Bottom: c as a function of κ^2 with $\theta = 0.025, 0.05, 0.07$ (right to left).

Derivation of the ODE

To derive an ordinary differential equation of which solutions are steady states of the gap junction model, we apply the Fourier transform to Equation (2.47) to obtain

$$F[-\kappa^2 u^{''}] + F[u] = F[w]F[f(u)]. \tag{2.74}$$

Using the Fourier transform identity

$$F[-\kappa^2 u^{''}] = \kappa^2\alpha^2 F[u] \tag{2.75}$$

in Equation (2.74), we obtain

$$(1+\kappa^2\alpha^2)F[u] = F[w]F[f(u)]. \tag{2.76}$$

We substitute for $F[w]$ in Equation (2.76) with Equation (2.21) and multiply both sides by the denominator of $F[w]$ to obtain

$$(1+\kappa^2\alpha^2)(k^2m^2 + (k^2+m^2)\alpha^2 + \alpha^4)F[u] = 2(km^2K - k^2mM + (kK - mM)\alpha^2 F[f(u)]. \tag{2.77}$$

Using the Fourier transform identities

$$F[u^{(iv)}] = \alpha^4 F[u], F(-u^{(vi)}) = \alpha^6 F(u) \text{ and } F[-u^{''}] = \alpha^2 F[u] \tag{2.78}$$

we obtain

$$\begin{aligned} F[-\kappa^2 u^{(vi)} + (1+\kappa^2(k^2+m^2))u^{(iv)} - (k^2+m^2+k^2m^2\kappa^2)u^{''} + k^2m^2u] = \\ 2km(mK-kM)F[f(u)] + 2(kK-mM)F[f^{''}(u)]. \end{aligned} \tag{2.79}$$

Applying inverse Fourier transforms to Equation (2.79)

$$\begin{aligned} -\kappa^2 u^{(vi)} + (1+\kappa^2(k^2+m^2))u^{(iv)} - (k^2+m^2+k^2m^2\kappa^2)u^{''} + k^2m^2u \\ = 2km(mK-kM)f(u) + 2(kK-mM)f^{''}(u). \end{aligned} \tag{2.80}$$

If u is a solution of the ODE in Equation (2.80) satisfying Equation (2.73) then Equations (2.74) – (2.79) are satisfied. We claim that u is a solution of Equation (2.47). Hence the problem of finding single-bump solutions of Equation (2.47) is reduced to finding single-bump solutions of the ODE in Equation (2.80).

Construction of solutions

As for the Amari model in the previous section, we find symmetric single-bump steady state solutions of width $2c$, with a step firing rate function, for $x \in \mathbb{R}_0^+$ only. We decompose

u into two functions, u_T and u_L, such that $u_T(x) > \theta$ and $u_L(x) < \theta$, as in Section 2.2

$$u(x) = \begin{cases} u_T, & 0 \leq x < c \\ u_L, & c < x. \end{cases} \tag{2.81}$$

We write the ODE in Equation (2.80) as two linear differential equations

$$-\kappa^2 u_T^{(vi)} + (1 + \kappa^2(k^2 + m^2))u_T'''' - (k^2 + m^2 + k^2m^2\kappa^2)u_T'' + k^2m^2u_T = 2km(mK - kM), \quad \text{for } 0 \leq x < c \tag{2.82}$$

$$-\kappa^2 u_L^{(vi)} + (1 + \kappa^2(k^2 + m^2))u_L'''' - (k^2 + m^2 + k^2m^2\kappa^2)u_L'' + k^2m^2u_L = 0, \quad \text{for } c < x. \tag{2.83}$$

Solutions of u_T must satisfy the nonhomogeneous ODE in Equation (2.82) on the interval $0 \leq x < c$. Solutions are of the form

$$u_T(x) = D_1(e^{kx} + e^{-kx}) + D_2(e^{mx} + e^{-mx}) + D_3(e^{x/\kappa} + e^{-x/\kappa}) + \frac{2(mK - kM)}{km}, \quad (D_1, D_2, D_3 \in \mathbb{R}). \tag{2.84}$$

Solutions of u_L must satisfy the homogeneous ODE in Equation (2.83) for $c < x$. They must also satisfy the boundary condition

$$\lim_{x \to \infty} u_L \to 0. \tag{2.85}$$

Thus, solutions are of the form

$$u_L(x) = D_4e^{-kx} + D_5e^{-mx} + D_6e^{-x/\kappa}, \qquad (D_4, D_5, D_6 \in \mathbb{R}). \tag{2.86}$$

The functions u_T and u_L and their first five derivatives must satisfy matching conditions at $x = c$, with a jump discontinuity in the fourth derivative. This creates a set of six matching conditions

$$u_T(c) = u_L(c) = \theta \tag{2.87}$$

$$u_T'(c) = u_L'(c) \tag{2.88}$$

$$u_T''(c) = u_L''(c) \tag{2.89}$$

$$u_T'''(c) = u_L'''(c) \tag{2.90}$$

$$u_T^{(iv)}(c) = u_L^{(iv)}(c) + \frac{2(kK - mM)}{\kappa^2} \tag{2.91}$$

$$u_T^{(v)}(c) = u_L^{(v)}(c). \tag{2.92}$$

The first four matching conditions are a result of the continuity of u, u', u'', u'''. Note that $u^{(iv)}$ has a discontinuity at $x = c$ as there is a jump in $u^{(iv)}(c)$ given the shifted Heaviside firing rate function. Evaluation of Equations (2.87)–(2.92) gives the system of equations

$$D_1(e^{kc} + e^{-kc}) + D_2(e^{mc} + e^{-mc}) + D_3(e^{c/\kappa} + e^{-c/\kappa}) + \frac{2(mK - kM)}{km} = D_4e^{-kc} + D_5e^{-mc} + D_6e^{-c/\kappa} \tag{2.93}$$

$$kD_1(e^{kc} - e^{-kc}) + mD_2(e^{mc} - e^{-mc}) + D_3(e^{c/\kappa} - e^{-c/\kappa})/\kappa = - kD_4e^{-kc} - mD_5e^{-mc} - D_6e^{-c/\kappa}/\kappa \tag{2.94}$$

$$k^2D_1(e^{kc} + e^{-kc}) + m^2D_2(e^{mc} + e^{-mc}) + D_3(e^{c/\kappa} + e^{-c/\kappa})/\kappa^2 = k^2D_4e^{-kc} + m^2D_5e^{-mc} + D_6e^{-c/\kappa}/\kappa^2 \tag{2.95}$$

$$k^3D_1(e^{kc} - e^{-kc}) + m^3D_2(e^{mc} - e^{-mc}) + D_3(e^{c/\kappa} - e^{-c/\kappa})/\kappa^3 = - k^3D_4e^{-kc} - m^3D_5e^{-mc} - D_6e^{-c/\kappa}/\kappa^3 \tag{2.96}$$

$$k^4D_1(e^{kc} + e^{-kc}) + m^4D_2(e^{mc} + e^{-mc}) + D_3(e^{c/\kappa} + e^{-c/\kappa})/\kappa^4 = k^4D_4e^{-kc} + m^4D_5e^{-mc} + D_6e^{-c/\kappa}/\kappa^4 + \frac{2(kK - mM)}{\kappa^2} \tag{2.97}$$

$$k^5D_1(e^{kc} - e^{-kc}) + m^5D_2(e^{mc} - e^{-mc}) + D_3(e^{c/\kappa} - e^{-c/\kappa})/\kappa^5 = - k^5D_4e^{-kc} - m^5D_5e^{-mc} - D_6e^{-c/\kappa}/\kappa^5 \tag{2.98}$$

Equations (2.87)–(2.92) can be solved in terms of c for given parameter values K, M, k, m, κ^2:

$$D_1 = \frac{Ke^{-kc}}{k(k^2\kappa^2 - 1)} \tag{2.99}$$

$$D_2 = \frac{Me^{-mc}}{m(m^2\kappa^2 - 1)} \tag{2.100}$$

$$D_3 = \left(\frac{Mm\kappa^2}{m^2\kappa^2 - 1} - \frac{Kk\kappa^2}{k^2\kappa^2 - 1}\right)e^{-c/\kappa} \tag{2.101}$$

$$D_4 = \frac{K(e^{-kc} - e^{kc})}{k(k^2\kappa^2 - 1)} \tag{2.102}$$

$$D_5 = \frac{M(e^{-mc} - e^{mc})}{m(m^2\kappa^2 - 1)} \tag{2.103}$$

$$D_6 = \left(\frac{Kk^2\kappa^2}{k(k^2\kappa^2 - 1)} - \frac{Mm^2\kappa^2}{m(m^2\kappa^2 - 1)} \right) (e^{c/\kappa} - e^{-c/\kappa}). \tag{2.104}$$

Substituting for $D_1 - D_6$ from Equations (2.99)–(2.104) into the formulas for u_T and u_L in Equations (2.84) and (2.86) respectively gives

$$\begin{aligned} u_T(x) = {} & \frac{K}{k(k^2\kappa^2 - 1)} \left(e^{-k(x+c)} + e^{k(x-c)} - k^2\kappa^2 (e^{(x-c)/\kappa} + e^{-(x+c)/\kappa}) \right) \\ & - \frac{M}{m(m^2\kappa^2 - 1)} \left(e^{-m(x+c)} + e^{m(x-c)} - m^2\kappa^2 (e^{(x-c)/\kappa} + e^{-(x+c)/\kappa}) \right) \\ & + \frac{2(mK - kM)}{km} \end{aligned} \tag{2.105}$$

$$\begin{aligned} u_L(x) = {} & \frac{K}{k(k^2\kappa^2 - 1)} \left(e^{-k(x+c)} - e^{-k(x-c)} + k^2\kappa^2 (e^{-(x-c)/\kappa} - e^{-(x+c)/\kappa}) \right) \\ & - \frac{M}{m(m^2\kappa^2 - 1)} \left(e^{-m(x+c)} - e^{-m(x-c)} - m^2\kappa^2 (e^{-(x-c)/\kappa} - e^{-(x+c)/\kappa}) \right). \end{aligned} \tag{2.106}$$

Setting $x = c$ in Equation (2.106) and $u(c) = \theta$, we obtain the same existence condition for a single-bump steady state as in Equation (2.69) in Section 2.3, where Green's functions were used to solve for $u(x)$. A change of variables of $x \to -x$ permits construction of the other half of the solution for $x \in (-\infty, 0]$. Therefore, Equation (2.81) defines an explicit single-bump steady state solution of the gap junction model in Equation (2.5) for $x \in \mathbb{R}$ with lateral inhibition and a step firing rate function.

In Chapter 4 we use the method in this section to find steady state solutions of both the Amari model and the gap junction model using an oscillatory coupling function introduced in the next chapter. We find solutions for both a step firing rate function and a piecewise linear firing rate function. We also use continuation methods to find the bifurcation curve of solutions as we vary a parameter in the coupling function.

2.4 Conclusion

In this chapter we have presented the two one-dimensional neural field models that are studied in the thesis. These are the Amari model from the 1977 work of Amari [1] and

the gap junction model which we have developed as an extension of the Amari model.

We restricted the firing rate function to be a step function in order to analytically find steady state solutions of the models. We also assumed lateral-inhibition for the neural coupling as in the work of Amari [1]. We reviewed the existence criteria for both spatially uniform steady states and single-bump steady states of the Amari model. We then presented a method previously used by Guo [47] for constructing symmetric, single-bump stationary solutions. The method used a piecewise differential framework based upon an fourth-order ODE derived from the expression for steady states. A single-bump steady state solution was separated into an above-threshold region and a below-threshold region, with matching conditions at the threshold. This formed a set of nonlinear, algebraic equations which were solved numerically to find the solution. We reviewed the results of Guo [47] for the Amari model.

Following this, we found solutions of the gap junction model using these methods, to see how the inclusion of the term to model gap junctions changed the solutions previously found for the Amari model. We determined the existence criteria of both spatially uniform and single-bump steady states of the gap junction model. We found that spatially uniform solutions of the gap junction model were the same as those of the Amari model. We used Green's functions to form an explicit formula for single-bump stationary solutions of the gap junction model. It was found that as the strength of the term modelling gap junctions increases, the threshold must drop for single-bump solutions to be sustained.

Finally, we applied the method of piecewise construction of single-bump solutions to find single-bump steady state solutions of the gap junction model. This relied upon the derivation of a sixth-order ODE, solutions of which are stationary solutions of the model.

Chapter 3

Finding steady states numerically

3.1 Introduction

In this chapter, the analysis of Chapter 2 is extended to the study of N-bump solutions. Amari (1977) found single spatially localised regions of high activity, or "bumps", in a partial integro-differential equation modelling a single layer of neurons. By relaxing the restrictions on the coupling function and firing rate function, Laing *et al.* [70] extended this model to find "multi-bump" solutions, given an appropriate range of parameters. These "multi-bump" solutions are known as N-bump solutions, as discussed in Chapter 1.

Labelling studies have shown that coupled groups of neurons in the prefrontal cortex form spatially approximate periodic stripes [50]. Laing *et al.* [70] modelled this type of neural connectivity by considering a *decaying oscillatory* coupling function which changes sign infinitely often. The extension of the firing rate function from a step function to a *continuous* firing rate function allowed those authors to derive an ODE, specific solutions of which are steady states of their model. We followed this approach in Chapter 2 where we derived an ODE from the full, time-dependent model with Mexican hat coupling function and Heaviside firing rate function.

In this chapter, we study the model of [70]

$$\frac{\partial u(x,t)}{\partial t} = -u(x,t) + \int_{-\infty}^{\infty} w(x-y) f(u(y,t))\, dy \tag{3.1}$$

where $f(u)$ is the smooth firing rate function

$$f(u) = 2e^{-r/(u-\theta)^2}\Theta(u-\theta) \tag{3.2}$$

and w is the decaying oscillatory coupling function

$$w(x) = e^{-b|x|}\left(b\sin(|x|) + \cos(x)\right). \tag{3.3}$$

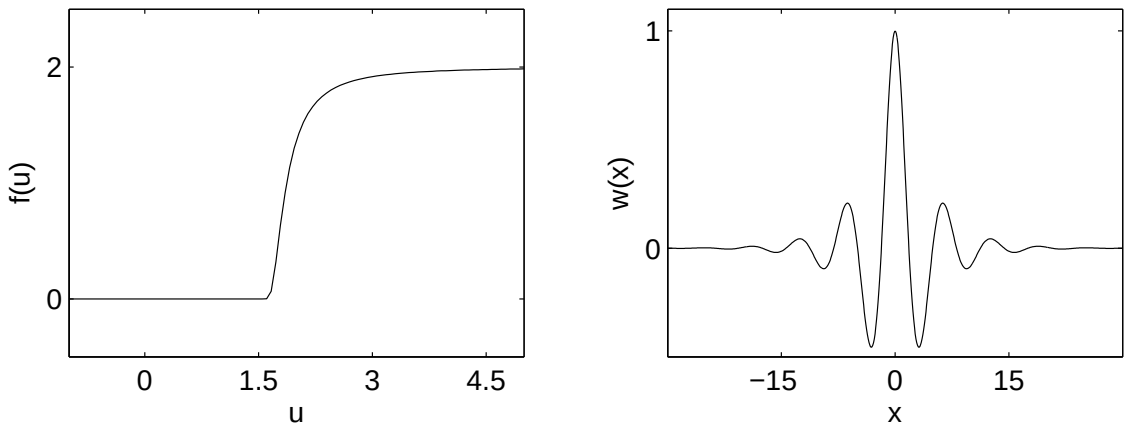

Figure 3.1: Left: smooth firing rate function of Equation (3.2) with $(r, \theta) = (0.095, 1.5)$. Right: Decaying oscillatory coupling function of Equation (3.3) with $b = 0.25$.

The model includes a threshold parameter $\theta > 0$, a steepness parameter $r > 0$ and a coupling decay parameter $b > 0$. Throughout this chapter $\theta = 1.5$. See Figure 3.1 for function f in Equation (3.2) with $r = 0.095$ and function w in Equation (3.3) with $b = 0.25$.

The coupling function $w(x)$ in Equation (3.3) has the following useful qualities:

1. $w(x)$ is symmetric, that is, $w(-x) = w(x)$;
2. $w(x)$ is an oscillatory function that tends to zero as $x \to \pm\infty$;
3. $w(x)$ changes sign infinitely often on $(0, \infty)$;
4. The parameter b controls the rate at which the oscillations in $w(x)$ decay with distance; and,
5. w is continuous on $\mathbb{R}$.

The particular form of $w(x)$ in Equation (3.3) in [70] was chosen as it has a Fourier transform that allows derivation of an ODE from the model in Equations (3.1)–(3.3).

The firing rate function $f(u)$ in Equation (3.2) is a smooth function. The function has a threshold parameter θ and a parameter r, which controls the steepness of the function f for $u > \theta$. For $u < \theta$, $f(u) = 0$. As $r \to 0^+$ the firing rate function tends towards twice a step function. Therefore, when $r = 0$ there is a discontinuity in $f(u)$ at $u = \theta$ and $f(u)$ becomes twice the Heaviside function. For $r > 0$, $f(u)$ is a continuous function with $\lim_{u\to\infty} f(u) = 2$. The rate at which $f(u)$ approaches 2 depends upon the steepness of $f(u)$. The function f is a C^∞ function when $r > 0$. The left plot of Figure 3.1 shows $f(u)$ with $r = 0.095$ and $\theta = 1.5$.

The chapter proceeds as follows. In Section 3.2, we review the results of [70] for the model in Equations (3.1)–(3.3). Given the nonlinearity in the model, we cannot find solutions analytically. We therefore find N-bump solutions using numerical integration techniques. A fourth-order ODE is derived from the expression for time-independent solutions of the model. By discretising over a finite domain and using periodic boundaries, continuation methods can be used. The solution curves show both single and multiple bump solutions as the coupling parameter b is varied. We find that the system is multi-stable.

In Section 3.3, we extend our analysis to the gap junction model developed in Chapter 1. We investigate how the addition of the term modelling gap junctions changes the results of the previous section. A sixth-order ODE is derived, solutions of which are steady state solutions of the model. Continuation techniques are used with the ODE to find solution curves. Families of solutions are destroyed through saddle-node bifurcations as the strength of the term modelling gap junctions is increased. The stability of solutions is indicated on bifurcation diagrams. The method used to calculate stability is presented in Chapter 7.

3.2 Amari model

N-bump solutions

We now review the results of [70]. We find N-bump solutions of the model in Equations (3.1)–(3.3) by numerically integrating with an appropriate initial condition. To apply computational methods, a finite domain must be used. Equations (3.1)–(3.3) are defined on an infinite domain. We approximate an infinite domain by choosing a finite domain sufficiently large that there is no activity near the boundaries. Hence, we assume a finite domain of $\Omega\colon [-10\pi, 10\pi]$. We use an initial condition for $u(x,t)$ from [70] where

$$u(x,0) = 2.5\cos\left(\frac{Lx}{10\pi}\right)\exp\left(-\left(\frac{Lx}{10\pi}\right)^2\right), \quad -10\pi < x < 10\pi, \quad L \in \mathbb{R}^+. \tag{3.4}$$

As L decreases, the width of the initial condition $u(x,0)$ increases. The domain Ω is discretised over a uniform grid. The convolution on the right hand side of Equation (3.1) is evaluated using a Riemann sum. In MATLAB [74], the system is integrated using a forward Euler step in time until convergence is reached. This is an explicit method of numerical integration and is explained further in the Appendix. The solutions found using numerical integration are approximations to stable steady state solutions of Equation (3.1).

The uniform zero steady state, $u(x,t) = 0$ for all $x \in \Omega$, is also a solution of Equation (3.1).

We investigate solutions for $(b, r, \theta) = (0.25, 0.095, 1.5)$. Numerically integrating Equations (3.1)–(3.3), initial conditions for $L = 6, 2.5, 1.5$ in Equation (3.4) evolve into steady state solutions as $t \to \infty$ (see Figure 3.2). As the initial excitation (dashed line) widens (L falls from 6 to 2.5 to 1.5), the number of bumps in the solution we find increases from 1 to 2 to 3. The system in Equations (3.1)–(3.3) is multi-stable. Different initial conditions move to different steady states under numerical integration.

Only stable steady states can be found using numerical integration. To find unstable steady states, we require continuation methods. We derive the ODE in [70] and then apply continuation methods to find families of solutions of Equation (3.1).

Derivation of the ODE

This section reviews the derivation of the ODE in [70]. The approach is the same as in Section 2.2. Time-independent solutions of Equation (3.1) satisfy

$$u(x) = \int_{-\infty}^{\infty} w(x-y) f(u(y))\, dy. \tag{3.5}$$

We assume that u is a solution of Equation (3.5), that u, u', u'', u''' and $u^{(iv)}$ are continuous on $\mathbb{R}$ and $\lim_{x \to \pm\infty} (u, u', u'', u''') = (0, 0, 0, 0)$. Therefore, Fourier transforms can be applied to Equation (3.5). The Fourier transform is

$$F[p](\alpha) = \int_{-\infty}^{\infty} p(x) e^{-i\alpha x}\, dx \tag{3.6}$$

where $p \in L^1(\mathbb{R})$ and $\alpha \in \mathbb{R}$ is the transform variable. The inverse Fourier transform is

$$p(x) = \frac{1}{2\pi} \int_{-\infty}^{\infty} F[p](\alpha) e^{i\alpha x}\, d\alpha. \tag{3.7}$$

Applying the Fourier transform to Equation (3.5) we obtain

$$F[u] = F[w] F[f(u)]. \tag{3.8}$$

The coupling function $w(x)$ in Equation (3.3) has the Fourier transform

$$F[w] = \frac{4b(b^2+1)}{\alpha^4 + 2\alpha^2(b^2-1) + (b^2+1)^2}. \tag{3.9}$$

Substituting Equation (3.9) into Equation (3.8) and multiplying both sides by the denominator on the right hand side results in

$$\left(\alpha^4 + 2\alpha^2(b^2-1) + (b^2+1)^2\right) F[u] = 4b(b^2+1) F[f(u)]. \tag{3.10}$$

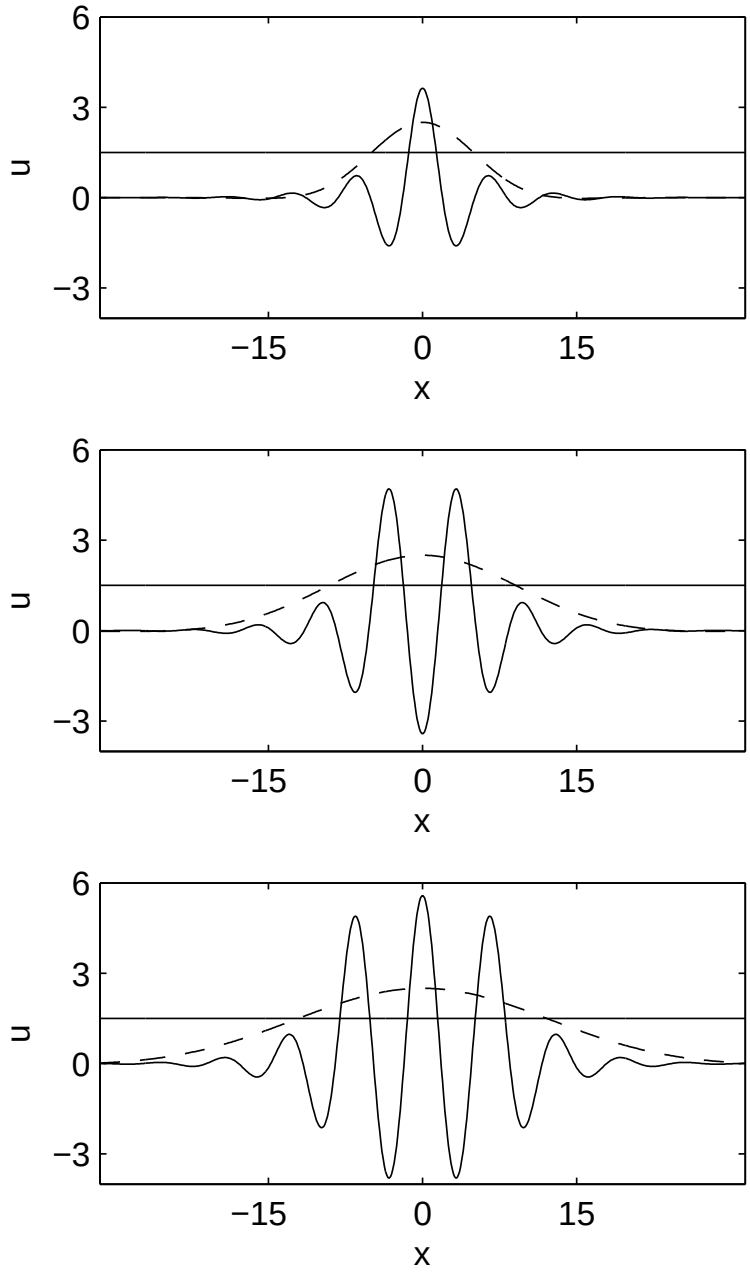

Figure 3.2: Steady state solutions (solid line) of Equation (3.1) found using numerical integration. The domain is $[-10\pi, 10\pi]$ with $b = 0.25$ and $r = 0.095$. There is a horizontal line at $u = \theta$. From top to bottom, $L = 6, 2.5, 1.5$. As the initial excitation profile (dashed line) widens, different steady states are found.

Using the Fourier transform identities $F[u^{(iv)}] = \alpha^4 F[u]$ and $F[-u''] = \alpha^2 F[u]$, Equation (3.10) simplifies to

$$F[u^{(iv)} + 2(1-b^2)u'' + (b^2+1)^2 u] = 4b(b^2+1)F[f(u)]. \tag{3.11}$$

Applying inverse Fourier transforms, the fourth-order ODE from [70] is obtained

$$\begin{cases} u^{(iv)} + 2(1-b^2)u'' + (b^2+1)^2 u &= 4b(b^2+1)f(u), \\ \lim\limits_{x\to\pm\infty}(u, u', u'', u''') &= (0,0,0,0). \end{cases} \tag{3.12}$$

We have therefore reduced our problem of finding N-bump stationary solutions of the model in Equation (3.1) to that of finding N-bump solutions of the ODE in Equation (3.12), as any solution of Equation (3.12) is also a steady state solution of Equation (3.1). Separate "families" of solutions with an odd number of bumps and with an even number of bumps were found in [70]. We restrict our interest to even solutions of the model in Equation (3.1), that is, $u'(0) = u'''(0) = 0$, and look for 1-, 3- and 5-bump solutions.

The fourth-order ODE in Equation (3.12) has a fixed point at $u = 0$ for $\theta > 0$. Letting $v_0 = u$ and $\mathbf{v} = (v_0, v_1, v_2, v_3)$, we write Equation (3.12) as the first-order system

$$\begin{aligned} v_0' &= v_1 \\ v_1' &= v_2 \\ v_2' &= v_3 \\ v_3' &= 2(b^2-1)v_2 - (b^2+1)^2 v_0 + 4b(b^2+1)f(v_0). \end{aligned} \tag{3.13}$$

So $\mathbf{v} = (u, u', u'', u''')$. The system in Equation (3.13) has a fixed point at the origin, that is, $\mathbf{v} = (0,0,0,0)$. As $f'(0) = 0$ and $\theta > 0$, by linearising about $\mathbf{v} = \mathbf{0}$, we find the Jacobian

$$\mathbf{J}|_{\mathbf{v}=\mathbf{0}} = \begin{pmatrix} 0 & 1 & 0 & 0 \\ 0 & 0 & 1 & 0 \\ 0 & 0 & 0 & 1 \\ -(b^2+1)^2 & 0 & 2(b^2-1) & 0 \end{pmatrix} \tag{3.14}$$

which has eigenvalues $\pm(b \pm i)$. Therefore, the origin is a saddle-focus fixed point. Also, solutions of Equation (3.12) are homoclinic orbits to the origin. We briefly explain this.

Definition 3.2.1 *Let the function φ be the flow of an ordinary differential equation such that $\varphi(x,t) : \mathbb{R} \times \mathbb{R}^+ \to \mathbb{R}$. Let φ have a stationary point at $\bar{x}$ and $\varphi(x,0) \neq \bar{x}$. A homoclinic orbit is an orbit $\varphi(x,t)$ such that $\varphi(x,t) \to \bar{x}$ as $t \to \pm\infty$ [42].*

In Equation (3.13), a homoclinic trajectory to the fixed point at $\mathbf{v} = \mathbf{0}$ is the flow $\varphi(\mathbf{v}, x) : \mathbb{R}^4 \times \mathbb{R} \to \mathbb{R}^4$ where $\varphi(\mathbf{v}, x) \to \mathbf{0}$ as $x \to \pm\infty$. The homoclinic trajectory is in

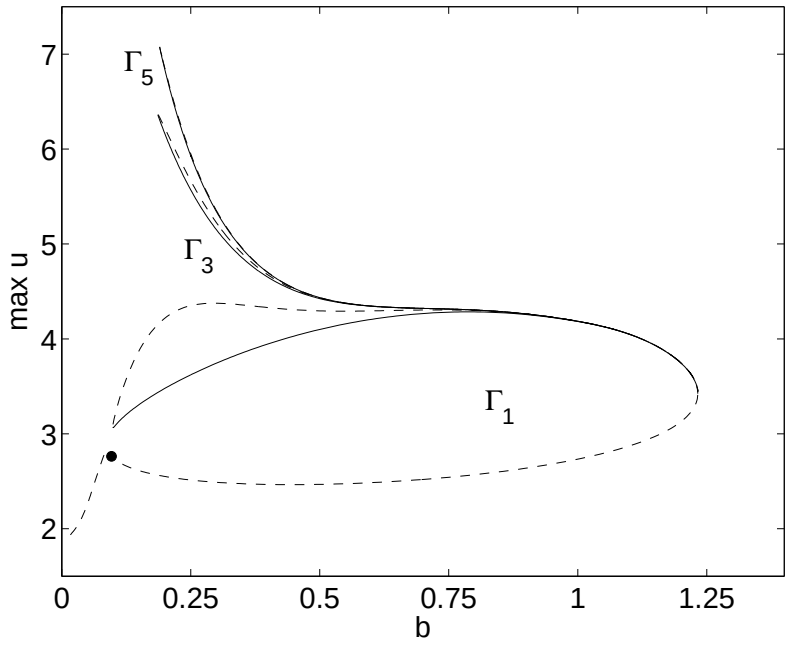

Figure 3.3: Solution curves for Equations (3.1)–(3.3) where $r = 0.095$, $\theta = 1.5$ and b is the continuation parameter. 1-, 3- and 5-bump solutions are indicated by the symbols Γ_1, Γ_3 and Γ_5 respectively. Solutions to the left of the solid circle are N-bump solutions where $N > 1$. Solid line: stable solutions; dashed line: unstable solutions.

space, not time. Hence, in (u, u', u'', u''') phase space, solutions of the ODE in Equation (3.12) are homoclinic orbits that move to the saddle-focus fixed point $(u, u', u'', u''') = (0, 0, 0, 0)$ as $x \to \pm\infty$. We note that the ODE in Equation (3.12) is Hamiltonian. In Chapter 5 we take a phase space approach and use the properties of a reversible Hamiltonian system to look for homoclinic solutions.

Bifurcation analysis

To apply continuation methods to Equation (3.12), the domain must be finite. As with the numerical integration, we discretise the domain Ω: $[-10\pi, 10\pi]$ over a uniform grid of n points. Periodic boundary conditions are applied. We use continuation methods to find the solution curves for 1-, 3- and 5-bump solutions of Equation (3.12) where $r > 0$ in $f(u)$ from Equation (3.2). These solutions are N-bump stationary solutions of the time-dependent model in Equations (3.1)–(3.3). The continuation methods are discussed in the Appendix.

We set $r = 0.095$ and $\theta = 1.5$. We plot the global maximum of $u(x)$ over all $x \in \Omega$ as a function of the continuation parameter, b. The results in Figure 3.3 were generated using AUTO [23]. For Figures 3.3–3.7 and Figures 3.10–3.11, the symbols Γ_1, Γ_3 and Γ_5 indicate

1-, 3- and 5-bump solutions respectively. Solid lines show branches of stable solutions and dashed lines show branches of unstable solutions. Stability changes at saddle-node bifurcations. There are other N-bump solutions. We choose to concentrate on 1-, 3- and 5-bump solutions only.

As b continues to increase, 1-, 3- and 5-bump solutions are eventually destroyed in saddle-node bifurcations. As $b \to 0^+$, the number of bumps in the solution increases until the entire domain is filled by bumps. On the domain Ω, this is a maximum of ten bumps. We see that in general, for $N = 1, 3$ and 5, N-bump solutions come in pairs. For example, at $b = 0.25$, there are two single-bump solutions of two different amplitudes on Γ_1. In each pair, the solution with a larger maximum value of u is stable and the solution with a smaller maximum value of u is unstable. This is a general result common to this type of neural field model and was discussed in terms of the work of Amari [1] in Chapter 1.

We now change the steepness of $f(u)$ by varying r from 0.095. We keep θ fixed at 1.5. First, we allow the firing rate function to become less steep than for $r = 0.095$ by letting $r = 0.110$. Figure 3.4 shows the solution curve for $r = 0.110$. The qualitative difference as r changes from 0.095 (Figure 3.3) to 0.110 (Figure 3.4) is that the branch of unstable 3-bump solutions becomes disconnected from the branch of stable 1-bump solutions. The branch of unstable 3-bump solutions is now joined to the branch of unstable N-bump solutions where $N > 3$ as $b \to 0^+$. As the curves for 3- and 5- bump solutions meet the upper branch of 1-bump solutions, the separation in the curves for different "families" of solutions is hard to see. In the bifurcation diagram in Figure 3.3, we plotted the maximum value of u as a function of b using AUTO. AUTO also provides the L^2-norm of u. By plotting the L^2-norm as a function of b, a "snaking" phenomenon can be seen in the solution branches (see Figure 3.5). As the curve climbs in the L^2-norm, "bumps" are added to the homoclinic orbit at saddle-nodes. "Snaking" has been seen in higher order scalar systems and in systems with homoclinic orbits [52, 63, 80].

Next, we allow $f(u)$ to become progressively steeper. Figure 3.6 shows the solution curve for $r = 0.090$. A small kink has developed in the upper branch of single-bump solutions around $b = 1$. This kink was not in the curve for $r = 0.095$ in Figure 3.3. We make $f(u)$ even steeper by dropping r to 0.085 (see Figure 3.7). Further qualitative changes are evident. The upper branch of stable 1-bump solutions has become discontinuous around $b \approx 1$. On each side of the discontinuity, the solution curve terminates in a tight spiral. Moving around this spiral toward the terminating end, the solutions become progressively broader and develop a "dimple". Figure 3.8 shows a single-bump solution for $b = 0.87378$.

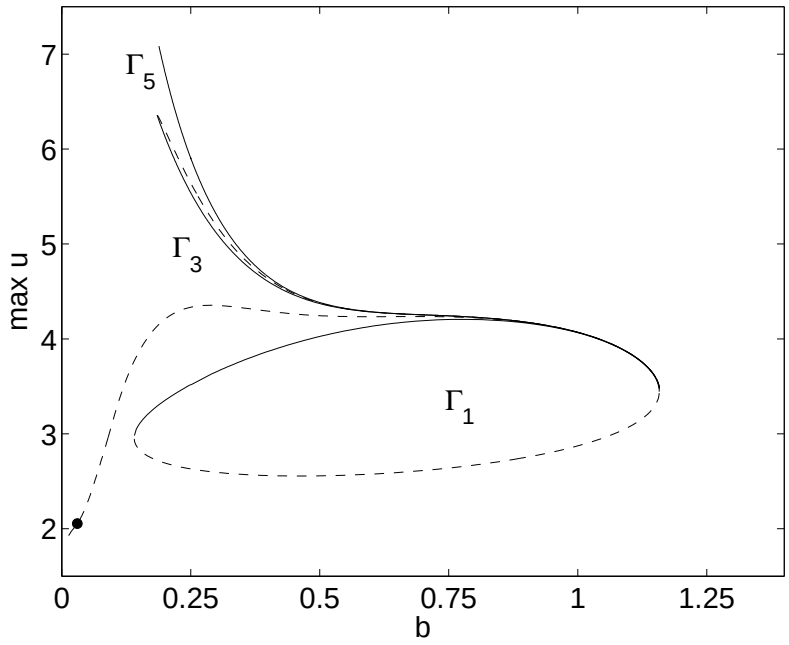

Figure 3.4: Solution curves for Equations (3.1)–(3.3) where $r = 0.110$ and b is the continuation parameter. Solutions to the left of the solid circle are N-bump solutions where $N > 3$.

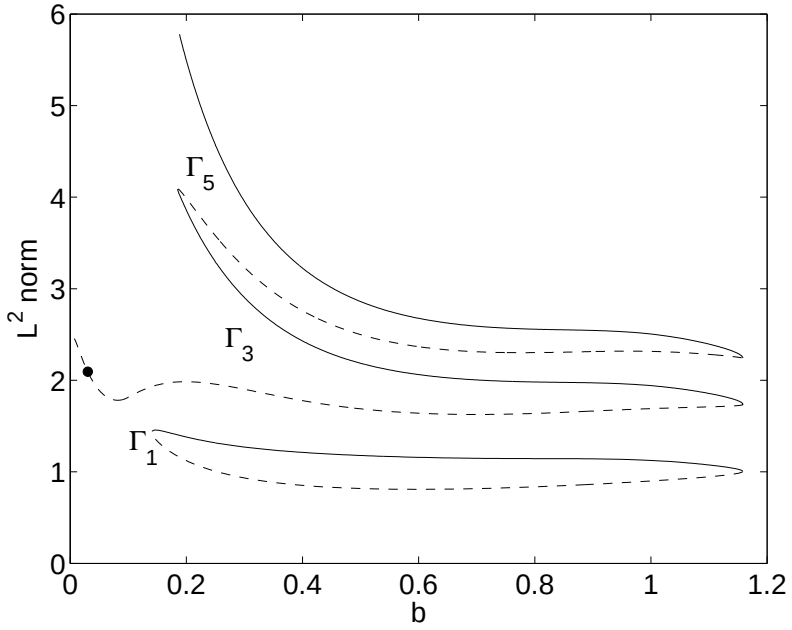

Figure 3.5: Same curves as in Figure 3.4 except with the L^2-norm on the y-axis.

There is a broad "dimple" on the top of the bump. It has not been possible to numerically determine the stability of solutions on the spirals. We expect that stability changes in saddle-node bifurcations on the spirals. As far as we are aware, breaks in the solution curves for this type of one-dimensional neural field model have not been seen previously, so we examine the breaks further in Chapter 5.

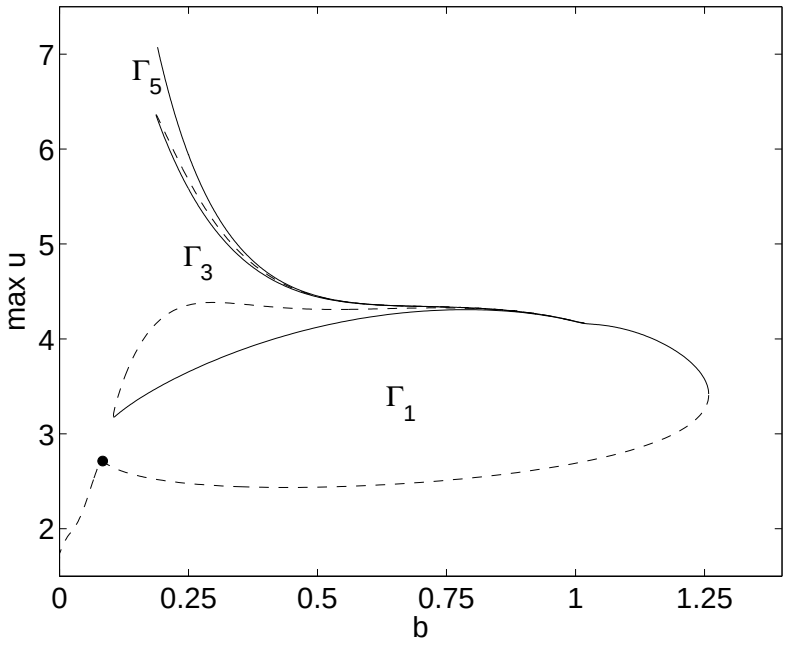

Figure 3.6: Solution curves for Equations (3.1)–(3.3) where $r = 0.090$ and b is the continuation parameter. Solutions to the left of the solid circle are N-bump solutions where $N > 1$. A small kink has appeared around $b = 1$ in the upper branch of solutions.

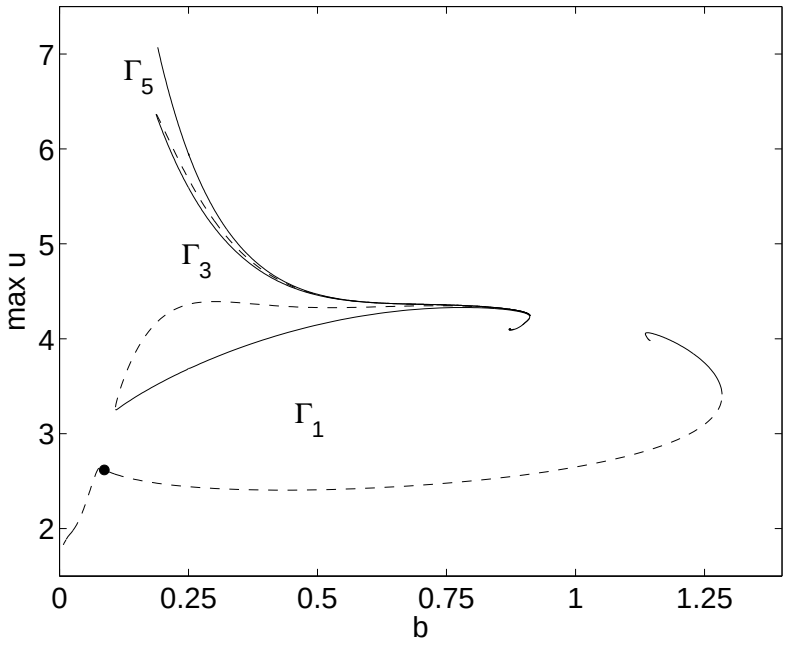

Figure 3.7: Solution curves for Equations (3.1)–(3.3) where $r = 0.085$ and b is the continuation parameter. Solutions to the left of the solid circle are N-bump solutions where $N > 1$. The upper branch of single-bump solutions has developed a discontinuity.

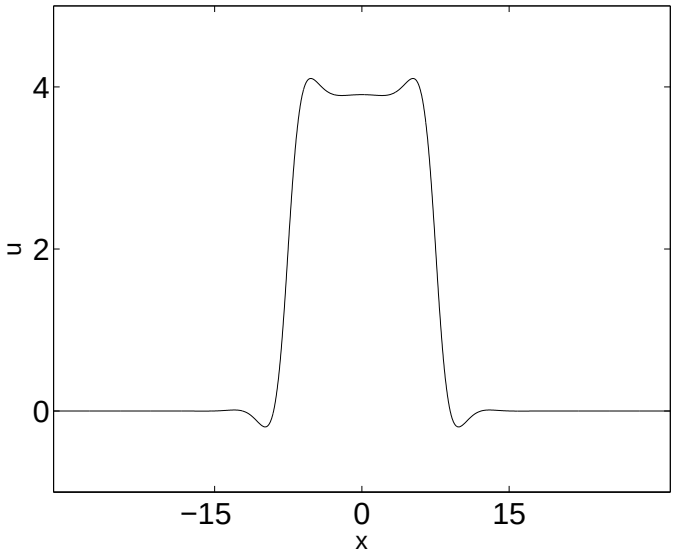

Figure 3.8: A "dimple" single-bump solution for $b = 0.87378$ and $r = 0.085$ on the left hand spiral in the break of the upper branch of single-bump solutions in the bifurcation diagram in Figure 3.7.

3.3 Gap junction model

N-bump solutions

Consider the gap junction model derived in Chapter 1 of

$$\frac{\partial u(x,t)}{\partial t} = \kappa^2 \frac{\partial^2 u}{\partial x^2} - u(x,t) + \int_{-\infty}^{\infty} w(x-y) f(u(y,t))\, dy \tag{3.15}$$

with $\kappa^2 > 0$. Functions $w(x)$ and $f(u)$ are as in Equations (3.2)–(3.3). When $\kappa^2 = 0$, Equation (3.15) becomes the Amari model in Equation (3.1). We find N-bump solutions of the gap junction model using numerical integration. The explicit method of integration used in Section 3.2 is not suitable for the gap junction model. As κ^2 increases, the time step used for the explicit method must reduce rapidly in order to maintain numerical stability. Integration then becomes very slow and eventually numerically unstable. Elvin and Laing [25] developed a hybrid numerical integration method based on the Crank-Nicolson finite difference method. We use this hybrid method for numerical integration of the gap junction model. See the Appendix for an explanation of the method.

We use the same initial conditions and parameter values as in the numerical integration in Section 3.2. That is, $L = 6, 2.5, 1.5$ in Equation (3.4), a domain of Ω: $[-10\pi, 10\pi]$ and $(b, r, \theta) = (0.25, 0.095, 1.5)$. Letting $\kappa^2 = 0.05$ and numerically integrating, we find the stable steady states in Figure 3.9. Again, as the initial excitation condition widens, the number of bumps in the solution increases. When compared to the solutions where $\kappa^2 = 0$ (see Figure 3.2), we see that the inclusion of the term modelling gap junctions has the

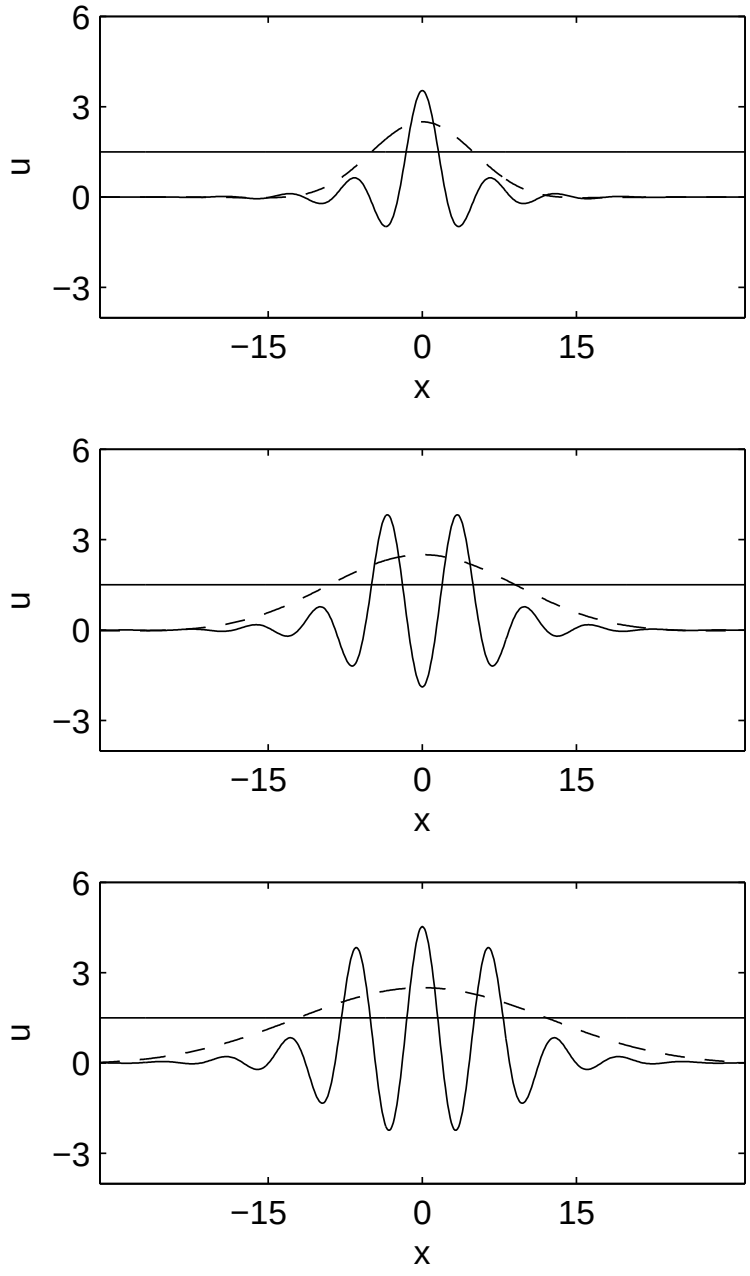

Figure 3.9: Steady state solutions (solid line) of Equation (3.15) found using numerical integration with $\kappa^2 = 0.05$ and different initial conditions (dashed line). From top to bottom, $L = 6, 2.5, 1.5$. The domain is $[-10\pi, 10\pi]$. Parameter values are $b = 0.25$ and $r = 0.095$. There is a horizontal line at $u = \theta$. Compare with Figure 3.2.

effect of reducing the amplitude of the solutions.

Derivation of the ODE

Time-independent solutions of Equation (3.15) satisfy

$$u(x) = \kappa^2 \frac{d^2u}{dx^2} + \int_{-\infty}^{\infty} w(x-y) f(u(y))\, dy. \tag{3.16}$$

We derive an ODE from Equation (3.16). Assuming that u is a solution of our equation, that u and its first five derivatives are continuous on $\mathbb{R}$, and that $(u, u', u'', u''', u^{(iv)}, u^{(v)}) \to (0,0,0,0,0,0)$ exponentially fast as $x \to \pm\infty$, we can apply the Fourier transform to Equation (3.16). Thus, we have

$$F[-\kappa^2 u''] + F[u] = F[w]F[f(u)]. \tag{3.17}$$

Substituting for $F[w]$ from Equation (3.9), Equation (3.17) becomes

$$F[-\kappa^2 u''] + F[u] = \frac{4b(b^2+1)}{\alpha^4 + 2\alpha^2(b^2-1) + (b^2+1)^2} F[f(u)]. \tag{3.18}$$

Using the identity $F[-\kappa^2 u''] = \kappa^2\alpha^2 F[u]$ and multiplying both sides by the denominator on the right hand side, we obtain

$$\left((1+\kappa^2\alpha^2)(\alpha^4 + 2\alpha^2(b^2-1) + (b^2+1)^2)\right) F[u] = 4b(b^2+1)F[f(u)]. \tag{3.19}$$

With the use of the identities $F[u^{(iv)}] = \alpha^4 F[u]$ and $F[-u^{(vi)}] = \alpha^6 F[u]$, Equation (3.19) simplifies to

$$\begin{aligned} F[-\kappa^2 u^{(vi)} + (1 + 2\kappa^2(b^2-1))u^{(iv)} - (2(b^2-1) + \kappa^2(b^2+1)^2)u'' \\ + (b^2+1)^2 u] = 4b(b^2+1)F[f(u)]. \end{aligned} \tag{3.20}$$

We claim that Equation (3.20) is satisfied if u is a solution of the ODE

$$\begin{aligned} -\kappa^2 u^{(vi)} + (1 + 2\kappa^2(b^2-1))u^{(iv)} - (2(b^2-1) + \kappa^2(b^2+1)^2)u'' \\ +(b^2+1)^2 u = 4b(b^2+1)f(u) \end{aligned} \tag{3.21}$$

where $\lim_{x\to\pm\infty} (u, u', u'', u''', u^{(iv)}, u^{(v)}) = (0,0,0,0,0,0)$.

Since $r > 0$, from the definition of $f(u)$, if u is a solution of (3.21), then u and its first five derivatives are continuous on $\mathbb{R}$, therefore (3.20) holds. Hence (3.18) to (3.21) also hold. Our problem of finding N-bump steady states of the original equation in Equation (3.15) is now reduced to that of finding N-bump solutions of Equation (3.21), as any solution of

Equation (3.21) is also a steady state of Equation (3.15). When $\kappa^2 = 0$, Equation (3.21) becomes the ODE for the Amari model in Equation (3.12).

Consider $\kappa^2 > 0$. The sixth-order ODE in Equation (3.21) has a fixed point at $u = 0$ for $\theta > 0$. Letting $v_0 = u$ and $\mathbf{v} = (v_0, v_1, v_2, v_3, v_4, v_5)$, we write Equation (3.21) as the first-order system

$$\begin{aligned} v_0' &= v_1 \\ v_1' &= v_2 \\ v_2' &= v_3 \\ v_3' &= v_4 \\ v_4' &= v_5 \\ v_5' &= \frac{1}{\kappa^2}\Big\{ \big(1 + 2\kappa^2(b^2-1)\big)\, u_4 - \big(2(b^2-1) + \kappa^2(b^2+1)^2\big)\, v_2 + \\ &\qquad (b^2+1)^2 v_0 - 4b(b^2+1) f(v_0)\Big\}. \end{aligned} \tag{3.22}$$

So $\mathbf{v} = (u, u', u'', u''', u^{(iv)}, u^{(v)})$. The system has a fixed point at the origin, that is, $\mathbf{v} = (0,0,0,0,0,0)$. We linearise about $\mathbf{v} = \mathbf{0}$ and since $f'(0) = 0$ and $\theta > 0$, the Jacobian is

$$\mathbf{J}|_{\mathbf{v}=\mathbf{0}} = \begin{pmatrix} 0 & 1 & 0 & 0 & 0 & 0 \\ 0 & 0 & 1 & 0 & 0 & 0 \\ 0 & 0 & 0 & 1 & 0 & 0 \\ 0 & 0 & 0 & 0 & 1 & 0 \\ 0 & 0 & 0 & 0 & 0 & 1 \\ \dfrac{(b^2+1)^2}{\kappa^2} & 0 & \dfrac{2(1-b^2) - \kappa^2(b^2+1)^2}{\kappa^2} & 0 & \dfrac{1 + 2\kappa^2(b^2-1)}{\kappa^2} & 0 \end{pmatrix}. \tag{3.23}$$

The eigenvalues of the equation linearised about the origin are therefore $\pm(b \pm i)$ and $\pm 1/\kappa^2$. The local dynamics are determined by these eigenvalues. Trajectories approaching the stationary point at the origin as $x \to \infty$ are tangential to the eigenspace spanned by the eigenvector(s) corresponding to the eigenvalue(s) with smallest negative real part. These eigenvalues are known as the leading negative eigenvalues and for the gap junction model are the eigenvalues $-b \pm i$. Similarly, trajectories approaching the stationary point at the origin as $x \to -\infty$ are tangential to the eigenspace spanned by the eigenvector(s) corresponding to the eigenvalue(s) with smallest positive real part, that is, the eigenvalues $b \pm i$. These are the leading positive eigenvalues. Hence, the new eigenvalues of the gap junction model, $\pm 1/\kappa^2$, have very little impact on the behaviour of u as $x \to \pm\infty$ for small κ^2 and the behaviour of homoclinic orbits to the origin is mainly determined by the eigenvalues $\pm(b \pm i)$.

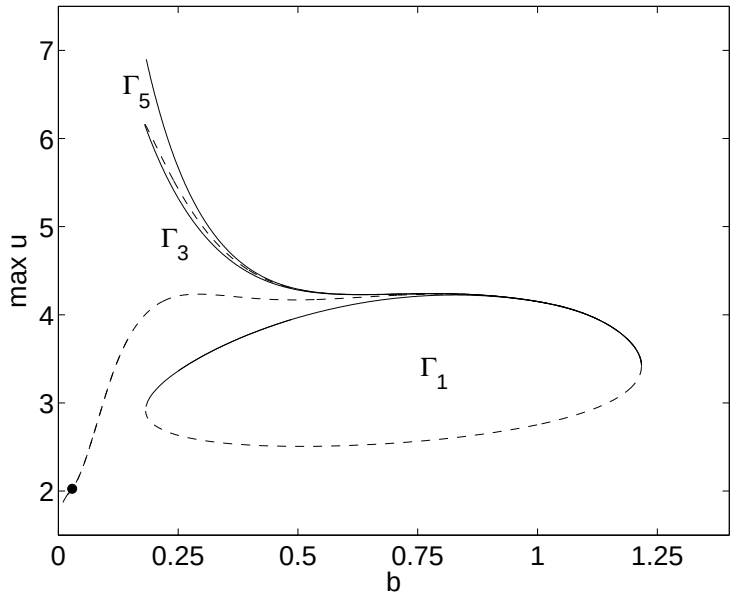

Figure 3.10: Solution curves for $\kappa^2 = 0.05$ in Equation (3.15) with firing rate function in Equation (3.2) and coupling function in Equation (3.3). b is the continuation parameter. Solutions to the left of the solid circle are N-bump solutions where $N > 3$. Compare with Figure 3.3.

Bifurcation analysis

We now find the solution curves of Equation (3.21). Let parameter b be the continuation parameter, $r = 0.095$, $\theta = 1.5$ and the domain be Ω: $[-10\pi, 10\pi]$. When $\kappa^2 = 0$, the solution curves are those for the Amari model in Figure 3.3. As the strength of the term modelling gap junctions is increased (by increasing its coefficient κ^2), qualitative changes are seen. Figure 3.10 shows the solution curves with $\kappa^2 = 0.05$. As $b \to 0^+$, the number of bumps in the solution increases until the entire domain is filled by bumps. On Ω, this is a maximum of ten bumps.

Increasing κ^2 to 0.25, the solution curves change qualitatively. See Figure 3.11. Comparing to $\kappa^2 = 0.05$ in Figure 3.10, we see that single-bump solutions exist over a smaller range of b.

By fixing b and using κ^2 as the continuation parameter, we see how increasing κ^2 changes solutions. See Figure 3.12 for the solution curves of 1-, 3- and 5-bump solutions where $(b, r, \theta) = (0.25, 0.095, 1.5)$. As κ^2 increases, 1-bump solutions are destroyed in a saddle-node bifurcation while 3- and 5-bump solutions still exist. As κ^2 increases further, 3-bump solutions are destroyed in a saddle-node bifurcation. Eventually, κ^2 increases to a value at which 5-bump solutions are destroyed, also through a saddle-node bifurcation. As κ^2 increases, the global maximum of u decreases. Therefore, increasing the magnitude

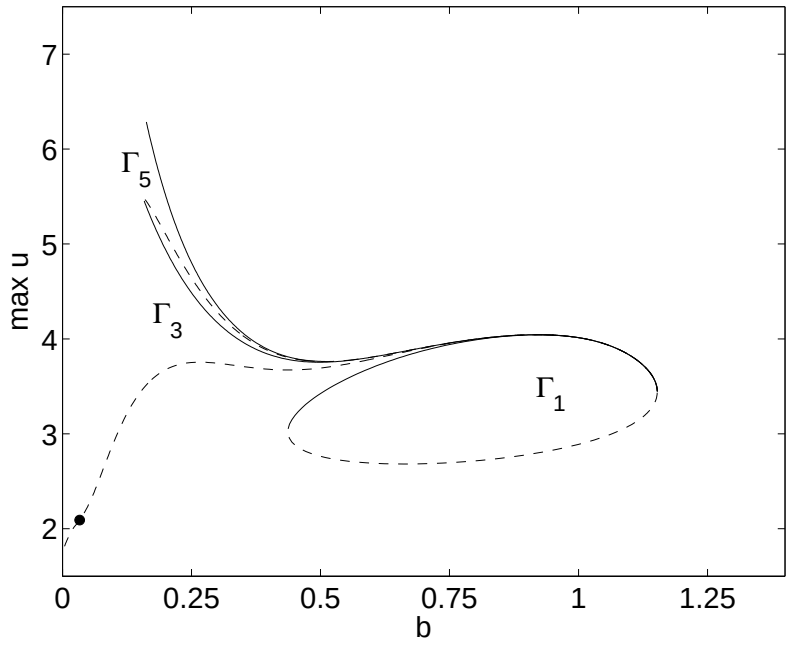

Figure 3.11: Solution curves for $\kappa^2 = 0.25$ in Equation (3.15) with firing rate function in Equation (3.2) and coupling function in Equation (3.3). b is the continuation parameter. Solutions to the left of the solid circle are N-bump solutions where $N > 3$.

of the term modelling gap junctions acts to spread out the N-bump stationary solutions. This diffusion-like effect is expected given that the second spatial derivative is used to model gap junctions.

3.4 Conclusion

In this chapter we introduced the decaying oscillatory coupling function and smooth firing rate function of [70]. The decaying oscillatory coupling function permits multiple bump (N-bump) steady state solutions. Numerical techniques must be used to find solutions given the nonlinearity of the model. We reviewed the results of [70] where 1-, 3- and 5-bump stable steady state solutions were found for the Amari model through numerical integration. We found that different initial conditions led to different steady states. We also derived the fourth-order ODE and solution curves for 1-, 3- and 5-bump solutions found in [70]. The system was found to be multi-stable as N-bump solutions, in general, came in pairs of one stable solution and one unstable solution. Stability changed at saddle-node bifurcations.

By varying the steepness of the firing rate function, we found qualitative changes in the solution curves. The effect of increasing the steepness of the firing rate function (decreasing

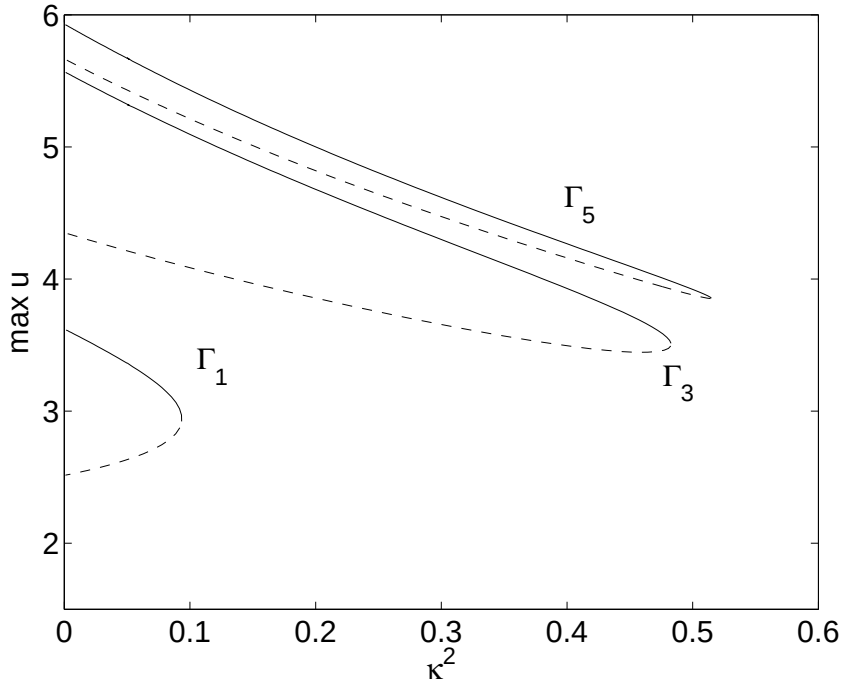

Figure 3.12: Solution curves for Equation (3.15) with the smooth firing rate function in Equation (3.2) and decaying oscillatory coupling function in Equation (3.3). κ^2 is the continuation parameter, $b = 0.25$ and $r = 0.095$.

r) was that discontinuities appeared in the solution curves. These discontinuities were not described in [70].

In Section 3.3 numerical integration was used to find 1-, 3- and 5-bump solutions of the gap junction model from Chapter 1 with the decaying oscillatory coupling function and smooth firing rate function in [70]. Using the Fourier transform technique of [70], a sixth-order ODE was derived from the gap junction model. Solutions of the ODE are steady states of the gap junction model. Solution curves of 1-, 3- and 5-bump solutions were found. The system was multi-stable. The effect of increasing the strength of the term modelling gap junctions (increasing κ^2) was to destroy families of solutions in saddle-node bifurcations.

Chapter 4

Piecewise construction of solutions

4.1 Introduction

In this chapter we construct explicit piecewise symmetric single-bump steady state solutions of both the Amari model and the gap junction model. In Chapter 2 we used the piecewise method in [47] to construct symmetric, single-bump steady states with a shifted Heaviside firing rate function and lateral inhibition coupling function. We use the same method here with the decaying oscillatory coupling function of Chapter 3 and both the shifted Heaviside firing rate function and a piecewise linear firing rate function. Use of a linear firing rate function permits the construction of explicit solutions. In Chapter 3, we had to find steady states numerically given that a smooth firing rate function was used. For a sufficiently steep firing rate function, we found breaks in the upper branch of solutions. There were no stable spatially localised steady state solutions in the region of the break. We want to understand what causes these breaks. We therefore find the solution curves for a step function and then for a piecewise linear function with varying steepness.

4.2 Amari model

We construct symmetric single-bump steady states of the Amari model

$$\frac{\partial u(x,t)}{\partial t} = -u(x,t) + \int_{-\infty}^{\infty} w(x-y) f(u(y,t))\, dy \tag{4.1}$$

with the decaying oscillatory coupling function from Chapter 3 of

$$w(x) = e^{-b|x|}\left(b\sin(|x|) + \cos(x)\right) \tag{4.2}$$

where $b > 0$. In Chapter 3, we derived the fourth-order ODE in [70] of

$$\begin{cases} u^{(iv)} + 2(1-b^2)u'' + (b^2+1)^2 u &= 4b(b^2+1)f(u), \\ \lim\limits_{x\to\pm\infty}(u, u', u'', u''') &= (0,0,0,0). \end{cases} \tag{4.3}$$

Solutions of the ODE are steady state solutions of Equations (4.1)–(4.2). The ODE is used to construct steady states of the Amari model. We first allow $f(u)$ to be a step function, then a piecewise linear function. We set the threshold to be $\theta = 1.5$ for the chapter.

Step firing rate function

In this section we use double the shifted Heaviside firing rate function from Chapter 2 (see Equation (2.3)) of

$$f(u) = 2\Theta(u-\theta) = \begin{cases} 2, & \text{if } u \geq \theta \\ 0, & \text{if } u < \theta. \end{cases} \tag{4.4}$$

We note that the function in Equation (4.4) can also be obtained by taking the limit of $r \to 0$ in the smooth firing rate function in Chapter 3 of

$$f(u) = 2e^{-r/(u-\theta)^2}\Theta(u-\theta). \tag{4.5}$$

Substituting for $f(u)$ from Equation (4.4), we have $c \in \mathbb{R}^+$ such that $u(c) = \theta$. The ODE in Equation (4.3) becomes the two linear differential equations

$$\begin{aligned} &u^{(iv)} + 2(1-b^2)u'' + (b^2+1)^2 u = 0, && \text{for } c < x \\ &u^{(iv)} + 2(1-b^2)u'' + (b^2+1)^2 u = 8b(b^2+1), && \text{for } 0 \leq x < c. \end{aligned} \tag{4.6}$$

We have, therefore, a nonhomogeneous ODE for an above-threshold region and a homogeneous ODE for a below-threshold region. At the threshold, we have matching conditions on u and its derivatives to obtain a smooth and continuous function on $\mathbb{R}$. There is also the boundary condition in Equation (4.3).

As in Chapter 2, we decompose u into two functions, u_T and u_L, such that $u_T(x) > \theta$ and $u_L(x) < \theta$. See Figure 4.1. Then $u_T(c) = u_L(c) = \theta$ and

$$u(x) = \begin{cases} u_T, & 0 \leq x < c \\ u_L, & c < x. \end{cases} \tag{4.7}$$

The ODEs in Equation (4.6) can be written as the two linear differential equations

$$u_L^{(iv)} + 2(1-b^2)u_L'' + (b^2+1)^2 u_L = 0, \quad \text{for } c < x \tag{4.8}$$

$$u_T^{(iv)} + 2(1-b^2)u_T'' + (b^2+1)^2 u_T = 8b(b^2+1), \quad \text{for } 0 \leq x < c. \tag{4.9}$$

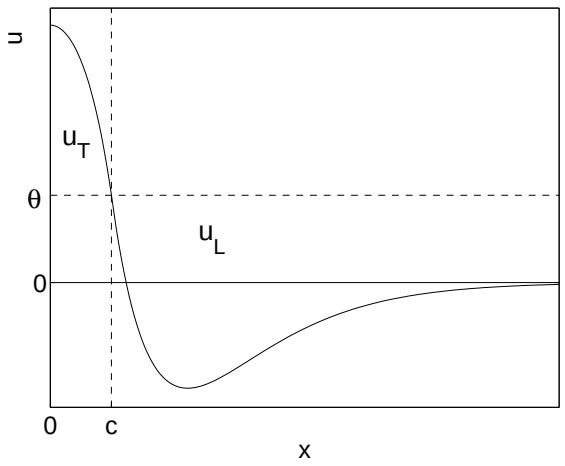

Figure 4.1: Piecewise construction of a symmetric single-bump solution for $x \in \mathbb{R}_0^+$ with a step firing rate function, horizontal line at $u = \theta$. The above-threshold function u_T and below-threshold function u_L meet at the threshold at $x = c$.

Solutions of u_T must satisfy the nonhomogeneous ODE in Equation (4.9) on the interval $0 \leq x < c$. At this stage, c is unknown and must be determined. Solutions are of the form

$$u_T(x) = e^{bx}\left(C_1\cos(x) + C_2\sin(x)\right) + e^{-bx}\left(C_3\cos(x) + C_4\sin(x)\right) + \frac{8b}{b^2+1} \tag{4.10}$$

where $C_1, C_2, C_3, C_4 \in \mathbb{R}$. As solutions are symmetric in space, the function u_T satisfies the initial conditions

$$\begin{aligned} u_T(0) &= u(0) \\ u_T'(0) &= 0 \\ u_T''(0) &= u''(0) \\ u_T'''(0) &= 0. \end{aligned} \tag{4.11}$$

We solve for C_1–C_4 in terms of $u(0), u''(0)$ and the coupling decay parameter $b > 0$ to obtain

$$\begin{pmatrix} C_1 \\ C_2 \\ C_3 \\ C_4 \end{pmatrix} = \begin{pmatrix} \dfrac{u(0)(b^2+1) - 8b}{2(b^2+1)} \\ \dfrac{8b(b^2-1) - u(0)(b^4-1) + u''(0)(b^2+1)}{4b(b^2+1)} \\ \dfrac{u(0)(b^2+1) - 8b}{2(b^2+1)} \\ -\dfrac{8b(b^2-1) - u(0)(b^4-1) + u''(0)(b^2+1)}{4b(b^2+1)} \end{pmatrix}. \tag{4.12}$$

Noting from Equation (4.12) that $C_3 = C_1$ and $C_4 = -C_2$, we can write Equation (4.10)

in the form

$$u_T(x) = C_1 \cos(x)(e^{bx} + e^{-bx}) + C_2 \sin(x)(e^{bx} - e^{-bx}) + \frac{8b}{b^2+1}. \tag{4.13}$$

The constants C_1 and C_2 depend on $u(0)$ and $u''(0)$. Solutions of u_L must satisfy the homogeneous ODE in Equation (4.8) for $c < x$ and the boundary condition $\lim_{x\to\infty} u_L \to 0$. Thus, solutions are of the form

$$u_L(x) = C_5 e^{-bx} \cos(x) + C_6 e^{-bx} \sin(x) \tag{4.14}$$

where $C_5, C_6 \in \mathbb{R}$. The functions u_T and u_L and their derivatives must meet at $x = c$ for a continuous function $u(x)$, creating a set of five matching conditions

$$\begin{aligned} u_T(c) &= u_L(c) \\ u_T(c) &= \theta \\ u_T'(c) &= u_L'(c) \\ u_T''(c) &= u_L''(c) \\ u_T'''(c) &= u_L'''(c). \end{aligned} \tag{4.15}$$

Evaluation of Equation (4.15) results in the system of equations

$$\begin{aligned} &C_1 \cos(c)[e^{bc} + e^{-bc}] + C_2 \sin(c)[e^{bc} - e^{-bc}] + \frac{8b}{b^2+1} - \\ &C_5 e^{-bc} \cos(c) - C_6 e^{-bc} \sin(c) = 0. \end{aligned} \tag{4.16}$$

$$C_1 \cos(c)[e^{bc} + e^{-bc}] + C_2 \sin(c)[e^{bc} - e^{-bc}] + \frac{8b}{b^2+1} - \theta = 0. \tag{4.17}$$

$$\begin{aligned} &C_1[e^{bc}(b\cos(c) - \sin(c)) - e^{-bc}(b\cos(c) + \sin(c))] + \\ &C_2[e^{bc}(b\sin(c) + \cos(c)) + e^{-bc}(b\sin(c) - \cos(c))] + \\ &C_5 e^{-bc}[b\cos(c) + \sin(c)] + C_6 e^{-bc}[b\sin(c) - \cos(c)] = 0. \end{aligned} \tag{4.18}$$

$$\begin{aligned} &C_1 \left(e^{bc}[(b^2-1)\cos(c) - 2b\sin(c)] + e^{-bc}[(b^2-1)\cos(c) + 2b\sin(c)]\right) + \\ &C_2 \left(e^{bc}[(b^2-1)\sin(c) + 2b\cos(c)] + e^{-bc}[(1-b^2)\sin(c) + 2b\cos(c)]\right) + \\ &C_5 e^{-bc}[(1-b^2)\cos(c) - 2b\sin(c)] + \\ &C_6 e^{-bc}[(1-b^2)\sin(c) + 2b\cos(c)] = 0. \end{aligned} \tag{4.19}$$

$$\tag{4.20}$$

$$C_1\left(e^{bc}[(b^3-3b)\cos(c)-(1-3b^2)\sin(c)]+e^{-bc}[(3b-b^3)\cos(c)+(1-3b^2)\sin(c)]\right)+$$
$$C_2\left(e^{bc}[(3b^2-1)\cos(c)+(b^3-3b)\sin(c)]+e^{-bc}[(1-3b^2)\cos(c)+(b^3-3b)\sin(c)]\right)+$$
$$C_5e^{-bc}[(b^3-3b)\cos(c)+(3b^2-1)\sin(c)]+$$
$$C_6e^{-bc}[(1-3b^2)\cos(c)+(b^3-3b)\sin(c)]=0. \tag{4.21}$$

We have five unknowns in five nonlinear equations. We set $b = 0.16$ and $\theta = 1.5$. Using Newton's method [60], we solve the set of nonlinear equations in Equations (4.16)–(4.21) and find the two steady states in Table 4.1. Each line corresponds to a particular steady state.

Table 4.1: Coefficients for steady states of Equations (4.8)–(4.9) with $b = 0.16$ and $\theta = 1.5$ found using piecewise construction.

$u(0)$	$u''(0)$	C_5	C_6	c
4.02513	-3.22676	3.86037	1.07307	1.34803
1.63558	-1.56776	1.63388	0.27748	0.42113

We construct the two steady states given by the entries in Table 4.1 by evaluating functions u_T and u_L in Equations (4.13) and (4.14). See Figure 4.2 where the solid line is the first entry and the dashed line is the second entry in Table 4.1. Single-bump solutions do not exist for small b. As expected, when solutions come in pairs, there is one wider, taller solution and one narrower, smaller solution. Numerically, the wider, taller solution appears to be a stable solution and the narrower, smaller solution an unstable solution. Using AUTO 2000, we find the solution curve in Figure 4.3. Here we see that the upper branch of solutions breaks at $b = 0.451, 2.215$. This causes a very wide gap between the upper and lower branches. We see that as b increases along the upper branch toward the gap, $u''(0)$ becomes positive. Solutions where $u''(0) > 0$ are "dimple" single-bump solutions. Solutions on the upper branch are stable for all b. We note that we also used our own code of the pseudo-arclength continuation method for the bifurcation analysis in the chapter. We found the same results as with AUTO 2000. See the Appendix for a description of the method.

There appears to be a change of stability on the lower solution branch in Figure 4.3. As we restrict solutions to single-bump solutions only and do not consider all possible N-bump solutions, we cannot see what kind of bifurcation occurs. Index theory, however, tells us that there must be a bifurcation given the change in stability. We used numerical

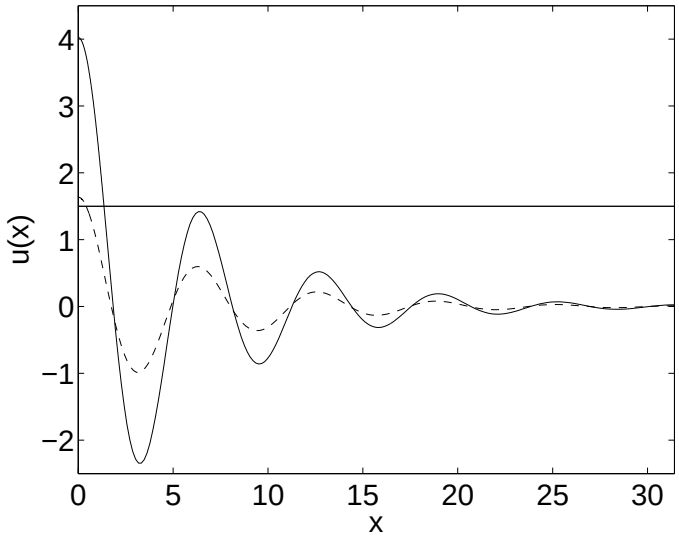

Figure 4.2: Piecewise construction of the two single-bump solutions given by the first (solid line) and second entry (dashed line) in Table 4.1 found for Equation (4.6) with $b = 0.16$. Horizontal line at $\theta = 1.5$.

simulation to determine the solution stability (see Chapter 7). To do this, a steady state solution is constructed for a particular value of b. We numerically integrate with the solution as an initial condition. If the initial condition is a stable solution, the numerical integration leaves the initial condition unchanged. For a range of b in Figure 4.3, only unstable steady state solutions exist. Numerical integration with a solution in this region as the initial condition results in a region of high activity that expands in both directions with time. If the numerical integration continues for a sufficiently long length of time, the high activity eventually fills the entire domain.

Piecewise linear firing rate function

We define a piecewise linear firing rate function

$$f(u) = \begin{cases} 0, & u < \theta \\ \alpha(u - \theta), & \theta < u < \theta + \beta/\alpha \\ \beta, & \theta + \beta/\alpha < u \end{cases} \tag{4.22}$$

with $\alpha, \beta, \theta > 0$. See Figure 4.4. Equation (4.22) has two thresholds, one at θ and another at $\theta + \beta/\alpha$. We use the notation of $\theta_T = \theta + \beta/\alpha$ for the remainder of this section.

By varying the steepness parameter α, it is possible to approximate the smooth firing rate function in Equation (4.5), as seen in Fig. 4.4. Increasing α makes $f(u)$ steeper and is similar to decreasing r in the smooth firing rate function. The advantage of using a piecewise linear firing rate function is that we can calculate explicit piecewise

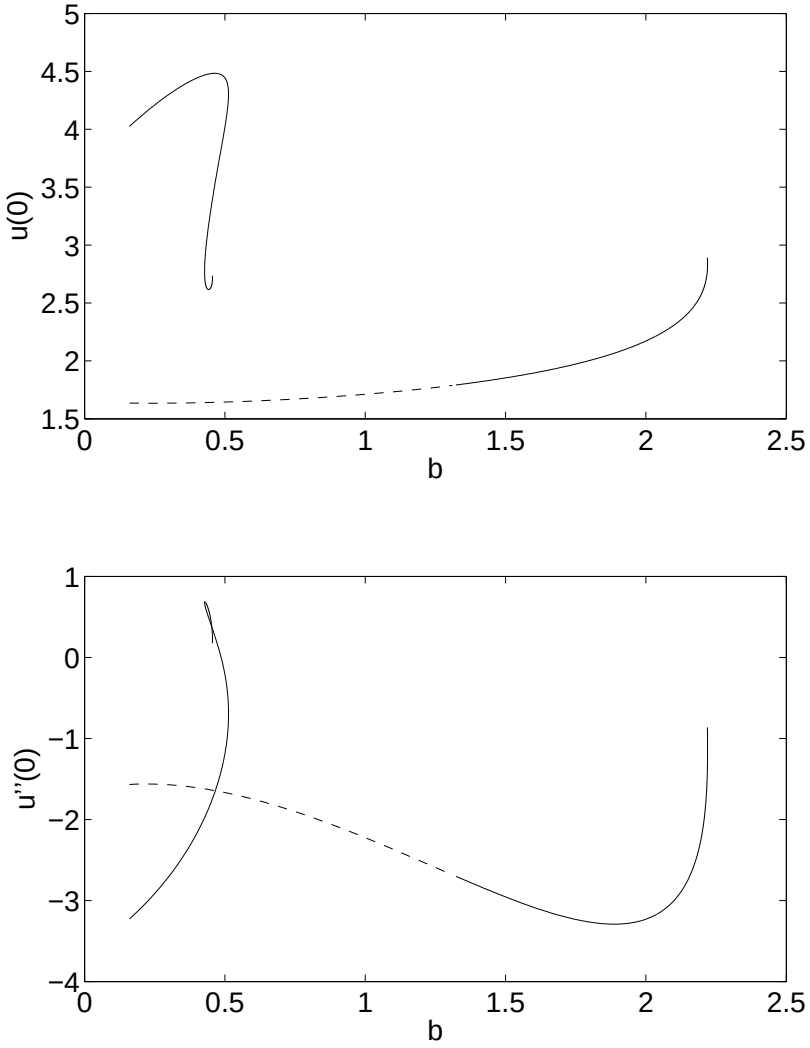

Figure 4.3: Solution curves for the Amari model with decaying oscillatory coupling function and step firing rate function, found using piecewise solution construction with Equation (4.6). Threshold is $\theta = 1.5$. Top: $u(0)$ as a function of b with breaks at $b = 0.451, 2.215$ causing a wide gap between the upper and lower branches. There is a change of stability on the lower branch. Bottom: $u''(0)$ as a function of b. Solid line: stable solutions; dashed line: unstable solutions.

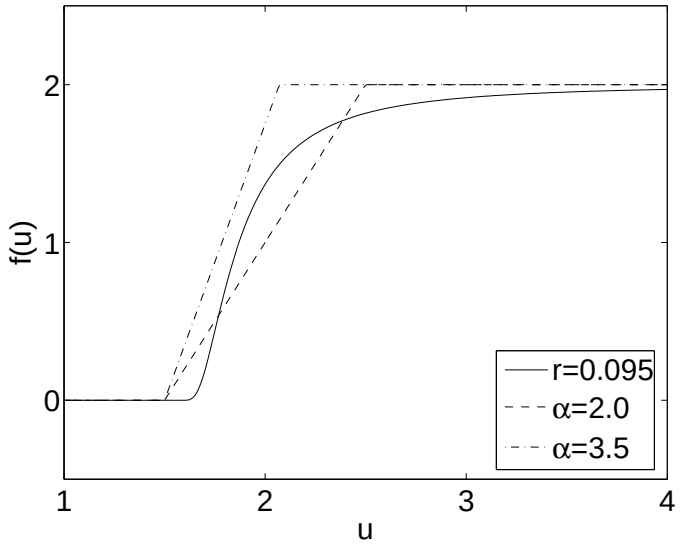

Figure 4.4: The piecewise linear firing rate function in Equation (4.22) with $\alpha = 2, 3.5$ and $\beta = 2$ shown with the smooth firing rate function in Equation (4.5) for $r = 0.095$. The threshold is $\theta = 1.5$.

solutions using the piecewise differential framework of the previous section, rather than only being able to undertake numerical simulations. This approach is used to gain a better understanding of the qualitative changes seen in solutions of the full model in Chapter 3 as r is varied from 0.095.

Using $f(u)$ from Equation (4.22) in the ODE for the Amari model in Equation (4.3), we have $c, d \in \mathbb{R}^+$ such that $u(c) = \theta_T$ and $u(d) = \theta$. Hence we obtain the three linear differential equations

$$u^{(iv)} + 2(1-b^2)u'' + (b^2+1)^2 u = 0, \quad \text{for } d < x \tag{4.23}$$

$$u^{(iv)} + 2(1-b^2)u'' + (b^2+1)(b^2 - 4\alpha b + 1)u = -4\alpha b(b^2+1), \quad \text{for } c < x < d \tag{4.24}$$

$$u^{(iv)} + 2(1-b^2)u'' + (b^2+1)^2 u = 4\beta b(b^2+1), \quad \text{for } 0 \leq x < c. \tag{4.25}$$

We decompose u into three functions, u_L, u_M, u_T such that

$$u(x) = \begin{cases} u_T(x), & 0 \leq x < c \\ u_M(x), & c < x < d \\ u_L(x), & d < x. \end{cases} \tag{4.26}$$

Therefore $u_T(c) = u_M(c) = \theta_T$ and $u_M(d) = u_L(d) = \theta$. See Figure 4.5. Equations (4.23)–

(4.25) can be written as

$$u_L^{(iv)} + 2(1-b^2)u_L'' + (b^2+1)^2 u_L = 0, \quad \text{for } d < x \tag{4.27}$$

$$u_M^{(iv)} + 2(1-b^2)u_M'' + (b^2+1)(b^2-4\alpha b+1)u_M = -4\alpha\theta b(b^2+1), \quad \text{for } c < x < d \tag{4.28}$$

$$u_T^{(iv)} + 2(1-b^2)u_T'' + (b^2+1)^2 u_T = 4\beta b(b^2+1), \quad \text{for } 0 \le x < c. \tag{4.29}$$

There is a set of matching conditions at $x = c$ and another at $x = d$. Solutions of u_T must satisfy the nonhomogeneous ODE for u_T in Equation (4.29) on the interval $0 \le x < c$. Solutions are of the form

$$u_T(x) = e^{bx}\left(C_1\cos(x) + C_2\sin(x)\right) + e^{-bx}\left(C_3\cos(x) + C_4\sin(x)\right) + \frac{4\beta b}{b^2+1} \tag{4.30}$$

where $C_1, C_2, C_3, C_4 \in \mathbb{R}$. Again, the function u_T satisfies the initial conditions in Equation (4.11). We solve for C_1–C_4 in terms of $u(0), u''(0)$ and $b > 0$ to obtain

$$\begin{pmatrix} C_1 \\ C_2 \\ C_3 \\ C_4 \end{pmatrix} = \begin{pmatrix} \dfrac{u(0)}{2} - \dfrac{2\beta b}{(b^2+1)} \\ \dfrac{\beta(b^2-1)}{(b^2+1)} + \dfrac{u(0)(1-b^2)+u''(0)}{4b} \\ \dfrac{u(0)}{2} - \dfrac{2\beta b}{(b^2+1)} \\ -\left(\dfrac{\beta(b^2-1)}{(b^2+1)} + \dfrac{u(0)(1-b^2)+u''(0)}{4b}\right) \end{pmatrix}. \tag{4.31}$$

We see from Equation (4.31) that $C_3 = C_1$ and $C_4 = -C_2$. Equation (4.30) can be simplifed to

$$u_T(x) = C_1\cos(x)(e^{bx} + e^{-bx}) + C_2\sin(x)(e^{bx} - e^{-bx}) + \frac{4\beta b}{b^2+1}. \tag{4.32}$$

The function u_M is found by solving the nonhomogeneous ODE for u_M in Equation (4.28) on the interval $c < x < d$ where $u_M(c) = \theta_T$ and $u_M(d) = \theta$. The ODE for u_M in Equation (4.28) has eigenvalues

$$\pm\sqrt{b^2 - 1 \pm 2\sqrt{\alpha b(b^2+1) - b^2}}. \tag{4.33}$$

Single-bump solutions do not exist for such small b. For the range of b for which single-bump solutions exist, the eigenvalues are a pure imaginary conjugate pair, $\pm m_1 i$, and a real pair of same magnitude but different signs, $\pm m_2$, where $m_1, m_2 \in \mathbb{R}^+$. Hence u_M has the form

$$u_M(x) = D_1\cos(m_1 x) + D_2\sin(m_1 x) + D_3 e^{m_2 x} + D_4 e^{-m_2 x} + \frac{4\alpha\theta b}{(4\alpha b - b^2 - 1)} \tag{4.34}$$

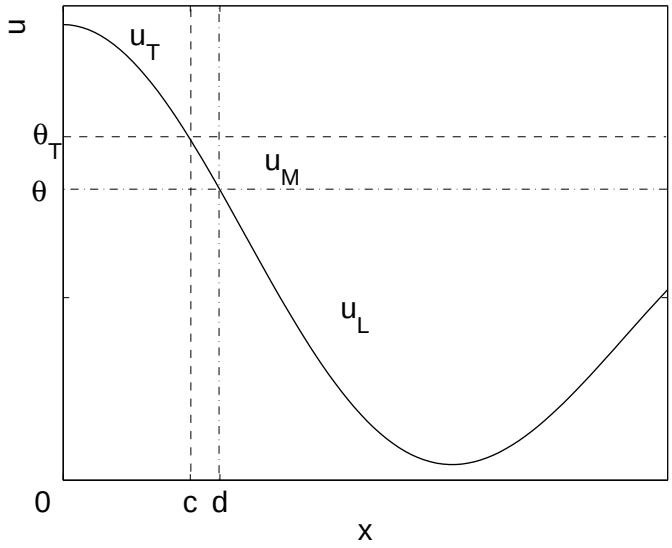

Figure 4.5: Construction of piecewise single-bump solution where u is decomposed into three separate functions as in Equation (4.26).

where $D_1, D_2, D_3, D_4 \in \mathbb{R}$ and

$$m_1 = \sqrt{1 - b^2 + 2\sqrt{b\alpha(b^2+1) - b^2}} \tag{4.35}$$

$$m_2 = \sqrt{b^2 - 1 + 2\sqrt{b\alpha(b^2+1) - b^2}}. \tag{4.36}$$

Functions u_T and u_M must satisfy the matching conditions

$$\begin{aligned} u_T(c) &= u_M(c) \\ u_T(c) &= \theta_T \\ u_T'(c) &= u_M'(c) \\ u_T''(c) &= u_M''(c) \\ u_T'''(c) &= u_M'''(c). \end{aligned} \tag{4.37}$$

Evaluation of Equation (4.37) gives the system of equations

$$\begin{aligned} &C_1 \cos(c)[e^{bc} + e^{-bc}] + C_2 \sin(c)[e^{bc} - e^{-bc}] + \frac{4\beta b}{b^2+1} - \\ &D_1 \cos(m_1 c) - D_2 \sin(m_1 c) - D_3 e^{m_2 c} - D_4 e^{-m_2 c} - \frac{4\alpha\theta b}{(4\alpha b - b^2 - 1)} = 0. \end{aligned} \tag{4.38}$$

$$C_1\cos(c)[e^{bc}+e^{-bc}]+C_2\sin(c)[e^{bc}-e^{-bc}]+\frac{4\beta b}{b^2+1}-\theta-\beta/\alpha=0. \tag{4.39}$$

$$\begin{aligned}&C_1[e^{bc}(b\cos(c)-\sin(c))-e^{-bc}(b\cos(c)+\sin(c))]+\\&C_2[e^{bc}(b\sin(c)+\cos(c))+e^{-bc}(b\sin(c)-\cos(c))]+\\&m_1[D_1\sin(m_1c)-D_2\cos(m_1c)]+m_2[D_4e^{-m_2c}-D_3e^{m_2c}]=0.\end{aligned} \tag{4.40}$$

$$\begin{aligned}&C_1\left(e^{bc}[(b^2-1)\cos(c)-2b\sin(c)]+e^{-bc}[(b^2-1)\cos(c)+2b\sin(c)]\right)+\\&C_2\left(e^{bc}[(b^2-1)\sin(c)+2b\cos(c)]+e^{-bc}[(1-b^2)\sin(c)+2b\cos(c)]\right)+\\&m_1^2[D_1\cos(m_1c)+D_2\sin(m_1c)]-m_2^2[D_4e^{-m_2c}+D_3e^{m_2c}]=0.\end{aligned} \tag{4.41}$$

$$\begin{aligned}&C_1\left(e^{bc}[(b^3-3b)\cos(c)+(1-3b^2)\sin(c)]+e^{-bc}[(3b-b^3)\cos(c)+(1-3b^2)\sin(c)]\right)+\\&C_2\left(e^{bc}[(3b^2-1)\cos(c)+(b^3-3b)\sin(c)]+e^{-bc}[(1-3b^2)\cos(c)+(b^3-3b)\sin(c)]\right)+\\&m_1^3[D_2\cos(m_1c)-D_1\sin(m_1c)]+m_2^3[D_4e^{-m_2c}-D_3e^{m_2c}]=0.\end{aligned} \tag{4.42}$$

Solutions of u_L must satisfy the homogeneous ODE in Equation (4.27) for $d<x$ and the boundary condition $\lim_{x\to\infty}u_L\to 0$. Thus, solutions are of the form

$$u_L(x)=A_1e^{-bx}\cos(x)+A_2e^{-bx}\sin(x) \tag{4.43}$$

where $A_1,A_2\in\mathbb{R}$. The functions u_M and u_L must meet at $x=d$ for a continuous function $u(x)$, creating a second set of matching conditions

$$\begin{aligned}u_M(d)&=u_L(d)\\u_M(d)&=\theta\\u_M'(d)&=u_L'(d)\\u_M''(d)&=u_L''(d)\\u_M'''(d)&=u_L'''(d).\end{aligned} \tag{4.44}$$

Evaluating Equation (4.44) we get the system of equations

$$\begin{aligned}&D_1\cos(m_1d)+D_2\sin(m_1d)+D_3e^{m_2d}+D_4e^{-m_2d}+\frac{\theta(b^2+1)}{(4\alpha b-b^2-1)}-\\&A_1e^{-bd}\cos(d)-A_2e^{-bd}\sin(d)=0.\end{aligned} \tag{4.45}$$

$$D_1\cos(m_1d)+D_2\sin(m_1d)+D_3e^{m_2d}+D_4e^{-m_2d}+\frac{\theta(b^2+1)}{(4\alpha b-b^2-1)}=0. \tag{4.46}$$

$$m_1[D_2\cos(m_1 d) - D_1\sin(m_1 d)] + m_2[D_3 e^{m_2 d} - D_4 e^{-m_2 d}] +$$
$$A_1 e^{-bd}[b\cos(d) + \sin(d)] + A_2 e^{-bd}[b\sin(d) - \cos(d)] = 0. \tag{4.47}$$

$$-m_1^2[D_1\cos(m_1 d) + D_2\sin(m_1 d)] + m_2^2[D_4 e^{-m_2 d} + D_3 e^{m_2 d}] +$$
$$A_1 e^{-bd}[(1-b^2)\cos(d) - 2b\sin(d)] + A_2 e^{-bd}[(1-b^2)\sin(d) + 2b\cos(d)] = 0. \tag{4.48}$$

$$m_1^3[D_1\sin(m_1 d) - D_2\cos(m_1 d)] + m_2^3[D_3 e^{m_2 d} - D_4 e^{-m_2 d}] +$$
$$A_1 e^{-bd}[(b^3 - 3b)\cos(d) + (3b^2 - 1)\sin(d)] +$$
$$A_2 e^{-bd}[(b^3 - 3b)\sin(d) + (1 - 3b^2)\cos(d)] = 0. \tag{4.49}$$

We set $\alpha = 2, \beta = 2$ and $b = 0.25$. We want to solve for $C_1, C_2, D_1, D_2, D_3, D_4, A_1, A_2$, c and d. We use Newton's method [60] on the nonlinear equations given by the matching conditions in Equations (4.38)–(4.42) and Equations (4.45)–(4.49) to find the two steady state solutions in Table 4.2. The first entry is for a single-bump solution that appears to be numerically stable and the second entry for a smaller solution that appears to be numerically unstable. We do the same for $\alpha = 3$ and find the solutions in Table 4.3.

Table 4.2: Coefficients for functions u_T, u_M, u_L in Equations (4.32), (4.34) and (4.43) found using piecewise construction method. Parameter values are $\alpha = 2$, $b = 0.25$, $\beta = 2$ and $\theta = 1.5$.

$u(0)$	$u''(0)$	D_1	D_2	D_3	D_4	A_1	A_2	c	d
3.743	-2.900	0.950	0.324	-0.673	0.300	3.5829	1.4041	0.969	1.364
2.568	-2.243	0.719	0.006	-0.682	-0.668	2.535	0.785	0.248	1.047

Table 4.3: Coefficients for functions u_T, u_M, u_L in Equations (4.32), (4.34) and (4.43) found using piecewise construction method. Parameter values are $\alpha = 3$, $b = 0.25$, $\beta = 2$ and $\theta = 1.5$.

$u(0)$	$u''(0)$	D_1	D_2	D_3	D_4	A_1	A_2	c	d
3.969	-2.951	0.780	0.540	-0.305	1.307	3.738	1.600	1.178	1.421
2.187	-1.974	0.545	0.001	-0.341	-0.339	2.171	0.633	0.145	0.881

Using the solutions in Tables 4.2–4.3 as starting solutions in AUTO 2000, we find the bifurcation diagram in Figure 4.6. We see that when $\alpha = 2$ in the piecewise firing rate

function, a continuous solution curve is found. Numerically, stability appears to change via a saddle-node bifurcation. For a steeper firing rate function, $\alpha = 3$, the solution curve is discontinuous. We saw similar behaviour in Figure 4.3 when we found piecewise solutions using a step firing rate function, however, the gap was wider. A similar discontinuity was seen in Chapter 3 when the smooth firing rate function was sufficiently steep. It appears that the width of the discontinuity in the solution curve increases as the firing rate function becomes steeper.

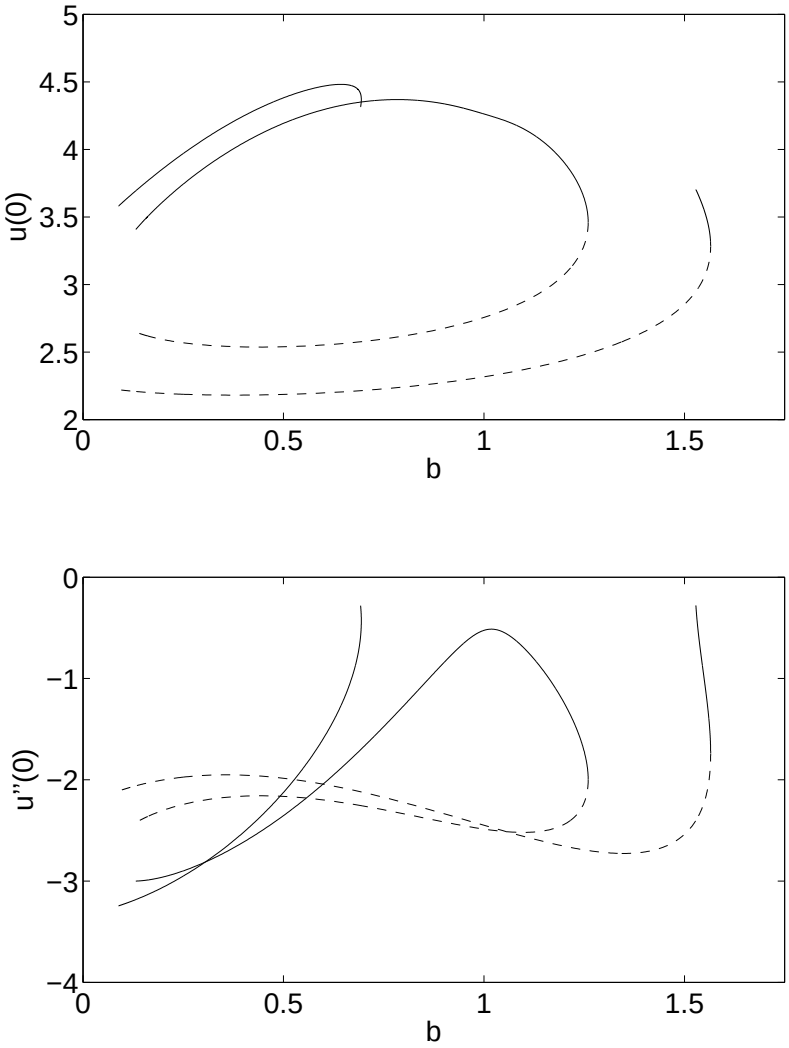

Figure 4.6: Solution curves of the Amari model with oscillatory coupling function and piecewise linear firing rate function, found using piecewise construction method with Equations (4.27)–(4.29). Parameters are $\beta = 2, \theta = 1.5$ and $\alpha = 2, 3$. Top: $u(0)$ as a function of b. The solution curve does not break for $\alpha = 2$. The upper and lower solution branches are disconnected for $\alpha = 3$ with breaks at $b = 0.655, 1.527$. Stability changes in saddle-node bifurcations. Bottom: $u''(0)$ as a function of b. Solid line: stable solutions; dashed line: unstable solutions. Compare to Figure 4.3.

4.3 Gap junction model

We now apply the method of piecewise construction of symmetric single-bump steady states in Section 4.2 to the gap junction model from Chapter 3 of

$$\frac{\partial u(x,t)}{\partial t} = \kappa^2 \frac{\partial^2 u}{\partial x^2} - u(x,t) + \int_{-\infty}^{\infty} w(x-y) f(u(y,t))\, dy \tag{4.50}$$

with the decaying oscillatory coupling function in Equation (4.2). In Chapter 3, we derived a sixth-order ODE, solutions of which are steady states of Equation (4.50) with the decaying oscillatory coupling function

$$\begin{cases} -\kappa^2 u^{(vi)} + \left(1 + 2\kappa^2(b^2-1)\right) u^{(iv)} + \left(2(1-b^2) - \kappa^2(b^2+1)^2\right) u'' + \\ \qquad\qquad (b^2+1)^2 u = 4b(b^2+1) f(u) \\ \lim\limits_{x \to \pm\infty} (u, u', u'', u''', u^{(iv)}, u^{(v)}) = (0,0,0,0,0,0). \end{cases} \tag{4.51}$$

Step firing rate function

In the ODE in Equation (4.51) we set $f(u)$ to be the Heaviside type firing rate function from Equation (4.4). We define an above-threshold function, u_T, and a below-threshold function, u_L, such that $u_T(c) = u_L(c) = \theta$ as in Equation (4.7). We therefore obtain the two linear differential equations

$$\begin{aligned} -\kappa^2 u_L^{(vi)} + \left(1 + 2\kappa^2(b^2-1)\right) u_L^{(iv)} + \left(2(1-b^2) - \kappa^2(b^2+1)^2\right) u_L'' + \\ (b^2+1)^2 u_L = 0, \text{ for } c < x. \\ -\kappa^2 u_T^{(vi)} + \left(1 + 2\kappa^2(b^2-1)\right) u_T^{(iv)} + \left(2(1-b^2) - \kappa^2(b^2+1)^2\right) u_T'' + \\ (b^2+1)^2 u_T = 8b(b^2+1), \text{ for } 0 \le x < c. \end{aligned} \tag{4.52}$$

As for the Amari model with step $f(u)$ in Section 4.2, we have a nonhomogeneous ODE for an above-threshold region and a homogeneous ODE for a below-threshold region. To obtain a smooth and continuous function on $\mathbb{R}$, we have matching conditions on u and its derivatives at the threshold. We also have the boundary condition in Equation (4.51) to satisfy.

Solutions of the function u_T must satisfy the nonhomogeneous ODE in Equation (4.52) on the interval $0 \le x < c$. Therefore solutions of u_T are of the form

$$\begin{aligned} u_T(x) = & e^{bx}\left(C_1 \cos(x) + C_2 \sin(x)\right) + C_3 e^{x/\kappa} + \\ & e^{-bx}\left(C_4 \cos(x) + C_5 \sin(x)\right) + C_6 e^{-x/\kappa} + \frac{8b}{b^2+1} \end{aligned} \tag{4.53}$$

where C_1–$C_6 \in \mathbb{R}$. Again, solutions are symmetric in space so the odd derivatives at the origin are zero. There are six initial conditions that u_T must satisfy given that u_T is a solution of a sixth-order ODE. These initial conditions are:

$$\begin{aligned} u_T(0) &= u(0) \\ u_T'(0) &= 0 \\ u_T''(0) &= u''(0) \\ u_T'''(0) &= 0 \\ u_T^{(iv)}(0) &= u^{(iv)}(0) \\ u_T^{(v)}(0) &= 0. \end{aligned} \tag{4.54}$$

Let $u_0 = u(0)$, $u_2 = u''(0)$ and $u_4 = u^{(iv)}(0)$. We solve Equation (4.54) for C_1–C_6 in terms of u_0, u_2, u_4 and the coupling decay parameter $b > 0$. We obtain

$$\begin{aligned} C_1 &= \frac{a_1\kappa^4 + a_2\kappa^2 + u_0(b^2+1) - 8b}{2(b^2+1)a_5} \\ C_2 &= -\frac{a_3\kappa^4 + a_4\kappa^2 + u_0(b^4-1) - u_2(b^2+1) + 8b(1-b^2)}{4b(b^2+1)a_5} \\ C_3 &= \frac{\kappa^4\left(u_4 + 2u_2(1-b^2) + u_0(b^4+2b^2+1) - 8b(b^2+1)\right)}{2a_5} \\ C_4 &= C_1 \\ C_5 &= -C_2 \\ C_6 &= C_3 \end{aligned} \tag{4.55}$$

where

$$\begin{aligned} a_1 &= 2u_2(b^4-1) - u_4(b^2+1) \\ a_2 &= 2u_0(1-b^4) + 16b(b^2-1) \\ a_3 &= u_2(1-5b^2-5b^4+b^6) + u_4(1-b^4) \\ a_4 &= u_0(5b^4+5b^2-b^6-1) + u_4(b^2+1) + 8b(1-6b^2) \\ a_5 &= \kappa^4(b^2+1)^2 + 2\kappa^2(1-b^2) + 1. \end{aligned}$$

We can now write Equation (4.53) in the form

$$u_T(x) = C_1\cos(x)(e^{bx}+e^{-bx}) + C_2\sin(x)(e^{bx}-e^{-bx}) + C_3(e^{x/\kappa}+e^{-x/\kappa}) + \frac{8b}{b^2+1}. \tag{4.56}$$

Solutions of u_L must satisfy the homogeneous ODE in Equation (4.52) for $c < x$ and the boundary condition $\lim_{x\to\infty} u_L \to 0$. Solutions are of the form

$$u_L(x) = A_1e^{-bx}\cos(x) + A_2e^{-bx}\sin(x) + A_3e^{-x/\kappa} \tag{4.57}$$

where $A_1, A_2, A_3 \in \mathbb{R}$. For a continuous function $u(x)$, u_T and u_L and their derivatives meet at $x = c$, creating a set of seven matching conditions

$$\begin{aligned} u_T(c) &= u_L(c) \\ u_T(c) &= \theta \\ u_T'(c) &= u_L'(c) \\ u_T''(c) &= u_L''(c) \\ u_T'''(c) &= u_L'''(c) \\ u_T^{(iv)}(c) &= u_L^{(iv)}(c) \\ u_T^{(v)}(c) &= u_L^{(v)}(c). \end{aligned} \tag{4.58}$$

Evaluation of Equation (4.58) gives the nonlinear system of equations

$$\begin{aligned} &C_1 \cos(c)[e^{bc} + e^{-bc}] + C_2 \sin(c)[e^{bc} - e^{-bc}] + C_3[e^{c/\kappa} + e^{-c/\kappa}] + \frac{8b}{b^2+1} - \\ &A_1 e^{-bc} \cos(c) - A_2 e^{-bc} \sin(c) - A_3 e^{-c/\kappa} = 0. \end{aligned} \tag{4.59}$$

$$C_1 \cos(c)[e^{bc} + e^{-bc}] + C_2 \sin(c)[e^{bc} - e^{-bc}] + C_3[e^{c/\kappa} + e^{-c/\kappa}] + \frac{8b}{b^2+1} - \theta = 0. \tag{4.60}$$

$$\begin{aligned} &C_1 \left[b\cos(c)(e^{bc} - e^{-bc}) - \sin(c)(e^{bc} + e^{-bc}) \right] + \\ &C_2 \left[\cos(c)(e^{bc} - e^{-bc}) + b\sin(c)(e^{bc} + e^{-bc}) \right] + C_3 \frac{e^{c/\kappa} - e^{-c/\kappa}}{\kappa} + \\ &e^{-bc} \left[A_1(b\cos(c) + \sin(c)) + A_2(-\cos(c) + b\sin(c)) \right] + A_3 \frac{e^{-c/\kappa}}{\kappa} = 0. \end{aligned} \tag{4.61}$$

$$\begin{aligned} &C_1 \left[(b^2-1)\cos(c)(e^{bc} + e^{-bc}) - 2b\sin(c)(e^{bc} - e^{-bc}) \right] + \\ &C_2 \left[2b\cos(c)(e^{bc} + e^{-bc}) + (b^2-1)\sin(c)(e^{bc} - e^{-bc}) \right] + C_3 \frac{e^{c/\kappa} + e^{-c/\kappa}}{\kappa^2} + \\ &A_1 e^{-bc} \left[(1-b^2)\cos(c) - 2b\sin(c) \right] + A_2 e^{-bc} \left[2b\cos(c) + (1-b^2)\sin(c) \right] - \\ &A_3 \frac{e^{-c/\kappa}}{\kappa^2} = 0. \end{aligned} \tag{4.62}$$

$$C_1\left[(b^3-3b)\cos(c)(e^{bc}-e^{-bc})+(1-3b^2)\sin(c)(e^{bc}+e^{-bc})\right]+$$
$$C_2\left[(3b^2-1)\cos(c)(e^{bc}-e^{-bc})+(b^3-3b)\sin(c)(e^{bc}+e^{-bc})\right]+$$
$$C_3\frac{e^{c/\kappa}-e^{-c/\kappa}}{\kappa^3}+A_1e^{-bc}\left[(b^3-3b)\cos(c)+(3b^2-1)\sin(c)\right]+$$
$$A_2e^{-bc}\left[(1-3b^2)\cos(c)+(b^3-3b)\sin(c)\right]+A_3\frac{e^{-c/\kappa}}{\kappa^3}=0. \tag{4.63}$$

$$C_1\left[(b^4-6b^2+1)\cos(c)(e^{bc}+e^{-bc})+(4b-4b^3)\sin(c)(e^{bc}-e^{-bc})\right]+$$
$$C_2\left[(4b^3-4b)\cos(c)(e^{bc}+e^{-bc})+(b^4-6b^2+1)\sin(c)(e^{bc}-e^{-bc})\right]+$$
$$C_3\frac{e^{c/\kappa}+e^{-c/\kappa}}{\kappa^4}+A_1e^{-bc}\left[(6b^2-b^4-1)\cos(c)+(4b-4b^3)\sin(c)\right]+$$
$$A_2e^{-bc}\left[(4b^3-4b)\cos(c)+(6b^2-b^4-1)\sin(c)\right]-A_3\frac{e^{-c/\kappa}}{\kappa^4}=0. \tag{4.64}$$

$$C_1\left[(b^5-10b^3+5b)\cos(c)(e^{bc}-e^{-bc})+(10b^2-5b^4-1)\sin(c)(e^{bc}+e^{-bc})\right]+$$
$$C_2\left[(5b^4-10b^2+1)\cos(c)(e^{bc}-e^{-bc})+(b^5-10b^3+5b)\sin(c)(e^{bc}+e^{-bc})\right]+$$
$$C_3\frac{e^{c/\kappa}-e^{-c/\kappa}}{\kappa^5}+A_1e^{-bc}\left[(b^5-10b^3+5b)\cos(c)+(5b^4-10b^2+1)\sin(c)\right]+$$
$$A_2e^{-bc}\left[(10b^2-1-5b^4)\cos(c)+(b^5-10b^3+5b)\sin(c)\right]+A_3\frac{e^{-c/\kappa}}{\kappa^5}=0. \tag{4.65}$$

We set $\kappa^2 = 0.05$, $b = 0.25$, $\theta = 1.5$. We solve for $C_1, C_2, C_3, A_1, A_2, A_3$ and c by using Newton's method [60] on the nonlinear system of equations in Equations (4.59)–(4.65). We find the two sets of coefficients in Table 4.4. Each line gives the coefficients to construct solutions of Equation (4.52) which are steady states of the gap junction model with oscillatory coupling function and double shifted Heaviside $f(u)$.

Table 4.4: Coefficients for functions u_T, u_L in Equations (4.56) and (4.57) found using piecewise construction method. Parameter values are $\kappa^2 = 0.05$, $b = 0.25$ and $\theta = 1.5$.

$u(0)$	$u''(0)$	$u^{(iv)}(0)$	A_1	A_2	A_3	c
4.0669	-2.7792	2.7423	3.6058	1.9077	1.9380	1.4947
1.6429	-1.4945	2.7807	1.6260	0.4772	0.0173	0.4439

Using the coefficients in Table 4.4 we construct the solutions. With b as the continuation parameter, we find the solution curve for $\kappa^2 = 0.05$ using AUTO 2000. We also find solution curves for $\kappa^2 = 0.25$ and 0.50 to see how increasing κ^2 changes the solution

curves. We plot $u(0)$ as a function of b in a top plot and $u''(0)$ as a function of b in a bottom plot for each value of κ^2 in Figure 4.7. Single-bump solutions do not exist for small b. For all three values of κ^2, the upper and lower solution branches are two disconnected curves when they first appear as b increases from zero. The upper and lower branches do not meet as b increases. For all three values of κ^2, the upper branch is stable for all b. As with the Amari model with step $f(u)$ in Figure 4.3, there is a large region where stable single-bump solutions do not exist. As κ^2 increases from 0.05 to 0.50, the upper branch decreases in $u(0)$ and the right end curls around and becomes longer. When $\kappa^2 = 0.50$, the lower and upper branches have met for small b and there is a change of stability for two values of b on the lower solution branch. We saw a similar change of stability in the Amari model with step $f(u)$ (see Figure 4.3). As we are restricting solutions to single-bump solutions only and do not consider all possible N-bump solutions, we cannot see what kind of bifurcation occurs. As in Section 4.2, index theory tells us there must be a bifurcation given the change in stability. In the bottom plots, we see that $u''(0) > 0$ for $\kappa^2 = 0.25, 0.50$ at the right end of the upper branch. Therefore "dimple" bump solutions exist at these parameter values. Again, similar behaviour was seen in Chapter 3 for the smooth $f(u)$ at the break in the upper branch of solutions (see Figure 3.7).

Piecewise linear firing rate function

We now find steady states of the gap junction model using the piecewise linear firing rate function in Equation (4.22). Let $\theta_T = \theta + \beta/\alpha$. We define three functions, u_T, u_M and u_L, as in Equation (4.26). We have $c, d \in \mathbb{R}^+$ such that $u_T(c) = u_M(c) = \theta_T$ and $u_M(d) = u_L(d) = \theta$. The ODE in Equation (4.51) becomes the three linear differential equations

$$-\kappa^2 u_L^{(vi)} + \left(1 + 2\kappa^2(b^2-1)\right) u_L^{(iv)} + \left(2(1-b^2) - \kappa^2(b^2+1)^2\right) u_L'', + \\ (b^2+1)^2 u_L = 0, \qquad d < x \tag{4.66}$$

$$-\kappa^2 u_M^{(vi)} + \left(1 + 2\kappa^2(b^2-1)\right) u_M^{(iv)} + \left(2(1-b^2) - \kappa^2(b^2+1)^2\right) u_M'' + \\ (b^2+1)(b^2 - 4\alpha b + 1) u_M = -4\alpha\theta b(b^2+1), \qquad c < x < d \tag{4.67}$$

$$-\kappa^2 u_T^{(vi)} + \left(1 + 2\kappa^2(b^2-1)\right) u_T^{(iv)} + \left(2(1-b^2) - \kappa^2(b^2+1)^2\right) u_T'' + \\ (b^2+1)^2 u_T = 4\beta b(b^2+1), \qquad 0 \le x < c. \tag{4.68}$$

From $u_T(c) = u_M(c) = \theta_T$ and $u_M(d) = u_L(d) = \theta$, there are two sets of matching conditions.

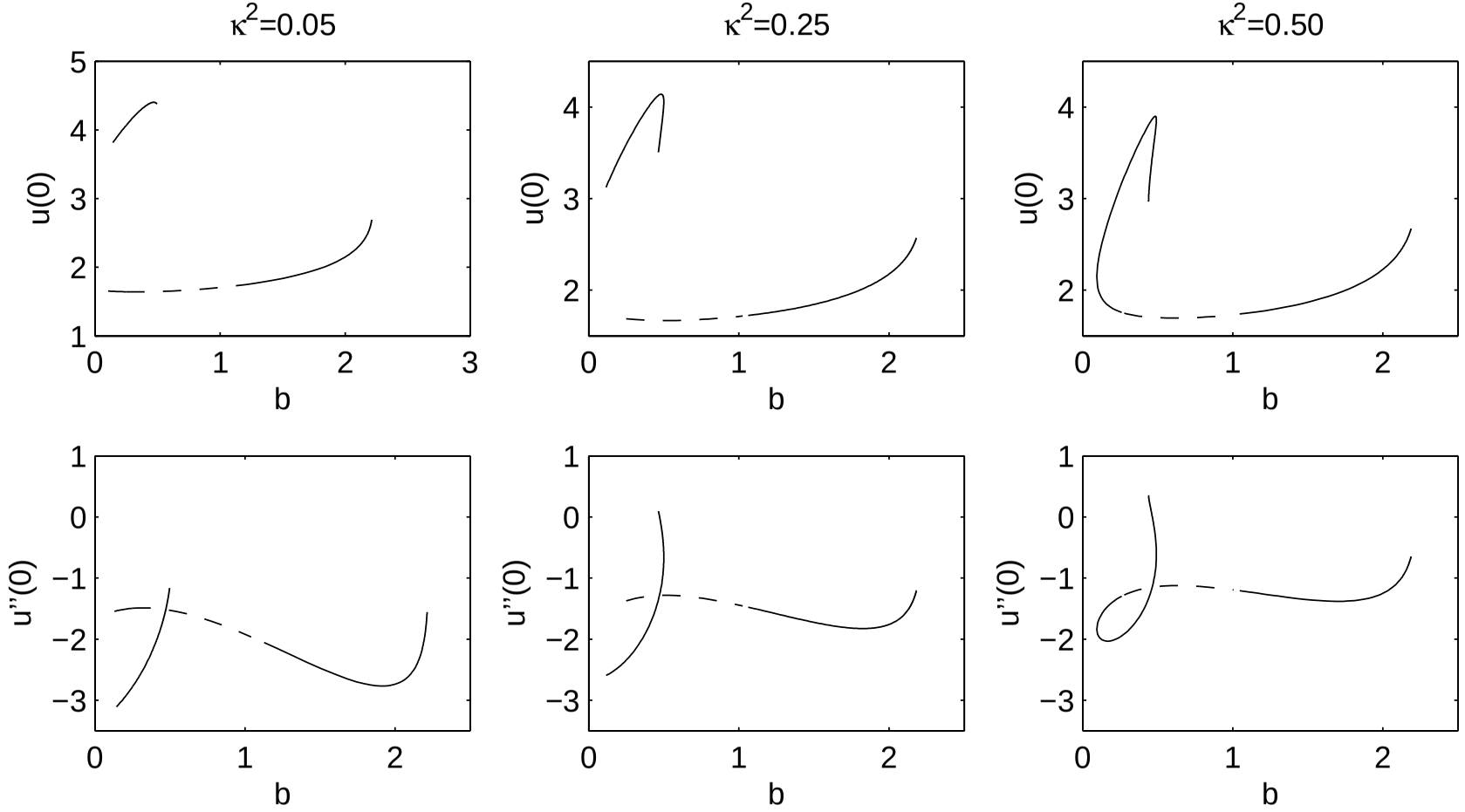

Figure 4.7: Solution curves for the gap junction model with decaying oscillatory coupling function and step firing rate function ($\theta = 1.5$), found using piecewise solution construction with Equation (4.52) and $\kappa^2 = 0.05, 0.25, 0.50$. Top: $u(0)$ as a function of b. Upper and lower solution branches are disconnected for large b for all three κ^2. There is a change of stability on the lower branch. Bottom: $u''(0)$ as a function of b. Solid line: stable solutions; dashed line: unstable solutions. Compare to Figure 4.3.

Solutions of u_T are the same as for the step $f(u)$, as u_T must satisfy Equation (4.68). Solutions must also satisfy the initial conditions in Equation (4.54). We solve Equation (4.53) for C_1–C_6 in terms of $u(0), u''(0), u^{(iv)}(0)$ and $b > 0$. So C_1–C_6 are as in Equation (4.55) and solutions of u_T are of the form

$$u_T(x) = C_1\cos(x)(e^{bx}+e^{-bx}) + C_2\sin(x)(e^{bx}-e^{-bx}) + C_3(e^{x/\kappa}+e^{-x/\kappa}) + \frac{8b}{b^2+1}. \quad (4.69)$$

We solve for u_M in Equation (4.67) on the interval $c < x < d$ where $u_M(c) = \theta_T$ and $u_M(d) = \theta$. Solutions have eigenvalues of two real pairs of same magnitude but opposite sign and one pure imaginary conjugate pair, say $\pm m_1 i, \pm m_2, \pm m_3$ where $0 < m_3 < m_2$ and $m_1, m_2, m_3 \in \mathbb{R}$. Hence u_M has the form

$$u_M(x) = D_1\cos(m_1x)+D_2\sin(m_1x)+D_3e^{m_2x}+D_4e^{-m_2x}+D_5e^{m_3x}+D_6e^{-m_3x}+\frac{4\alpha\theta b}{(4\alpha b-b^2-1)} \quad (4.70)$$

where D_1–$D_6 \in \mathbb{R}$.

Functions u_T and u_M must satisfy the seven matching conditions

$$\begin{aligned} u_T(c) &= u_M(c) \\ u_T(c) &= \theta_T \\ u_T'(c) &= u_M'(c) \\ u_T''(c) &= u_M''(c) \\ u_T'''(c) &= u_M'''(c) \\ u_T^{(iv)}(c) &= u_M^{(iv)}(c) \\ u_T^{(v)}(c) &= u_M^{(v)}(c). \end{aligned} \quad (4.71)$$

Evaluation of Equation (4.71) gives the system of equations

$$\begin{aligned} &C_1\cos(c)[e^{bc}+e^{-bc}] + C_2\sin(c)[e^{bc}-e^{-bc}] + \frac{4\beta b}{b^2+1} - D_1\cos(m_1c) - \\ &D_2\sin(m_1c) - D_3e^{m_2c} - D_4e^{-m_2c} - D_5e^{m_3c} - D_6e^{-m_3c} - \frac{4\alpha\theta b}{(4\alpha b-b^2-1)} = 0. \end{aligned} \quad (4.72)$$

$$C_1\cos(c)[e^{bc}+e^{-bc}] + C_2\sin(c)[e^{bc}-e^{-bc}] + \frac{4\beta b}{b^2+1} - \theta_T = 0. \quad (4.73)$$

$$C_1\left[b\cos(c)(e^{bc}-e^{-bc})-\sin(c)(e^{bc}+e^{-bc})\right]+$$
$$C_2\left[\cos(c)(e^{bc}-e^{-bc})+b\sin(c)(e^{bc}+e^{-bc})\right]+C_3\frac{(e^{c/\kappa}-e^{-c/\kappa})}{\kappa}+$$
$$m_1\left[D_1\sin(m_1c)-D_2\cos(m_1c)\right]-m_2\left[D_3e^{m_2c}-D_4e^{-m_2c}\right]-$$
$$m_3\left[D_5e^{m_3c}-D_6e^{m_3c}\right]=0. \tag{4.74}$$

$$C_1\left[(b^2-1)\cos(c)(e^{bc}+e^{-bc})-2b\sin(c)(e^{bc}-e^{-bc})\right]+$$
$$C_2\left[2b\cos(c)(e^{bc}+e^{-bc})+(b^2-1)\sin(c)(e^{bc}-e^{-bc})\right]+C_3\frac{(e^{c/\kappa}+e^{-c/\kappa})}{\kappa^2}+$$
$$m_1^2\left[D_1\cos(m_1c)+D_2\sin(m_1c)\right]-m_2^2\left[D_3e^{m_2c}+D_4e^{-m_2c}\right]-$$
$$m_3^2\left[D_5e^{m_3c}+D_6e^{m_3c}\right]=0. \tag{4.75}$$

$$C_1\left[(b^3-3b)\cos(c)(e^{bc}-e^{-bc})-(1-3b^2)\sin(c)(e^{bc}+e^{-bc})\right]+$$
$$C_2\left[(3b^2-1)\cos(c)(e^{bc}-e^{-bc})+(b^3-3b)\sin(c)(e^{bc}+e^{-bc})\right]+$$
$$C_3\frac{(e^{c/\kappa}-e^{-c/\kappa})}{\kappa^3}-m_1^3\left[D_1\sin(m_1c)-D_2\cos(m_1c)\right]-m_2^3\left[D_3e^{m_2c}-D_4e^{-m_2c}\right]-$$
$$m_3^3\left[D_5e^{m_3c}-D_6e^{m_3c}\right]=0. \tag{4.76}$$

$$C_1\left[(b^4-6b^2+1)\cos(c)(e^{bc}+e^{-bc})+(4b-4b^3)\sin(c)(e^{bc}-e^{-bc})\right]+$$
$$C_2\left[(4b^3-4b)\cos(c)(e^{bc}+e^{-bc})+(b^4-6b^2+1)\sin(c)(e^{bc}-e^{-bc})\right]+$$
$$C_3\frac{(e^{c/\kappa}+e^{-c/\kappa})}{\kappa^4}-m_1^4\left[D_1\cos(m_1c)+D_2\sin(m_1c)\right]-m_2^4\left[D_3e^{m_2c}+D_4e^{-m_2c}\right]-$$
$$m_3^4\left[D_5e^{m_3c}+D_6e^{m_3c}\right]=0. \tag{4.77}$$

$$C_1\left[(b^5-10b^3+5b)\cos(c)(e^{bc}-e^{-bc})-(10b^2-5b^4-1)\sin(c)(e^{bc}+e^{-bc})\right]+$$
$$C_2\left[(5b^4-10b^2+1)\cos(c)(e^{bc}-e^{-bc})+(b^5-10b^3+5b)\sin(c)(e^{bc}+e^{-bc})\right]+$$
$$C_3\frac{(e^{c/\kappa}-e^{-c/\kappa})}{\kappa^5}+m_1^5\left[D_1\sin(m_1c)-D_2\cos(m_1c)\right]-m_2^5\left[D_3e^{m_2c}-D_4e^{-m_2c}\right]-$$
$$m_3^5\left[D_5e^{m_3c}-D_6e^{m_3c}\right]=0. \tag{4.78}$$

Solutions of u_L must satisfy the homogeneous ODE in Equation (4.66) for $d \leq x$ and the boundary condition $\lim_{x\to\infty} u_L \to 0$. Thus, solutions are of the form

$$u_L(x) = A_1e^{-bx}\cos(x) + A_2e^{-bx}\sin(x) + A_3e^{-x/\kappa} \tag{4.79}$$

where $A_1, A_2, A_3 \in \mathbb{R}$. The functions u_M and u_L must meet at $x = d$ for a continuous

function $u(x)$, creating a second set of seven matching conditions

$$\begin{aligned} u_M(d) &= u_L(d) \\ u_M(d) &= \theta \\ u'_M(d) &= u'_L(d) \\ u''_M(d) &= u''_L(d) \\ u'''_M(d) &= u'''_L(d). \\ u^{(iv)}_M(d) &= u^{(iv)}_L(d) \\ u^{(v)}_M(d) &= u^{(v)}_L(d). \end{aligned} \tag{4.80}$$

Evaluating Equation (4.80) we get the system of equations

$$\begin{aligned} &D_1\cos(m_1 d) + D_2\sin(m_1 d) + D_3 e^{m_2 d} + D_4 e^{-m_2 d} + D_5 e^{m_3 d} + D_6 e^{-m_3 d} + \\ &\frac{4\alpha\theta b}{(4\alpha b - b^2 - 1)} - A_1 e^{-bd}\cos(d) - A_2 e^{-bd}\sin(d) - A_3 e^{-d/\kappa} - \theta = 0. \end{aligned} \tag{4.81}$$

$$\begin{aligned} &D_1\cos(m_1 d) + D_2\sin(m_1 d) + D_3 e^{m_2 d} + D_4 e^{-m_2 d} + D_5 e^{m_3 d} + D_6 e^{-m_3 d} + \\ &\frac{4\alpha\theta b}{(4\alpha b - b^2 - 1)} - \theta = 0. \end{aligned} \tag{4.82}$$

$$\begin{aligned} &-m_1\left[D_1\sin(m_1 d) - D_2\cos(m_1 d)\right] + m_2\left[D_3 e^{m_2 d} - D_4 e^{-m_2 d}\right] + \\ &m_3\left[D_5 e^{m_3 c} - D_6 e^{-m_3 c}\right] + e^{-bd}\left[A_1(b\sin(d) + \cos(d)) + A_2(b\sin(d) - \cos(d))\right] + \\ &A_3\frac{e^{-d/\kappa}}{\kappa} = 0. \end{aligned} \tag{4.83}$$

$$\begin{aligned} &-m_1^2\left[D_1\cos(m_1 d) + D_2\sin(m_1 d)\right] + m_2^2\left[D_3 e^{m_2 d} + D_4 e^{-m_2 d}\right] + \\ &m_3^2\left[D_5 e^{m_3 d} + D_6 e^{-m_3 d}\right] + A_1 e^{-bd}\left[(1-b^2)\cos(d) - 2b\sin(d)\right] + \\ &A_2 e^{-bd}\left[2b\cos(d) + (1-b^2)\sin(d)\right] - A_3\frac{e^{-d/\kappa}}{\kappa^2} = 0. \end{aligned} \tag{4.84}$$

$$\begin{aligned} &m_1^3\left[D_1\sin(m_1 d) - D_2\cos(m_1 d)\right] + m_2^3\left[D_3 e^{m_2 d} - D_4 e^{-m_2 d}\right] + \\ &m_3^3\left[D_5 e^{m_3 d} - D_6 e^{-m_3 d}\right] + A_1 e^{-bd}\left[(b^3 - 3b)\cos(d) + (3b^2 - 1)\sin(d)\right] + \\ &A_2 e^{-bd}\left[(1-3b^2)\cos(d) + (b^3 - 3b)\sin(d)\right] + A_3\frac{e^{-d/\kappa}}{\kappa^3} = 0. \end{aligned} \tag{4.85}$$

$$m_1^4\left[D_1\cos(m_1 d)+D_2\sin(m_1 d)\right]+m_2^4\left[D_3e^{m_2 d}+D_4e^{-m_2 d}\right]+$$
$$m_3^4\left[D_5e^{m_3 d}+D_6e^{-m_3 d}\right]+A_1e^{-bd}\left[(6b^2-b^4-1)\cos(d)+(4b-4b^3)\sin(d)\right]+$$
$$A_2e^{-bd}\left[(4b^3-4b)\cos(d)+(6b^2-b^4-1)\sin(d)\right]-A_3\frac{e^{-d/\kappa}}{\kappa^4}=0. \tag{4.86}$$

$$-m_1^5\left[D_1\sin(m_1 d)-D_2\cos(m_1 d)\right]+m_2^5\left[D_3e^{m_2 d}-D_4e^{-m_2 d}\right]+$$
$$m_3^5\left[D_5e^{m_3 d}-D_6e^{-m_3 d}\right]+A_1e^{-bd}\left[(b^5-10b^3+5b)\cos(d)+(5b^4-10b^2+1)\sin(d)\right]+$$
$$A_2e^{-bd}\left[(10b^2-5b^4-1)\cos(d)+(b^5-10b^3+5b)\sin(d)\right]+A_3\frac{e^{-d/\kappa}}{\kappa^5}=0. \tag{4.87}$$

We solve the two sets of matching conditions with $\kappa^2 = 0.05$ to see how single-bump steady states change from those of the Amari model with the piecewise linear firing rate function in Section 4.2. We use only the one value of κ^2, as we saw how increasing κ^2 qualitatively changes the solution curves in the analysis using a step $f(u)$ in Figure 4.7. Two different values of the steepness parameter, α, are used to see how steepness changes solutions. We set $\alpha = 2$, $\beta = 2$ and $\theta = 1.5$ in Equation (4.22). With $b = 0.25$, we solve for C_1–C_3, D_1–D_6, A_1, A_2, A_3, c and d using Newton's method [60] on the nonlinear equations in Equations (4.72)–(4.78) and Equations (4.81)–(4.87). We find the two steady state solutions in the first subtable within Table 4.5. The first entry is for a single-bump solution that appears to be numerically stable and the second entry for a smaller solution that appears to be numerically unstable. We now follow the same approach but with a steeper $f(u)$. Setting $\alpha = 3$, we find the solutions in the second subtable in Table 4.5. We use our own pseudo-arclength continuation code in MATLAB [74] with b as the continuation parameter and find the solution curves in Figure 4.8.

When $\alpha = 2$, the solution curve is a simple, closed curve with stability changing in saddle-node bifurcations. For $\alpha = 3$, $f(u)$ is steeper and the solution curve breaks and separates into two pieces. As single-bump solutions cannot exist for small b, the two solution branches are disconnected as $b \to 0$. Compare to Figure 4.6 where we see the solution branches are also disconnected for the Amari model when $\alpha = 3$ in the piecewise linear $f(u)$. We do not, however, see the saddle-node bifurcation at the right end of the lower solution branch in Figure 4.8 as continuation is not able to go any further along the branch to where a saddle-node bifurcation would be expected. There are no "dimple" bump solutions for $\kappa^2 = 0.05$ as the bottom plot shows that $u''(0) < 0$ for all b.

We therefore see similar behaviour in the gap junction model with piecewise linear $f(u)$

as we did for the Amari model in Section 4.2 in that the solution curves are two separate branches when $f(u)$ becomes sufficiently steep.

Table 4.5: Coefficients for functions u_T, u_M, u_L in Equations (4.69), (4.70) and (4.79) found using piecewise construction method. Parameter values are $\kappa^2 = 0.05$, $b = 0.25$ $\beta = 2$ and $\theta = 1.5$. $\alpha = 2$ for the first subtable and $\alpha = 3$ for the second subtable.

$u(0)$	$u''(0)$	$u^{(iv)}(0)$	D_1	D_2	D_3	D_4	D_5	D_6	A_1	A_2	A_3	c	d
3.5450	-2.7150	3.1984	0.902	0.250	0.000	-0.055	-0.652	0.139	3.34	1.38	0.48	0.91	1.34
2.6517	-2.2217	3.1986	0.731	0.018	0.000	-0.001	-0.662	-0.616	2.58	0.88	0.11	0.37	1.09

$u(0)$	$u''(0)$	$u^{(iv)}(0)$	D_1	D_2	D_3	D_4	D_5	D_6	A_1	A_2	A_3	c	d
3.8238	-2.7939	3.0400	0.757	0.467	0.000	-0.319	-0.292	1.237	3.53	1.61	0.88	1.16	1.42
2.2222	-1.9266	3.0500	0.547	0.005	0.000	0.000	-0.329	-0.319	2.18	0.70	0.05	0.24	0.91

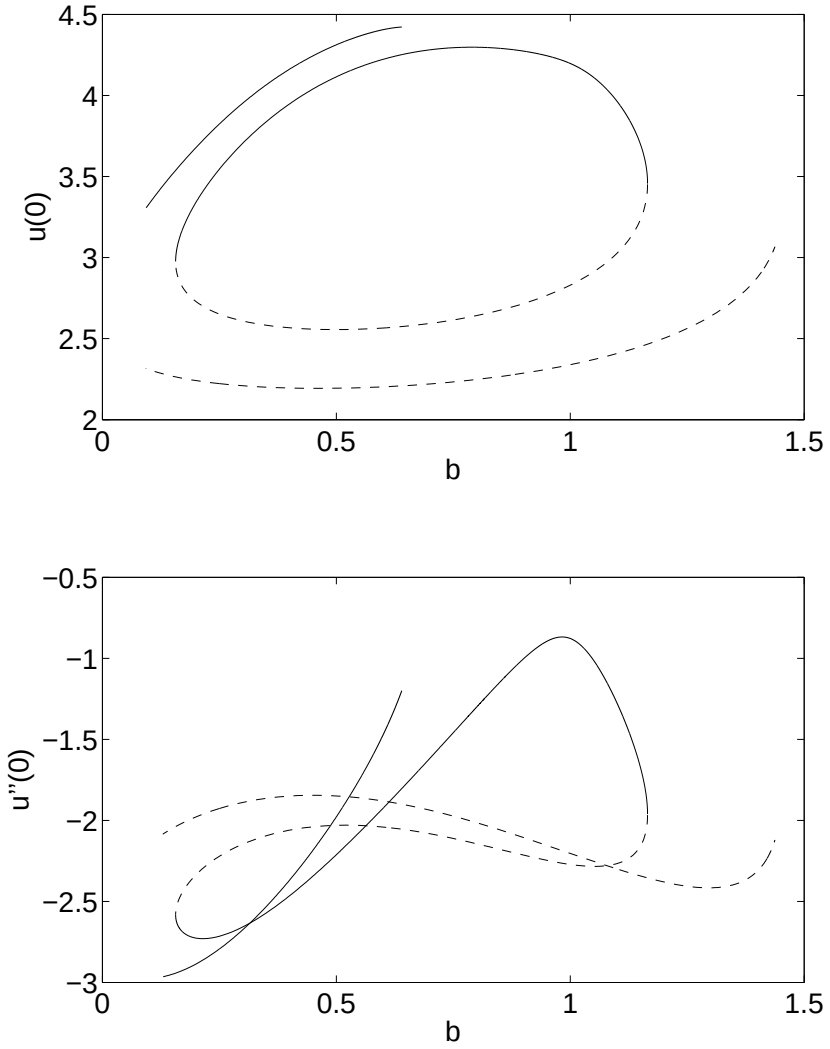

Figure 4.8: Solution curves of the gap junction model with oscillatory coupling function and piecewise linear firing rate function, found using piecewise construction method with Equations (4.66)–(4.68). Parameters are $\kappa^2 = 0.05$, $\beta = 2, \theta = 1.5$ and steepness parameter $\alpha = 2, 3$. Top: $u(0)$ as a function of b. The solution curve is a simple closed curve for $\alpha = 2$. There are two solution branches for $\alpha = 3$ with the upper curve breaking at $b = 0.678$ and the lower curve at $b = 1.4376$. Stability changes in saddle-node bifurcations. Bottom: $u''(0)$ as a function of b. Solid line: stable solutions; dashed line: unstable solutions. Compare to Figure 4.6.

4.4 Conclusion

We have used a piecewise differential framework to construct explicit piecewise symmetric single-bump steady state solutions of both the Amari model and the gap junction model. The decaying oscillatory coupling function from Chapter 3 was used. The method of solution construction entails solving a system of nonlinear algebraic equations using Newton's method.

In Chapter 3 there were breaks in the solution curves when the smooth firing rate function was sufficiently steep. To try and understand these breaks we used two different firing rate functions. The first was a step function. We found that there were breaks in the upper branch of solutions for both the Amari model and the gap junction model. The width of the break was wider than that seen in Chapter 3 with the smooth firing rate function. For the Amari model, solutions became "dimple" single-bumps at the break. Similar solutions were seen at the breaks in the solution curves in the gap junction model for larger values of κ^2. "Dimple" bump solutions were also seen where the solution curves break for a sufficiently steep smooth firing rate function in Chapter 3. For both the Amari model and the gap junction model, a change of stability is seen in the lower branch of solutions. However, this change in stability does not occur in a saddle-node bifurcation as was expected. Given that we restrict solutions to be single-bump solutions only and do not consider all possible N-bump solutions, we are unable to determine the bifurcation causing the change in stability.

The second firing rate function we used was a piecewise linear function with a steepness parameter. In Chapter 3, we used a smooth firing rate function and had to employ numerical methods to find steady state solutions of both the Amari model and the gap junction model. With the piecewise linear firing rate function, we were able to approximate the smooth firing rate function but construct solutions explicitly, rather than numerically. Again, both the Amari model and gap junction model showed breaks in the upper branch of solutions when the firing rate function was sufficiently steep. It was found that the width of the break increased as the steepness of the firing rate function increased. For both the Amari model and the gap junction model, stability changed in saddle-node bifurcations.

Chapter 5

A Hamiltonian approach

5.1 Introduction

Our goal in this chapter is to use the Hamiltonian structure and reversibility properties of our system to study the homoclinic solutions we have found in earlier chapters. We use phase space techniques to search areas of parameter space where the solution curves become discontinuous as the steepness of the firing rate function is varied. These techniques can find asymmetric homoclinic orbits as well as symmetric orbits.

In Chapter 3 we found solution curves for the Amari model in [70] of

$$\frac{\partial u(x,t)}{\partial t} = -u(x,t) + \int_{-\infty}^{\infty} w(x-y) f(u(y,t))\, dy \tag{5.1}$$

with decaying oscillatory coupling function

$$w(x) = e^{-b|x|}(b\sin(|x|) + \cos(x)) \tag{5.2}$$

and smooth firing rate function

$$f(u) = 2e^{-r/(u-\theta)^2}\Theta(u-\theta), \tag{5.3}$$

with parameters $b, r, \theta \in \mathbb{R}^+$. Solution curves were found by following homoclinic orbits to $(u,\, u',\, u'',\, u''') = (0,0,0,0)$ of the fourth-order ordinary differential equation

$$\begin{cases} u^{(iv)} + 2(1-b^2)u'' + (b^2+1)^2 u = 4b(b^2+1)f(u), \\ \lim\limits_{x\to\pm\infty} (u,\, u',\, u'',\, u''') = (0,0,0,0) \end{cases} \tag{5.4}$$

as the parameter b was varied. The homoclinic orbits are N-bump steady states of Equation (5.1). Equation (5.4) is Hamiltonian and is also reversible in space as it contains only even order derivatives.

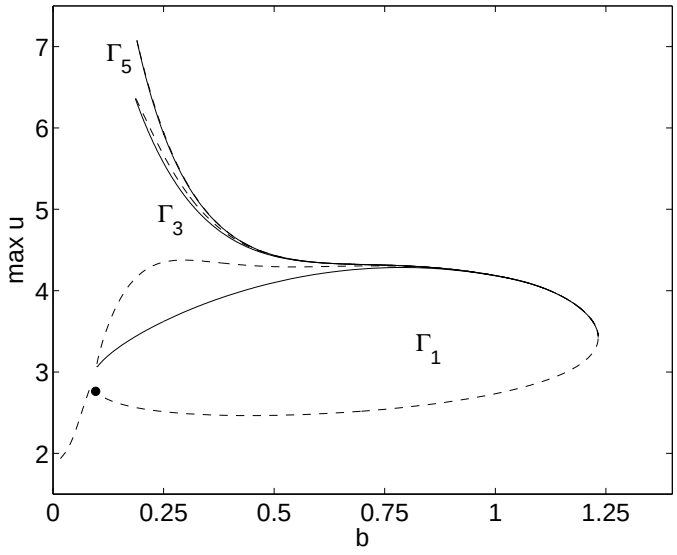

Figure 5.1: Solution curves for Equations (5.1)–(5.3) where $r = 0.095$. b is the continuation parameter and $\theta = 1.5$. See text for explanation of labels.

The system was found to be multi-stable as N-bump solutions, in general, came in pairs of one stable solution and one unstable solution. In Chapter 3 we presented the bifurcation diagrams for Equation (5.4) seen here in Figures 5.1–5.2. For Figures 5.1–5.2, the symbols Γ_1, Γ_3 and Γ_5 indicate 1-, 3- and 5-bump solutions respectively. Solid lines show branches of stable solutions and dashed lines show branches of unstable solutions. By varying the steepness of the firing rate function from $r = 0.095$ (see Figure 5.1) to $r = 0.085$ (see Figure 5.2), we found qualitative changes in the solution curves. The effect of increasing the steepness of the firing rate function (decreasing r) was that discontinuities appeared. The sudden break in the solution curve in Figure 5.2 is unexpected and unexplained. We are not aware of any similar bifurcation phenomenon in the literature. In view of the modelling dogma where qualitative results should not depend upon the fine details of the model, the sudden break in the solution curve is disturbing. In this chapter, we seek an explanation for these results. Previously in the thesis we have only found even (spatially symmetric) homoclinic orbits. We want to find spatially asymmetric homoclinic orbits, if possible.

The outline of this chapter is as follows. In the next section we discuss reversible structure and Hamiltonian structure. We write Equation (5.4) as a reversible, Hamiltonian system. In Section 5.3 we find both symmetric and asymmetric single-bump homoclinic orbits to the fixed point at the origin using a numerical technique which reduces the problem of finding single-bump symmetric and asymmetric homoclinic orbits to finding the zeros of a real scalar function. In Section 5.4 other nonzero fixed points of the system

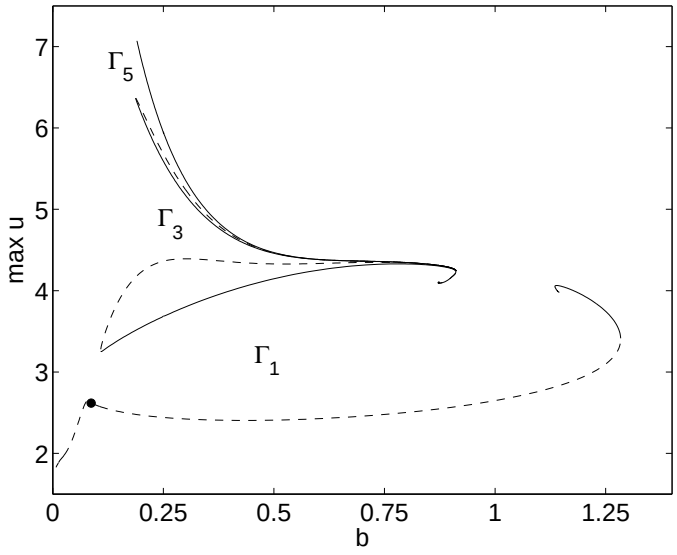

Figure 5.2: Solution curves for Equations (5.1)–(5.3) where $r = 0.085$. b is the continuation parameter and $\theta = 1.5$.

are analysed using level sets of the Hamiltonian with the three different firing rate functions of Chapters 3 and 4. The three functions are a step function, a piecewise linear function and a smooth function. In Section 5.5 we use a travelling front approach with the time-dependent system. To find heteroclinic orbits, we write the time-dependent system with step firing rate function in moving coordinates in integral form and look for stationary patterns. In Chapter 3, discontinuities were seen in the solution curves with a sufficiently steep smooth firing rate function. We conjecture there are travelling fronts in the regions of discontinuity. We therefore use the smooth firing rate function in the time-dependent system and discuss possible future work in finding travelling fronts.

5.2 Hamiltonian structure of the system

We will show that the ODE in Equation (5.4) can be formulated as a reversible, four-dimensional, Hamiltonian dynamical system. We refer the reader to the work of Champneys [12] for a review of the theory and application of homoclinic orbits to equilibria in reversible dynamical systems. Champneys concentrates on even-order reversible systems in four or more dimensions where the homoclinic orbit and the equilibrium are both reversible.

Reversible structure

Consider an even-dimensional system

$$\dot{x} = f(x), \quad x \in \mathbb{R}^{2n}. \tag{5.5}$$

All derivatives are with respect to time, that is, $\dot{x} = dx/\,dt$. We will study systems with linear reversing symmetries.

Definition 5.2.1 *A* linear involution *of* $\mathbb{R}^{2n}$ *is a linear map* $R : \mathbb{R}^{2n} \to \mathbb{R}^{2n}$ *whose square is the identity, ie.* $R^2 = \mathrm{Id}$.

Definition 5.2.2 *A system* $\dot{x} = f(x)$ *is invariant under time reversal if*

$$Rf(x) = -f(Rx).$$

Definition 5.2.3 *Let* $\mathrm{fix}(R)$ *be the set of all points in* $\mathbb{R}^{2n}$ *that are fixed under the reversibility* R. *A symmetric section* $\mathcal{S}$ *is a linear subspace of* $\mathbb{R}^{2n}$ *such that*

$$\mathcal{S} = \mathrm{fix}(R).$$

Consider an involution R that fixes half the variables in the system and under which the system is invariant after time reversal. Then the system has a set $\mathcal{S} = \mathrm{fix}(R)$ where $\mathcal{S}$ is the symmetric section of the reversibility R.

Hamiltonian structure

Consider the system $\dot{\mathbf{x}} = f(\mathbf{x})$ where $\mathbf{x} = (\mathbf{q}(t), \mathbf{p}(t)) \in \mathbb{R}^{2n}$. Then the system is a Hamiltonian system if it can be written in the form

$$\frac{dq_i}{dt} = \frac{\partial H}{\partial p_i}, \quad \frac{dp_i}{dt} = -\frac{\partial H}{\partial q_i}$$

for a *Hamiltonian function* where $i = 1, \ldots, n$. This is often simply called the *Hamiltonian*, $H(\mathbf{p}, \mathbf{q}, t)$, and comes from a generalised form of Newton's laws of motion where $\mathbf{p} \in \mathbb{R}^n$ is the generalised momentum and $\mathbf{q} \in \mathbb{R}^n$ is the generalised coordinate of a mechanical system of degree of freedom n. Very frequently the Hamiltonian is of the form

$$H = \sum_{i=1}^{n} p_i^2 + V(\mathbf{q})$$

where $\mathbf{p} = (p_1, p_2, \ldots, p_n)$ and $V \colon \mathbb{R}^n \to \mathbb{R}$. Such a Hamiltonian is called "separable" if it is additively separable in each coordinate. If the Hamiltonian system is also reversible

with the reversibility $R : (q, p) \to (q, -p)$, then this form of the Hamiltonian is separable under R. The reversibility R usually reverses all the momentum variables. A Hamiltonian system preserves volume in $2n$-dimensional phase space.

Definition 5.2.4 *A symmetric fixed point is a fixed point of a reversible system that is invariant under the linear involution, R, used to define reversibility.*

Consider a $2n$-dimensional reversible system with a symmetric fixed point that lies in $\mathcal{S}$. Take the case where the unstable manifold, W^u, of the fixed point has dimension n. This occurs when symmetric homoclinic orbits are of codimension-zero and asymmetric homoclinic orbits are of codimension-one.

Definition 5.2.5 *An orbit is said to be symmetric if it is invariant under the reversibility R. Therefore a symmetric orbit is mapped into itself under the reversibility R.*

Definition 5.2.6 *An orbit is said to be asymmetric if it is not invariant under the reversibility R. Asymmetric orbits are mapped into the time reversal of themselves under the reversibility R.*

Thus asymmetric homoclinic orbits come in pairs where each orbit is the time reversal of the other under R. See Figure 5.3 for a schematic of homoclinic orbits in phase space. The left plot shows a homoclinic orbit that is symmetric under time reversal. That is, the orbit is symmetric under reflection in the x-axis. The right plot shows a pair of asymmetric homoclinic orbits. Let Υ_1, Υ_2 be the two asymmetric orbits. The orbits are not symmetrical under time reversal. Each orbit is the time reversal of the other, so $R(\Upsilon_1) = \Upsilon_2$ and $R(\Upsilon_2) = \Upsilon_1$.

Our system

We now show that our system in Equation (5.4) has both reversible structure and Hamiltonian structure, although the Hamiltonian is not separable and the involution R is not the standard one. The independent variable in our system is space, not time, so all derivatives are with respect to space. That is, $u' = du/dx$. First, we write Equation (5.4) in the form

$$u^{(iv)} + au'' + cu + g(u) = 0 \tag{5.6}$$

where $a = 2(1 - b^2), c = (b^2 + 1)^2$ and $g(u) = -4b(b^2 + 1)f(u)$. The threshold is set at $\theta = 1.5$ in this section. Following the approach of [34], we choose position variables u and

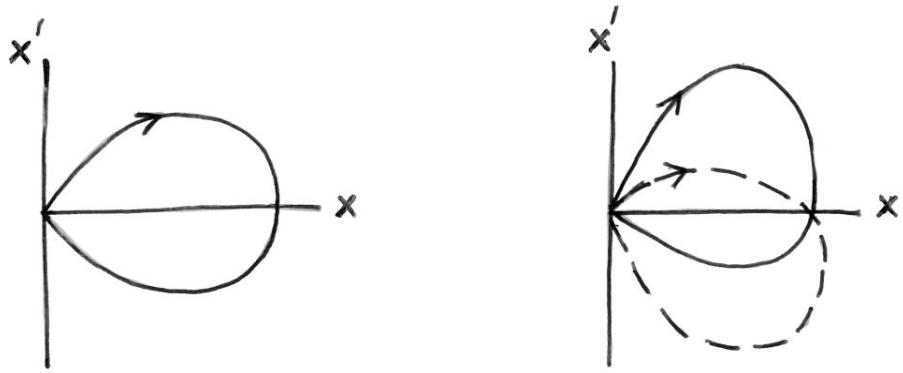

Figure 5.3: Schematics of homoclinic orbits in (x, x') phase space where $x' = dx/\,dt$. Left: The homoclinic orbit is symmetric under reflection in the x-axis and is invariant under time reversal. Right: A pair of asymmetric homoclinic orbits. Each orbit is the time reversal of the other.

v and conjugate momenta p_u and p_v so that

$$\begin{aligned} u' &= v \\ v' &= p_v \\ p_u' &= cu + g(u) \\ p_v' &= -p_u - av. \end{aligned} \tag{5.7}$$

The Hamiltonian is defined as

$$H(u, v, p_u, p_v) = p_u v + \frac{p_v^2}{2} + \frac{av^2}{2} - \frac{cu^2}{2} - G(u) \tag{5.8}$$

where

$$G(u) = -\frac{8b}{(b^2+1)} \int_0^u e^{-r/(s-\theta)^2} \Theta(s-\theta)\, ds. \tag{5.9}$$

Note that $G'(u) = g(u)$. The system given by Equations (5.6)–(5.7) has the reversibility

$$R : (x, u, v, p_u, p_v) \mapsto (-x, u, -v, -p_u, p_v). \tag{5.10}$$

Classical Hamiltonian dynamical systems are invariant under time reversal and the reversal of all momentum variables. R is a non-standard reversibility as it does not reverse both the momentum variables. H is a conserved quantity

$$H' = \frac{\partial H}{\partial u} u' + \frac{\partial H}{\partial p_u} p_u' + \frac{\partial H}{\partial v} v' + \frac{\partial H}{\partial p_v} p_v' = 0 \tag{5.11}$$

and is non-separable. Also,

$$\begin{aligned} u' &= \frac{\partial H}{\partial p_u}, \\ v' &= \frac{\partial H}{\partial p_v}, \\ p_u' &= -\frac{\partial H}{\partial u}, \\ p_v' &= -\frac{\partial H}{\partial v}. \end{aligned} \tag{5.12}$$

There is another way to determine the Hamiltonian, or energy function [70, 98], where the ODE in Equation (5.6) is multiplied by u' and integrated to obtain

$$u'u''' - \frac{1}{2}(u'')^2 + \frac{a}{2}(u')^2 + \frac{c}{2}u^2 + G(u) = 0. \tag{5.13}$$

$G(u)$ is as in Equation (5.9). A small amount of algebra confirms the lefthand side of Equation (5.13) is the same as the Hamiltonian function in Equation (5.8).

We define level sets of the energy in Equation (5.8) by setting

$$H(u) = e, \qquad e \in \mathbb{R}. \tag{5.14}$$

Energy is conserved on the level sets $H(u) = e$ and hence for any homoclinic orbits that lie upon them. The system in Equations (5.7)–(5.8) is a canonical Hamiltonian system. The system can therefore be written in the standard form

$$\mathbf{y}' = \mathbf{J}\nabla H(\mathbf{y}) \tag{5.15}$$

where $\mathbf{y} = [u, v, p_u, p_v]^T$ and $\mathbf{J}$ is the skew–symmetric matrix in $\mathbb{R}^4$ of

$$\mathbf{J} = \begin{pmatrix} \mathbf{0} & \mathbf{Id} \\ -\mathbf{Id} & \mathbf{0} \end{pmatrix}. \tag{5.16}$$

In matrix $\mathbf{J}$, $\mathbf{Id}$ is the 2×2 identity matrix and $\mathbf{0}$ is the 2×2 zero matrix.

Let W^s be the stable manifold and W^u the unstable manifold of a fixed point of the system. Then homoclinic orbits lie in $W^s \cap W^u$. In a reversible, non-Hamiltonian system, symmetric homoclinic orbits are codimension-zero, therefore they persist under a generic perturbation that preserves reversibility. However, asymmetric homoclinic orbits are codimension-one and are destroyed by a generic perturbation that breaks the conserved quantity but still preserves reversibility. In a non-reversible Hamiltonian system, both symmetric and asymmetric homoclinic orbits are codimension-zero. This also holds for a Hamiltonian-reversible system.

When a fixed point of a reversible system is a saddle-focus, there are infinitely many N-pulses for each $N > 1$ as well as the primary transverse symmetric homoclinic orbit [12]. In Chapter 3 we found that Equation (5.4) has a saddle-focus fixed point at the origin with eigenvalues of $\pm(b \pm i)$. Numerical results presented in Chapter 3 showed multiple bump solutions (homoclinic orbits to the fixed point at the origin) as seen in the solution curve (see Figure 5.1). This is the manifestation of the multiple N-pulse solutions in [12].

The stable and unstable manifolds of a fixed point intersect transversally within a level set of the conserved integral for a conservative system. Homoclinic orbits lie on energy surfaces, therefore the topology of the level sets $\{u : H(u) = e\}$ can change only where the level set contains a critical point. That is, where $\nabla H(u) = 0$. These critical points are the fixed points of the system. For a conservative and reversible system, there are two codimension-one ways to lose transversality of the manifolds W^u and W^s within a level set without a local bifurcation, given a symmetric homoclinic orbit. This can happen either through coalescence or bifurcation. In Chapter 3, breaks were found in the solution curves when the firing rate function was sufficiently steep (see Figure 5.2). Homoclinic orbits disappeared as the parameter r was varied. We have only considered homoclinic orbits to the fixed point at the origin. However, there are other nonzero fixed points of our system for certain parameter ranges for a step firing rate function, a piecewise linear firing rate function and smooth firing rate function. To find a possible bifurcation causing the disappearance of solutions, we study the other fixed points of Equation (5.4) in later sections of this chapter.

5.3 Finding homoclinic orbits

We now describe a numerical technique that reduces the problem of finding single-bump symmetric and asymmetric homoclinic orbits to finding the zeros of a real scalar function.

Constructing a mapping

We search for homoclinic orbits to the origin of the reversible Hamiltonian system of Equations (5.7)–(5.8) by defining a two-dimensional mapping. The mapping allows a reduction of dimensions of the Hamiltonian system and permits greater clarity of the global dynamics. We find homoclinic orbits to $(u, v, p_u, p_v) \to (0, 0, 0, 0)$ as $x \to \pm\infty$ on the zero energy surface, the level set $H = 0$. The saddle-focus fixed point at the origin has eigenvalues $\pm b \pm i$, therefore it is a bi-focus [67]. The stable manifold W^s and unstable

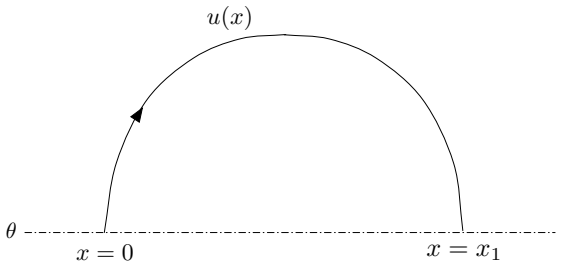

Figure 5.4: Schematic of numerically integrating an initial condition $\{u = \theta,\, v > 0\}$ from $x = 0$ until $u = \theta$ and $v < 0$ which is at $x = x_1$.

manifold W^u are both two dimensional.

We find homoclinic orbits by studying the trajectory for the above-threshold region, $u > \theta$, only rather than beginning the trajectory at $(u, v, p_u, p_v) = (0, 0, 0, 0)$. We can do this as the flow for $u < \theta$ is linear, therefore we know what W^s and W^u are for $u < \theta$. See Figure 5.4 for a schematic of numerically integrating an initial condition. As we are looking for homoclinic orbits on the zero energy surface, $H = 0$, we have already reduced the dimension of the system from four to three. We choose two sections that reduce the dimensions further to two dimensions. Let Σ_0 be the 2-dimensional section

$$\Sigma_0 = \{(u, v, p_u, p_v) | u = \theta, v > 0, H = 0\}. \tag{5.17}$$

The coordinates (v, p_v) define a unique point on the half-plane Σ_0 as p_u is defined uniquely in terms of (u, v, p_v) when $H = 0$ (see Equation (5.8)). Let Σ_1 be the 2-dimensional section

$$\Sigma_1 = \{(u, v, p_u, p_v) | u = \theta, v < 0, H = 0\}. \tag{5.18}$$

The sections Σ_0, Σ_1 are two halves of a single plane. Solutions on W^u for $u < \theta$ are of the form

$$u(x) = e^{bx}\big(A\sin(x) + B\cos(x)\big), \qquad A, B \in \mathbb{R}. \tag{5.19}$$

Given that steady state solutions of Equation (5.4) are translationally invariant, calculations can be simplified by setting $u(0) = \theta$. Therefore

$$u(x) = e^{bx}\big(A\sin(x) + \theta\cos(x)\big) \tag{5.20}$$

where $A > -b\theta$, given that $v > 0$ on Σ_0. We define the mapping

$$\mathcal{P}\colon \Sigma_0 \mapsto \Sigma_1 \qquad \forall \mathbf{y_0} \in \Sigma_0 \tag{5.21}$$

as the flow of the system from a particular initial condition $\mathbf{y_0} \in \Sigma_0$ to an endpoint $\mathbf{y_1} \in \Sigma_1$. Given that the fixed point at the origin has eigenvalues $\pm b \pm i$, the mapping

$\mathcal{P}(\mathbf{y}_0(A))$ (where $A > -b\theta$) will always meet the section Σ_1 for some $x > 0$. Therefore the mapping $\mathcal{P}$ is defined for all $\mathbf{y_0} \in \Sigma_0$. The flow from Σ_0 to Σ_1 is always transverse to the sections Σ_0, Σ_1 and is found by numerically integrating $\mathbf{y_0}$ using the ODE solver ODE45 in MATLAB [74]. We take initial conditions $\mathbf{y_0} \in \Sigma_0$ that lie on the 1-dimensional manifold $W^u \cap \Sigma_0$. We do this by taking an initial condition in (u, u', u'', u''') coordinates of

$$\begin{pmatrix} u(0) \\ u'(0) \\ u''(0) \\ u'''(0) \end{pmatrix} = \begin{pmatrix} \theta \\ A + b\theta \\ -\theta + 2Ab + b^2\theta \\ -A - 3b\theta + 3b^2A + b^3\theta \end{pmatrix} \tag{5.22}$$

which we write in Hamiltonian coordinates

$$\mathbf{y_0} = \begin{pmatrix} 1 & 0 & 0 & 0 \\ 0 & 1 & 0 & 0 \\ 0 & -a & 0 & -1 \\ 0 & 0 & 1 & 0 \end{pmatrix} \begin{pmatrix} u(0) \\ u'(0) \\ u''(0) \\ u'''(0) \end{pmatrix} = \begin{pmatrix} u(0) \\ v(0) \\ p_u(0) \\ p_v(0) \end{pmatrix}. \tag{5.23}$$

The stable manifold of the fixed point at the origin is $W^s = R(W^u)$ given the reversibility property of $x \to -x$. We take p_v and v as coordinates on the 2-dimensional section Σ_0. See Figure 5.5 for a schematic of a homoclinic orbit to a fixed point. W^u and W^s are the unstable and stable manifolds respectively of the fixed point. The orbit intersects the section Σ_0 transversally at the point $\mathbf{y_0}$ and the section Σ_1 transversally at the point $\mathbf{y_1}$.

Given that initial conditions lie on W^u, we now want to calculate $\mathcal{P}(W^u)$. Points in $\mathcal{P}(W^u) \cap W^s$ lie on homoclinic orbits. We find W^u from Equation (5.22) in terms of p_v as a function of v so

$$W^u \cap \Sigma_0 = \{(u, v, p_u, p_v) \mid u = \theta, v > 0, H = 0, p_v = 2bv - \theta(b^2 + 1)\}. \tag{5.24}$$

Since $W^s = R(W^u)$, we have

$$W^s \cap \Sigma_1 = \{(u, v, p_u, p_v) \mid u = \theta, v < 0, H = 0, p_v = -2bv - \theta(b^2 + 1)\}. \tag{5.25}$$

Take an initial condition $\mathbf{y_0} \in \Sigma_0$ so that $\mathbf{y_0}$ lies on W^u. We define $\mathbf{y_1} = \mathcal{P}(y_0)$. If $\mathbf{y_1}$ lies on W^s then $\mathbf{y_0}$ lies on a homoclinic orbit. Let v_0 be the v coordinate of $\mathbf{y_0}$ and v_1 be the v coordinate of $\mathbf{y_1}$. If $v_0 + v_1 = 0$ then $\mathbf{y_0}$ lies on a symmetric homoclinic orbit, otherwise $\mathbf{y_0}$ lies on an asymmetric homoclinic orbit. See Figure 5.6 for an example of W^u, W^s and the mapping of initial conditions for both symmetric and asymmetric homoclinic orbits.

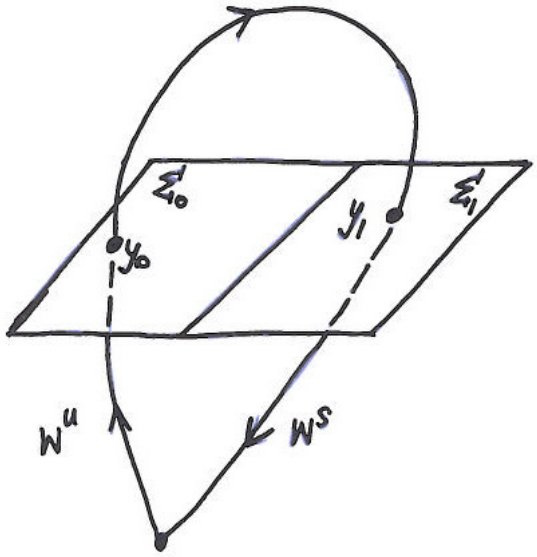

Figure 5.5: Schematic of a homoclinic orbit. The orbit intersects the section Σ_0 transversally at the point y_0 and the section Σ_1 transversally at the point y_1. The unstable and stable manifolds of the fixed point are W^u and W^s respectively.

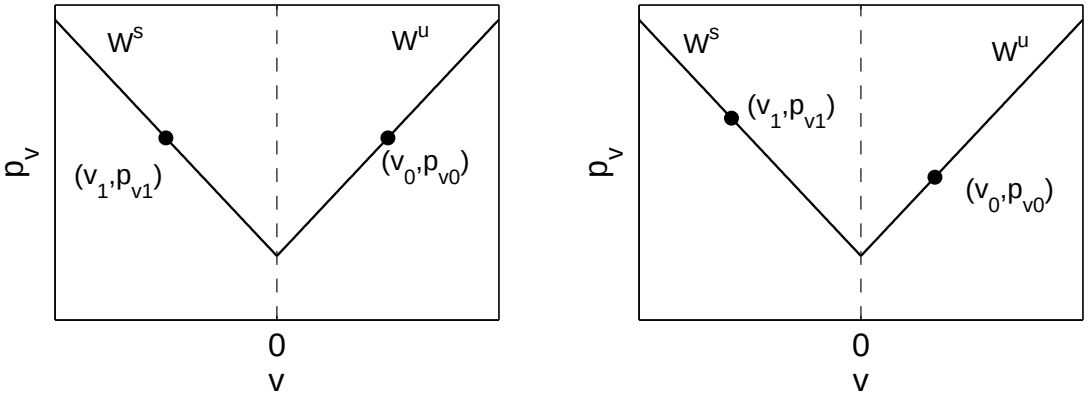

Figure 5.6: Examples of initial conditions that lie on homoclinic orbits. The stable and unstable manifolds are W^s and W^u respectively. The initial condition $(v_0, p_{v0}) \in W^u$ maps to $(v_1, p_{v1}) \in W^s$. Left: (v_0, p_{v0}) lies on a symmetric homoclinic orbit as $v_1 = -v_0$. Right: (v_0, p_{v0}) lies on an asymmetric homoclinic orbit as $v_1 \neq -v_0$.

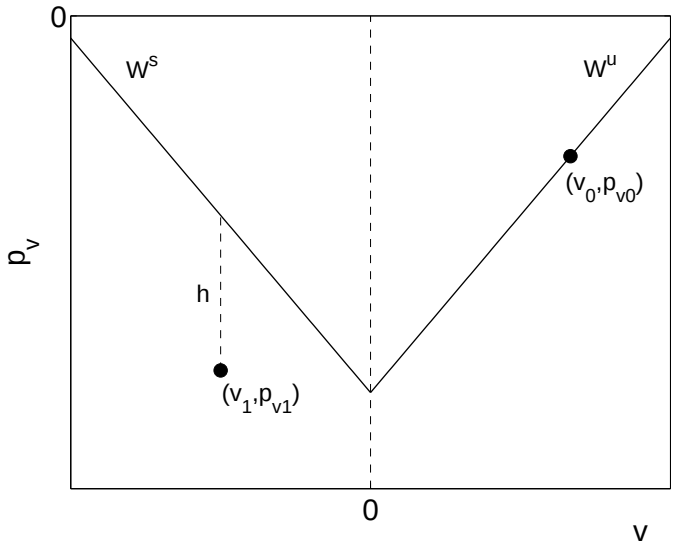

Figure 5.7: The point (v_1, p_{v1}) is the mapping of the initial condition (v_0, p_{v0}). Variable h measures the vertical distance from (v_1, p_{v1}) to W^s.

To see if $\mathbf{y_1}$ lies on W^s, we calculate the vertical distance, h, from $\mathcal{P}(\mathbf{y_0})$ to W^s:

$$\begin{aligned} h &= p_{v1} - p_{v0} \\ &= p_{v1} - (-2bv_1 - \theta(b^2+1)) \\ &= p_{v1} + 2bv_1 + \theta(b^2+1). \end{aligned} \tag{5.26}$$

If $h = 0$ then the initial condition $\mathbf{y_0}(A)$ is on W^s and therefore lies on a homoclinic orbit (see Figure 5.7). The distance h depends upon the initial condition in Equation (5.23), hence h is a function of A. To find values of A for which homoclinic orbits exist, we plot $h(A)$ as a function of A and look for values of A such that $h(A) = 0$.

As the mapping $\mathcal{P}$ of a point $\mathbf{y_0} \in \Sigma_0$ to Σ_1 defines the first time the flow of the system meets Σ_1, this method will only find single-bump solutions. These can be "dimple"-bumps as the "dimple" is above threshold, however, it will not find N-bump solutions for $N > 1$. The method can be easily modified to find N-bump solutions. For example, to find 2-bump solutions, we would change the mapping $\mathcal{P}$ to terminate on the second intersection of Σ_1. We restrict our work in this chapter to 1-bump solutions only.

Results

Set $(b, r) = (0.25, 0.095)$. We plot W^s, W^u, the mapping of initial conditions and the vertical distance, $h(A)$, of the initial conditions to the stable manifold W^s in Figure 5.8. The function $h(A)$ is continuous for this region of parameter space. Circles indicate the

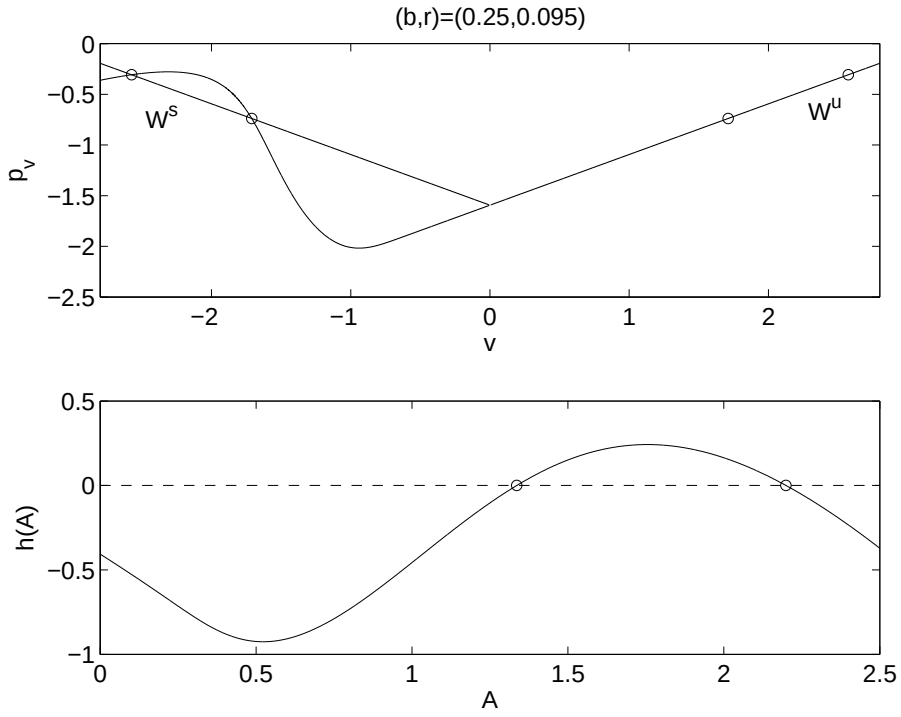

Figure 5.8: Parameter values $(b, r) = (0.25, 0.095)$. Top: Mapping of initial conditions on W^u. A symmetric homoclinic orbit exists for each initial condition on W^u that maps to W^s (circles). Bottom: Vertical distance $h(A)$ from mapped points to W^s. Homoclinic orbits exist for A such that $h(A) = 0$.

two initial conditions on W^u which map to W^s. These two initial conditions lie on two symmetric homoclinic orbits. We easily see the values of A for which this occurs by looking at the bottom plot of $h(A)$. These results agree with the solution curve in Figure 5.1 where there are two single-bump symmetric homoclinic orbits at $b = 0.25$.

We now look at $r < 0.095$ to try and find out what causes the break in the solution curve at $r = 0.085$. We saw a kink developing around $b = 1$ in the bifuration curve for $r = 0.090$ in Chapter 3, so we apply our mapping for $(b, r) = (1, 0.090)$ (see Figure 5.9). Initial conditions that lie on homoclinic orbits are given by circles. Given the results in Chapter 3, we expect to find only two homoclinic orbits, however, we find three. We construct the homoclinic orbits for these initial conditions at the circles and, using b as the continuation parameter, find solution curves. For $r = 0.090$ we find that there is a small, separate curve around $b = 1$ that almost touches the main curve (see Figure 5.10). A closer view is given in Figure 5.11. Solutions on this small curve are "dimple" 1-bump solutions. It has not proven possible to numerically determine the stability of solutions on this curve, however, numerical integration suggests solutions are stable homoclinic orbits. Continuation methods can only find solutions along the same branch as the initial solution point. In Chapter 3 we did not have an initial solution on the small separate curve, therefore it was not possible to find the curve with continuation methods only. The discovery of the small curve relies upon techniques such as the numerical technique we have developed here, where regions of parameter space can be searched for particular types of solutions.

We decrease r further (steeper $f(u)$) and use the mapping until we find where the small solution curve meets the main curve. This occurs at $(b, r) = (1.0167, 0.0899352)$ (see Figure 5.12). As r continues to decrease, the curve breaks and the gap widens with a spiral terminating each side of the break, as we saw at $r = 0.085$ in Figure 5.2. So, as $f(u)$ steepens from $r = 0.095$, a small separate curve appears, eventually causing a break in the main curve with spirals at each terminating end of the curve. In Figure 5.13 we see that particular branch of solutions for five different values of r. Continuation methods reveal a shrinking of the curve as r increases from 0.090. At $r = 0.091875$, the two endpoints of the small curve have met and the curve is continuous. Solutions on the curves in Figure 5.13 are "dimple" 1-bump solutions. In Section 5.4 we use level set analysis with the smooth firing rate function to find the parameter range for which this small curve exists.

We now consider asymmetric homoclinic orbits. Asymmetric homoclinic orbits are codimension-zero and are known to arise naturally from symmetric homoclinic orbits in

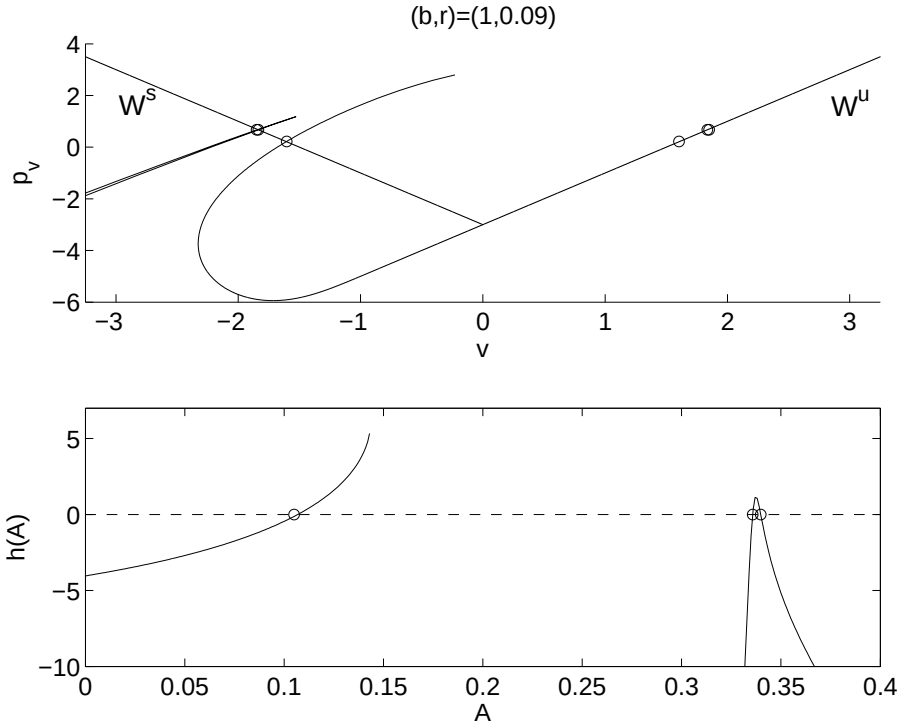

Figure 5.9: Parameter values $(b, r) = (1.0, 0.090)$. Top: Mapping of initial conditions on W^u. Bottom: Vertical distance $h(A)$ from mapped points to W^s. There are three symmetric homoclinic orbits.

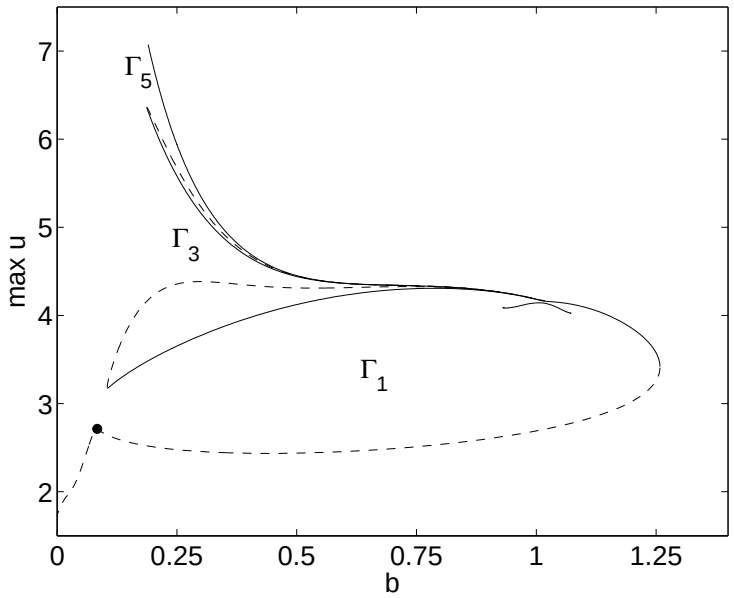

Figure 5.10: Solution curve for $r = 0.090$. Using a symmetric orbit found in Figure 5.9 and continuation methods, a small separate curve is found inside the main curve. See Figure 5.11 for a closer look at the small separate curve.

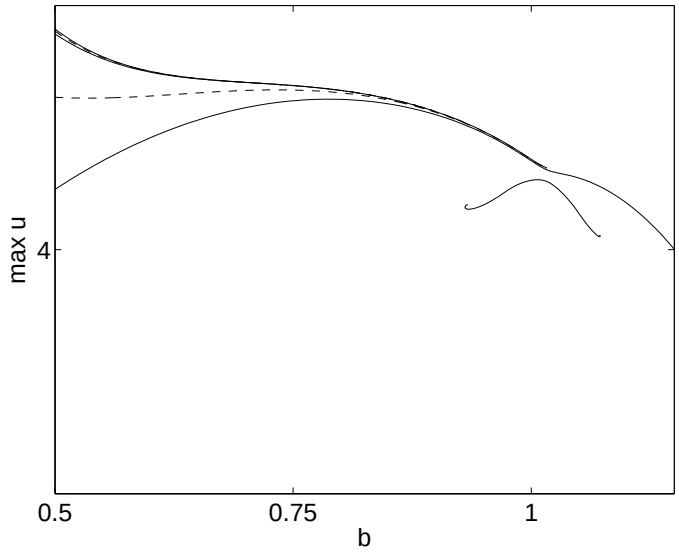

Figure 5.11: Closer look at the small curve in Figure 5.10.

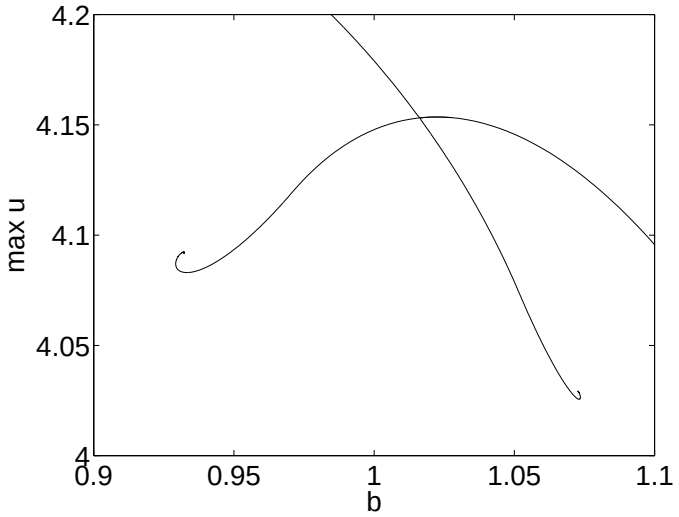

Figure 5.12: Closeup of where the small solution curve meets the main curve of 1-bump solutions at $(b, r) = (1.0167, 0.0899352)$.

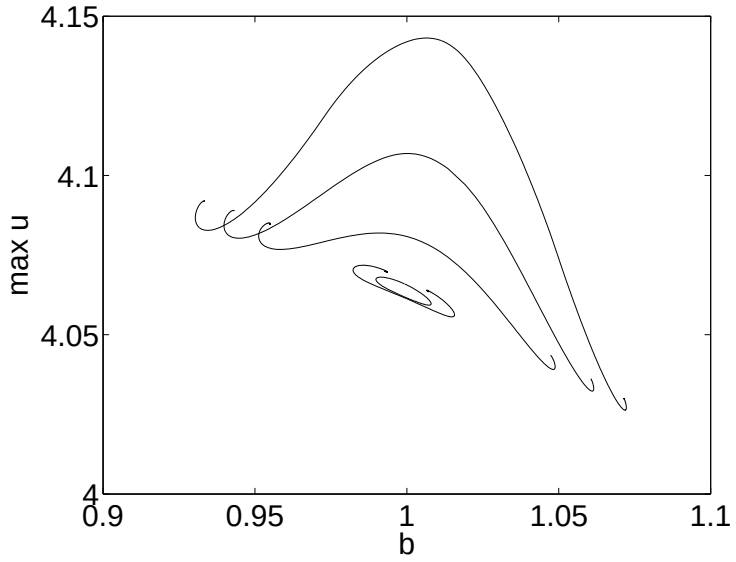

Figure 5.13: The topmost curve is the small curve found for $r = 0.090$ in Figure 5.10. As r increases to $0.0905, 0.0910, 0.0918$ and 0.091875, the curve shrinks and eventually joins up at the largest value of r, $r = 0.091875$.

generic bifurcations [12]. We found single-bump asymmetric homoclinic orbits using other numerical methods which are explained in the next chapter. Single-bump asymmetric homoclinic orbits existed for a very small region of parameter space around $b = 0.5225$ where $(r, \theta) = (0.085, 1.5)$. Interestingly, this is a value of r for which we saw breaks in the solution curve in Chapter 3 (see Figure 5.2). We therefore applied our mapping method for $(b, r, \theta) = (0.5225, 0.085, 1.5)$ and found both symmetric and asymmetric single-bump homoclinic orbits, as expected (see Figure 5.14). This region of parameter space shows more complex behaviour than we saw for $(b, r) = (0.25, 0.095)$ in Figure 5.8. Discontinuities occur in $\mathcal{P}$ and, therefore, in $h(A)$ also. Since $h(A) = 0$ for six different values of A, six homoclinic orbits exist. We take a closer view in Figure 5.15, where we see that four of these are symmetric (circles) and two are an asymmetric pair (solid diamonds).

We want to know if there are any more asymmetric single-bump solutions near $b = 0.5225$, therefore we find the solution curves of the asymmetric orbits shown in Figure 5.15. We can construct the single-bump, asymmetric homoclinic orbit given by the initial condition $A = 1.2346$, then continue in b to find the curve in Figure 5.16. As b increases from 0.5225 on the solution curve, the asymmetric single-bump solution becomes an asymmetric 2-bump solution with a "dimple" on one bump. The solution curve terminates in a spiral as seen in the symmetric 1-, 3- and 5-bump solutions in Figure 5.2. In Figure 5.17

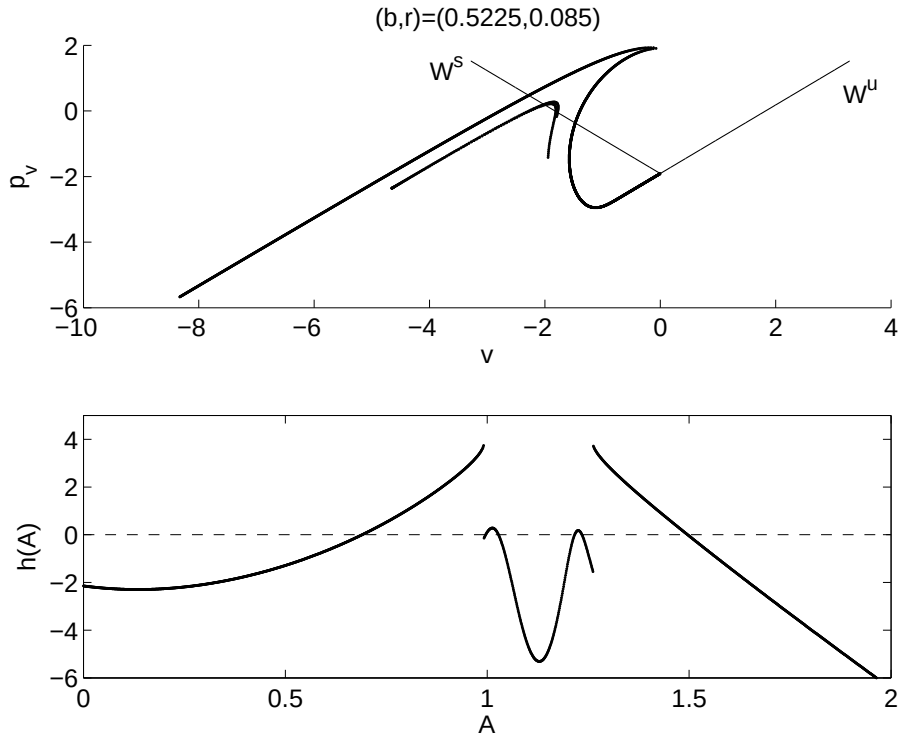

Figure 5.14: Parameter values $(b, r) = (0.5225, 0.085)$. Top: Mapping of initial conditions on W^u. Bottom: Vertical distance $h(A)$ from mapped points to W^s. See Figure 5.15 for a closer view.

we see both the starting orbit at $b = 0.5225$ and the orbit at the very end of the spiral in the solution curve in Figure 5.16.

5.4 Global bifurcation

In Chapter 3, we found breaks in the solution curve for small r (steeper $f(u)$) in the smooth firing rate function in Equation (5.3), but not for large r (flatter $f(u)$). Our model, therefore, supports different types of behaviour. The solutions are symmetric homoclinic orbits. There are no stable homoclinic orbits in the region of the break in the solution curves. To try and understand these breaks, we studied a step firing rate function in Chapter 4. This showed a very wide gap in the curve but did not help with finding the cause of the breaks. In Chapter 4 we then studied a piecewise linear $f(u)$ with steepness parameter α. We found breaks in the solution curves as the piecewise linear $f(u)$ became increasingly steep, as we did with the smooth $f(u)$ as it became increasingly steep. In the previous section, with smooth $f(u)$, we developed a numerical technique which we used to find homoclinic orbits to the fixed point at the origin. A curve of separate solutions was discovered for $r = 0.090$ around $b = 1$. As r decreased the small curve met the main

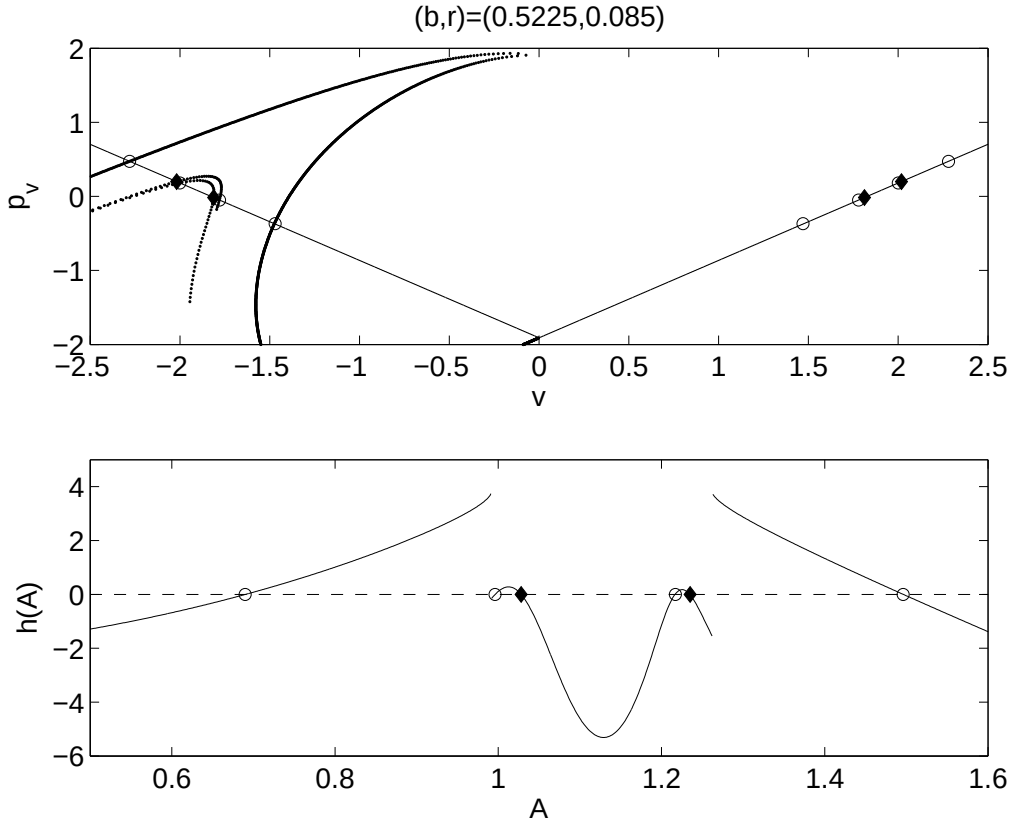

Figure 5.15: Closer view of Figure 5.14. Solid diamonds show initial conditions for two asymmetric homoclinic orbits and circles show them for four symmetric homoclinic orbits.

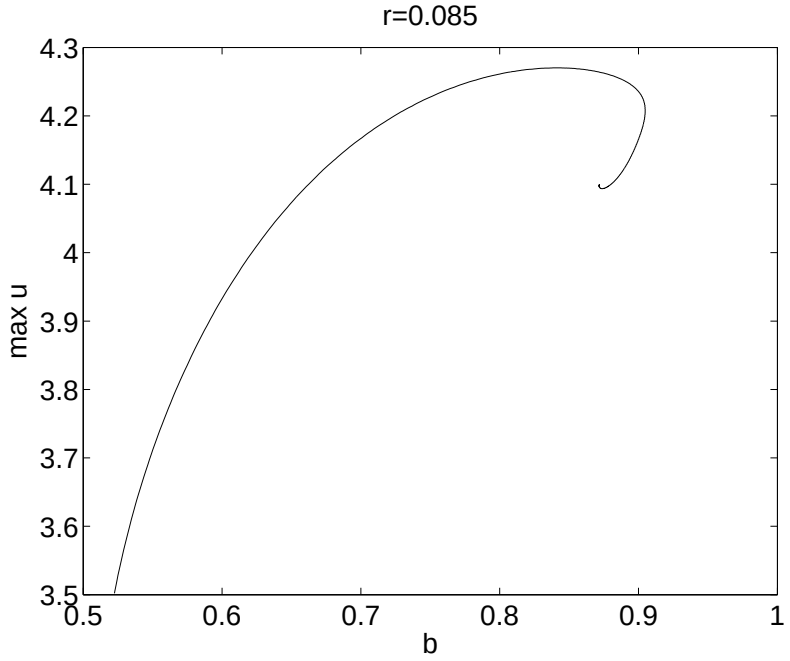

Figure 5.16: Solution curve for $r = 0.085$ starting with the asymmetric homoclinic orbit given by $A = 1.2346$ in Figure 5.15. The first and last orbits on this curve are shown in Figure 5.17.

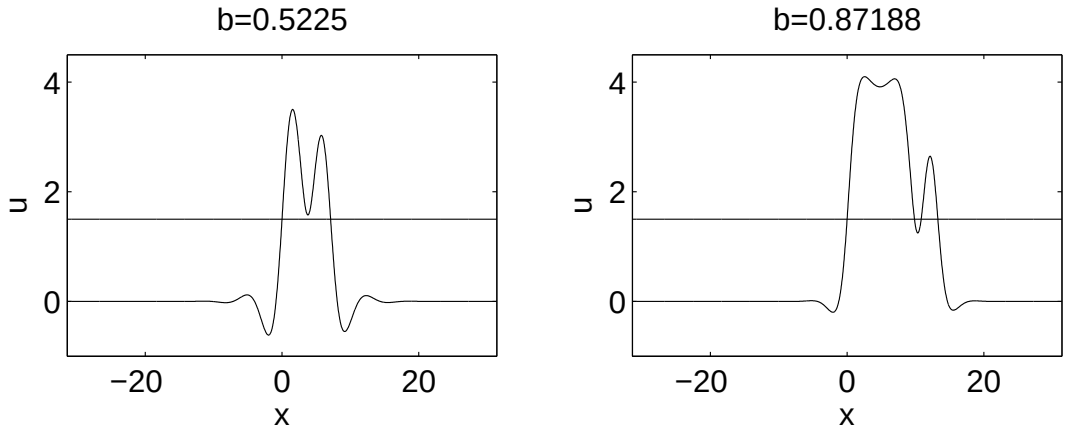

Figure 5.17: Homoclinic orbits for values of b in the solution curve in Figure 5.16. Left: Starting point on left of curve at $b = 0.5225$. Right: $b = 0.87188$ at end of spiral on right of curve.

solution curve at $(b, r) = (1.0167, 0.0899352)$, causing it to break as r decreased further. We want to understand what causes the solution curve to break and destroy homoclinic orbits to the origin. We also want to understand why this occurs for some firing rate functions but not for others.

There are other fixed points of the system aside from the one at the origin. We find these other fixed points to see if they can help in explaining the breaks in the solution curves seen in Chapters 3 and 4. In this section, we first investigate a step $f(u)$, then the piecewise linear $f(u)$, and finally, the smooth $f(u)$. We look for parameter values where symmetric single-bump homoclinic orbits to a nonzero fixed point of the system meet symmetric single-bump homoclinic orbits to the origin. For a step $f(u)$, we find two such intersection points at two different values of the coupling decay parameter b. At these intersection points, a heteroclinic connection is formed between the origin and the nonzero fixed point. This explains what is causing the breakpoints in the solution curve but does not explain the specific values of b for which the breakpoints occur. We next use a piecewise linear $f(u)$ and find intersection points when $f(u)$ is sufficiently steep and the threshold is at an appropriate level. We find a formula for the breakpoints in terms of b, the threshold and the steepness parameter. Finally, we use the smooth $f(u)$. The intersection points can be explained by the relationship between the steepness parameter, r, and the decay parameter, b, for a suitable threshold. We also find that there is a range of r for which there are two intersection points but the solution curve does not break. This is where heteroclinic connections between the origin and a nonzero fixed point exist at both ends of the small separate solution curve found in Section 5.3 for a limited range

of r.

Step firing rate function

With a double step firing rate function, $f(u) = 2\Theta(u-\theta)$, and $\theta > 0$, we have $c \in \mathbb{R}^+$ such that $u(-c) = u(c) = \theta$. The ODE in Equation (5.4) becomes the two linear ODEs

$$\begin{aligned} u^{(iv)} + 2(1-b^2)u^{(ii)} + (b^2+1)^2 u &= 0, && \text{for } c < |x| \\ u^{(iv)} + 2(1-b^2)u^{(ii)} + (b^2+1)^2 u &= 8b(b^2+1), && \text{for } |x| < c. \end{aligned} \tag{5.27}$$

Equation (5.28) has up to two fixed points. We denote the fixed points by $\mathbf{Z_i} = (u_i, u_i', u_i'', u_i''')$ $(i = 1, 2)$ where $u_i' = u_i'' = u_i''' = 0$. Then $\mathbf{Z_0} = (0,0,0,0)$ for all $b, \theta > 0$ and $\mathbf{Z_1} = (8b/(b^2+1), 0, 0, 0)$ for $8b/(b^2+1) > \theta > 0$, $b > 0$. Hence $\mathbf{Z_1}$ exists for $\left(4 - \sqrt{16-\theta^2}\right)/\theta < b < \left(4 + \sqrt{16-\theta^2}\right)/\theta$. So when $\theta = 1.5$, $\mathbf{Z_1}$ exists for $0.1946 < b < 5.1387$. See the left plot in Figure 5.18 for the fixed points. We write Equation (5.27) as a system of first-order differential equations where $\mathbf{v} = (v_0, v_1, v_2, v_3) = (u, u', u'', u''')$:

$$\begin{aligned} v_0' &= v_1 \\ v_1' &= v_2 \\ v_2' &= v_3 \\ v_3' &= 2(b^2-1)v_2 - (b^2+1)^2 v_0 - g(v_0) \end{aligned} \tag{5.28}$$

with $g(v_0) = 0$ for $v_0 < \theta$ and $g(v_0) = -8b(b^2+1)$ for $v_0 > \theta$. The Jacobian of the linearised system of equations is

$$\mathbf{J}(\mathbf{v}) = \begin{pmatrix} 0 & 1 & 0 & 0 \\ 0 & 0 & 1 & 0 \\ 0 & 0 & 0 & 1 \\ -\left((b^2+1)^2 + g'\right) & 0 & 2(b^2-1) & 0 \end{pmatrix}$$

where $g' = \dfrac{dg}{dv_0}$. We find the eigenvalues of the Jacobian for each fixed point. The fixed point at the origin, $\mathbf{Z_0}$, is a bi-focus as it has eigenvalues $\pm b \pm i$ for all $b > 0$. The fixed point $\mathbf{Z_1}$ has a real pair of eigenvalues and a pure imaginary pair of eigenvalues for $b < 1$ and two complex conjugate pairs of eigenvalues $(\pm\lambda \pm \omega i,\ \lambda, \omega \in \mathbb{R})$ for $b > 1$. Hence $\mathbf{Z_1}$ is a saddle-centre for $0 < b < 1$ and a bi-focus for $b > 1$. At $b = 1$, $\mathbf{Z_1}$ has four zero eigenvalues. This type of fixed point is referred to as a quadruple zero point in [12].

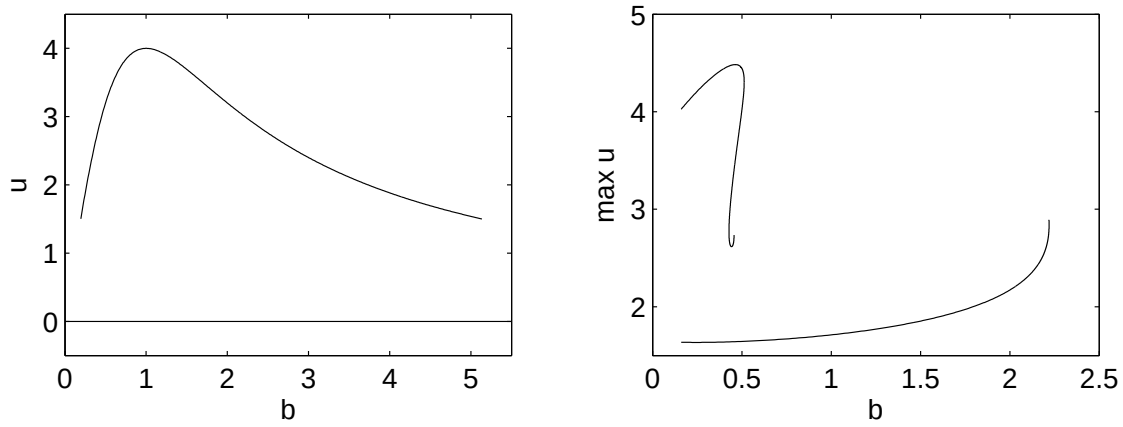

Figure 5.18: Left: The two fixed points of Equation (5.27) with $\theta = 1.5$. Right: Solution curves for 1-bump solutions show a wide gap in the upper branch of solutions.

Level set analysis

We know that symmetric homoclinic orbits to the origin, $\mathbf{Z_0}$, exist for a wide range of b. However, there is a very wide gap in the upper solution curve where no stable orbits are found. The right plot in Figure 5.18, which was first presented in Chapter 4, shows the bifurcation diagram. Homoclinic orbits to the origin lie on the zero energy surface which is the level set $H = 0$. So $H(\mathbf{Z_0}) = 0$. Generically, nonzero fixed points do not lie on the zero energy surface. However, there is a large unexpected gap in the solution curve, so we search for parameter values where $H(\mathbf{Z_1}) = 0$. Using the definition of the Hamiltonian in Equation (5.8) of $H(u, v, p_u, p_v) = p_u v + p_v^2/2 + av^2/2 - cu^2/2 - G(u)$ we find

$$H(\mathbf{Z_1}) = 32b^2 - 8\theta b(b^2 + 1). \tag{5.29}$$

Therefore $H(\mathbf{Z_1}) = 0$ when

$$\theta = \frac{4b}{(b^2 + 1)}. \tag{5.30}$$

Figure 5.19 shows the plot of Equation (5.30). When $\theta = 1.5$ in Equation (5.30), $b = 0.451, 2.215$ and these values of b correspond to where we have seen the breaks in the solution curve in the right plot in Figure 5.18. The curve in Figure 5.19 has a global maximum at $(b, \theta) = (1, 2)$. For $\theta > 2$, $H(\mathbf{Z}_1) \neq 0$ for all $b > 0$ and the solution curve does not break. For $\theta < 2$, the curve defines the two break points of the solution curve in (b, θ) parameter space. There appears to be some kind of global bifurcation where the stable and unstable manifolds of $\mathbf{Z_0}$ and $\mathbf{Z_1}$ intersect at the parameter values given by Equation (5.30). This is a codimension-one bifurcation. It is similar to a codimension-two heteroclinic bifurcation, called a T-point or terminal point, studied in two-dimensional parameter space in the Lorenz equations [43]. At the points (b, θ) satisfying Equation (5.30),

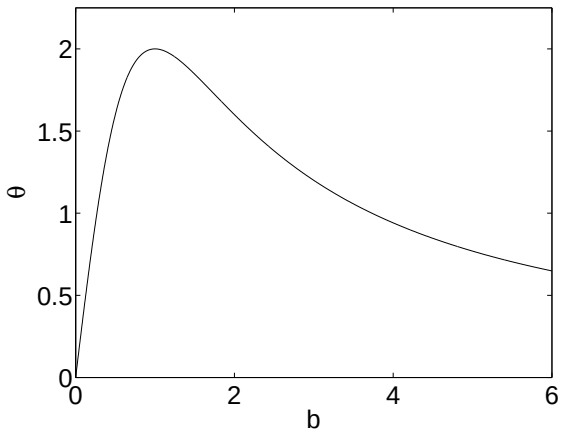

Figure 5.19: Points in (b, θ) space where the Hamiltonian of the fixed point $\mathbf{Z_1}$ meets the zero energy surface $H = 0$ for Equation (5.4) with double Heaviside firing rate function.

we conjecture there are heteroclinic orbits from the zero fixed point, $\mathbf{Z_0}$, to the nonzero fixed point $\mathbf{Z_1}$. In Section 5.5, we test this conjecture by using travelling coordinates in the full time-dependent model with step $f(u)$ and looking for stationary patterns.

System symmetry

We have another way of viewing the qualitative changes in the solution curve in the right plot in Figure 5.18. Through a change of variables we can find a particular symmetry for the system in Equation (5.27), thereby creating a new system which we refer to as a "conjugate system".

Let $w \to u_1 - u$ where u_1 is the u variable of the fixed point $\mathbf{Z_1}$, thus $u_1 = 8b/(b^2+1)$. Applying this change of variables to Equation (5.27) we obtain the conjugate system

$$\begin{aligned} w^{(iv)} + 2(1-b^2)w'' + (b^2+1)^2 w &= 0, && \text{for } |x| < c \\ w^{(iv)} + 2(1-b^2)w'' + (b^2+1)^2 w &= 8b(b^2+1), && \text{for } c < |x|. \end{aligned} \tag{5.31}$$

Using phase space variables (w, w', w'', w''') as before, Equation (5.31) has a fixed point at $(w, w', w'', w''') = (0, 0, 0, 0)$, which is the equivalent of the fixed point in (u, u', u'', u''') phase space of $\mathbf{Z_1} = (8b/(b^2+1), 0, 0, 0)$. Thus homoclinic orbits to the fixed point at the origin in the conjugate system are homoclinic orbits to the fixed point $\mathbf{Z_1}$ in the original system. The system in Equation (5.31) therefore provides a way of investigating homoclinic orbits to $\mathbf{Z_1}$ which would be difficult in the usual variables given that the u component of $\mathbf{Z_1}$ is above threshold.

We define $\theta_u = 1.5$ and the threshold in the conjugate system as $\theta_w = u_1 - \theta_u$. Using AUTO 2000, we find the solution curves of homoclinic orbits to the fixed point at the

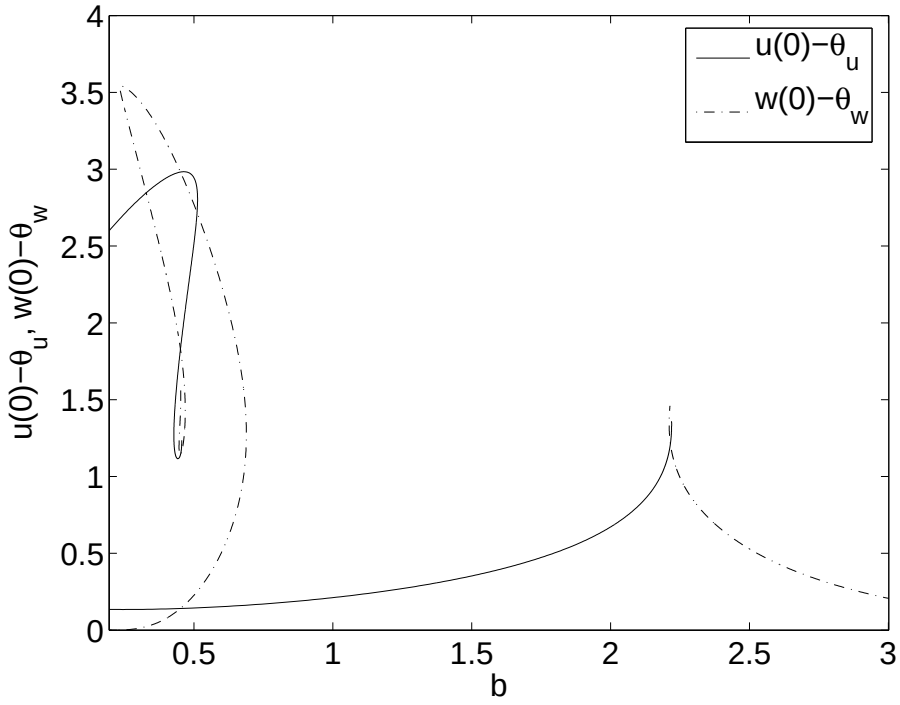

Figure 5.20: Representation of solution curves for Equation (5.27) and the conjugate system in Equation (5.31) found through the change of variables $w \to u_1 - u$. $\theta_u = 1.5$, u_1 is the u component of the fixed point $\mathbf{Z_1}$ of Equation (5.27) and $\theta_w = u_1 - \theta_u$.

origin in both Equation (5.27) and Equation (5.31). In Figure 5.20 we plot $w(0) - \theta_w$ and $u(0) - \theta_u$ as functions of b. We see that one of the variables for the conjugate system, w, meets u at $b = 0.451, 2.215$. These are the same values of b where $H(\mathbf{Z_1}) = H(\mathbf{Z_0})$ as given by Equation (5.30). These two values of b are also where the solution curve breaks (see Figure 5.18). At $b = 0.451, 2.215$, we know from Equation (5.30) that $\theta_u = 4b/(b^2+1)$, therefore $u_1 = 8b/(b^2+1) = 2\theta_u = 3$ and since $\theta_w = u_1 - \theta_u$, we have $\theta_w = 1.5$. Also, since $w = u_1 - u$, we have $w = 3 - u$. At the breakpoints $b = 0.451, 2.215$, we see from Figure 5.20 that $w(0) - \theta_w = u(0) - \theta_u$, so the symmetry of these two systems means that $w(0) = u(0) = \theta$ at the breakpoints. Therefore, these breakpoints are where a heteroclinic orbit exists from the fixed point at the origin of the system in Equation (5.27) to the fixed point at the origin of the conjugate system in Equation (5.31). This is the equivalent of a heteroclinic orbit from $\mathbf{Z_0}$ to $\mathbf{Z_1}$.

Piecewise linear firing rate function

Using the piecewise linear firing rate function from Chapter 4 of

$$f(u) = \begin{cases} 0, & u < \theta \\ \alpha(u-\theta), & \theta < u < \theta + \beta/\alpha \\ \beta, & \theta + \beta/\alpha < u, \end{cases} \tag{5.32}$$

we have $c, d \in \mathbb{R}^+$ such that $u(-c) = u(c) = \theta + \beta/\alpha$ and $u(-d) = u(d) = \theta$. Then the ODE in Equation (5.4) becomes

$$\begin{aligned} u^{(iv)} + 2(1-b^2)u^{(ii)} + (b^2+1)^2 u &= 0, && \text{for } d < |x| \\ u^{(iv)} + 2(1-b^2)u^{(ii)} + (b^2+1)(b^2+1-4\alpha b)u &= -4\alpha b(b^2+1)\theta, && \text{for } c < |x| < d \\ u^{(iv)} + 2(1-b^2)u^{(ii)} + (b^2+1)^2 u &= 4\beta b(b^2+1), && \text{for } |x| < c. \end{aligned} \tag{5.33}$$

Equation (5.33) is a four dimensional system, therefore fixed points are written in (u, u', u'', u''') coordinates. These fixed points have $u' = u'' = u''' = 0$. There are up to three fixed points depending upon the region of parameter space. We denote the fixed points by $\mathbf{Z_i} = (u_i, u_i', u_i'', u_i''')$ $(i = 1, 3)$ where $u_i' = u_i'' = u_i''' = 0$. Equation (5.33) has the fixed point $\mathbf{Z_0} = (0, 0, 0, 0)$ for all $b, \theta > 0$. There are two nonzero fixed points, $\mathbf{Z_1} = (4\alpha\theta b/(4\alpha b - b^2 - 1), 0, 0, 0)$ and $\mathbf{Z_2} = (4\beta b/(b^2+1), 0, 0, 0)$, for $\theta > 0$ and $b_1 \leq b \leq b_2$ where

$$b_1 = \left(2\alpha\beta - \sqrt{4\alpha^2\beta^2 - (\theta\alpha+\beta)^2)}\right)/(\theta\alpha+\beta) \tag{5.34}$$

$$b_2 = \left(2\alpha\beta + \sqrt{4\alpha^2\beta^2 - (\theta\alpha+\beta)^2)}\right)/(\theta\alpha+\beta). \tag{5.35}$$

The steepness of $f(u)$ changes the regions of parameter space where the fixed points $\mathbf{Z_1}$ and $\mathbf{Z_2}$ exist. The left plot in Figure 5.21 shows the fixed points of Equation (5.33) for $(\beta, \theta) = (2, 1.5)$ with $\alpha = 2$ on the left and $\alpha = 3$ on the right. We see that for the steeper $f(u)$ on the right, the nonzero fixed points $\mathbf{Z_1}$ and $\mathbf{Z_2}$ exist for a wider range of b. In the numerical results in Chapter 4, we found solution curves of single-bump solutions for the piecewise linear firing rate function in Equation (5.32) with $\theta = 1.5$, $\beta = 2$ and varying steepness of $f(u)$. We saw that the solution curve was continuous for $\alpha = 2$. For a steeper $f(u)$ of $\alpha = 3$, the solution curve was discontinuous for a wide range of b. Figure 5.22, which was first presented in Chapter 4, shows the bifurcation diagram for $\alpha = 2$ and $\alpha = 3$.

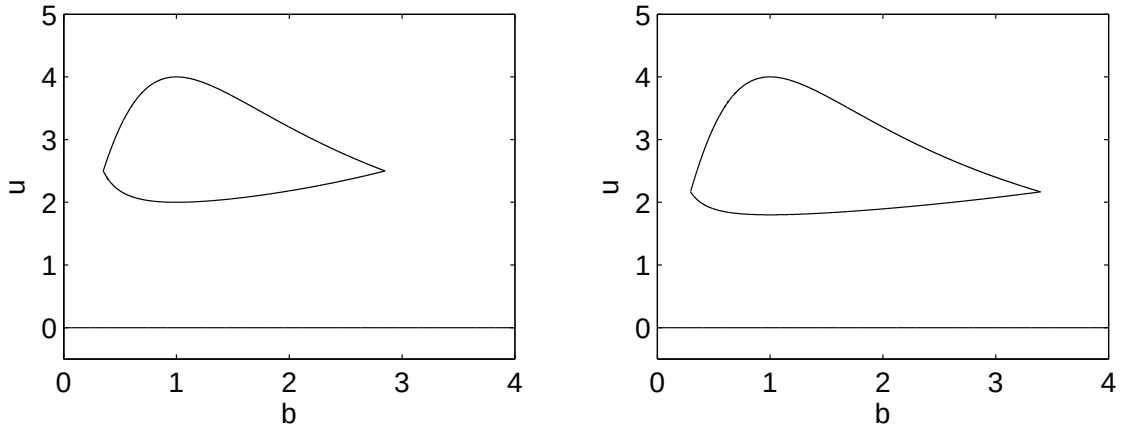

Figure 5.21: Fixed points of Equation (5.33) with $(\beta, \theta) = (2, 1.5)$ and $\alpha = 2$ (left) and $\alpha = 3$ (right).

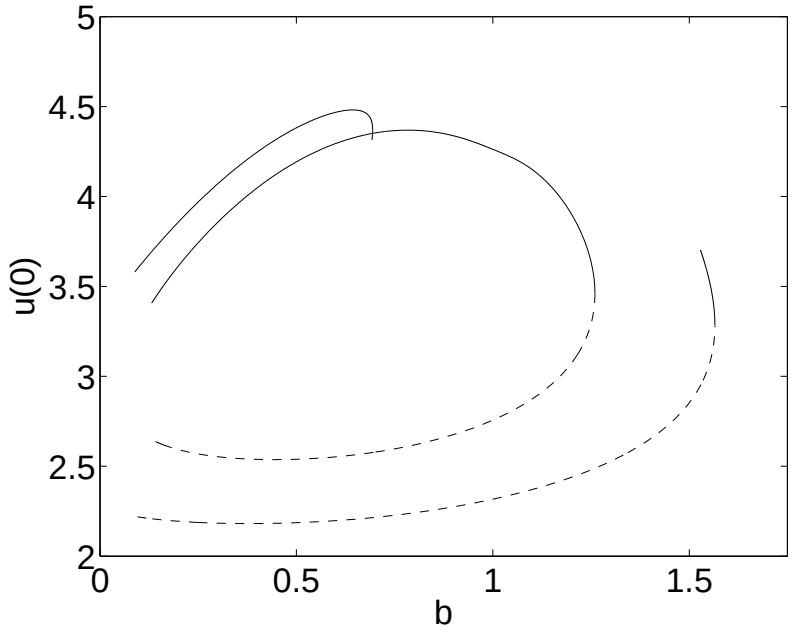

Figure 5.22: Solution curves for single-bump solutions of Equation (5.33) with $(\beta, \theta) = (2, 1.5)$ and $\alpha = 2, 3$. The function $f(u)$ is steeper for $\alpha = 3$ than for $\alpha = 2$. When $\alpha = 2$, the solution curve is continuous. When $\alpha = 3$, the solution curve is discontinuous.

Level set analysis

We calculate the Hamiltonian of $\mathbf{Z_1}$ and $\mathbf{Z_2}$ to see if there are any parameter values for which they meet the zero energy surface, $H = 0$, as in the previous section for the step $f(u)$. First we investigate $\mathbf{Z_1}$. Since

$$G(u) = -\frac{4b}{b^2+1}\int_\theta^u f(s)\,ds \tag{5.36}$$

we have

$$\begin{aligned} G(\mathbf{Z_1}) &= -4b(b^2+1)\alpha\int_\theta^{u_1}(s-\theta)ds \\ &= \frac{-2b(b^2+1)^2\theta^2(b^4+2b^2+1)}{(b^2+1-4\alpha b)^2} \end{aligned} \tag{5.37}$$

and

$$H(\mathbf{Z}_1) = \frac{2b(b^2+1)^2\alpha\theta^2}{b^2+1-4\alpha b}. \tag{5.38}$$

There are no real values of b, α, θ for which $H(\mathbf{Z_1}) = 0$ therefore the fixed point $\mathbf{Z_1}$ never crosses the zero energy surface.

For $\mathbf{Z_2}$,

$$\begin{aligned} G(\mathbf{Z_2}) &= -4b(b^2+1)\left[\alpha\int_\theta^{\theta+\beta/\alpha}(s-\theta)ds + \beta\int_{\theta+\beta/\alpha}^{u_2} ds\right] \\ &= 4b(b^2+1)\beta\left(\theta+\frac{\beta}{2\alpha}\right) - 16\beta^2b^2 \end{aligned} \tag{5.39}$$

and the Hamiltonian is

$$H(\mathbf{Z_2}) = -\frac{2\beta b}{\alpha}\left((2\theta\alpha+\beta)b^2 - 4\alpha\beta b + (2\alpha\theta+\beta)\right). \tag{5.40}$$

So for $\alpha, \beta > 0$, $H(\mathbf{Z_2}) = 0$ when $b = 0$ and

$$(\beta+2\theta\alpha)b^2 - 4\alpha\beta b + 2\alpha\theta + \beta = 0. \tag{5.41}$$

Equation (5.41) has roots

$$b = \frac{2\alpha\beta \pm \sqrt{(4\alpha^2-1)\beta^2 - 4\theta\alpha\beta - 4\theta^2\alpha^2}}{2\theta\alpha+\beta}. \tag{5.42}$$

Therefore Equation (5.42) has real values when $(4\alpha^2-1)\beta^2 - 4\theta\alpha\beta - 4\theta^2\alpha^2 \geq 0$.

We investigate the breakpoints in the solution curves, as seen in Figure 5.22, in terms of the threshold and steepness parameters in $f(u)$. We use Equation (5.41) to find where homoclinic orbits to the fixed point $\mathbf{Z_2}$ meet homoclinic orbits to the origin, that is, θ and α as functions of b such that $H(\mathbf{Z_2}) = H(\mathbf{Z_0}) = 0$.

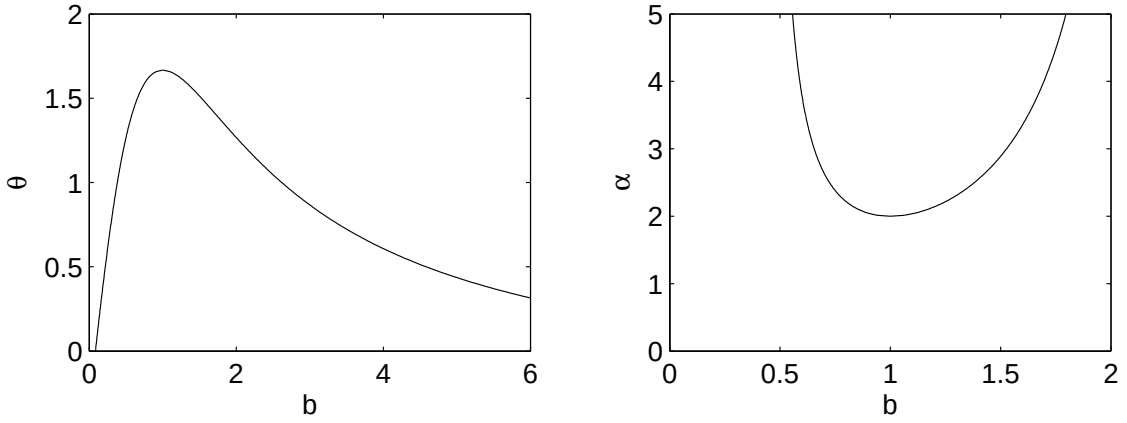

Figure 5.23: Points where $H(\mathbf{Z_2}) = H(\mathbf{Z_0})$ from Equation (5.42). Left: θ as a function of b with $(\alpha, \beta) = (3, 2)$ in Equation (5.32). Right: Steepness parameter α as a function of b, giving the values of (b, α) where the single-bump solution curve breaks with $(\beta, \theta) = (2, 1.5)$ in Equation (5.32).

First, we investigate the relationship between the threshold and the breakpoints. From Equation (5.41) we have

$$\theta = \frac{\beta(4\alpha b - b^2 - 1)}{2\alpha(b^2 + 1)}. \tag{5.43}$$

The left plot in Figure 5.23 shows $(\alpha, \beta) = (3, 2)$ in Equation (5.43). For $\theta < 5/3$ there are two values of b for which $H(\mathbf{Z_2})$ meets $H(\mathbf{Z_0})$. When $\theta > 5/3$, $H(\mathbf{Z_2})$ never meets $H(\mathbf{Z_0})$. We see that $b = 0.655, 1.527$ for $\theta = 1.5$ and this agrees with the breakpoints seen in the solution curve for $\alpha = 3$ in Figure 5.22. Next, we investigate the relationship between the steepness of $f(u)$, which is determined by α, and the breakpoints. From Equation (5.41) we find

$$\alpha = \frac{\beta(b^2 + 1)}{4\beta b - 2\theta(b^2 + 1)}. \tag{5.44}$$

We set $(\beta, \theta) = (2, 1.5)$ in Equation (5.44) and plot α as a function of b in the right plot of Figure 5.23. Equation (5.44) can have zero, one or two real roots, depending upon parameter values. At $\alpha = 2$, there is one value of b for which $H(\mathbf{Z_2}) = H(\mathbf{Z_0})$. As α increases past 2, ($f(u)$ becoming steeper), there are two values of b for which $H(\mathbf{Z_2}) = H(\mathbf{Z_0})$. As α continues to increase, the difference between these two values of b increases. This corresponds to an increasing width of the gap in the solution curve as $f(u)$ continues to steepen.

Hence, level set analysis has shown that for an appropriate level of threshold, the breaking in the solution curve for 1-bump solutions occurs with increasing steepness of the piecewise linear firing rate function. This is the same as the behaviour of the smooth firing rate function in Chapter 3.

Smooth firing rate function

With the smooth firing rate function

$$f(u) = 2e^{-r/(u-\theta)^2}\Theta(u-\theta) \tag{5.45}$$

from Chapter 3, we have $c \in \mathbb{R}^+$ such that $u(-c) = u(c) = \theta$. The ODE in Equation (5.4) becomes

$$\begin{aligned} &u^{(iv)} + 2(1-b^2)u^{(ii)} + (b^2+1)^2 u = 0, && \text{for } c < |x| \\ &u^{(iv)} + 2(1-b^2)u^{(ii)} + (b^2+1)^2 u = 8b(b^2+1)e^{-r/(u-\theta)^2}, && \text{for } |x| > c. \end{aligned} \tag{5.46}$$

Equation (5.46) is a four-dimensional system so again we use the phase space variables (u, u', u'', u''') to define fixed points. We find fixed points of Equation (5.46) by numerically solving for u in the steady state equation

$$u = \frac{8b}{(b^2+1)}e^{-r/(u-\theta)^2}\Theta(u-\theta) \tag{5.47}$$

and setting $(u', u'', u''') = (0, 0, 0)$. For this section we set $\theta = 1.5$. When $r = 0.095$, Equation (5.47) has three solutions, hence Equation (5.46) has three fixed points (see the top left plot of Figure 5.24). We denote the fixed points by $\mathbf{Z_i} = (u_i, u_i', u_i'', u_i''')$ $(i = 1, 3)$ where $u_i' = u_i'' = u_i''' = 0$. There is a fixed point at the origin, $\mathbf{Z_0} = (0, 0, 0, 0)$, for all $b > 0$. There are two other nonzero fixed points $\mathbf{Z_1}$ and $\mathbf{Z_2}$, where $u_2 > u_1 > \theta$. By writing (5.4) as a system of first order equations where $\mathbf{v} = (v_0, v_1, v_2, v_3) = (u, u', u'', u''')$, we can find the eigenvalues of each fixed point and see what type of fixed points they are. The system of first order equations is

$$\begin{aligned} v_0^{'} &= v_1 \\ v_1^{'} &= v_2 \\ v_2^{'} &= v_3 \\ v_3^{'} &= 2(b^2-1)v_2 - (b^2+1)^2 v_0 - g(v_0) \end{aligned} \tag{5.48}$$

where $g(v_0) = -8b(b^2+1)e^{-r/(v_0-\theta)^2}\Theta(v_0-\theta)$ and $g' = \dfrac{dg}{dv_0}$. The Jacobian of the linearised system of equations is

$$\mathbf{J}(\mathbf{v}) = \begin{pmatrix} 0 & 1 & 0 & 0 \\ 0 & 0 & 1 & 0 \\ 0 & 0 & 0 & 1 \\ -((b^2+1)^2 + g') & 0 & 2(b^2-1) & 0 \end{pmatrix}$$

and has eigenvalues $\lambda = \pm\sqrt{b^2 - 1 \pm \sqrt{-(4b^2+g')}}$. For $\mathbf{Z_0}$, $\lambda = \pm(b \pm i)$ so $\mathbf{Z_0}$ is a bi-focus for all b. As b increases, the eigenvalues of $\mathbf{Z_1}$ change from two complex conjugate

pairs, to two pure imaginary conjugate pairs, then one complex conjugate pair with a real pair of same magnitude but opposite sign, and finally two real pairs of same magnitude but opposite sign. The Jacobian evaluated at the fixed point $\mathbf{Z_2}$, $\mathbf{J}(\mathbf{Z_2})$, has eigenvalues of two complex conjugate pairs for $b \lessapprox 1.73$ and two real pairs of eigenvalues for $b \gtrapprox 1.73$. Therefore, $\mathbf{Z_2}$ is a saddle-focus for approximately $b \lessapprox 1.73$ and a saddle for $b \gtrapprox 1.73$. See Figure 5.24 for plots of the eigenvalues of the three fixed points.

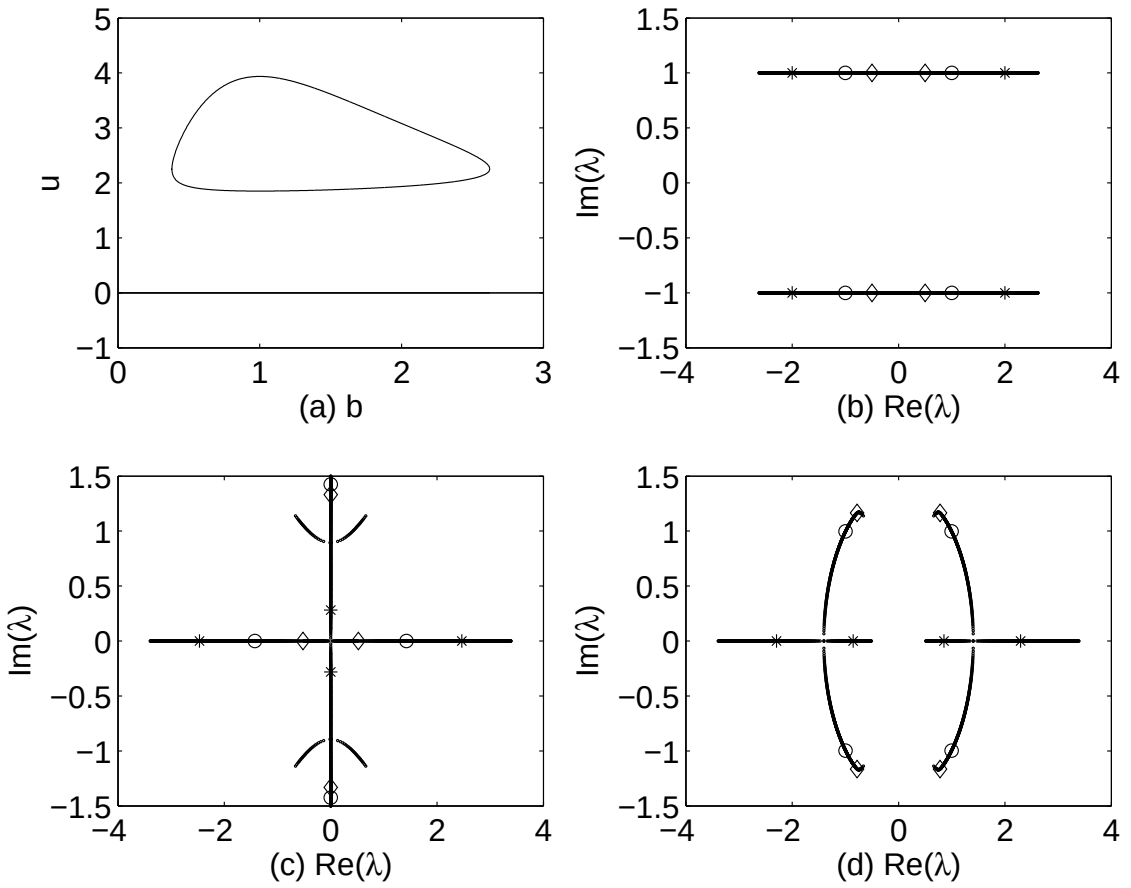

Figure 5.24: Equation (5.46) with $(r, \theta) = (0.095, 1.5)$: (a) the fixed points of the system and eigenvalues for: (b) the fixed point at the origin, $\mathbf{Z_0}$; (c) the middle nonzero fixed point $\mathbf{Z_1}$; (d) the upper nonzero fixed point $\mathbf{Z_2}$. Diamonds $b = 0.5$; circles $b = 1$; asterisks $b = 2$.

Again, to gain an understanding of the discontinuities in the solution curve for sufficiently steep firing rate functions as seen in Chapter 3, we vary the steepness of the firing rate function and look for parameter values where homoclinic orbits to the fixed points $\mathbf{Z_1}$ and $\mathbf{Z_2}$ can meet homoclinic orbits to the origin. We therefore look for b, r such that $H(\mathbf{Z_1}) = H(\mathbf{Z_0}) = 0$ and $H(\mathbf{Z_2}) = H(\mathbf{Z_0}) = 0$. To find these values of b, r, we see if the Hamiltonian at the fixed points changes sign as parameters vary. We know from Chapter 3 that the solution curve of stable 1-bump solutions is continuous for $r = 0.095$. Figure 5.25

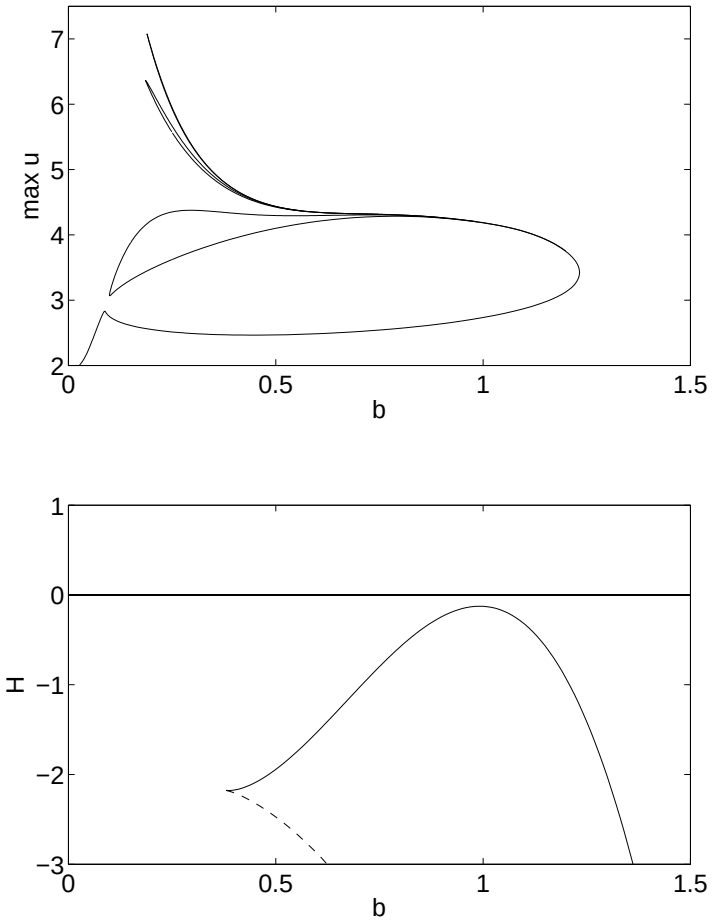

Figure 5.25: Top: The solution curves of homoclinic orbits to the origin are continuous for Equation (5.46) with $(r, \theta) = (0.095, 1.5)$. Bottom: The Hamiltonian of the two fixed points $\mathbf{Z_1}$ (dashed curve) and $\mathbf{Z_2}$ (solid curve) is always negative.

shows the bifurcation diagram and the Hamiltonian of the fixed points $\mathbf{Z}_1$ and $\mathbf{Z}_2$ for $(r, \theta) = (0.095, 1.5)$. We see that $H(\mathbf{Z_1})$ and $H(\mathbf{Z_2})$ are both negative for all $b > 0$.

In Section 5.3 we used a two-dimensional mapping to find homoclinic orbits in different regions of parameter space. We discovered a small separate solution curve near the main curve for $r = 0.090$ around $b = 1$ (see Figure 5.10). We used the mapping to investigate $r = 0.095$ around $b = 1$ but only found two 1-bump homoclinic orbits as expected given the bifurcation diagram in the top plot of Figure 5.25. We found that the small curve met the main solution curve at $r = 0.0899352$, causing it to break and terminate in tight spirals on each side of the break (see Figure 5.12). We also increased r from 0.090 and found that the small curve existed for a range of r above 0.090 but did not exist, however, for $r = 0.095$ (see Figure 5.11). For $r = 0.090$, we find the Hamiltonian of both $\mathbf{Z_1}$ and $\mathbf{Z_2}$. Again, $H(\mathbf{Z_1}) < 0$ for all $b > 0$, however $H(\mathbf{Z_2}) = 0$ at two values of b, one on each side of $b = 1$. The two values of b where $H(\mathbf{Z_2}) = 0$ are the endpoints of the small separate

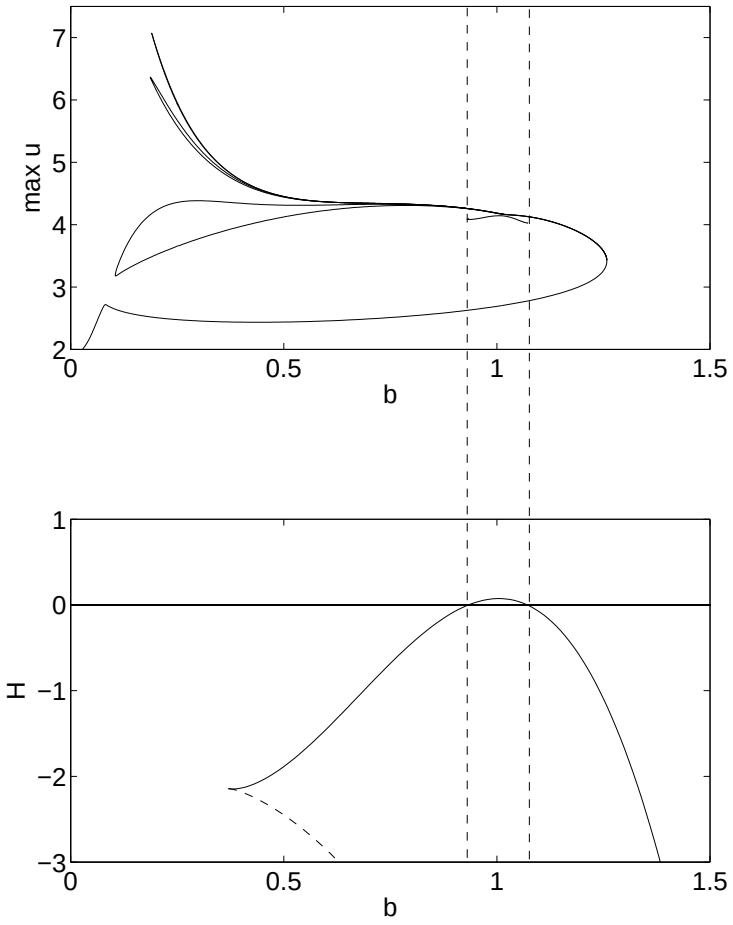

Figure 5.26: Top: For Equation (5.46) with $(r, \theta) = (0.090, 1.5)$, there is a small separate solution curve around $b = 1$. Bottom: Hamiltonian of the two nonzero fixed points: $\mathbf{Z_1}$ (dashed curve), $\mathbf{Z_2}$ (solid curve). The endpoints of the small separate solution curve correspond to the two values of b for which $H(\mathbf{Z_2}) = 0$. Compare to Figure 5.25.

solution curve (see Figure 5.26).

In Chapter 3 when we allowed $f(u)$ to become even steeper by setting $r = 0.085$, we found a large gap in the upper branch of 1-bump solutions. In Figure 5.27 we see that $H(\mathbf{Z_1}) < 0$ for all $b > 0$ again but $H(\mathbf{Z_2}) > 0$ for b between the two endpoints of the solution curve with the breaks. Therefore the terminating ends of the solution curve occur at the two values of b where $H(\mathbf{Z_2}) = 0$.

Hence for the smooth $f(u)$ in Equation (5.45), the fixed point $\mathbf{Z_1}$ never meets the zero energy surface $H = 0$ as $H(\mathbf{Z_1}) < 0$ and $\partial H(\mathbf{Z_1})/\partial b < 0$ for all b. For some values of r, we see that homoclinic orbits to the nonzero fixed point $\mathbf{Z_2}$ can meet homoclinic orbits to the origin. We conjecture that the breakpoints in the solution curve and the terminating ends of the small separate bifurcation curve are where $H(\mathbf{Z_2}) = H(\mathbf{Z_0}) = 0$ as this is the behaviour we have seen for $r = 0.085, 0.090, 0.095$. We therefore calculate the points (b, r)

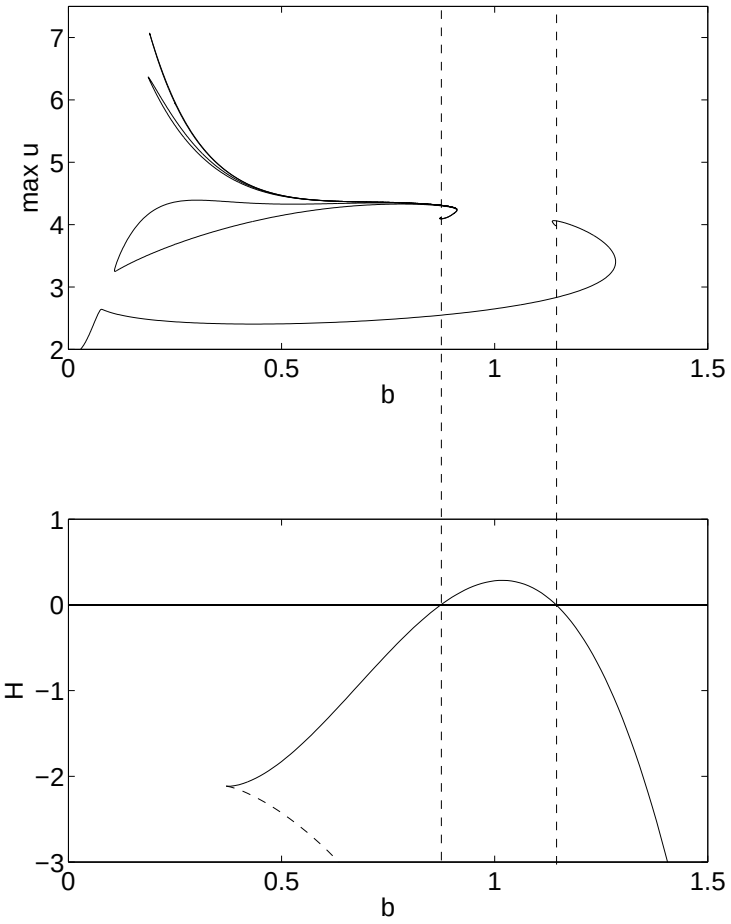

Figure 5.27: Top: The upper solution curve for Equation (5.46) with $(r, \theta) = (0.085, 1.5)$ breaks at two points. Bottom: Hamiltonian of two of the fixed points: $\mathbf{Z_1}$ (dashed curve), $\mathbf{Z_2}$ (solid curve). The endpoints of the breaks in the upper solution curve correspond to the two values of b for which $H(\mathbf{Z_2}) = 0$. Compare to Figures 5.25 and 5.26.

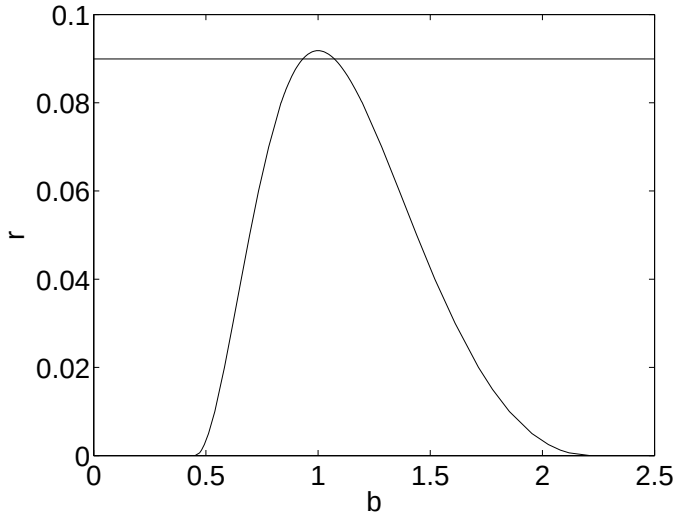

Figure 5.28: Points in (b, r) parameter space where $H(\mathbf{Z_2}) = H(\mathbf{Z_0}) = 0$ for $\theta = 1.5$ in Equation (5.45). At $r = 0.0899352$ (horizontal line), the small solution curve meets the main curve. Below the line, the curve gives the endpoints in the solution curve. Above the line, the curve gives the terminating ends of the small separate solution curve.

such that $H(\mathbf{Z_2}) = 0$ (see Figure 5.28). The curve above the horizontal line in Figure 5.28 defines the end points of a small separate solution curve inside the main curve. We saw this small curve for $r = 0.090$ in Figure 5.26. At $r = 0.0899352$ (horizontal line), the small solution curve meets the main curve (see Figure 5.12). The two values of b at which the horizontal line intersects the curve in Figure 5.28 are the values of b at the endpoints of the small curve. When $r < 0.0899352$, the small solution curve no longer exists and the curve for $r < 0.0899352$ in Figure 5.28 defines the end points of the break in the main solution curve in (b, r) parameter space, as we saw in Figure 5.27 for $r = 0.085$. As r decreases (steeper $f(u)$), the gap between the two values of b for which $H(\mathbf{Z_2}) = 0$ widens. This is seen in the bifurcation diagrams in Figures 5.27 and 5.18 where the discontinuity in the solution curves widens as r becomes smaller. When $r = 0$, $f(u)$ is a step function and at $r = 0$ the curve in Figure 5.28 defines the two values of b where the solution curve breaks in the right plot of Figure 5.18. Therefore Figure 5.28 appears to confirm our conjecture.

We also conjecture that the curve in Figure 5.28 defines where heteroclinic connections exist for Equation (5.46) with $r > 0$. We confirmed this for $r = 0$ in Section 5.3 with the analysis of the conjugate system. In the next section, Section 5.5, we examine travelling fronts to prove that heteroclinic orbits exist at the endpoints of the solution curves for $r = 0$.

As a final note to this section, the small solution curve we saw in Figures 5.10 and 5.11

seems to first appear around $(b, r) = (1, 0.0919)$. Examining the ODE of the system in Equation (5.4)

$$u^{(iv)} + 2(1 - b^2)u'' + (b^2 + 1)^2 u = 4b(b^2 + 1)f(u) \tag{5.49}$$

we see that u'' disappears from the ODE when $b = 1$. It would be interesting to look into this further and see if it is related to the appearance of the small solution curve.

5.5 Travelling fronts

The analysis in the chapter so far has been concerned with time-independent solutions of our system as given by the ODE in Equation (5.4). We now return to the time-dependent system in Equations (5.1)–(5.3).

Waves in the form of travelling fronts and pulses have been observed in slice preparations [45, 87]. Travelling waves are a feature of the type of neural model we are studying and there has been substantial work on modelling travelling waves [14, 15, 17, 16, 27, 81]. We can write the time-dependent system in moving coordinates and look for travelling patterns. A travelling wave or front, with speed $\bar{c}$, is a stationary pattern in time when written in moving coordinates. A standing wave or stationary front is a travelling wave that has zero speed ($\bar{c} = 0$), therefore the pattern is stationary spatially.

We first write our model with step firing rate function in integral form and find an expression for travelling fronts. By taking the special case of $\bar{c} = 0$, we find stationary fronts. We next want to find travelling fronts for the smooth firing rate function. To do this, we write the model as an ODE. We obtain a fifth-order ODE as the synapse model is first order.

Step firing rate function

In Section 5.4 we found that the system with step $f(u)$ in Equation (5.27) has two fixed points. One is at the origin, $\mathbf{Z_0} = (0, 0, 0, 0)$, and the other is $\mathbf{Z_1} = (8b/(b^2+1), 0, 0, 0)$. By calculating the Hamiltonian at $\mathbf{Z_1}$, we found that homoclinic orbits to $\mathbf{Z_1}$ meet homoclinic orbits to $\mathbf{Z_0}$ at the points (b, θ) that satisfy $\theta = 4b/(b^2 + 1)$. We saw that for $\theta < 2$, these points correspond to the breakpoints in the solution curve (see the right plot of Figure 5.18). With a change of variables and using bifurcation analysis, we were able to show that at the breakpoints in the curve defined by $\theta = 4b/(b^2 + 1)$, heteroclinic orbits exist between the two fixed points $\mathbf{Z_0}$ and $\mathbf{Z_1}$. A heteroclinic orbit can be perceived as a stationary front between two different fixed points. To find possible stationary fronts, and

therefore heteroclinic orbits, at the breakpoints in the solution curve in Figure 5.18, we write Equations (5.1)–(5.2) with step firing rate function, $f(u) = 2\Theta(u-\theta)$, in travelling coordinates and find an expression for travelling fronts. We set the speed of the travelling fronts to zero and see if this occurs at the parameters values of the breakpoints.

In [16], travelling fronts were constructed for the scalar equation of

$$\frac{1}{\alpha}\frac{\partial u(x,t)}{\partial t} = -u(x,t) + \int_{\infty}^{\infty} w(y) f(u(x-y, t-s-|y|/v))\, dy \tag{5.50}$$

which was written in integral form

$$u(x,t) = \int_{-\infty}^{\infty}\int_{0}^{\infty} w(y)\eta(s) f(u(x-y, t-s-|y|/v))\, ds\, dy. \tag{5.51}$$

Here, v is the velocity of action potential propagation, therefore the time the action potential takes to travel the distance y is $|y|/v$. Also, $\eta(t) = \alpha e^{\alpha t}$ for $t > 0$ and $\eta(t) = 0$ for $t < 0$. Using the standard approach for constructing travelling wave solutions, the coordinate $\xi = x - \bar{c}t$ was introduced and solutions of the form $U(\xi, t) = u(x - \bar{c}t, t)$ were sought. In (ξ, t) coordinates, Equation (5.51) becomes

$$U(\xi,t) = \int_{-\infty}^{\infty}\int_{0}^{\infty} w(y)\eta(s) f(u(\xi - y + \bar{c}s + \bar{c}|y|/v, t-s-|y|/v))\, ds\, dy. \tag{5.52}$$

Then a travelling wave is a solution $U(\xi, t) = q(\xi)$ where

$$q(\xi) = \int_{-\infty}^{\infty}\int_{0}^{\infty} w(y)\eta(s) f(q(\xi - y + \bar{c}s + \bar{c}|y|/v)\, ds\, dy. \tag{5.53}$$

Linearising about the steady state $q(\xi)$ in $U(\xi, t) = q(\xi) + u(\xi, t)$ results in

$$\begin{aligned} u(\xi,t) = \int_{-\infty}^{\infty}\int_{0}^{\infty} & w(y)\eta(s) f'(q(\xi - y + \bar{c}s + \bar{c}|y|/v)) \\ & \times u(\xi - y + \bar{c}s + \bar{c}|y|/v, t-s-|y|/v)\, ds\, dy. \end{aligned} \tag{5.54}$$

Looking for solutions of the form $u(\xi, t) = u(\xi)e^{\lambda t}$ leads to the eigenvalue equation

$$\begin{aligned} u(\xi) = \int_{-\infty}^{\infty}\int_{\xi - y + \bar{c}|y|/v}^{\infty} & w(y)\eta\left((y - \xi + s)/\bar{c} - |y|/v\right) \\ & \times e^{-\lambda(-\xi+y+s)/\bar{c}} f'(q(s))u(s)\, ds\, dy. \end{aligned} \tag{5.55}$$

In [16] it was assumed that linear stability implies nonlinear stability. Let $\mathcal{L}$ be a linear differential operator and $\sigma(\mathcal{L})$ be the spectrum of $\mathcal{L}$. Then a travelling wave was found to be linearly stable if

$$\max\{\mathrm{Re}(\lambda) \in \sigma(\mathcal{L}), \lambda \neq 0\} \leq -K \tag{5.56}$$

with $K > 0$ and $\lambda = 0$ a simple eigenvalue of $\mathcal{L}$. Therefore linearising about the travelling wave provided the normal spectrum of the linear differential operator $\mathcal{L}$.

To find the stability of the travelling wave in [16], an Evans function was used. The Evans function was originally defined by Evans in the study of the stability of Hodgkin-Huxley type excitable nerve axon equations [30]. Evans functions are an analytic function of the eigenvalues of the linearised operator and are used to locate the essential spectrum of this operator. The zeros of an Evans function correspond to the eigenvalues and the order of the zero is the algebraic multiplicity of the eigenvalue. Evans functions have been used for the stability analysis of travelling waves in PDEs and more recently have been applied to integral neural field models. It is not always possible to find an Evans function for a nonlinear evolution equation. Usually a Heaviside firing rate function is used as this makes an explicit formulation of an Evans function possible. We apply the analysis of [16] to our model in Equations (5.1)–(5.2) with $f(u) = 2\Theta(u-\theta)$ to find a formula for the speed of travelling fronts. As in our previous study in the thesis, we assume an infinitely fast propagation velocity, so we set $v \to \infty$. We then construct an Evans function to determine the stability of the stationary fronts.

Constructing a stationary front

We begin by writing Equation (5.1) as the integral model

$$u(x,t) = \int_{-\infty}^{\infty}\int_{0}^{\infty} \eta(s)w(y)f(u(x-y,t-s))\,ds\,dy \tag{5.57}$$

where $\eta(t) = e^{-t}$ $(t > 0)$ is the Green's function of the linearised differential operator $(1 + \partial/\partial t)$, and $f(u) = 2\Theta(u-\theta)$. Writing Equation (5.57) in travelling coordinates $\xi = x - \bar{c}t$ allows the construction of travelling wave solutions of the form $U(\xi,t) = u(x-\bar{c}t,t)$

$$U(\xi,t) = \int_{-\infty}^{\infty}\int_{0}^{\infty} \eta(s)w(y)f(U(\xi-y+\bar{c}s,t-s))\,ds\,dy. \tag{5.58}$$

Let us assume that $U(\xi,t) = q(\xi)$ where $q(\xi)$ is a steady state solution. We further assume that $q(\xi)$ is a travelling front and choose $q(\xi) > \theta$ for $\xi < 0$, $q(0) = \theta$ and $q(\xi) < \theta$ for $\xi > 0$. Then travelling fronts satisfy

$$q(\xi) = \int_{-\infty}^{\infty}\int_{0}^{\infty} \eta(s)w(y)f(q(\xi-y+\bar{c}s))\,ds\,dy. \tag{5.59}$$

Let

$$\varphi(\xi) = \int_{-\infty}^{\infty} w(y)f(q(\xi-y))\,dy. \tag{5.60}$$

Thus we can rewrite Equation (5.59) as

$$q(\xi) = \int_{0}^{\infty} \eta(s)\varphi(\xi+\bar{c}s)\,ds. \tag{5.61}$$

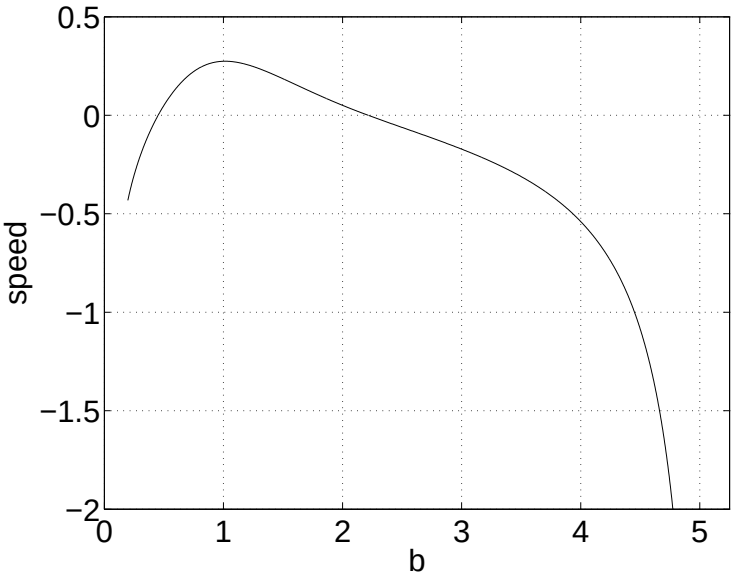

Figure 5.29: Speed of travelling fronts, $\bar{c}$, in Equation (5.59) as a function of b for $\theta = 1.5$. Stationary fronts occur at $b = 0.451, 2.215$.

From our definition of a travelling front, we know that $q(\xi - y) \geq \theta$ for $\xi - y \leq 0$, therefore, $f(q(\xi - y)) = 2$ if $\xi - y \leq 0$. So Equation (5.60) becomes

$$\varphi(\xi) = 2 \int_{\xi}^{\infty} w(y)\, dy. \tag{5.62}$$

We want to find stationary fronts so we set $\bar{c} = 0$. We also know that $q(\xi) = \theta$ at $\xi = 0$. Using Equation (5.62) and setting $\bar{c} = 0$ and $\xi = 0$ in the expression for $\varphi(\xi + cs)$, we find that

$$\varphi(0) = 2 \int_{0}^{\infty} e^{-by}(b \sin(y) + \cos(y))\, dy = \frac{4b}{b^2 + 1}. \tag{5.63}$$

Therefore Equation (5.59) is

$$q(0) = \int_{0}^{\infty} \eta(s)\varphi(0)\, ds. \tag{5.64}$$

As $q(0) = \theta$, we use Equation (5.64) to find that $\theta = 4b/(b^2 + 1)$. These are the same parameter values as in Equation (5.30) where the Hamiltonian of the fixed point $\mathbf{Z_1}$ meets the zero energy surface. Therefore stationary fronts, or heteroclinic connections, exist between the fixed point at the origin and the fixed point $\mathbf{Z_1}$ when $\theta = 4b/(b^2 + 1)$.

Using the expression for travelling fronts in Equation (5.61), we can also solve for all front speeds, $\bar{c}$. The full calculation is given in Chapter 7, Section 7.4. Figure 5.29 shows $\bar{c}$ as a function of b for $\theta = 1.5$.

Stability

The stability of the stationary fronts can be determined using the Evans function analysis of [16]. In Equation (5.58), let $U(\xi,t) = q(\xi) + u(\xi,t)$, where $u(\xi,t)$ is a perturbation to the stationary solution $q(\xi)$. By linearising about $q(\xi)$ in Equation (5.59), an expression can be found for the perturbation

$$u(\xi,t) = \int_{-\infty}^{\infty}\int_{0}^{\infty} \eta(s)w(y)f'(q(\xi-y+\bar{c}s))u(\xi-y+\bar{c}s,t-s)\,ds\,dy. \tag{5.65}$$

To find bounded continuous solutions on $\mathbb{R}$ for each fixed t, we look for solutions of the type $u(\xi,t) = u(\xi)e^{\lambda t}$, so with a change of variables in Equation (5.65), we obtain

$$u(\xi) = \int_{-\infty}^{\infty}\int_{\xi-y}^{\infty} \eta((s-\xi+y)/\bar{c})w(y)\frac{f'(q(s))}{\bar{c}}u(s)e^{\lambda(s-\xi+y)/\bar{c}}\,ds\,dy. \tag{5.66}$$

We now construct an Evans function, $\mathcal{E}(\lambda)$. λ is an eigenvalue of Equation (5.66) if and only if $\mathcal{E}(\lambda) = 0$. With a change of variables $z = q(s)$ and the fact that the origin is defined such that $q(0) = \theta$, Equation (5.66) can be written as

$$u(\xi) = \frac{u(0)}{\bar{c}|q'(0)|}\int_{-\infty}^{\infty} w(y)\eta(-\xi/\bar{c}+y/\bar{c})e^{-\lambda(y-\xi)/\bar{c}}\,dy. \tag{5.67}$$

A travelling front solution of Equation (5.57) is not necessarily monotonic, therefore q^{-1} is ill-defined. When $\xi = 0$, a self-consistent condition is found of

$$u(0) = \frac{u(0)}{\bar{c}|q'(0)|}\int_{-\infty}^{\infty} w(y)\eta(y/\bar{c})e^{-\lambda y/\bar{c}}\,dy. \tag{5.68}$$

Using this, and the fact that $\eta(t) = 0$ for $t < 0$, it is now possible to define the Evans function for the travelling front solution with $\bar{c} \geq 0$ of

$$\mathcal{E}(\lambda) = 1 - \frac{1}{\bar{c}|q'(0)|}\int_{0}^{\infty} w(y)\eta(y/\bar{c})e^{-\lambda y/\bar{c}}\,dy. \tag{5.69}$$

If $\lambda \in \mathbb{R}$, then $\mathcal{E}(\lambda) \in \mathbb{R}$. By writing $\mathcal{H}(\lambda) = \int_0^\infty w(y)\eta(y/\bar{c})e^{\lambda y/\bar{c}}\,dy$, an alternative expression for the Evans function in Equation (5.69) is found of

$$\mathcal{E}(\lambda) = 1 - \frac{\mathcal{H}(\lambda)}{\mathcal{H}(0)}. \tag{5.70}$$

For stationary fronts, $\bar{c} = 0$ and the Evans function is

$$\mathcal{E}(\lambda) = 1 - \frac{1}{1+\lambda}. \tag{5.71}$$

The only solution of $\mathcal{E}(\lambda) = 0$ is $\lambda = 0$, therefore the stationary fronts are exponentially stable. Hence, we have found stable heteroclinic connections where $\theta = 4b/(b^2+1)$.

To summarise, for a step firing rate function, Equation (5.4) has two fixed points, one the origin, $\mathbf{Z_0}$, and a nonzero one, $\mathbf{Z_1}$. Homoclinic orbits lie on the energy surfaces

$H = e,\ e \in \mathbb{R}$. Homoclinic orbits to the origin lie on the zero energy surface $H = 0$. We found that the Hamiltonian of $\mathbf{Z_1}$ crosses the level set $H = 0$ for $\theta = 4b/(b^2+1)$ which are the same values of b where the solution curve breaks (see Chapter 4). We conjectured that heteroclinic orbits existed between the two fixed points $\mathbf{Z_0}$ and $\mathbf{Z_1}$. We proved this by finding a conjugate system in Section 5.4. As heteroclinic orbits are stationary fronts, we have also taken a different approach to proving our conjecture. By linearising about a travelling wave and using Evans functions to find the isolated eigenvalues, we found stable stationary fronts at $\theta = 4b/(b^2+1)$. These stationary fronts are heteroclinic connections from the fixed point at the origin to the fixed point $\mathbf{Z_1}$, thereby confirming our conjecture again.

Hence, the breaks in the solution curve occur at the same values of b for which both stationary fronts exist and the Hamiltonian of the nonzero fixed point $\mathbf{Z_1}$ crosses the level set $H = 0$. There is some kind of global bifurcation where homoclinic orbits to $\mathbf{Z_1}$ meet homoclinic orbits to the zero fixed point, $\mathbf{Z_0}$. These results can be seen quite clearly in Figure 5.30, providing two very different approaches to explaining the discontinuity in the upper solution curve in the top plot.

Smooth firing rate function

In Section 5.4 we found discontinuities in the solution curve for Equations (5.4) with three different types of firing rate function for certain regions of parameter space. At the breakpoints of the discontinuities, heteroclinic orbits join the fixed point at the origin to another fixed point. Our conjecture is that there are travelling fronts in the region of discontinuity. To explore this, we examine the full system written in a moving coordinate frame.

Constructing a travelling front

We write the full, time-dependent system of Equation (5.1) with the smooth firing rate function in Equation (5.3) in the form

$$\left(\frac{\partial^4}{\partial x^4} + 2(1-b^2)\frac{\partial^2}{\partial x^2} + (b^2+1)^2\right)\left(1 + \frac{\partial}{\partial t}\right)u = 4b(b^2+1)f(u). \tag{5.72}$$

In moving coordinates $\eta = x - \hat{c}t$, where $\hat{c}$ is the speed, Equation (5.72) becomes the fifth-order ODE

$$\hat{c}\frac{d^5u}{d\eta^5} - \frac{d^4u}{d\eta^4} + 2\hat{c}(1-b^2)\frac{d^3u}{d\eta^3} + 2(b^2-1)\frac{d^2u}{d\eta^2} + \hat{c}(b^2+1)^2\frac{du}{d\eta} - (b^2+1)^2u = -4b(b^2+1)f(u). \tag{5.73}$$

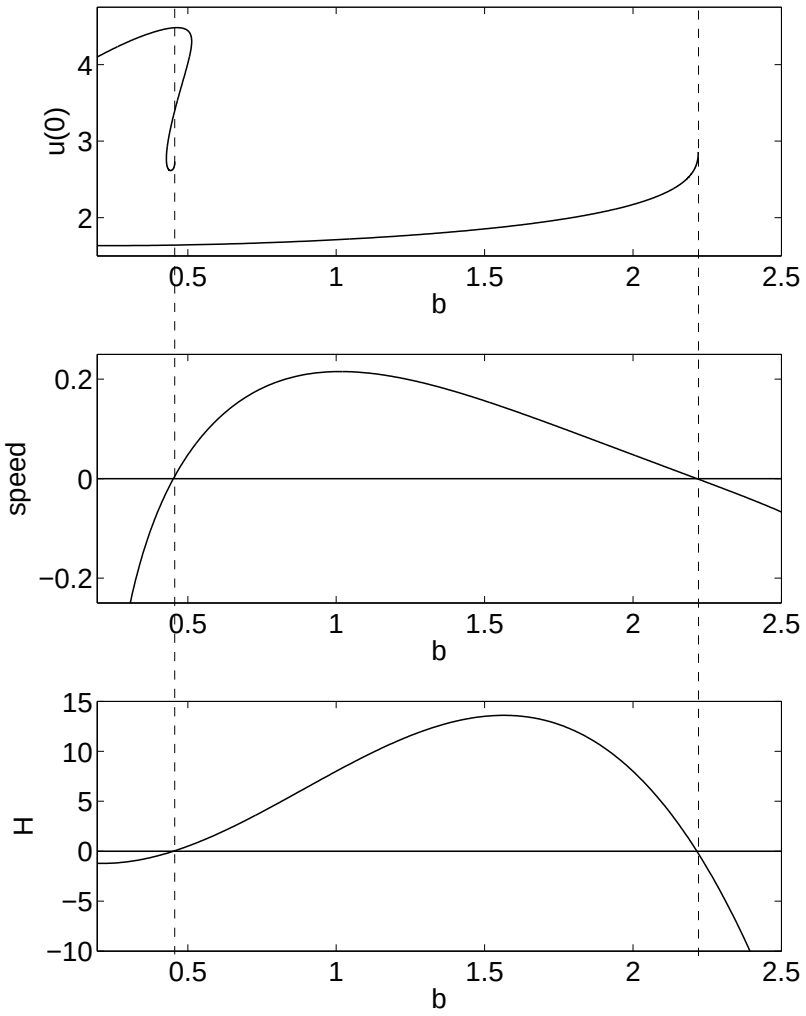

Figure 5.30: Top: Solution curve for 1-bump solutions of Equation (5.27) showing breaks at $b = 0.451, 2.215$. Middle: Speed of travelling fronts, $\bar{c}$, from the nonzero fixed point, $\mathbf{Z_1}$, to the zero fixed point, $\mathbf{Z_0}$. At the breakpoints, $\bar{c} = 0$, stationary fronts exist. These are heteroclinic orbits. Bottom: The Hamiltonian of the nonzero fixed point $\mathbf{Z_1}$ crosses the level set $H = 0$ at the breakpoints also.

When $\hat{c} = 0$ this reverts to the ODE in Equation (5.4), as expected. Writing Equation (5.73) as a system of first order equations where $v_0 = u$, we obtain

$$\begin{aligned} v_0' &= v_1 \\ v_1' &= v_2 \\ v_2' &= v_3 \\ v_3' &= v_4 \\ v_4' &= [v_4 + 2(1-b^2)v_2 + (b^2+1)^2 v_0 - 4b(b^2+1)f(v_0)]/\hat{c} \\ &\qquad -(b^2+1)^2 v_1 - 2(1-b^2)v_3. \end{aligned} \tag{5.74}$$

The system in Equation (5.74) has the Jacobian matrix

$$\mathbf{J} = \begin{pmatrix} 0 & 1 & 0 & 0 & 0 \\ 0 & 0 & 1 & 0 & 0 \\ 0 & 0 & 0 & 1 & 0 \\ 0 & 0 & 0 & 0 & 1 \\ n_1 & -(b^2+1)^2 & 2(1-b^2)/\hat{c} & -2(1-b^2) & 1/\hat{c} \end{pmatrix} \tag{5.75}$$

where $n_1 = (b^2+1)(b^2+1-4bf')/\hat{c}$ and

$$f' = \frac{df(v_0)}{dv_0} = \frac{4r}{(v_0-\theta)^3} e^{-r/(v_0-\theta)^2} \Theta(v_0-\theta). \tag{5.76}$$

The eigenvalues of the Jacobian for the fixed point at the origin are $1/\hat{c}, \pm(b \pm i)$. Singular perturbation theory is required to continue the analysis. We note the problem as a project for future study.

5.6 Conclusion

In this chapter we wrote the four-dimensional ODE describing steady states of the Amari model with decaying oscillatory coupling function as a reversible Hamiltonian system. We found that both symmetric and asymmetric homoclinic orbits to the fixed point at the origin are of co-dimension zero in our system. We then described a numerical technique that reduced the problem of finding single-bump symmetric and asymmetric homoclinic orbits of the system with smooth firing rate function to finding the zeros of a real function. Using this numerical technique, we found both symmetric and asymmetric single-bump homoclinic orbits to the fixed point at the origin. We discovered a small separate solution curve of symmetric single-bump homoclinic orbits inside the main single-bump solution curve for a sufficiently steep firing rate function, $f(u)$. As $f(u)$ continued to steepen, the

small curve met the main curve and caused it to break. The solution curve terminated in spirals on both sides of the break. As $f(u)$ steepened further, the gap widened. The small curve was not found by numerical analysis in Chapter 3 as it is a separate curve from the main solution curve previously found in [70]. It could only be discovered here because we had a numerical technique which found all symmetric and asymmetric single-bump homoclinic orbits for chosen parameter values. By exploring different regions of parameter space, we were able to determine that another solution curve existed.

Homoclinic orbits to the origin lie on the zero energy surface. The zero energy surface is where the Hamiltonian function is zero. Generically, nonzero fixed points do not lie on the zero energy surface. However, by looking at other nonzero fixed points of our system and using level set analysis, we found that homoclinic orbits to a nonzero fixed point met homoclinic orbits to the origin. That is, homoclinic orbits to the nonzero fixed points lie on the zero energy surface for particular parameter values. For a step $f(u)$, the parameter values for which homoclinic orbits to a nonzero fixed point meet the zero energy surface occur at the same parameter values as the terminating ends of the break in the upper solution curve. The same phenomenon was observed for both a piecewise linear $f(u)$ and a smooth $f(u)$ when $f(u)$ was sufficiently steep and the threshold was at an appropriate level. For the step $f(u)$, we found a relationship between the threshold and the parameter values of the breakpoints in the curve. For the piecewise linear $f(u)$ we were able to determine a relationship between the threshold, the steepness of $f(u)$ and the parameter values of the breakpoints in the curve. For the smooth $f(u)$, the parameter values correspond to the breaks in the main curve or the endpoints of a small separate solution curve, depending upon the steepness of $f(u)$.

For the system with step firing rate function we used a change of variables to find a conjugate system for which solutions were homoclinic orbits to the nonzero fixed point. Using the conjugate system we found heteroclinic connections between the origin and the nonzero fixed point of the system. We also found these heteroclinic connections by taking a travelling wave approach. By writing the time-dependent system with step $f(u)$ in moving coordinates we found stationary fronts at two parameter values. Using an Evans function, we found these stationary fronts were stable. The stationary fronts are the heteroclinic connections between the two fixed points of the system. In both cases, the heteroclinic orbits occur at the parameter values at which the solution curve breaks. We also briefly discussed possible future study on travelling fronts in the region of discontinuity in the solution curves. Singular perturbation theory would be required.

For all three types of firing rate functions, we found this generic phenomenon where the solution curve breaks and homoclinic orbits are destroyed in some kind of bifurcation as the firing rate function steepens. We highlight the determination of what happens at this bifurcation point as a project for future study. It appears that each break of the solution curve terminates in a spiral. Future study would include seeing what happens at the limit point of the spirals as we expect there to be some kind of bifurcation.

In this chapter, only the Amari model is analysed. We note that the analysis could be extended to the gap junction model. Steady states of the gap junction model are represented by a sixth-order ODE. If the sixth-order ODE can also be written as a reversible Hamiltonian system, the analysis will be far more complex than that of the fourth-order system.

We summarise the new phenomena discovered in this chapter:

- Using a numerical technique, we discovered a small solution curve inside the main solution curve for a sufficiently steep smooth firing rate function. The small solution curve has not been previously described in the literature.
- The small separate solution curve merges with the main curve as the smooth firing rate function steepens, causing the main curve to break in some kind of bifurcation.
- At each end of the break of the main solution curve there appears to be a spiral.
- Heteroclinic orbits are formed between the fixed point at the origin and a nonzero fixed point at the endpoints of the spirals.
- As the smooth firing rate function becomes flatter, the small separate solution curve eventually disappears.

Chapter 6

Finding asymmetric solutions

6.1 Introduction

In this chapter we present three different numerical methods that could be used to find asymmetric homoclinic orbits to the fixed point at the origin in the Amari model

$$\frac{\partial u(x,t)}{\partial t} = -u(x,t) + \int_{-\infty}^{\infty} w(x-y) f(u(y,t))\, dy \tag{6.1}$$

with the decaying oscillatory coupling function

$$w(x) = e^{-b|x|}\left(b\sin(|x|) + \cos(x)\right) \tag{6.2}$$

and smooth firing rate function

$$f(u) = 2e^{-r/(u-\theta)^2}\Theta(u-\theta). \tag{6.3}$$

As before, $\Theta(u)$ is the Heaviside function and the model has parameters $b, r, \theta > 0$. A fourth method for a piecewise firing rate function is also presented. Certain models, such as those describing cortical connectivity, assume asymmetric lateral connections [108]. For our study, we assume symmetric connectivity only, as given by Equation (6.2).

In the thesis so far, we have mainly found symmetric homoclinic orbits of both the Amari model and the gap junction model. In Chapter 5, by writing the Amari model in its reversible Hamiltonian form and developing a numerical technique, we found single-bump asymmetric homoclinic orbits. In the current chapter, two of the four methods are used to successfully find asymmetric orbits. The study is not limited to single-bump solutions.

The chapter is organised as follows. First, the use of numerical integration techniques to find stable asymmetric solutions is explained. Second, Newton's method for nonlinear

systems of equations is used to explore a particular region of parameter space. Thirdly, using the Hamiltonian structure of the system, a shooting method is constructed. Lastly, the method of piecewise construction of asymmetric homoclinic orbits is briefly discussed.

6.2 Numerical integration

In principle, steady states of Equations (6.1)–(6.3) can be found by numerically integrating with an initial condition to a steady state. The model in Equation (6.1) is defined on an infinite domain, however, computational methods require a finite domain. As in Chapter 3, we must approximate an infinite domain by choosing a finite domain sufficiently large that there is no activity near the boundaries. A finite domain of Ω: $[-10\pi, 10\pi]$ is used. An explicit method of numerical integration (see Appendix) is used for finding steady state solutions of Equations (6.1)–(6.3).

To find asymmetric solutions, an asymmetric initial condition is used. By fixing b, r and θ in Equations (6.2) and (6.3) and defining an initial profile on the domain Ω, numerical integration can be performed in MATLAB [74]. As $t \to \infty$, the initial condition evolves to a stable steady state. The steady state can be a zero solution, a symmetric solution or an asymmetric solution. To find a nonzero steady state solution, a stable nonzero solution must exist and the initial condition must be close enough to the attracting steady state. Although various initial conditions were used with numerical integration in different regions of parameter space, no stable asymmetric solutions were found.

As numerical integration only finds stable solutions, other methods must be used to find unstable solutions. A stable solution found using numerical integration can be used as a starting solution with continuation methods. The two methods presented in the next sections can be used to find both stable and unstable solutions.

6.3 Newton's method

Asymmetric homoclinic orbits of the Amari model can be found using Newton's method [60]. The advantage of the method is its speed as it has quadratic convergence, provided the initial guess is sufficiently close to the true solution. In Chapter 3, we derived the fourth-order ODE

$$\begin{cases} u^{(iv)} + 2(1-b^2)u'' + (b^2+1)^2 u = 4b(b^2+1)f(u), \\ \lim\limits_{x\to\pm\infty}(u,\, u',\, u'',\, u''') = (0,0,0,0) \end{cases} \tag{6.4}$$

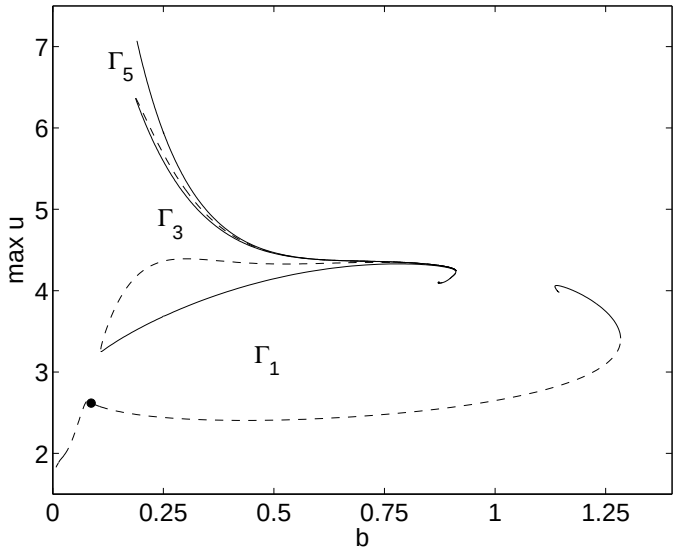

Figure 6.1: Solution curves for Equations (6.1)–(6.3) where $r = 0.085$, $\theta = 1.5$ and b is the continuation parameter. Solutions to the left of the solid circle are N-bump solutions where $N > 1$. Γ_1, Γ_3 and Γ_5 are 1-, 3- and 5-bump solutions respectively. Solid line: stable solutions; dashed line: unstable solutions. Figure first presented in Chapter 3.

where $f(u)$ is the firing rate function. Solutions of Equation (6.4) are steady states of the Amari model in Equations (6.1)–(6.3). We are interested in solutions of Equation (6.4) that are asymmetric homoclinic orbits to the bi-focus fixed point $(u, u', u'', u''') = (0, 0, 0, 0)$.

In Chapter 3, changes were seen in the stable solutions for the smooth firing rate function with $r = 0.085$ and $\theta = 1.5$. Stable N-bump solutions were not found in a small region around $b = 1$ (see Figure 6.1). The solutions on the curve on either side of this region are "dimple" bumps. We set $b = 0.875$ in Equation (6.2) and $r = 0.085$ and $\theta = 1.5$ in Equation (6.3). Discretising the finite domain Ω and using the ODE in Equation (6.4), Newton's method is applied to an initial condition. A 2-bump asymmetric solution is found (see Figure 6.2). Using the solution in Figure 6.2 as a starting solution with AUTO 2000 [23], the solution curve in the top plot of Figure 6.3 is found. At $b = 0.5225$, the solution is an asymmetric 1-bump solution with a very pronounced asymmetric "dimple". As b increases, this "dimple" falls below the threshold to create a 2-bump solution. The bottom plot in Figure 6.3 shows solutions for three values of b on the solution curve in the top plot. Each solution creates another asymmetric orbit under the transformation $x \to -x$. The solution curve in Figure 6.3 was also found in Chapter 5 by using a numerical technique we developed (see Figures 5.16 and 5.17). Numerical simulation suggests that the asymmetric orbits are unstable. In Figure 6.4, the family of unstable 2-bump asymmetric orbits from Figure 6.3 is shown by the dashed line labeled Γ_2^A. The labels

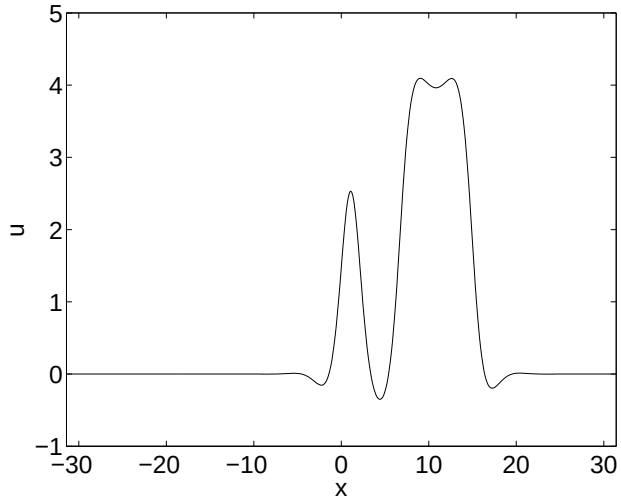

Figure 6.2: Two-bump asymmetric solution found using Newton's method. Parameter values are $b = 0.8725$, $r = 0.085$ and $\theta = 1.5$.

Γ_1, Γ_3 and Γ_5 indicate families of symmetric 1-, 3- and 5-bump solutions respectively.

6.4 A shooting method

Shooting methods can be used for the direct numerical computation of homoclinic orbits. Such methods have been used to find solutions of a fourth-order ODE (containing even order derivatives only and a given nonlinear function) derived from the Swift-Hohenberg equation and the Extended Fisher-Kolmogorov equation [80]. Shooting methods have also been applied to reversible Hamiltonian systems. A specific example is the fourth-order ODE used to model an elastic strut [13]. Steady state solutions of the Amari model are solutions of the fourth-order ODE in Equation (6.4). The ODE is a reversible Hamiltonian system. We use the structure of the system to develop a shooting method to find asymmetric solutions of the Amari model.

Method

We now develop a numerical method for finding homoclinic orbits to the fixed point at the origin, $(u, u', u'', u''') = (0, 0, 0, 0)$, as $x \to \pm\infty$. Such orbits are solutions of the fourth-order ODE in Equation (6.4). The ODE has the reversibility

$$R\colon (x, u, u', u'', u''') \to (-x, u, -u', u'', -u'''). \tag{6.5}$$

Our interest lies in asymmetric orbits. In this chapter, we will refer to homoclinic orbits as meaning homoclinic orbits to the origin. The trajectory of a homoclinic orbit tends to the

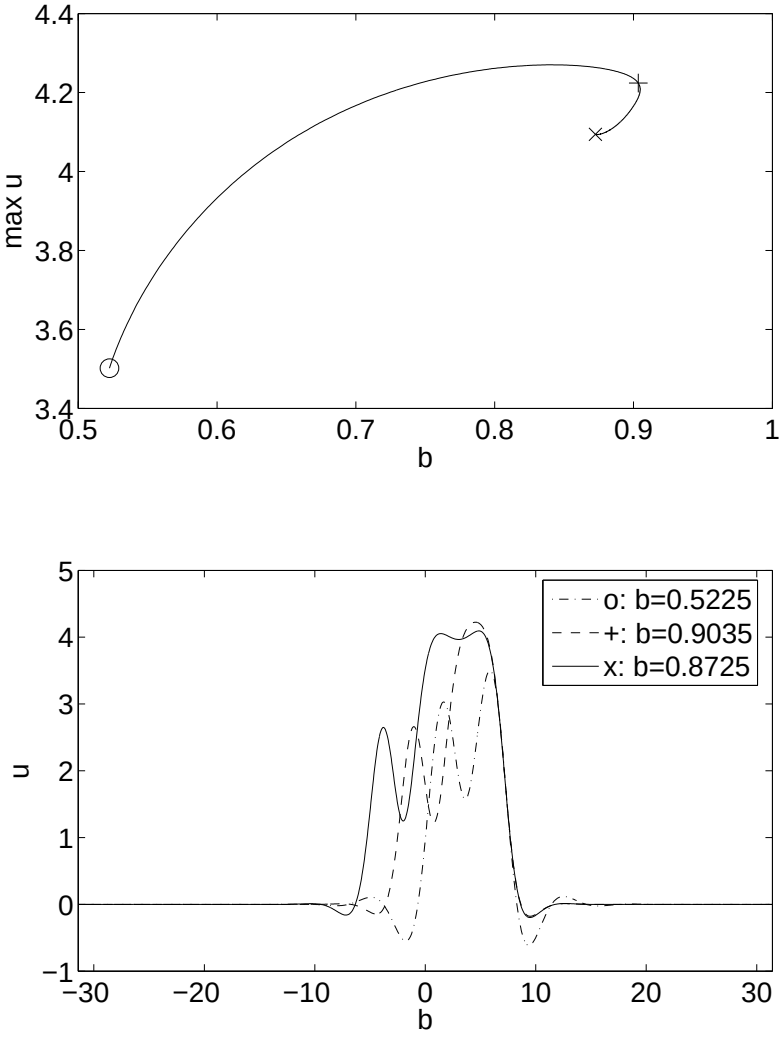

Figure 6.3: Top: Solution curve of asymmetric solutions for parameter values $(r, \theta) = (0.085, 1.5)$ using the solution in Figure 6.2 as the starting solution at $b = 0.8725$. Bottom: Solutions at the values of b indicated by the symbols in the top plot.

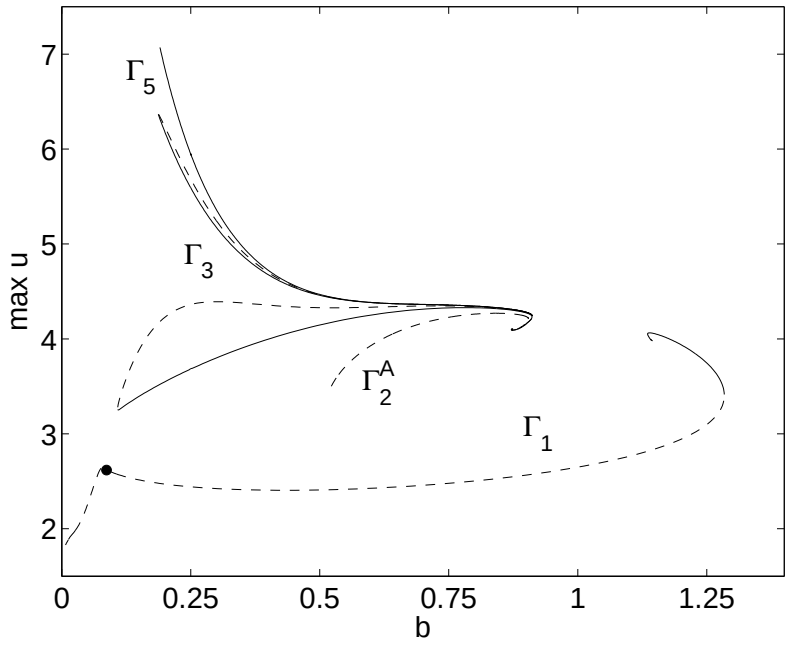

Figure 6.4: Solution curves of Equations (6.1)–(6.3) with $(r, \theta) = (0.085, 1.5)$. The solution curve labelled Γ_2^A is the family of asymmetric solutions in the top plot of Figure 6.3. Solid line: stable solutions; dashed line: unstable solutions.

fixed point as x goes to both plus infinity and minus infinity. So once we find any point lying on a homoclinic orbit, we can calculate the entire orbit. We use a shooting method with different "initial conditions" and see if any of these lie on a homoclinic orbit. The shooting method numerically integrates an initial condition at $x = 0$ both forwards and backwards until the two trajectories cross the threshold from above. If the endpoint of the trajectory for $x \leq 0$ lies on the unstable manifold of the fixed point and the endpoint of the trajectory for $x \geq 0$ lies on the stable manifold of the fixed point, then the initial condition lies on a homoclinic orbit to the origin. The initial condition is chosen so that any such homoclinic orbit is likely to be asymmetric. We denote the unstable manifold of the fixed point by W^u and the stable manifold of the fixed point by W^s.

As discussed in Chapter 5, the system given by the ODE in Equation (6.4) is a reversible Hamiltonian system. Also, homoclinic orbits to the origin lie on the zero energy surface, $H = 0$, where H is the Hamiltonian. In Chapter 5, the Hamiltonian of the system in Equation (6.4) was defined in two different ways. We are interested in the form in Equation (5.13) of

$$H(u, u', u'', u''') = u'u''' - \frac{1}{2}(u'')^2 + (1 - b^2)(u')^2 + \frac{(b^2 + 1)^2}{2}u^2 + G(u) \qquad (6.6)$$

where

$$G(u) = -\frac{8b}{(b^2+1)} \int_0^u e^{-r/(s-\theta)^2} \Theta(s-\theta)\, ds. \tag{6.7}$$

Let Σ_0 be the 2-dimensional section

$$\Sigma_0 = \{(u, u', u'', u''') \,|\, u' = 0,\, u'' > 0,\, u''' > 0,\, H = 0\}. \tag{6.8}$$

Let Σ_1 be the 2-dimensional section

$$\Sigma_1 = \{(u, u', u'', u''') \,|\, u = \theta,\, u' < 0,\, H = 0\}. \tag{6.9}$$

Let Σ_2 be the 2-dimensional section

$$\Sigma_2 = \{(u, u', u'', u''') \,|\, u = \theta,\, u' > 0,\, H = 0\}. \tag{6.10}$$

Define a vector $\mathbf{y}_i \in \mathbb{R}^4$ as $\mathbf{y}_i(x) = (u_i(x), u_i'(x), u_i''(x), u_i'''(x))$ for $i = 0, 1, 2$. We choose an initial condition $\mathbf{y}_0 = \big(u(0), 0, u''(0), u'''(0)\big) \in \Sigma_0$. Substituting for $u'(0) = 0$ and rearranging Equation (6.6), we find

$$u''(0) = \pm\sqrt{2G(u(0)) + (b^2+1)^2 u^2(0)}. \tag{6.11}$$

We choose $u''(0) > 0$. If $u'''(0) = 0$, then the invariance of solutions under the transformation $x \to -x$ ensures the trajectory is symmetric about $x = 0$. As asymmetric solutions are sought, we must have $u'''(0) \neq 0$. We choose to set $u'''(0) > 0$.

Two mappings are now defined, one for $x \geq 0$ and another for $x \leq 0$. The mapping $\mathcal{P}_+$ is defined on $x \geq 0$ such that

$$\mathcal{P}_+ \colon \Sigma_0 \to \Sigma_1, \qquad \forall \mathbf{y_0} \in \Sigma_0. \tag{6.12}$$

The mapping $\mathcal{P}_-$ is defined on $x \leq 0$ such that

$$\mathcal{P}_- \colon \Sigma_0 \to \Sigma_2, \qquad \forall \mathbf{y_0} \in \Sigma_0. \tag{6.13}$$

Let $\mathbf{y}_1 = \mathcal{P}_-(\mathbf{y}_0) \in \Sigma_1$ and $\mathbf{y}_2 = \mathcal{P}_+(\mathbf{y}_0) \in \Sigma_2$. See Figure 6.5 for a schematic of the mappings $\mathcal{P}_+$ and $\mathcal{P}_-$.

From the definition of the vector $\mathbf{y}_i$, u_0, u_1 and u_2 are the u components of $\mathbf{y}_0, \mathbf{y}_1$ and $\mathbf{y}_2$ respectively. In Figure 6.6 we show a schematic of the flow of in both spatial directions from an initial condition $u_0 < \theta$ to the threshold, θ. The solution for $x > 0$ meets the threshold at $x = x_1$, that is, $u_1(x_1) = \theta$. Similarly, the solution for $x < 0$ meets the threshold at $x = x_2$, that is, $u_2(x_2) = \theta$. If $u_0 > \theta$, only 1-bump solutions can be found as the mappings $\mathcal{P}_+, \mathcal{P}_-$ are defined for the first time the trajectories in both directions cross

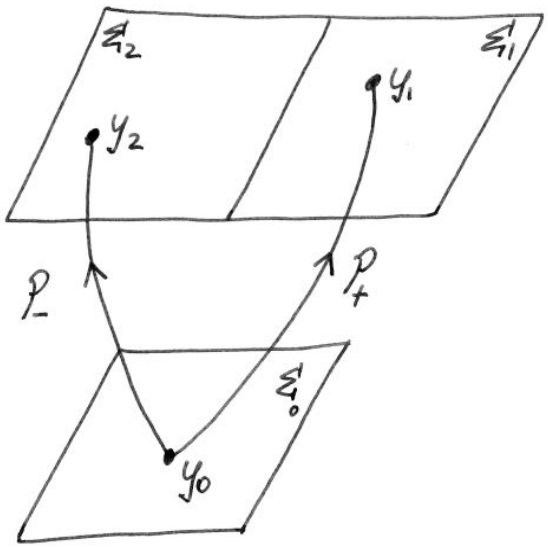

Figure 6.5: Schematic of the mapping $\mathcal{P}_+$ in Equation (6.12) from $\mathbf{y}_0 \in \Sigma_0$ to $\mathbf{y}_1 \in \Sigma_1$ for $x \geq 0$ and the mapping $\mathcal{P}_-$ in Equation (6.13) from $\mathbf{y}_0 \in \Sigma_0$ to $\mathbf{y}_2 \in \Sigma_2$ for $x \leq 0$.

$u = \theta$ from above. If $u_0 < \theta$, only 2-bump solutions can be found. A homoclinic orbit satisfies a linear ODE on the interval $(-\infty, x_2]$ and on the interval $[x_1, \infty)$, therefore we study only the trajectory shown in Figure 6.6. If $\mathbf{y}_1$ lies on W^s and $\mathbf{y}_2$ lies on W^u, then the initial condition $\mathbf{y}_0$ lies on a homoclinic orbit to the origin.

We check if $\mathbf{y}_1$ lies on W^s. The ODE in Equation (6.4) has the eigenvalues $\pm b \pm i$ so W^s is two-dimensional. Given that $(u, u', u'', u''') \to (0, 0, 0, 0)$ as $x \to \infty$, W^s is

$$U_s(x) = e^{-bx}\big(C_1 \cos(x) + C_2 \sin(x)\big) + e^{bx}\big(D_1 \cos(x) + D_2 \sin(x)\big) \tag{6.14}$$

where $C_1, C_2, D_1, D_2 \in \mathbb{R}$. We know that $u_1(x_1) = \theta$. If $\mathbf{y}_1$ lies on W^s, then the coefficients of the growth terms, D_1, D_2 are zero and there exist $C_1, C_2 \in \mathbb{R}$ such that

$$[U_s(x_1); U_s'(x_1); U_s''(x_1); U_s'''(x_1)] = \mathbf{y}_1. \tag{6.15}$$

We calculate the lefthand side of Equation (6.15). Define the following four 4×1 vectors

$$\mathbf{J}_A = e^{-bx} \begin{pmatrix} \cos(x) \\ -b\cos(x) - \sin(x) \\ (b^2 - 1)\cos(x) + 2b\sin(x) \\ (3b - b^3)\cos(x) + (1 - 3b^2)\sin(x) \end{pmatrix}, \tag{6.16}$$

$$\mathbf{J}_B = e^{-bx} \begin{pmatrix} \sin(x) \\ \cos(x) + -b\sin(x) \\ -2b\cos(x) + (b^2 - 1)\sin(x) \\ (3b^2 - 1)\cos(x) + (3b - b^3)\sin(x) \end{pmatrix}, \tag{6.17}$$

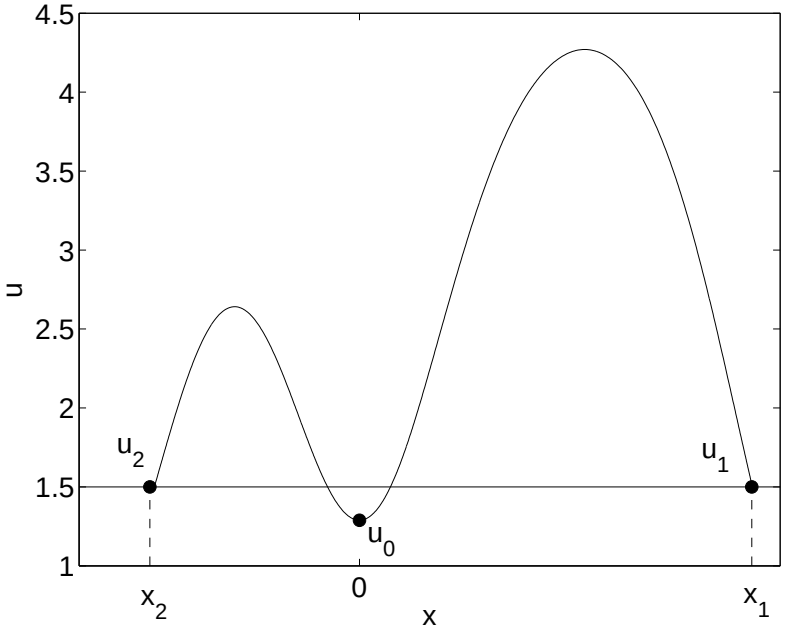

Figure 6.6: A schematic of the flow in both directions from an initial condtion $u_0 = u(0)$ where $u'(0) = 0, u''(0) > 0$ and $u'''(0) > 0$. The solution meets the threshold $\theta = 1.5$ from above at x_1 and x_2. Hence, $u_1(x_1) = u_2(x_2) = \theta$.

$$\mathbf{J}_C = e^{bx} \begin{pmatrix} \cos(x) \\ b\cos(x) - \sin(x) \\ (b^2-1)\cos(x) - 2b\sin(x) \\ (b^3-3b)\cos(x) + (1-3b^2)\sin(x) \end{pmatrix}, \tag{6.18}$$

$$\mathbf{J}_D = e^{bx} \begin{pmatrix} \sin(x) \\ \cos(x) + b\sin(x) \\ 2b\cos(x) + (b^2-1)\sin(x) \\ (3b^2-1)\cos(x) + (b^3-3b)\sin(x) \end{pmatrix}. \tag{6.19}$$

Let $\mathbf{J}_1$ be the 4×4 matrix

$$\mathbf{J}_1 = \begin{bmatrix} \mathbf{J}_A & \mathbf{J}_B & \mathbf{J}_C & \mathbf{J}_D \end{bmatrix}_{x=x_1}. \tag{6.20}$$

Then

$$\begin{pmatrix} U_s \\ U_s' \\ U_s'' \\ U_s''' \end{pmatrix}_{x=x_1} = \mathbf{J}_1 \begin{pmatrix} C_1 \\ C_2 \\ D_1 \\ D_2 \end{pmatrix} \tag{6.21}$$

and Equation (6.15) can be written as

$$\begin{pmatrix} C_1 \\ C_2 \\ D_1 \\ D_2 \end{pmatrix} = \mathbf{J}_1^{-1}\mathbf{y}_1. \tag{6.22}$$

We solve for the four unknowns C_1, C_2, D_1, D_2 in Equation (6.22). If $D_1 = D_2 = 0$ and there exist $C_1, C_2 \in \mathbb{R}$ such that Equation (6.22) has a solution, then $\mathbf{y}_1$ lies on W^s.

We now follow similar analysis to check if $\mathbf{y}_2$ lies on W^u, the two-dimensional unstable manifold. Given that $(u, u', u'', u''') \to (0, 0, 0, 0)$ as $x \to -\infty$, W^u is

$$U_u(x) = e^{bx}\big(C_3\cos(x) + C_4\sin(x)\big) + e^{-bx}\big(D_3\cos(x) + D_4\sin(x)\big) \tag{6.23}$$

where $C_3, C_4, D_3, D_4 \in \mathbb{R}$. We know that $u_2(x_2) = \theta$. If $\mathbf{y}_2$ lies on W^u, then the coefficients of the decay terms, D_3, D_4, are zero and there exist $C_3, C_4 \in \mathbb{R}$ such that

$$[U_u(x_2); U_u'(x_2); U_u''(x_2); U_u'''(x_2)] = \mathbf{y}_2. \tag{6.24}$$

Using J_A, J_B, J_C, J_D in Equations (6.16)–(6.19), we define $\mathbf{J}_2$ to be the 4×4 matrix

$$\mathbf{J}_2 = \Big[\ \mathbf{J}_C \quad \mathbf{J}_D \quad \mathbf{J}_A \quad \mathbf{J}_B\ \Big]_{x=x_2}. \tag{6.25}$$

Then the lefthand side of Equation (6.24) becomes

$$\begin{pmatrix} U_u \\ U_u' \\ U_u'' \\ U_u''' \end{pmatrix}_{x=x_2} = \mathbf{J}_2 \begin{pmatrix} C_3 \\ C_4 \\ D_3 \\ D_4 \end{pmatrix} \tag{6.26}$$

and we write Equation (6.24) in the form

$$\begin{pmatrix} C_3 \\ C_4 \\ D_3 \\ D_4 \end{pmatrix} = \mathbf{J}_2^{-1}\mathbf{y}_2. \tag{6.27}$$

We solve for C_3, C_4, D_3, D_4 in Equation (6.27). If $D_3 = D_4 = 0$ and there exist $C_3, C_4 \in \mathbb{R}$ such that Equation (6.27) has a solution then $\mathbf{y}_2$ lies on W^u.

Hence, the initial condition $\mathbf{y}_0$ lies on a homoclinic orbit if both Equation (6.22) and Equation (6.27) have solutions where $D_1 = D_2 = D_3 = D_4 = 0$. Computationally, an

initial condition, $\mathbf{y}_0$, is chosen. The coefficients C_1–C_4 and D_1–D_4 in Equations (6.14) and (6.23) are found by solving Equations (6.22) and (6.27). We calculate the square root of the sum of squares of the coefficients $D_1 = D_2 = D_3 = D_4$:

$$s = \sqrt{D_1^2 + D_2^2 + D_3^2 + D_4^2}. \tag{6.28}$$

A minimisation routine is then used to find the values of $u(0)$ and $u'''(0)$ such that s is minimised. If s is zero then the initial condition $\mathbf{y}_0$ lies on a homoclinic orbit.

The shooting method described above was coded in MATLAB [74]. The minimisation routine *fminsearch* in MATLAB is used to search for the values of $u(0)$ and $u'''(0)$ that make s in Equation (6.28) as small as possible. In computations, the minimisation routine was found to be very sensitive to small changes in b in some regions of parameter space. The routine was more successful in finding an asymmetric solution if the parameter b was allowed to vary slightly. A solution could then be found in a sufficiently small neighbourhood of the initial value of b. Thus the minimisation routine searches $(u(0), u''(0), b)$ space.

Results

To find an asymmetric orbit, parameters b, r and θ are set to particular values. We search for two-bump asymmetric solutions so we choose an initial condition $\mathbf{y}_0$ with $u_0 < \theta$. Two-bump asymmetric orbits were found at $(r, \theta) = (0.085, 1.5)$. See Figure 6.7. In Section 6.3, a 2-bump asymmetric solution was found using Newton's method. Continuation methods found the solution curve of asymmetric solutions in Figure 6.4. Applying continuation methods to the solutions in Figure 6.7 results in the same solution curve as in Figure 6.4. This curve was also found in Chapter 5 using a different numerical technique that we developed, see Figures 5.16 and 5.17.

The reversibility of the system given in Equation (6.5) means that asymmetric orbits come in pairs where each orbit is the reversal in space of the other. So the third derivative in the initial condition of one will be of the same magnitude but opposite sign in the other. We therefore plot $u'''(0)$ as a function of b for the family of asymmetric solutions in Figure 6.7 and the 1-bump symmetric solutions shown in Figure 6.1 (see Figure 6.8). Symmetric orbits are given by $u'''(0) = 0$. Asymmetric orbits are given by $u'''(0) \neq 0$.

The method above has been used to find 2-bump asymmetric solutions only. Continuation methods found a small parameter region where 1-bump asymmetric solutions also exist. We expect that there are many more asymmetric solutions than those given in

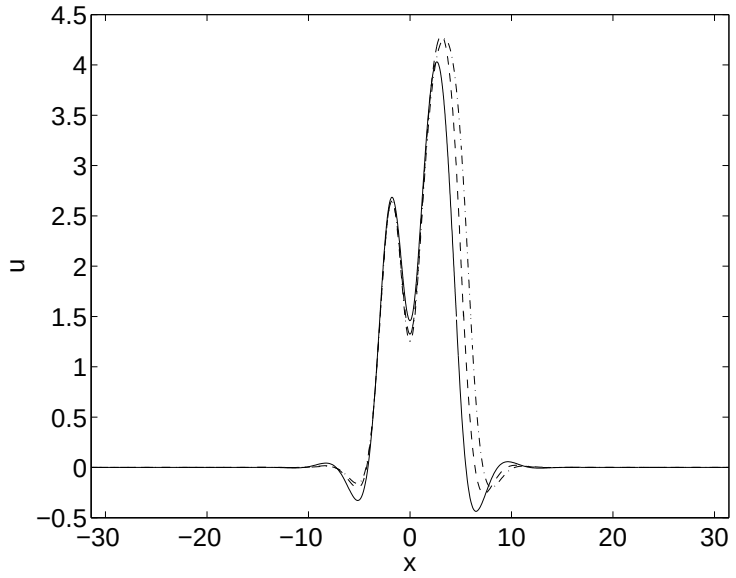

Figure 6.7: Asymmetric orbits at $(r, \theta) = (0.085, 1.5)$ found using the shooting method. The values of b for the widest to narrowest solution are 0.8725, 0.80 and 0.65 respectively.

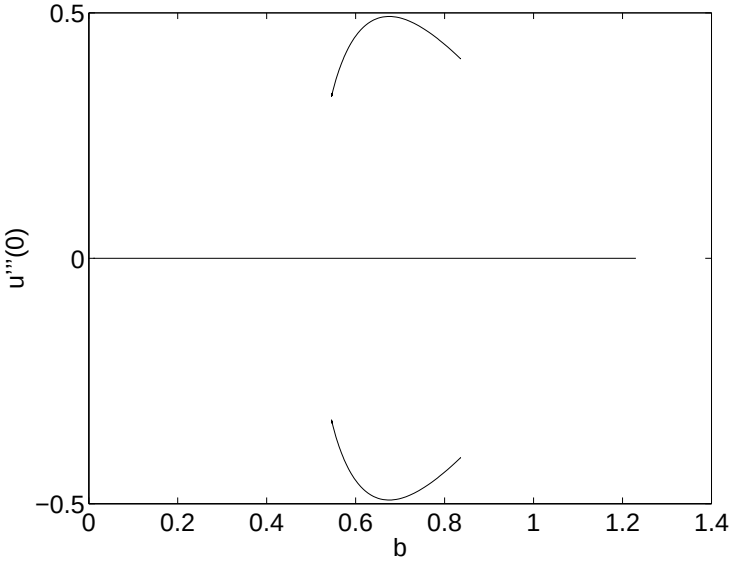

Figure 6.8: $u'''(0) = 0$ defines symmetric solutions where $x = 0$ denotes a turning point on the nonlinear part of a homoclinic orbit. Asymmetric orbits exist when $u'''(0) \neq 0$ and come in pairs due to system invariance under the transformation $x \to -x$.

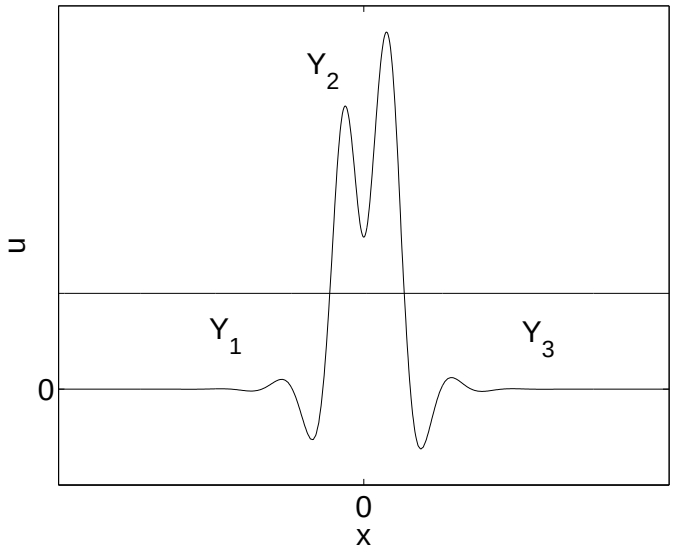

Figure 6.9: Piecewise construction of an asymmetric single-bump solution of the Amari model with step firing rate function. The threshold is indicated by the horizontal line. Three functions, Y_1, Y_2 and Y_3, create two sets of matching conditions at the threshold.

Figure 6.8. Other N-bump asymmetric solutions can be found by varying the number of times the trajectories in each spatial direction are permitted to cross the threshold from above.

6.5 Piecewise construction

In Chapters 2 and 4, a piecewise differential framework was used to construct symmetric single-bump solutions to both the Amari model and the gap junction model. The symmetry of solutions under the transformation $x \to -x$ permitted construction of one half of the solution only. The solution was centred at $x = 0$ and the solution was constructed for $x \geq 0$. A similar method of construction can be used to construct asymmetric solutions. Given that asymmetric solutions have no axis of symmetry, however, asymmetric solutions must be constructed over the entire domain. The method can only be used where the ODE can be solved analytically. The smooth firing rate function from Chapter 3 is a special case and the method does not work for this. To solve the ODE analytically, a piecewise linear firing rate function is used. For the Amari model with decaying oscillatory coupling function, an asymmetric steady state solution, $u(x)$, is a solution of the fourth-order ODE in Equation (6.4).

If a step firing rate function is assumed, three functions are required to construct an asymmetric single-bump solution using a piecewise differential framework. See Figure 6.9

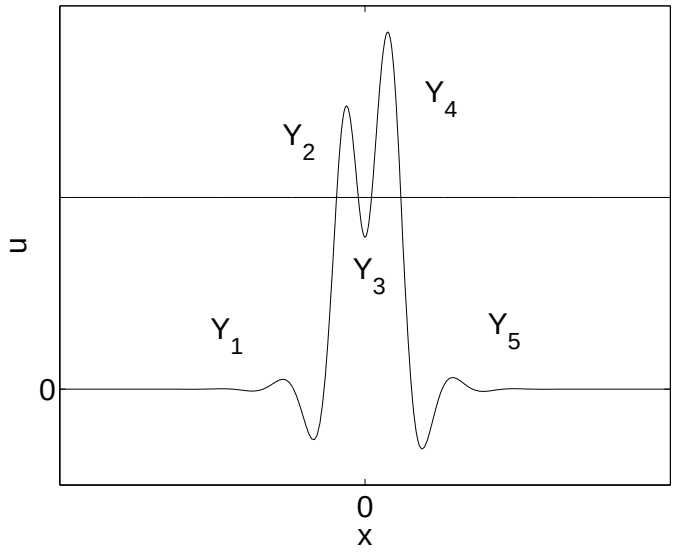

Figure 6.10: Piecewise construction of an asymmetric 2-bump solution of the Amari model with step firing rate function. The threshold is indicated by the horizontal line. Five functions, Y_1, Y_2, Y_3, Y_4 and Y_5, create four sets of matching conditions at the threshold.

for a schematic. There are two below-threshold functions, Y_1 and Y_3, and one above-threshold function, Y_2. Matching conditions are created whenever functions meet at the threshold, therefore there are two sets of matching conditions. One set is where Y_1 meets Y_2 and another where Y_2 meets Y_3. Construction of an asymmetric 2-bump solution is more complicated as $u(x)$ is decomposed into five functions. Four sets of matching conditions are formed. See Figure 6.10 for a schematic. With a piecewise linear firing rate function, as in Chapter 4, five functions are required to construct an asymmetric 1-bump solution, and the construction creates four sets of matching conditions. An asymmetric 2-bump solution requires nine functions and eight sets of matching conditions. We note the construction of asymmetric solutions using a piecewise differential framework as a project for future work.

6.6 Conclusion

In this chapter we discussed four methods that can be used to find asymmetric homoclinic orbits to the Amari model. We used the methods with the decaying oscillatory coupling function, however, the methods could be extended to other models of neural connectivity. Two of the methods, Newton's method and a shooting method, were successfully used to find a family of one- and two-bump asymmetric solutions. Numerical integration and Newton's method require that the infinite domain of the model be approximated by a finite domain. The domain is chosen to be sufficiently large that there is no activity on the boundaries.

We first assumed a smooth firing rate function. In principle, it is possible to find stable asymmetric solutions using numerical integration with a suitable asymmetric initial condition. Despite a comprehensive search over many different regions of parameter space however, we were unable to find any stable asymmetric solutions using numerical integration. Newton's method for a system of nonlinear equations was successfully used to find several 2-bump asymmetric solutions. By using continuation methods, these solutions were found to lie on the same solution curve as that found in Chapter 5 using another numerical technique. The solution curve lies in a region of parameter space where the firing rate function is sufficiently steep that stable N-bump solutions do not exist for a region about $b = 1$.

Steady state solutions are also solutions of a fourth-order ODE that was derived in Chapter 3. We developed a shooting method utilising the reversible Hamiltonian structure of the ODE. The shooting method found the same family of asymmetric solutions as that found using Newton's method earlier in the chapter. We limited our search to 1- and 2-bump solutions, however the method could be easily modified to search for any N-bump solutions, where $N > 2$.

Finally, we assumed a piecewise continuous firing rate function. An example of this would be the piecewise linear function from Chapter 4. A method of piecewise construction of 1- and 2-bump asymmetric solutions was presented. We note the implementation of this method as a project for future study. Although all the methods presented in the chapter were applied to the Amari model only, they could be extended to the gap junction model.

Chapter 7

Stability analysis

7.1 Introduction

Throughout this thesis, we have studied two neural field models, the Amari model and the gap junction model. The two models are based upon a partial integro-differential equation developed over thirty years ago to model a single layer of neurons [1]. There has been much study of the model over recent years [14, 27, 70]. In this thesis, various combinations of coupling functions and firing rate functions have been used. Spatially localised regions of high activity, or "bumps", have been found. These "bump" solutions are steady state solutions of the models. For the Amari model, a fourth-order ODE was derived, solutions of which are steady state solutions of the partial integro-differential equation. The fourth-order ODE is a reversible Hamiltonian system. A gap junction model was formed by adding a term to the Amari model. A sixth-order ODE was derived for the gap junction model, solutions of which are steady states of the model. We have been able to utilise the properties of these systems to find solutions both analytically and numerically. In phase space, solutions of the ODE for each model are homoclinic orbits that move to a bi-focus fixed point at the origin.

In various sections of this thesis, solution stability has been indicated. The reader has been referred to this chapter for the methods used to determine solution stability. We present five different approaches to determining the stability of steady state solutions. The first three methods have been presented previously in the literature and require a step firing rate function. For each method, where possible, two coupling functions are used. The coupling functions are the Mexican hat function introduced in Chapter 2 and the decaying oscillatory coupling function introduced in Chapter 3. A fourth method of eigenvalue analysis is presented which is used with a smooth firing rate function and the decaying

oscillatory coupling function. Finally, we briefly discuss using numerical integration to determine solution stability. The method can be used with different coupling/firing rate combinations.

The chapter proceeds as follows. In Section 7.2, we apply Amari's linear stability analysis to both the Amari model and the gap junction model. In Section 7.3, the method of Pinto and Ermentrout is applied to both models. Both Amari's linear stability analysis and Pinto and Ermentrout's method are used to find the stability of the single-bump steady state solutions found analytically in Chapter 2. The methods are also applied to piecewise solutions of the Amari and gap junction models with a step firing rate function found in Chapter 4. In Section 7.4, an Evans function analysis is presented and applied to travelling fronts in the Amari model. The analysis is then extended to the gap junction model. Evans function analysis was used in Chapter 5 to find the stability of stationary fronts, or heteroclinic orbits, in the Amari model with a step firing rate function. None of these three methods can be applied when the smooth firing rate function is used, only a step function may be used. In Section 7.5, an eigenvalue analysis is developed for both the Amari model and the gap junction model with the smooth firing rate function and decaying oscillatory coupling function. The method of eigenvalue analysis was used to find the stability of the solutions found numerically for both models in Chapter 3. In Section 7.6, we discuss a numerical simulation technique that was used in Chapter 4 to find the stability of solutions constructed with either a step or a piecewise linear firing rate function.

7.2 Amari's linear stability analysis

Amari [1] used linear stability analysis to calculate the stability of steady state solutions of a one-dimensional neural field model with lateral inhibition and step firing rate function. We apply linear stability analysis to both the Amari model and the gap junction model, first with the lateral inhibition coupling function in Chapter 2, then with the decaying oscillatory coupling function of Chapter 3.

Amari model

Consider the Amari model in Chapter 2 of

$$\frac{\partial u(x,t)}{\partial t} = -u(x,t) + \int_{-\infty}^{\infty} w(x-y) f(u(y,t))\, dy. \tag{7.1}$$

Lateral inhibition

Let $w(x)$ be the Mexican hat coupling function from Chapter 2 of

$$w(x) = Ke^{-k|x|} - Me^{-m|x|} \tag{7.2}$$

($K > M > 0$ and $k > m > 0$, $K, M, k, m \in \mathbb{R}^+$) and $f(u)$ be the shifted Heaviside function

$$f(u) = \Theta(u - \theta) = \begin{cases} 1, & \text{if } u \geq \theta \\ 0, & \text{if } u < \theta \end{cases} \tag{7.3}$$

where $\theta > 0$. Assume a single peaked solution of $u(x,t)$ in Equation (7.1) which is not necessarily a steady state solution. Define the excited region as

$$R[u(x,t)] = (x_1(t), x_2(t)) \tag{7.4}$$

where $u(x_1,t) = u(x_2,t) = \theta$. Let the gradients of $u(x,t)$ on the boundaries x_1 and x_2 of the excited region be

$$c_1 = \frac{\partial u(x_1,t)}{\partial x} > 0, \quad c_2 = -\frac{\partial u(x_2,t)}{\partial x} > 0. \tag{7.5}$$

After a short period of time dt, the excited region is

$$R[u(x,t+dt)] = (x_1(t+dt), x_2(t+dt)). \tag{7.6}$$

The boundaries of R satisfy

$$u(x_i,t) = \theta, \quad \text{at time } t \tag{7.7}$$

$$u(x_i + dx_i, t+dt) = \theta, \quad \text{at time } t+dt \tag{7.8}$$

where $x_i(t+dt) = x_i + dx_i$ $(i = 1,2)$. Substituting $u(x_i,t) = \theta$ in Equation (7.1) we obtain

$$\frac{\partial u(x_i,t)}{\partial t} = -u(x_i,t) + \int_{x_1(t)}^{x_2(t)} w(x_i - y)\, dy \tag{7.9}$$

$$= -\theta + W(x_i - x_1) - W(x_i - x_2) \tag{7.10}$$

where $W(x) = \int_0^x w(y)\, dy$, that is, $W(x) = \frac{K}{k}(1 - e^{-kx}) - \frac{M}{m}(1 - e^{-mx})$. Thus

$$\frac{\partial u(x_1,t)}{\partial t} = -\theta - W(x_1 - x_2) \tag{7.11}$$

$$\frac{\partial u(x_2,t)}{\partial t} = -\theta + W(x_2 - x_1). \tag{7.12}$$

Using a Taylor expansion and $u(x_i,t) = \theta$, $u(x_i + dx_i, t+dt) = \theta$ can be written as

$$\frac{\partial u(x_i,t)}{\partial x} dx_i + \frac{\partial u(x_i,t)}{\partial t} dt = 0 \quad (i = 1,2) \tag{7.13}$$

for very small dx_i and dt. Thus

$$c_1 \frac{dx_1}{dt} = \theta - W(x_2 - x_1). \tag{7.14}$$

and

$$c_2 \frac{dx_2}{dt} = W(x_2 - x_1) - \theta. \tag{7.15}$$

Define the width of the bump at time t as

$$a(t) = x_2(t) - x_1(t). \tag{7.16}$$

Hence

$$\frac{da}{dt} = \left(\frac{1}{c_1} + \frac{1}{c_2}\right)[W(a) - \theta]. \tag{7.17}$$

We have a steady state solution if

$$g(a) = \frac{da}{dt} = \left(\frac{1}{c_1} + \frac{1}{c_2}\right)[W(a) - \theta] = 0. \tag{7.18}$$

This solution, or bump, is stable when $g'(a) < 0$, that is, when

$$\left(\frac{1}{c_1} + \frac{1}{c_2}\right) W'(a) < 0. \tag{7.19}$$

From the definitions of c_1 and c_2 in Equation (7.5), this reduces to a stability condition of

$$W'(a) < 0. \tag{7.20}$$

Figure 7.1 shows the integral of $w(x)$, W. When the threshold is less than the maximum of W but greater than $\lim_{a\to\infty} W(a)$, there is at least one solution. In Figure 7.1, the threshold is given by the horizontal line so there are two solutions, as in Chapter 2. The narrow solution of width $a1$ is unstable as $W'(a1) > 0$. The wider solution of width $a2$ is stable as $W'(a2) < 0$. The stability analysis here is used to calculate the stability of the solutions in Section 2.2.

Decaying oscillatory coupling function

We now consider the model in Equation (7.1) with the decaying oscillatory coupling function in Chapter 3 of

$$w(x) = e^{-b|x|}\left(b\sin(|x|) + \cos(x)\right). \tag{7.21}$$

Earlier in the thesis where the decaying oscillatory coupling function has been used, the firing rate function has either been a smooth function with a steepness parameter, as in Chapter 3, or twice the shifted Heaviside function as in Chapter 4. When the smooth firing

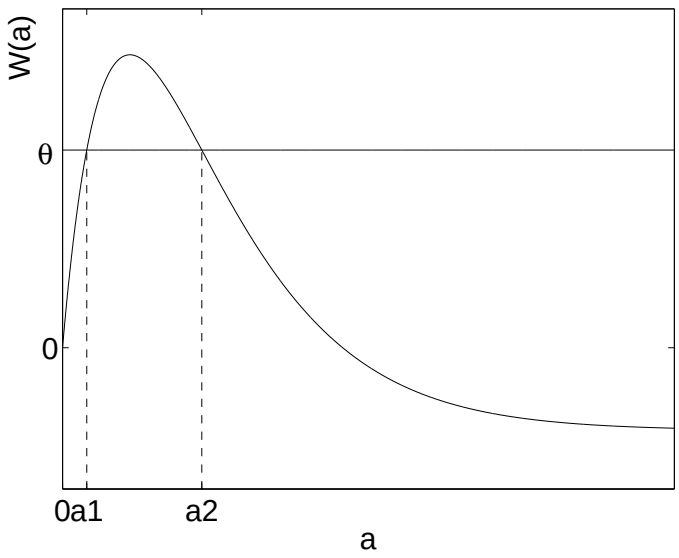

Figure 7.1: Integral, W, of the Mexican hat coupling function in Equation (7.2). For a threshold, θ, at the horizontal line, there are two steady states of widths $a1$ and $a2$. The solution with width $a1$ is unstable as $W'(a1) > 0$. The solution with width $a2$ is stable as $W'(a2) < 0$.

rate function was allowed to become infinitely steep, twice the shifted Heaviside function was obtained. Therefore, whenever we use the decaying oscillatory coupling function in Sections 7.2–7.4, we let the firing rate function be twice the shifted Heaviside function of

$$f(u) = 2\Theta(u-\theta) = \begin{cases} 2, & \text{if } u \geq \theta \\ 0, & \text{if } u < \theta. \end{cases} \tag{7.22}$$

Linear stability analysis is now applied to solutions of Equations (7.1), (7.21) and (7.22).

Again, assume a solution with excited region $R[u(x,t)] = (x_1(t), x_2(t))$. Let the gradients of $u(x,t)$ on the boundaries x_1 and x_2 of the excited region be

$$c_1 = \frac{\partial u(x_1,t)}{\partial x} > 0, \quad c_2 = -\frac{\partial u(x_2,t)}{\partial x} > 0. \tag{7.23}$$

Following the analysis above, we find that

$$\frac{\partial u(x_i,t)}{\partial t} = -u(x_i,t) + 2\int_{x_1(t)}^{x_2(t)} w(x_i - y)\, dy. \tag{7.24}$$

Hence, we have a steady state solution if

$$g(a) = \frac{da}{dt} = \left(\frac{1}{c_1} + \frac{1}{c_2}\right)[2W(a) - \theta] = 0 \tag{7.25}$$

where $W(x) = \int_0^x w(y)\, dy$, that is,

$$W(x) = \frac{e^{-bx}}{b^2+1}\left[(1-b^2)\sin(x) - 2b\cos(x)\right] + \frac{2b}{b^2+1}. \tag{7.26}$$

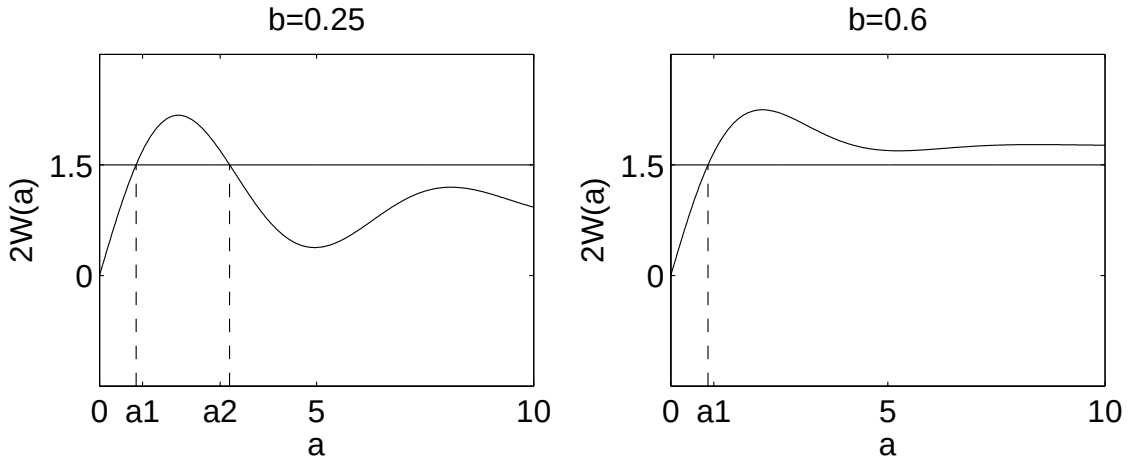

Figure 7.2: Twice the integral of decaying oscillatory coupling function in Equation (7.21) , $W(a)$ with $\theta = 1.5$ (horizontal line). Left: For $b = 0.25$, two single-bump solutions exist. Amari's linearised stability analysis shows that width $a1 = 0.84207$ is unstable ($W'(a1) > 0$) and that width $a2 = 2.9988$ is stable ($W'(a2) < 0$). Right: For $b = 0.6$, there is one unstable solution of width $a1 = 0.85758$ as $W'(a1) > 0$.

Since $c_1, c_2 > 0$, a solution with width a is stable if

$$W'(a) < 0. \tag{7.27}$$

Equation (7.27) is the same stability condition as for lateral inhibition with shifted Heaviside $f(u)$ in Equation (7.20). We set $b = 0.25$ in Equation (7.21) and $\theta = 1.5$ in Equation (7.22). The left plot in Figure 7.2 shows twice the integral of $w(x)$, W. The threshold is $\theta = 1.5$. Single-bump steady state solutions are given by $2W(a) = \theta$ so there are two solutions, with widths $a2 > a1 > 0$. Using Amari's linearised stability analysis, the solution with width $a1$ is unstable as $W'(a1) > 0$ and the solution with width $a2$ is stable as $W'(a2) < 0$.

The shape of the function $W(a)$ changes as the decay parameter b changes. We choose $b = 0.6$ and plot $2W(a)$ with $\theta = 1.5$. See the right plot in Figure 7.2. As $2W(a) = \theta$ only once, there is only one solution. The solution has width $a1$. By Amari's linearised stability analysis, the solution is unstable as $W'(a1) > 0$. In Chapter 4, solution curves were found for the Amari model with the decaying oscillatory coupling function and twice the shifted Heaviside firing rate function. There were no stable single-bump solutions for a wide range of b. Only an unstable solution was found. The bifurcation diagram was shown in Figure 4.3. We reproduce part of the diagram in Figure 7.3. We see that when $b = 0.6$, only an unstable solution exists,

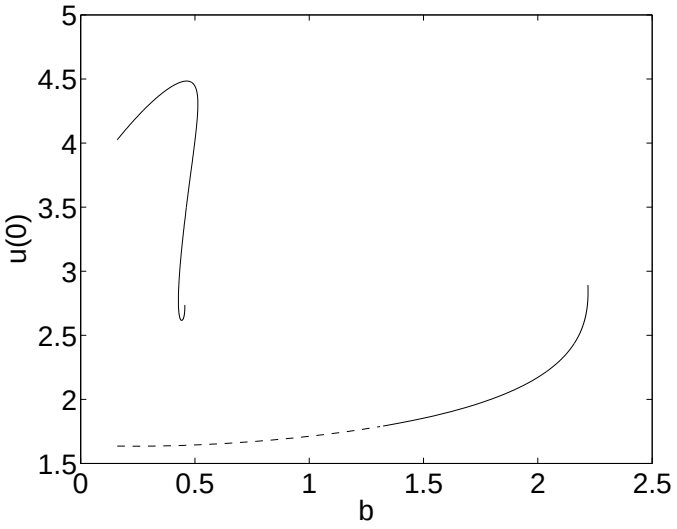

Figure 7.3: Solution curves of single-bump solutions for the Amari model with decaying oscillatory coupling function and shifted Heaviside firing rate function. Solid lines: stable solutions; dashed lines: unstable solutions. Diagram first presented as part of Figure 4.3.

Gap junction model

We now apply Amari's [1] linear stability analysis to the gap junction model

$$\frac{\partial u(x,t)}{\partial t} = \kappa^2 \frac{\partial^2 u(x,t)}{\partial x^2} - u(x,t) + \int_{-\infty}^{\infty} w(x-y) f(u(y,t))\, dy. \tag{7.28}$$

Lateral inhibition

We first let $w(x)$ be the Mexican hat coupling function in Equation (7.2) and $f(u)$ be the shifted Heaviside firing rate function in Equation (7.3). We apply the analysis as for the Amari model. Then with the boundaries of the excited region at x_1, x_2 where $u(x_1,t) = u(x_2,t) = \theta$,

$$\begin{aligned}\frac{\partial u(x_i,t)}{\partial t} =& \kappa^2 \frac{\partial^2 u(x_i,t)}{\partial x^2} - u(x_i,t) + \int_{x_1(t)}^{x_2(t)} w(x_i - y)\, dy & (7.29)\\ =& \kappa^2 \frac{\partial^2 u(x_i,t)}{\partial x^2} - \theta + W(x_i - x_1) - W(x_i - x_2) & (7.30)\end{aligned}$$

for $i = 1, 2$. Using a Taylor expansion, we obtain

$$\begin{aligned} c_1 \frac{dx_1}{dt} &= \theta - W(x_2 - x_1) - \kappa^2 \frac{\partial^2 u(x_1,t)}{\partial x^2} & (7.31)\\ c_2 \frac{dx_2}{dt} &= W(x_2 - x_1) - \theta + \kappa^2 \frac{\partial^2 u(x_2,t)}{\partial x^2}. & (7.32)\end{aligned}$$

Then

$$\frac{da}{dt} = \left(\frac{1}{c_1} + \frac{1}{c_2}\right)[W(a) - \theta] + \kappa^2 \left(\frac{1}{c_1}\frac{\partial^2 u(x_1,t)}{\partial x^2} + \frac{1}{c_2}\frac{\partial^2 u(x_2,t)}{\partial x^2}\right) \tag{7.33}$$

where $a(t) = x_2(t) - x_1(t)$ is the width of the bump at time t. Define

$$c_3 = \frac{\partial^2 u(x_1,t)}{\partial x^2}, \quad c_4 = \frac{\partial^2 u(x_2,t)}{\partial x^2}. \tag{7.34}$$

We have an equilibrium width (steady state solution) if

$$g(a) = \frac{da}{dt} = \kappa^2 \left(\frac{c_3}{c_1} + \frac{c_4}{c_2}\right) + \left(\frac{1}{c_1} + \frac{1}{c_2}\right)[W(a) - \theta] = 0. \tag{7.35}$$

As c_3, c_4 are the second spatial derivatives of u where $u = \theta$, in contrast to the Amari model, it is not possible to find the width of solutions. As expected, when $\kappa^2 = 0$ the stability condition reverts to that of the Amari model in Equation (7.18). Let $c_5 = \kappa^2(c_3/c_1 + c_4/c_2)$ and $c_6 = 1/c_1 + 1/c_2 > 0$. Then we can write Equation (7.35) as $g(a) = c_5 + c_6[W(a) - \theta] = 0$. Steady state solutions of width a exist for a satisfying $W(a) = \theta - c_5/c_6$. Thus a solution is stable when $g'(a) = dg/\,da < 0$, that is,

$$W'(a) < 0. \tag{7.36}$$

Therefore the gap junction model with lateral inhibition and the shifted Heaviside firing rate function has the same stability condition as the Amari model (see previous section). Note that if a solution is a symmetric bump then $c_3/c_1 = c_4/c_2$.

Decaying oscillatory coupling function

Now consider the gap junction model in Equation (7.28) with the decaying oscillatory coupling function in Equation (7.21) and $f(u)$ twice the shifted Heaviside function in Equation (7.22). Following the analysis above, Equation (7.29) becomes

$$\frac{\partial u(x_i,t)}{\partial t} = \kappa^2 \frac{\partial^2 u(x_i,t)}{\partial x^2} - u(x_i,t) + 2\int_{x_1(t)}^{x_2(t)} w(x_i - y)\,dy. \tag{7.37}$$

Working through the analysis as for the gap junction model with lateral-inhibition, we find there is an equilibrium width (steady state solution) if

$$g(a) = \frac{da}{dt} = \kappa^2 \left(\frac{c_3}{c_1} + \frac{c_4}{c_2}\right) + \left(\frac{1}{c_1} + \frac{1}{c_2}\right)[2W(a) - \theta] = 0. \tag{7.38}$$

Again, when $\kappa^2 = 0$ the stability condition reverts to that of the Amari model in Equation (7.18). Let $c_7 = \kappa^2(c_3/c_1 + c_4/c_2)$ and $c_8 = 1/c_1 + 1/c_2 > 0$. Then we can write Equation (7.38) as

$$g(a) = c_7 + c_8[2W(a) - \theta] = 0. \tag{7.39}$$

Steady state solutions of width a exist for a satisfying $W(a) = \theta/2 - c_7/(2c_8)$. A solution is stable when $g'(a) = dg/\,da < 0$, that is, when

$$W'(a) < 0. \tag{7.40}$$

Again, the stability condition is the same as the stability condition for the Amari model with decaying oscillatory coupling function. As above, if a solution is a symmetric bump then $c_3/c_1 = c_4/c_2$.

7.3 Pinto and Ermentrout's stability analysis

Pinto and Ermentrout [82] investigated the existence and stability of stationary single-bump solutions (standing pulses) in one-dimensional, two population network of excitatory and inhibitory neurons with lateral–inhibition. Use of a Heaviside firing rate function permitted Pinto and Ermentrout's stability analysis of the linearised system. With the assumption of instantaneous inhibition, the stabilty results of Amari [1] held for their two population model. They found two stationary single-bump solutions, one wide and stable, the other narrow and unstable. When inhibitory delays were included in the network, a more complicated analysis of the linearisation about a steady state solution showed that the wide solution lost stability through a Hopf bifurcation. We apply Pinto and Ermentrout's stability analysis to the Amari model and then to the gap junction model. For each model, both lateral inhibition and the decaying oscillatory coupling function are analysed. There is no Hopf bifurcation in our type of neural field model [35].

Amari model

Lateral inhibition

Let $w(x)$ be the Mexican hat coupling function in Equation (7.2) and $f(u)$ be the shifted Heaviside firing rate function in Equation (7.3). Then the Amari model in Equation (7.1) becomes

$$\frac{\partial u(x,t)}{\partial t} = -u(x,t) + \int_{-\infty}^{\infty} w(x-y)\Theta(u(y,t)-\theta)\,dy. \tag{7.41}$$

Assume a steady state single-bump solution $\bar{u}$ of Equation (7.41) centred about the origin with width a such that $\bar{u}(-a/2) = \bar{u}(a/2) = \theta$. Therefore

$$\bar{u}(x) = \int_{-\infty}^{\infty} w(x-y)\Theta(\bar{u}(y)-\theta)\,dy. \tag{7.42}$$

Given a perturbation z we have $u(x,t) = \bar{u}(x)+z(x,t)$. Linearising about $\bar{u}$, Equation (7.1) becomes

$$\frac{\partial z(x,t)}{\partial t} = -z(x,t) + \int_{-\infty}^{\infty} w(x-y)z(y,t)\delta(\bar{u}(y)-\theta)\,dy \tag{7.43}$$

where $\delta(x)$ is the Dirac delta function. Assuming solutions are of the form $z(x,t) = e^{\lambda t}\bar{z}(x)$, Equation (7.43) is

$$(1+\lambda)\bar{z}(x) = \int_{-\infty}^{\infty} w(x-y)\bar{z}(y)\delta(\bar{u}(y)-\theta)\,dy. \tag{7.44}$$

Since $\bar{u}(\pm a/2) = \theta$, Equation (7.44) can be written as

$$(1+\lambda)\bar{z}(x) = \frac{1}{|\bar{u}'(a/2)|}[w(x+a/2)\bar{z}(-a/2) + w(x-a/2)\bar{z}(a/2)]. \tag{7.45}$$

We can also write Equation (7.42) as

$$\bar{u}(x) = \int_{-a/2}^{a/2} w(x-y)\,dy, \tag{7.46}$$

hence we calculate $\bar{u}'(a/2) = w(a) - w(0)$. Then

$$(1+\lambda)\bar{z}(x) = \frac{1}{|w(a)-w(0)|}[w(x+a/2)\bar{z}(-a/2) + w(x-a/2)\bar{z}(a/2)], \tag{7.47}$$

which implies that $\bar{z}(\pm a/2) = 0 \Leftrightarrow \bar{z}(x) = 0$. When $x = \pm a/2$, we have the two equations:

$$(1+\lambda)\bar{z}(a/2) = \frac{1}{|w(a)-w(0)|}[w(0)\bar{z}(a/2) + w(a)\bar{z}(-a/2)] \tag{7.48}$$

$$(1+\lambda)\bar{z}(-a/2) = \frac{1}{|w(a)-w(0)|}[w(a)\bar{z}(a/2) + w(0)\bar{z}(-a/2)]. \tag{7.49}$$

As $w(0) > w(a)$, $|w(a)-w(0)| = w(0)-w(a) > 0$. Letting

$$\mathbf{A} = \frac{1}{w(0)-w(a)}\begin{pmatrix} w(0) & w(a) \\ w(a) & w(0) \end{pmatrix} \tag{7.50}$$

and rearranging Equations (7.48)–(7.49), we obtain

$$\begin{pmatrix} 1+\lambda & 0 \\ 0 & 1+\lambda \end{pmatrix}\begin{pmatrix} \bar{z}(a/2) \\ \bar{z}(-a/2) \end{pmatrix} = \mathbf{A}\begin{pmatrix} \bar{z}(a/2) \\ \bar{z}(-a/2) \end{pmatrix}. \tag{7.51}$$

Let $\mathbf{Id}$ be the 2×2 identity matrix, $\mathbf{0}$ be the 2×1 zero vector and $\bar{\mathbf{Z}} = [\bar{z}(a/2), \bar{z}(-a/2)]^T$, where T denotes the transpose of a vector. Then Equation (7.50) can be written in the matrix form

$$[\mathbf{A} - (1+\lambda)\mathbf{Id}]\bar{\mathbf{Z}} = \mathbf{0}. \tag{7.52}$$

Equation (7.52) has nontrivial solutions if the determinant of the matrix $[\mathbf{A} - (1+\lambda)\mathbf{Id}]$ is nonzero. As $w(0) - w(a)$ is nonzero, we solve for λ in

$$\lambda\big([w(0)-w(a)]\lambda - 2w(a)\big) = 0. \tag{7.53}$$

One solution is $\lambda_- = 0$ which is predicted by the translational invariance of solutions. The other solution is

$$\lambda_+ = \frac{2w(a)}{w(0)-w(a)}. \tag{7.54}$$

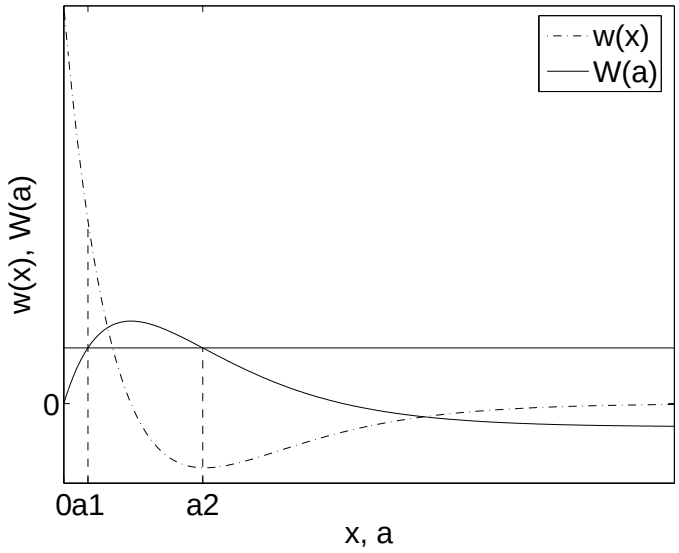

Figure 7.4: Mexican hat function $w(x)$ in Equation (7.2) (dash-dot line). The integral of $w(x)$, W (solid line). For a threshold given by the horizontal line, there are two steady states of widths $a1, a2$ given by $W(a1) = \theta$ and $W(a2) = \theta$.

If $\lambda_+ < 0$ then the solutions with width a are stable. Hence, the stability condition is that a steady state with width a is stable if

$$w(a) < 0. \tag{7.55}$$

From the analysis in Section 7.2, we know that for an appropriate level of threshold there are two single-bump solutions of width $a2 > a1 > 0$ given by $W(a1) = W(a2) = \theta$. From Figure 7.4, we can determine the sign of $w(a)$. For $a = a1$, $w(a1) > 0$ therefore $\lambda_+ > 0$. For $a = a2$, $w(a2) < 0$, therefore $\lambda_+ < 0$. The wider, taller bump is stable and the narrower, shorter bump is unstable. These stability results agree with Amari's linearised stability analysis in Section 7.2.

Decaying oscillatory coupling function

As for Section 7.2, we set $w(x)$ to be the decaying oscillatory coupling function in Equation (7.21) and $f(u)$ to be twice the shifted Heaviside function as in Equation (7.22). The following system is created

$$\frac{\partial u(x,t)}{\partial t} = -u(x,t) + 2\int_{-\infty}^{\infty} w(x-y)\Theta(u(y,t)-\theta)\,dy. \tag{7.56}$$

Assume a steady state single-bump solution $\bar{u}$ of Equation (7.56) centred about the origin with width a such that $\bar{u}(-a/2) = \bar{u}(a/2) = \theta$. Then

$$\bar{u}(x) = 2\int_{-\infty}^{\infty} w(x-y)\Theta(\bar{u}(y)-\theta)\,dy. \tag{7.57}$$

Given a perturbation z we have $u(x,t) = \bar{u}(x) + z(x,t)$. Linearising about $\bar{u}$, Equation (7.56) becomes

$$\frac{\partial z(x,t)}{\partial t} = -z(x,t) + 2\int_{-\infty}^{\infty} w(x-y)z(y,t)\delta(\bar{u}(y)-\theta)\,dy. \tag{7.58}$$

Assuming solutions are of the form $z(x,t) = e^{\lambda t}\bar{z}(x)$, Equation (7.58) is

$$(1+\lambda)\bar{z}(x) = 2\int_{-\infty}^{\infty} w(x-y)\bar{z}(y)\delta(\bar{u}(y)-\theta)\,dy. \tag{7.59}$$

Since $\bar{u}(\pm a/2) = \theta$, Equation (7.59) can be written as

$$(1+\lambda)\bar{z}(x) = \frac{2}{|\bar{u}'(a/2)|}[w(x+a/2)\bar{z}(-a/2) + w(x-a/2)\bar{z}(a/2)]. \tag{7.60}$$

Equation (7.57) can also be written as

$$\bar{u}(x) = 2\int_{-a/2}^{a/2} w(x-y)\,dy, \tag{7.61}$$

so $\bar{u}'(a/2) = 2[w(a) - w(0)]$. Therefore Equation (7.59) becomes

$$(1+\lambda)\bar{z}(x) = \frac{1}{|w(a)-w(0)|}[w(x+a/2)\bar{z}(-a) + w(x-a/2)\bar{z}(a)]. \tag{7.62}$$

We have obtained the same eigenvalue equation as that of the Amari model with lateral inhibition in Equation (7.47). The analysis is therefore the same. The Amari model with decaying oscillatory coupling function has a zero eigenvalue and another eigenvalue as in Equation (7.54). Therefore the stability condition is the same as in Equation (7.55).

As discussed in Section 7.2, the shape of the integral of $w(x)$ changes as the decay parameter b changes. The number of single-bump solutions can be zero, one, two or more, depending upon the level of the threshold and the value of b. See Figure 7.5 for a plot of $w(x)$ and $2W(a)$ for $b = 0.25$ (left) and $b = 0.6$ (right). The threshold is set at 1.5. When $b = 0.25$, there are two single-bump solutions of widths $a1 = 0.8420$ and $a2 = 2.9988$. Using Equation (7.55) and $w(x)$ in Figure 7.5, we see that $w(a1) > 0$. Therefore the narrower solution of width $a1$ is unstable. We find that $w(a2) < 0$ so the wider solution of $a2$ is stable. When $b = 0.6$, we know from the bifurcation analysis in Chapter 4 that only an unstable single-bump solution exists with width $a1 = 0.85758$. In the right plot, we see that the threshold only intersects $W(a)$ at one point which is $a1 = 0.85758$. Pinto and Ermentrout's stability analysis above tells us that this is an unstable solution as $w(a1) > 0$. Therefore the stability result is the same for the Amari model with either lateral inhibition and the shifted Heaviside firing rate function, or with the decaying oscillatory coupling function and twice the shifted Heaviside firing rate function.

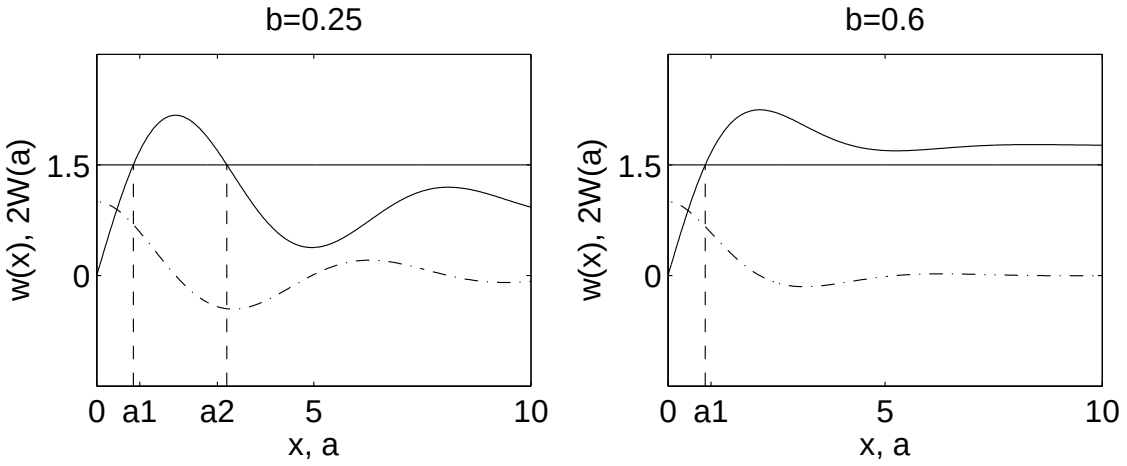

Figure 7.5: Plot of decaying oscillatory coupling function in Equation (7.21), $w(x)$ (dash-dot line) and twice the integral of $w(x)$, $W(a)$ (solid line). Threshold is set at $\theta = 1.5$ (horizontal line). Left: For $b = 0.25$, two single-bump solutions exist. Pinto and Ermentrout's stability analysis shows the narrow one of width $a1 = 0.8420$ is unstable and the wider one of width $a2 = 2.9988$ is stable. Right: For $b = 0.6$, Pinto and Ermentrout's stability analysis shows the single solution of width $a1 = 0.85758$ is unstable.

Gap junction model

We write the time dependent gap junction model of Equation (7.28) as

$$\frac{\partial u}{\partial t} = \kappa^2 \frac{\partial^2 u}{\partial x^2} - u + \int_{-\infty}^{\infty} w(x-y) f(u(y,t))\, dy. \tag{7.63}$$

Lateral inhibition

Let $w(x)$ be the Mexican hat function in Equation (7.2) and $f(u)$ be the shifted Heaviside function in Equation (7.3). Assume a steady state single-bump solution $\bar{u}$ of Equation (7.63) centred about the origin with width a such that $\bar{u}(-a/2) = \bar{u}(a/2) = \theta$. Therefore

$$\bar{u}(x) = \kappa^2 \frac{\partial^2 u}{\partial x^2} + \int_{-\infty}^{\infty} w(x-y) \Theta(\bar{u}(y) - \theta)\, dy. \tag{7.64}$$

Given a perturbation z and linearising Equation (7.63) about the steady state $\bar{u}$ we have

$$\frac{\partial z}{\partial t} = \kappa^2 \frac{\partial^2 z}{\partial x^2} - z + \int_{-\infty}^{\infty} w(x-y) z(y) \delta(\bar{u} - \theta)\, dy. \tag{7.65}$$

By assuming solutions of the form $z(x,t) = e^{\lambda t}\bar{z}(x)$, Equation (7.65) becomes

$$(1+\lambda)\bar{z} = \kappa^2 \frac{\partial^2 \bar{z}}{\partial x^2} + \int_{-\infty}^{\infty} w(x-y) z(y) \delta(\bar{u} - \theta)\, dy. \tag{7.66}$$

Given that $\bar{u}(\pm a/2) = \theta$,

$$\int_{-\infty}^{\infty} w(x-y) z(y) \delta(\bar{u} - \theta)\, dy = \frac{1}{|\bar{u}'(a/2)|}[w(x+a/2)\bar{z}(-a/2) + w(x-a/2)\bar{z}(a/2)]. \tag{7.67}$$

Substituting back into Equation (7.66) we obtain

$$(1+\lambda)\bar{z} = \kappa^2 \frac{\partial^2 \bar{z}}{\partial x^2} + \frac{1}{|\bar{u}'(a/2)|}\left(w(x+a/2)\bar{z}(-a/2) + w(x-a/2)\bar{z}(a/2)\right). \tag{7.68}$$

Using the definition of the steady state $\bar{u}$ in Equation (7.64), we write

$$\begin{aligned}\bar{u}(x) =& \kappa^2 \frac{d^2u(x)}{dx^2} + \int_{-a/2}^{a/2} w(x-y)\,dy \\ =& \kappa^2 \frac{d^2u(x)}{dx^2} + \int_{x-a/2}^{x+a/2} w(y)\,dy.\end{aligned} \tag{7.69}$$

Therefore

$$\bar{u}'(a/2) = \kappa^2 \frac{d^3u(a/2)}{dx^3} + w(a) - w(0). \tag{7.70}$$

Substituting for $u'(a/2)$ in Equation (7.68) we obtain

$$(1+\lambda)\bar{z} = \kappa^2 \frac{d^2\bar{z}}{dx^2} + \frac{w(x+a/2)\bar{z}(-a/2) + w(x-a/2)\bar{z}(a/2)}{\left|\kappa^2 \dfrac{d^3u(a/2)}{dx^3} + w(a) - w(0)\right|}. \tag{7.71}$$

Evaluating Equation (7.71) at $x = \pm a/2$ gives the two equations

$$(1+\lambda)\bar{z}(-a/2) = \kappa^2 \frac{d^2\bar{z}(-a/2)}{dx^2} + \frac{w(0)\bar{z}(-a/2) + w(a)\bar{z}(a/2)}{\left|\kappa^2 \dfrac{d^3\bar{u}(a/2)}{dx^3} + w(a) - w(0)\right|} \tag{7.72}$$

$$(1+\lambda)\bar{z}(a/2) = \kappa^2 \frac{d^2\bar{z}(a/2)}{dx^2} + \frac{w(a)\bar{z}(-a/2) + w(0)\bar{z}(a/2)}{\left|\kappa^2 \dfrac{d^3\bar{u}(a/2)}{dx^3} + w(a) - w(0)\right|}. \tag{7.73}$$

In matrix form we have

$$\begin{pmatrix} \bar{z}(a/2) \\ \\ \bar{z}(-a/2) \end{pmatrix} = \kappa^2 \begin{pmatrix} \dfrac{d^2\bar{z}(a/2)}{dx^2} \\ \\ \dfrac{d^2\bar{z}(-a/2)}{dx^2} \end{pmatrix} + \alpha_1 \begin{pmatrix} w(0) & w(a) \\ \\ w(2c) & w(0) \end{pmatrix} \begin{pmatrix} \bar{z}(a/2) \\ \\ \bar{z}(-a/2) \end{pmatrix} \tag{7.74}$$

where

$$\alpha_1^{-1} = \left|\kappa^2 \frac{d^3\bar{u}(a/2)}{dx^3} + w(a) - w(0)\right|. \tag{7.75}$$

The spatial derivatives at $\bar{u}(a/2)$ and $\bar{z}(\pm a/2)$ are not known. So unlike the perturbation analysis for the Amari model, it is not possible to derive a stability result for the perturbation z in the gap junction model. Instead, numerical integration is used to see if the gap junction model has similar stability characteristics to the Amari model. In Section 7.2, we analysed the Amari model with lateral inhibition. Parameters were $\theta = 0.07$ in Equation (7.3) and $K = 3.5$, $M = 3$, $k = 1.8$ and $m = 1.52$ in Equation (7.2). A stable single-bump solution was found with width of 1.1384. The Amari model is

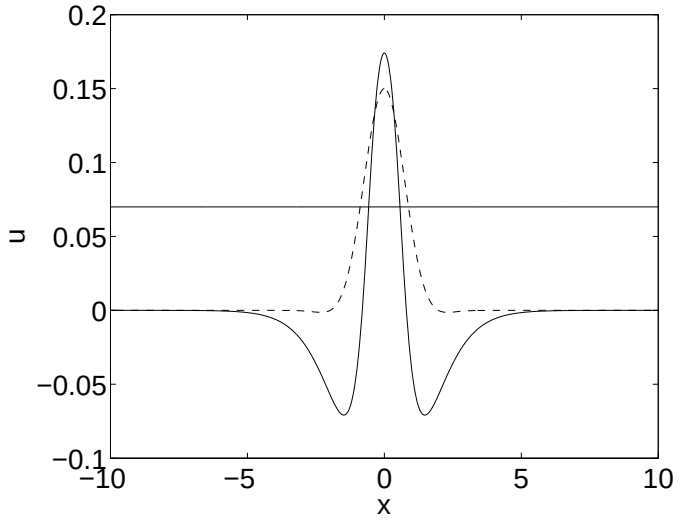

Figure 7.6: Steady state (solid line) found by numerically integrating with an initial condition (dotted line) in the gap junction model of Equation (7.63) with Mexican hat coupling function in Equation (7.2) and shifted Heaviside firing rate function in Equation (7.3). Parameter values: $\kappa^2 = 0.05$, $\theta = 0.07$, $K = 3.5$, $M = 3$, $k = 1.8$ and $m = 1.52$.

recovered from the gap junction model by setting $\kappa^2 = 0$. For the same parameter values but with small positive κ^2, we expect a stable solution to the gap junction model to be slightly narrower than that of the Amari model given the diffusive effect of increasing κ^2 from zero. We set $\kappa^2 = 0.05$ in Equation (7.63) with the parameter values above in Equations (7.2)–(7.3). An initial condition is numerically integrated over the domain $[-10, 10]$. As $t \to \infty$, a stable single-bump solution is found (see Figure 7.6). The solution has a width of approximately 1.1 therefore the result is as expected. The stability results for the gap junction model appear to be similar to those of the Amari model.

Decaying oscillatory coupling function

Now consider the gap junction model in Equation (7.63) with the decaying oscillatory coupling function of Equation (7.21) and $f(u)$ twice the shifted Heaviside function as in Equation (7.22). Assume a steady state single-bump solution $\bar{u}$ of Equation (7.63) centred about the origin with width a such that $\bar{u}(-a/2) = \bar{u}(a/2) = \theta$. Therefore

$$\bar{u}(x) = \kappa^2 \frac{\partial^2 u}{\partial x^2} + 2\int_{-\infty}^{\infty} w(x-y)\Theta(\bar{u}(y) - \theta)\, dy. \tag{7.76}$$

Given a perturbation z and linearising Equation (7.63) about the steady state $\bar{u}$ we have

$$\frac{\partial z}{\partial t} = \kappa^2 \frac{\partial^2 z}{\partial x^2} - z + 2\int_{-\infty}^{\infty} w(x-y)z(y)\delta(\bar{u} - \theta)\, dy. \tag{7.77}$$

Following the same analysis as used for the gap junction with lateral inhibition, we obtain

$$(1+\lambda)\bar{z} = \kappa^2 \frac{d^2\bar{z}}{dx^2} + \frac{2[w(x+a/2)\bar{z}(-a/2) + w(x-a/2)\bar{z}(a/2)]}{\left|\kappa^2 \frac{d^3u(a/2)}{dx^3} + 2[w(a) - w(0)]\right|}. \tag{7.78}$$

Evaluating Equation (7.78) at $x = \pm a/2$ gives the two equations

$$(1+\lambda)\bar{z}(a/2) = \kappa^2 \frac{d^2\bar{z}(a/2)}{dx^2} + \frac{2[w(a)\bar{z}(-a/2) + w(0)\bar{z}(a/2)]}{\left|\kappa^2 \frac{d^3\bar{u}(a/2)}{dx^3} + 2[w(a) - w(0)]\right|} \tag{7.79}$$

$$(1+\lambda)\bar{z}(-a/2) = \kappa^2 \frac{d^2\bar{z}(-a/2)}{dx^2} + \frac{2[w(0)\bar{z}(-a/2) + w(a)\bar{z}(a/2)]}{\left|\kappa^2 \frac{d^3\bar{u}(a/2)}{dx^3} + 2[w(a) - w(0)]\right|}. \tag{7.80}$$

In matrix form we have

$$\begin{pmatrix} \bar{z}(a/2) \\ \\ \bar{z}(-a/2) \end{pmatrix} = \kappa^2 \begin{pmatrix} \dfrac{d^2\bar{z}(a/2)}{dx^2} \\ \\ \dfrac{d^2\bar{z}(-a/2)}{dx^2} \end{pmatrix} + \alpha_1 \begin{pmatrix} w(0) & w(a) \\ \\ w(a) & w(0) \end{pmatrix} \begin{pmatrix} \bar{z}(a/2) \\ \\ \bar{z}(-a/2) \end{pmatrix} \tag{7.81}$$

where

$$\alpha_1 = \frac{2}{\left|\kappa^2 \frac{d^3\bar{u}(a/2)}{dx^3} + 2[w(a) - w(0)]\right|}. \tag{7.82}$$

Again, the spatial derivatives at $\bar{u}(a/2)$ and $\bar{z}(\pm a/2)$ are not known. So it is not possible to derive a stability result for the gap junction model. We use numerical integration to see if the gap junction model has similar stability characteristics to the Amari model. In Section 7.2, we analysed the Amari model with the decaying oscillatory coupling function. For $\theta = 1.5$ in Equation (7.22) and $b = 0.25$ in Equation (7.21), a stable single-bump solution was found with width of 2.9988. We set $\kappa^2 = 0.05$ in Equation (7.63) with parameter values as before in Equations (7.21)–(7.22). Numerically integrating with an initial condition over the domain $[-10, 10]$, we find that as $t \to \infty$, a stable single-bump solution is found (see Figure 7.7). The solution has an almost identical width to that of the Amari model but is of smaller magnitude. The result is as expected. We conclude that using Pinto and Ermentrout's stability analysis, the stability results for the gap junction model are similar to those of the Amari model.

7.4 Evans function analysis

In Section 5.5 of Chapter 5, we found an expression for travelling fronts of the Amari model with decaying oscillatory coupling function and shifted Heaviside firing rate function. The

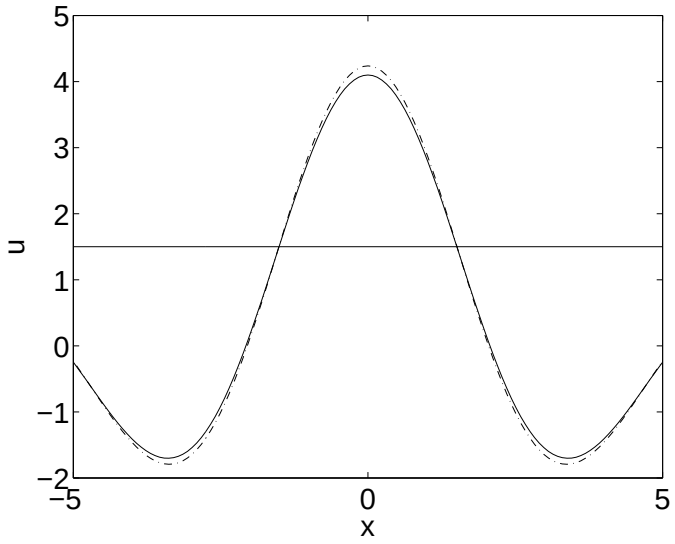

Figure 7.7: Closeup of stable solutions for $b = 0.25$ in the decaying oscillatory coupling function in Equation (7.21) and $\theta = 1.5$ in twice the shifted Heaviside firing rate function of Equation (7.22). Solid line: stable solution for the gap junction model in Equation (7.63) with $\kappa^2 = 0.05$. Dashed-dot line: stable solution for the Amari model in Equation (7.1).

stability of travelling fronts was calculated by the constructing an Evans function. The analysis depends upon a step $f(u)$ and requires the partial integro-differential equation to be written as a scalar integral equation. We review the derivation of an Evans function for travelling fronts in the Amari model [16] but take the specific case of infinitely fast propagation velocity and no local feedback. We then extend the analysis to the gap junction model.

Amari model

The Amari model in Equation (7.1) can be written in the form

$$\mathcal{L}u = \int_{-\infty}^{\infty} w(y) f(u(x-y,t))\, dy \tag{7.83}$$

where $\mathcal{L}$ is the differential operator $\mathcal{L} = (1 + \partial/\partial t)$. We find the Green's function of $\mathcal{L}$, $\eta(t) = e^{-t}$ for $t > 0$. Using $\eta(t)$, Equation (7.83) can be written as the scalar integral equation

$$u(x,t) = \int_{-\infty}^{\infty} \int_{0}^{\infty} \eta(s) w(y) f(u(x-y, t-s))\, ds\, dy, \tag{7.84}$$

as in Equation (5.57). For clarity, we expand on the analysis in Section 5.5. Let $\bar{c}$ be the speed of a travelling wave. If $\bar{c} > 0$, then the wave is moving to the right. If $\bar{c} < 0$ the wave is moving to the left. If $\bar{c} = 0$, the wave is stationary. Using the standard approach for

constructing travelling wave solutions, the coordinate $\xi = x - \bar{c}t$ is introduced. Solutions of the form $U(\xi, t) = u(x - \bar{c}t, t)$ are sought. In (ξ, t) coordinates, Equation (7.84) becomes

$$U(\xi, t) = \int_{-\infty}^{\infty} \int_{0}^{\infty} w(y)\eta(s) f(u(\xi - y + \bar{c}s, t - s))\, ds\, dy. \tag{7.85}$$

Then a travelling wave is a travelling solution $U(\xi, t) = q(\xi)$ where

$$q(\xi) = \int_{-\infty}^{\infty} \int_{0}^{\infty} w(y)\eta(s) f(q(\xi - y + \bar{c}s)\, ds\, dy. \tag{7.86}$$

Write

$$q(\xi) = \int_{0}^{\infty} \eta(s)\varphi(\xi + \bar{c}s)\, ds \tag{7.87}$$

where

$$\varphi(\xi) = \int_{-\infty}^{\infty} w(y) f(q(\xi - y))\, dy. \tag{7.88}$$

We look for travelling front solutions where $q(\xi) > \theta$ for $\xi < 0$ and $q(\xi) < \theta$ for $\xi > 0$. So the origin is defined as $q(0) = \theta$. Linearising about the steady state $q(\xi)$ in $U(\xi, t) = q(\xi) + u(\xi, t)$ results in

$$u(\xi, t) = \int_{-\infty}^{\infty} \int_{0}^{\infty} w(y)\eta(s) f'(q(\xi - y + \bar{c}s))u(\xi - y + \bar{c}s, t - s)\, ds\, dy. \tag{7.89}$$

Smooth bounded solutions on $\mathbb{R}$ for each fixed t are of particular importance. Looking for solutions of the form $u(\xi, t) = u(\xi)e^{\lambda t}$ leads to the eigenvalue equation

$$u(\xi) = \int_{-\infty}^{\infty} \int_{\xi - y}^{\infty} w(y)\eta\left((y - \xi + s)/\bar{c}\right) e^{-\lambda(-\xi + y + s)/\bar{c}} f'(q(s))u(s)\, ds\, dy. \tag{7.90}$$

To calculate the essential spectrum of the eigenvalue equation in Equation (7.90), we find the Fourier transform of $\eta(t)$,

$$\hat{\eta}(k) = \int_{0}^{\infty} e^{-t(1+ik)}\, dt = \frac{1}{1 + ik}, \tag{7.91}$$

where k is the transform variable. From [16], we look for solutions of the form $u(\xi) = e^{ip\xi}$, where $p \in \mathbb{R}$, in

$$\frac{1}{\hat{\eta}(-i\lambda - p\bar{c})} = 0. \tag{7.92}$$

We calculate $\lambda = -1 + ip\bar{c}$. So the real part of the essential spectrum has a uniformly negative upper bound of -1 and is not important in determining the stability of waves. The Evans function is used to find the isolated eigenvalues in order to determine wave stability. We present the general method of construction of an Evans function, with a shifted Heaviside $f(u)$, for all $\bar{c}$. Let $z = q(s)$ in Equation (7.90)

$$\begin{aligned} u(\xi) = \int_{-\infty}^{\infty} \int_{q(\xi - y)}^{q(\infty)} & w(y)\eta\left((y - \xi + q^{-1}(z))/\bar{c}\right) \\ & \times e^{-\lambda(-\xi + y + q^{-1}(z))/\bar{c}} \frac{\delta(z - \theta)}{|q'(q^{-1}(z))|} u(q^{-1}(z))\, dz\, dy. \end{aligned} \tag{7.93}$$

From the condition $q(0) = \theta$, $z = \theta$ when $q^{-1}(\theta) = 0$. So

$$u(\xi) = \frac{u(0)}{\bar{c}|q'(0)|} \int_{-\infty}^{\infty} w(y)\eta((y-\xi)/\bar{c})e^{-\lambda(y-\xi)/\bar{c}}\, dy. \tag{7.94}$$

By setting $\xi = 0$, a self-consistent equation for the value of the perturbation at $\xi = 0$ is obtained of

$$u(0) = \frac{u(0)}{\bar{c}|q'(0)|} \int_{-\infty}^{\infty} w(y)\eta(y/\bar{c})e^{-\lambda y/\bar{c}}\, dy. \tag{7.95}$$

There are only nontrivial solutions if $\mathcal{E}(\lambda) = 0$ where

$$\mathcal{E}(\lambda) = 1 - \frac{1}{\bar{c}|q'(0)|} \int_{-\infty}^{\infty} w(y)\eta(y/\bar{c})e^{-\lambda y/\bar{c}}\, dy. \tag{7.96}$$

As $\eta(t) = 0$ for $t < 0$, for $\bar{c} \geq 0$

$$\mathcal{E}(\lambda) = 1 - \frac{1}{\bar{c}|q'(0)|} \int_{0}^{\infty} w(y)\eta(y/\bar{c})e^{-\lambda y/\bar{c}}\, dy. \tag{7.97}$$

For $\bar{c} < 0$

$$\mathcal{E}(\lambda) = 1 - \frac{1}{\bar{c}|q'(0)|} \int_{-\infty}^{0} w(y)\eta(y/\bar{c})e^{-\lambda y/\bar{c}}\, dy. \tag{7.98}$$

The function $\mathcal{E}(\lambda)$ is identified as the Evans function associated with a travelling front solution of the integral equation in Equation (7.84). The complex number λ is an eigenvalue of Equation (7.84) if and only if $\mathcal{E}(\lambda) = 0$. The algebraic multiplicity of the eigenvalue is equal to the order of the Evans function. An analysis of this is given in [16] and it is shown that $q'(\xi) = u(\xi)|_{\lambda=0}$. Hence, when $\bar{c} \geq 0$ we write

$$\mathcal{H}(\lambda) = \int_{0}^{\infty} w(y)\eta(y/\bar{c})e^{-\lambda y/\bar{c}}\, dy \tag{7.99}$$

and when $\bar{c} < 0$

$$\mathcal{H}(\lambda) = \int_{-\infty}^{0} w(y)\eta(y/\bar{c})e^{-\lambda y/\bar{c}}\, dy. \tag{7.100}$$

Then, using the fact that $\mathcal{E}(0) = 0$, the Evans function can be written in the form

$$\mathcal{E}(\lambda) = 1 - \frac{\mathcal{H}(\lambda)}{\mathcal{H}(0)}. \tag{7.101}$$

Eigenvalues are λ such that $\mathcal{E}(\lambda) = 0$. We now look for travelling fronts and attempt to construct an Evans function for the Amari model, then the gap junction model. In each case, where possible, we use both a Mexican hat coupling function and the decaying oscillatory coupling function.

Lateral inhibition

Let $f(u)$ be the shifted Heaviside function in Equation (7.3). Then Equation (7.88) becomes

$$\varphi(\xi) = \int_{-\infty}^{\infty} w(y)\Theta(q(\xi - y) - \theta)\, dy. \tag{7.102}$$

Let $w(x)$ be the Mexican hat function in Equation (7.2). From Equation (7.102)

$$\varphi(\xi) = \begin{cases} \dfrac{K}{k}(2 - e^{k\xi}) - \dfrac{M}{m}(2 - e^{m\xi}), & \xi < 0 \\ \\ \dfrac{K}{k}e^{-k\xi} - \dfrac{M}{m}e^{-m\xi}, & \xi \geq 0. \end{cases} \tag{7.103}$$

Since $q(0) = \theta$, an implicit equation for the speed of travelling fronts, $\bar{c}$, as a function of parameters can be created. From Equation (7.87) we evaluate

$$q(0) = \int_0^{\infty} \eta(s)\varphi(\bar{c}s)\, ds \tag{7.104}$$

for both $\bar{c} = \bar{c}_+ \geq 0$ and $\bar{c} = \bar{c}_- < 0$. Thus

$$q(0) = \frac{K}{k(k\bar{c}_+ + 1)} - \frac{M}{m(m\bar{c}_+ + 1)} \tag{7.105}$$

and

$$q(0) = \frac{K}{k}\left[2 - \frac{1}{1 - k\bar{c}_-}\right] - \frac{M}{m}\left[2 - \frac{1}{1 - m\bar{c}_-}\right]. \tag{7.106}$$

Let $K = 3.5$, $M = 3$, $k = 1.8$, $m = 1.52$ and $\theta = 0.07$. Using the condition $q(0) = \theta$ and solving Equations (7.105)–(7.106), there are no real values for $\bar{c}_+$ or $\bar{c}_-$. So there are no travelling fronts for these parameter values and an Evans function is not constructed. There are parameter values for which lateral inhibition can support travelling fronts [14]. Given that a travelling front solution satisfies $\lim_{\xi \to -\infty} q(\xi) > \theta$, we have the condition $\int_{\mathbb{R}} w(x) > \theta$. The parameter values above do not satisfy this condition.

We now analyse the Amari model with the decaying oscillatory coupling function.

Decaying oscillatory coupling function

Let $w(x)$ be the decaying oscillatory function in Equation (7.21). As before, we also take $f(u) = 2\Theta(u - \theta)$. Then from Equation (7.102)

$$\varphi(\xi) = \begin{cases} \dfrac{2e^{b\xi}}{b^2 + 1}[(b^2 - 1)\sin(\xi) - 2b\cos(\xi)] + \dfrac{8b}{b^2 + 1}, & \xi < 0 \\ \\ \dfrac{2e^{-b\xi}}{b^2 + 1}[(b^2 - 1)\sin(\xi) + 2b\cos(\xi)], & \xi \geq 0. \end{cases} \tag{7.107}$$

Again, the choice of $q(0) = \theta$ gives an implicit equation for the speed of the travelling front as a function of the coupling decay parameter b and the firing threshold θ. We evaluate

$$q(0) = \int_0^\infty \eta(s)\varphi(\bar{c}s)\, ds \tag{7.108}$$

for both $\bar{c} = \bar{c}_+ > 0$ and $\bar{c} = \bar{c}_- < 0$. We find that

$$q(0) = 2\left[\frac{(3b^2-1)\bar{c}_+ + 2b}{(b^2+1)((b^2+1)\bar{c}_+^2 + 2b\bar{c}_+ + 1)}\right] \tag{7.109}$$

and

$$q(0) = 2\left[\frac{4b(b^2+1)\bar{c}_-^2 - (5b^2+1)\bar{c}_- + 2b}{(b^2+1)((b^2+1)\bar{c}_-^2 - 2b\bar{c}_- + 1)}\right]. \tag{7.110}$$

Let $\theta = 1.5$. Using the condition $q(0) = \theta$ and solving for $\bar{c}_+$ and $\bar{c}_-$, the speed of travelling fronts as a function of b can be found. Travelling fronts can only exist when $\lim_{\xi\to-\infty} q(\xi) > \theta$, that is,

$$2\int_{-\infty}^\infty w(x)\, dx > \theta.$$

So a travelling front can only exist for b, θ satisfying the existence condition

$$8b/(b^2+1) > \theta. \tag{7.111}$$

For $\theta = 1.5$, travelling fronts can exist for $0.1946 < b < 5.1387$. The existence condition in Equation (7.111) must be checked when solving Equations (7.109)–(7.110). In Section 5.5, we showed that the system has two fixed points, the origin and a nonzero fixed point with a u component of $8b/(b^2+1)$. Fronts connect the nonzero fixed point to the fixed point at the origin, therefore a front can only exist for the range of b for which the nonzero fixed point exists, which is $0.1946 < b < 5.1387$.

We construct an Evans function to determine stability of the fronts. By letting $z = q(s)$ in Equation (7.90), we obtain

$$\begin{aligned} u(\xi) = 2\int_{-\infty}^\infty \int_{q(\xi-y)}^{q(\infty)} & w(y)\eta\left((y-\xi+q^{-1}(z))/\bar{c}\right) \\ & \times e^{-\lambda(-\xi+y+q^{-1}(z))/\bar{c}} \frac{\delta(z-\theta)}{|q'(q^{-1}(z))|} u(q^{-1}(z))\, dz\, dy. \end{aligned} \tag{7.112}$$

From the condition $q(0) = \theta$, $z = \theta$ when $q^{-1}(\theta) = 0$. A travelling front solution of Equation (7.84) is not necessarily monotonic, therefore q^{-1} is ill-defined. So

$$u(\xi) = \frac{2u(0)}{\bar{c}|q'(0)|}\int_{-\infty}^\infty w(y)\eta((y-\xi)/\bar{c})e^{-\lambda(y-\xi)/\bar{c}}\, dy. \tag{7.113}$$

By setting $\xi = 0$, a self-consistent equation for the value of the perturbation at $\xi = 0$ is obtained of

$$u(0) = \frac{2u(0)}{\bar{c}|q'(0)|}\int_{-\infty}^\infty w(y)\eta(y/\bar{c})e^{-\lambda y/\bar{c}}\, dy. \tag{7.114}$$

There are only nontrivial solutions if $\mathcal{E}(\lambda) = 0$ where

$$\mathcal{E}(\lambda) = 1 - \frac{2}{\bar{c}|q'(0)|}\int_{-\infty}^{\infty} w(y)\eta(y/\bar{c})e^{-\lambda y/\bar{c}}\,dy. \tag{7.115}$$

When $\bar{c} \geq 0$, we write

$$\mathcal{E}(\lambda) = 1 - \frac{2}{\bar{c}|q'(0)|}\int_{0}^{\infty} w(y)\eta(y/\bar{c})e^{-\lambda y/\bar{c}}\,dy. \tag{7.116}$$

Hence, using Equation (7.99) we find that

$$\mathcal{H}(\lambda) = \int_{0}^{\infty} e^{-y(b+(1+\lambda)/\bar{c})}\big(b\sin(y) + \cos(y)\big)\,dy. \tag{7.117}$$

Evaluating Equation (7.117) we obtain

$$\mathcal{H}(\lambda) = \frac{\bar{c}(\lambda + 1 + 2b\bar{c})}{(b^2+1)\bar{c}^2 + \lambda(\lambda + 2b\bar{c} + 2) + 2b\bar{c} + 1}. \tag{7.118}$$

Again, since $\mathcal{E}(0) = 0$, the Evans function can be written in the form $\mathcal{E}(\lambda) = 1 - \mathcal{H}(\lambda)/\mathcal{H}(0)$. Thus,

$$\mathcal{E}(\lambda) = \frac{\lambda\big((3b^2-1)\bar{c}^2 + \lambda(2b\bar{c}+1) + 4b\bar{c} + 1\big)}{\big((b^2+1)\bar{c}^2 + \lambda(\lambda + 2b\bar{c} + 2) + 2b\bar{c} + 1\big)(2b\bar{c}+1)}. \tag{7.119}$$

Then $\mathcal{E}(\lambda) = 0$ when $\lambda = 0$ and when

$$\lambda = \frac{(1-3b^2)\bar{c}^2 - 4b\bar{c} - 1}{2b\bar{c} + 1}. \tag{7.120}$$

The zero eigenvalue is expected given the translational invariance of the system. Therefore, the stability condition for a travelling front with speed $\bar{c} \geq 0$ is that

$$(1-3b^2)\bar{c}^2 - 4b\bar{c} < 1. \tag{7.121}$$

We can find the speed of travelling fronts where $\bar{c} \geq 0$ using Equation (7.109), then use Equation (7.121) to determine front stability.

When $\bar{c} < 0$, we write

$$\mathcal{E}(\lambda) = 1 - \frac{2}{\bar{c}|q'(0)|}\int_{-\infty}^{0} w(y)\eta(y/\bar{c})e^{-\lambda y/\bar{c}}\,dy. \tag{7.122}$$

Using Equation (7.100),

$$\mathcal{H}(\lambda) = \int_{-\infty}^{0} e^{y(b-(1+\lambda)/\bar{c})}\big(-b\sin(y) + \cos(y)\big)\,dy. \tag{7.123}$$

Thus

$$\mathcal{H}(\lambda) = \frac{\bar{c}(\lambda + 1 - 2b\bar{c})}{(b^2+1)\bar{c}^2 + \lambda(\lambda - 2b\bar{c} + 2) - 2b\bar{c} + 1} \tag{7.124}$$

and the Evans function is

$$\mathcal{E}(\lambda) = \frac{\lambda\big((1-3b^2)\bar{c}^2 + \lambda(2b\bar{c}-1) + 4b\bar{c} - 1\big)}{\big((b^2+1)\bar{c}^2 + \lambda(\lambda - 2b\bar{c} + 2) - 2b\bar{c} + 1\big)(2b\bar{c}-1)}. \tag{7.125}$$

Then $\mathcal{E}(\lambda) = 0$ when $\lambda = 0$ and when

$$\lambda = \frac{(3b^2 - 1)\bar{c}^2 - 4b\bar{c} + 1}{2b\bar{c} - 1}. \tag{7.126}$$

So the stability condition for a travelling front with speed $\bar{c} < 0$ is that

$$(3b^2 - 1)\bar{c}^2 - 4b\bar{c} + 1 < 0. \tag{7.127}$$

We can find the speed of travelling fronts where $\bar{c} < 0$ using Equation (7.110) and use Equation (7.127) to determine front stability.

We set $\theta = 1.5$ and calculate the speed of travelling fronts using Equations (7.109) and (7.110). The nonzero eigenvalue is found using Equations (7.120) for $\bar{c} \geq 0$ and Equation (7.126) for $\bar{c} < 0$. As expected, $\bar{c} = 0$ at $b = 0.451, 2.215$. The values of b where stationary fronts occur are the same as the values of b where the Hamiltonian of the nonzero fixed point meets the Hamiltonian of the fixed point at the origin (see Section 5.4). When $\bar{c} = 0$ and $b = 0.451, 2.215$, the Evans function reduces to $\mathcal{E}(\lambda) = 1 + 1/\lambda$. Solving $\mathcal{E}(\lambda) = 0$, it is found that $\lambda = -1$. Therefore the stationary fronts are stable.

From the existence condition in Equation (7.111), fronts only exist for $0.1946 < b < 5.1387$. So there are travelling fronts with $\bar{c} < 0$ for $0.1946 < b < 0.4514$ and $2.215 < b < 5.1387$. There are travelling fronts with $\bar{c} > 0$ for $0.4154 < b < 2.215$. Using Equations (7.120) and (7.126) for fronts with positive speed and negative speed respectively, we find all the fronts are stable. Figure 7.8 shows $\bar{c}$ as a function of b. Numerical simulation confirms Figure 7.8.

Gap junction model

We now extend the Evans function stability analysis to the gap junction model. To do this, we must write the time-dependent gap junction model in integral form. This involves finding the Green's function in two variables, t and x, such that

$$\frac{\partial g}{\partial t} - \kappa^2 \frac{\partial^2 g}{\partial x^2} + g = \delta(x - \xi)\delta(t - \tau). \tag{7.128}$$

The Fourier transform in space, where ω is the transform variable, for a function $g(x, t)$ is defined as

$$\hat{g}(\omega, t) = \int_{-\infty}^{\infty} e^{-i\omega x} g(x, t)\, dx \tag{7.129}$$

and the inverse Fourier transform as

$$g(x, t) = \frac{1}{2\pi} \int_{-\infty}^{\infty} e^{i\omega x} \hat{g}(\omega, t)\, d\omega. \tag{7.130}$$

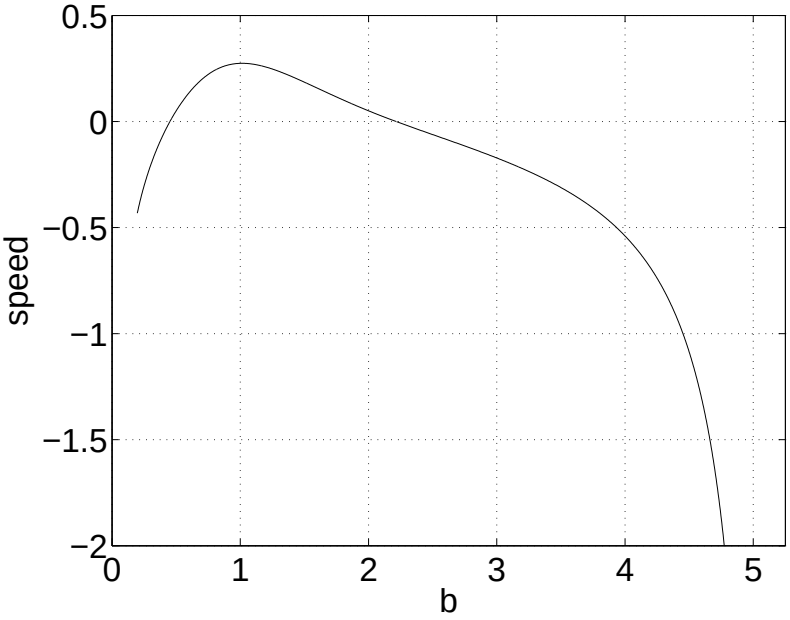

Figure 7.8: Speed of travelling fronts, $\bar{c}$, as a function of b using Equations (7.109) and (7.110). Threshold at $\theta = 1.5$. Stationary fronts occur at $\bar{c} = 0$ ($b = 0.451, 2.215$). Stability is found using Evans function analysis. The curve has an endpoint at $b = 0.1946$ as the nonzero fixed point of the system does not exist for $b < 0.1946$.

Taking the Fourier transform of (7.128) and using the identity properties of the transform for the second spatial derivative, we obtain

$$\hat{g}_t + (1 + \kappa^2\omega^2)\hat{g} = e^{-i\omega\xi}\delta(t - \tau) \tag{7.131}$$

which, through the use of an integrating factor, can be written as

$$\frac{d}{dt}\left(e^{(1+\kappa^2\omega^2)t}\hat{g}\right) = \alpha e^{-i\omega\xi+\alpha(1+\kappa^2\omega^2)t}\,\delta(t - \tau). \tag{7.132}$$

This gives an expression for the spatial Fourier transform of g

$$\hat{g}(x, t; \xi, \tau) = e^{-(i\omega\xi+\alpha(1+\kappa^2\omega^2)(t-\tau))}\,\Theta(t - \tau), \tag{7.133}$$

where Θ is the Heaviside function. Applying inverse Fourier transforms in space we have the Green's function

$$g(x, t; \xi, \tau) = \frac{\sqrt{\alpha}\, e^{-(x-\xi)^2/(4\kappa^2(t-\tau))-(t-\tau)}}{2\kappa\sqrt{\pi(t - \tau)}}\,\Theta(t - \tau). \tag{7.134}$$

From the integral expression for $u(x, t)$ of

$$u(x, t) = \int_{-\infty}^{\infty}\int_{-\infty}^{\infty}\int_{-\infty}^{t} g(x, t; \xi, \tau)w(\xi - y)f(u(y, \tau))d\tau\, dy\, d\xi \tag{7.135}$$

and using the Green's function in Equation (7.134)

$$u(x,t) = \int_{-\infty}^{\infty}\int_{-\infty}^{\infty}\int_{-\infty}^{t} \frac{e^{-(x-\xi)^2/(4\kappa^2(t-\tau))-(t-\tau)}}{2\kappa\sqrt{\pi(t-\tau)}} w(\xi-y) f(u(y,\tau))\, d\tau\, dy\, d\xi. \qquad (7.136)$$

Letting $s = t - \tau$ and rearranging we obtain

$$u(x,t) = \int_{-\infty}^{\infty}\int_{-\infty}^{\infty}\int_{0}^{\infty} \frac{e^{-(x-\xi)^2/(4\alpha\kappa^2 s)-\alpha s}}{2\kappa\sqrt{\pi s}} w(\xi-y) f(u(y,t-s))\, ds\, dy\, d\xi. \qquad (7.137)$$

To apply the Evans function analysis as for the Amari model, the triple integral in Equation (7.137) must be reduced to a double integral. It has not been possible to reduce the integral any further from the triple integral. We note this as a potential project for future study.

7.5 Eigenvalue analysis

Here we develop a method of eigenvalue analysis to find the stability of steady states of both the Amari model and the gap junction model with the decaying oscillatory coupling function in Equation (7.21) and the smooth firing rate function of

$$f(u) = 2e^{-r/(u-\theta)^2}\Theta(u-\theta). \qquad (7.138)$$

Eigenvalue analysis was used to determine the stability of the steady states found numerically in Chapter 3.

Throughout the thesis, steady state solutions have been found using continuation methods. AUTO [23] has often been used to find solution curves of steady state solutions. AUTO uses pseudo-arclength continuation for following branches. A description of the pseudo-arclength continuation method is given in the Appendix. Various convergence criteria were set in AUTO and these criteria define the accuracy with which solutions are found. The relative convergence criterion of solution parameters and the relative convergence criterion for solution components in the Newton/Chord method were set at $1e^{-7}$. We also coded the pseudo-arclength continuation method in MATLAB [74]. The MATLAB code was successfully used to find solutions. Accuracy of the solutions found depended upon the finite difference approximations of the spatial and temporal derivatives. In general, solutions were of first order accuracy, as finite difference approximations were of first order accuracy.

Amari model

In Chapter 3, a fourth-order ODE was derived, solutions of which are steady state solutions of the time-dependent Amari model in Equation (7.1). The ODE is

$$u^{(iv)} + 2(1-b^2)u'' + (b^2+1)^2 u = 4b(b^2+1)f(u). \tag{7.139}$$

Using the ODE, the Amari model in Equation (7.1) can be written in the form

$$\left(\frac{\partial^4}{\partial x^4} + 2(1-b^2)\frac{\partial^2}{\partial x^2} + (b^2+1)^2\right)\left(1+\frac{\partial}{\partial t}\right)u(x,t) = 4b(b^2+1)f(u(x,t)). \tag{7.140}$$

Let $u(x,t) = \bar{u}(x) + z(x,t)$ where $\bar{u}$ is a steady state and z is a spatial temporal perturbation. Linearising about the steady state $\bar{u}$ and Taylor expanding we have

$$f(u(x,t)) = f(\bar{u}(x)) + z(x,t)f'(\bar{u}(x)) + \mathcal{O}(z^2). \tag{7.141}$$

So Equation (7.140) can be written as

$$\mathbf{L}\bar{u}(x) + \mathbf{L}\left(1+\frac{\partial}{\partial t}\right)z(x,t) = 4b(b^2+1)\left[f(\bar{u}(x)) + z(x,t)f'(\bar{u}(x))\right] \tag{7.142}$$

where $\mathbf{L} = \dfrac{\partial^4}{\partial x^4} + 2(1-b^2)\dfrac{\partial^2}{\partial x^2} + (b^2+1)^2$. Bounded solutions of the form $z(x,t) = \bar{z}(x)e^{\lambda t}$ are sought. Substituting for $z(x,t)$ in Equation (7.142) results in

$$\mathbf{L}(1+\lambda)\bar{z}(x) = 4b(b^2+1)f'(\bar{u}(x))\bar{z}(x). \tag{7.143}$$

If $\lambda \leq 0$, then the perturbation $z(x,t) \to 0$ as $t \to \infty$ and $\bar{u}(x)$ is a stable steady state.

We wish to find the stability of steady states found using numerical methods such as numerical integration and continuation. To do this, we numerically evaluate the eigenvalues in Equation (7.143). Steady states are found over a finite domain Ω on $\mathbb{R}$. For the numerical analysis here, we take Ω: $[-10\pi, 10\pi]$. The domain is discretised by dividing Ω into n equal intervals of size h such that

$$h = \frac{20\pi}{n}. \tag{7.144}$$

Let $x_i = -10\pi + ih$ for $i = 0, 1, \ldots, n$. The steady state $\bar{u}$ is discretised using the same discretisation as for the domain. Therefore an $n \times 1$ vector, $\mathbf{v}$, is formed such that $\mathbf{v} = [v_0; v_1; \ldots; v_{n-1}]$ where $v_i \approx \bar{u}(-10\pi + ih)$ for $i = 0, 1, \ldots, n-1$. Using finite difference approximations, the $n \times n$ matrix $\mathbf{L}$ is created. From Equation (7.138), the derivative of f with respect to u is

$$\frac{df}{du} = \frac{4r}{(u-\theta)^3}e^{-r/(u-\theta)^2}\Theta(u-\theta). \tag{7.145}$$

Let **Df** be the $n \times n$ sparse diagonal matrix where the diagonal entries are $\dfrac{df(\mathbf{v})}{du}$. Let **Id** be the $n \times n$ identity matrix. Then we have the equation

$$\mathbf{E} = -\mathbf{Id} + 4b(b^2+1)\mathbf{L}^{-1}\mathbf{Df} \tag{7.146}$$

where **E** is an $n \times n$ matrix. In computations, rather than calculating the inverse of the matrix **L**, Gaussian elimination is used as it is faster. We find the eigenvalues of **E**. One eigenvalue will always be zero, as expected from the translational invariance of the model. The eigenvalue with maximum real part, therefore, dictates the stability. Consider the eigenvalue of **E** with maximum real part. If the real part is zero then the steady state $\bar{u}$ is stable. If the real part is positive, then $\bar{u}$ is unstable.

In Chapter 3, solution curves were found using continuation. Solution stability was determined using the method of eigenvalue analysis described above. Therefore the eigenvalues were found for each solution point on the curve, that is, for a steady state associated with a particular value of b. In practice, the top three eigenvalues are plotted for a solution curve. If all three eigenvalues are nonpositive for a particular value of b, then the steady state solution is stable. If one or more of the top three eigenvalues are positive, then the steady state solution is unstable. Slight variation was seen about zero for one eigenvalue. The number of points in the discretisation, n, was chosen so that the eigenvalue curves as a function of b appeared to be smooth curves. To find the most suitable discretisation, the eigenvalue analysis was performed for a particular value of n. The number of points in the discretisation was then doubled to $2n$ and the eigenvalue analysis performed again. If the two eigenvalue analyses were qualitatively similar, then the discretisation of n points was seen as sufficiently accurate for the stability analysis. In general, a discretisation of the domain $[-10\pi, 10\pi]$ into 1999 points was found to be sufficiently accurate.

Gap junction model

In Chapter 3, a sixth-order ODE was derived, solutions of which are steady state solutions of the time-dependent gap junction model in Equation (7.28). The ODE is

$$-\kappa^2 u^{(vi)} + \big(1 + 2\kappa^2(b^2-1)\big)u^{(iv)} - \big(2(b^2-1) + \kappa^2(b^2+1)^2\big)u'' + (b^2+1)^2 u = 4b(b^2+1)f(u). \tag{7.147}$$

For ease of reading, let $c_1 = 1+2\kappa^2(b^2-1)$, $c_2 = -\big(2(b^2-1)+\kappa^2(b^2+1)^2\big)$ and $c_3 = (b^2+1)^2$. Then Equation (7.147) becomes

$$-\kappa^2 u^{(vi)} + c_1 u^{(iv)} + c_2 u'' + c_3 u = 4b(b^2+1)f(u). \tag{7.148}$$

We begin by using the ODE to write the time-dependent gap junction model in Equation (7.28) in the form

$$\left(-\kappa^2 \frac{\partial^6}{\partial x^6} + c_1 \frac{\partial^4}{\partial x^4} + c_2 \frac{\partial^2}{\partial x^2} + c_3 \right) \left(1 + \frac{\partial}{\partial t} \right) u(x,t) = 4b(b^2+1) f(u(x,t)). \tag{7.149}$$

Following the analysis for the Amari model, we have the equation

$$\mathbf{E} = -\mathbf{Id} + 4b(b^2+1)\mathbf{L}^{-1}\mathbf{Df} \tag{7.150}$$

where $\mathbf{L}$ is the discretised version of $-\kappa^2 \frac{\partial^6}{\partial x^6} + c_1 \frac{\partial^4}{\partial x^4} + c_2 \frac{\partial^2}{\partial x^2} + c_3$ and $\mathbf{E}$ is an $n \times n$ matrix. We find the eigenvalues of $\mathbf{E}$ for a steady state for a particular value of b. Again, one eigenvalue will be zero. If any eigenvalue is positive then the steady state is unstable. If all the eigenvalues are nonpositive, then the steady state is stable.

7.6 Numerical integration

Numerical integration can also be used to determine solution stability. In Chapter 4, we constructed piecewise steady state solutions of the neural field models using a step firing rate function. The method of eigenvalue analysis presented in Section 7.5 cannot be used with a piecewise firing rate function. Instead, we add a small perturbation to a steady state and numerically integrate. If the solution tends to the steady state as $t \to \infty$, then it is stable. Otherwise the steady state is unstable. Suitable numerical integration methods are discussed in the Appendix.

7.7 Conclusion

In this chapter we have discussed five methods that can be used to determine the stability of solutions of the Amari model and the gap junction model. The first three of these have been presented previously in the literature and require a step firing rate function. We have applied them to both the models, with a Mexican hat function, then with the decaying oscillatory coupling function. The last two methods require numerical analysis to determine stability and can be used with the smooth firing rate function.

Amari's [1] linearised stability analysis finds the stability of single-bump solutions. The stability condition is the same for both coupling and firing rate function combinations in both models. If two single-bump steady states exist for particular system parameters, then there is a stable wider, taller one and an unstable narrower, shorter one. These stability results agree with the numerical analysis in the thesis. We also used Amari's analysis in

Chapter 2 where steady state solutions of both models with lateral inhibition and a step firing rate function were found analytically.

Pinto and Ermentrout's stability analysis method [82] uses a perturbation analysis of single-bump steady states. For the Amari model, the stability results agree with Amari's linearised stability analysis. The analysis could not be extended to the gap junction model as the second spatial derivatives of both the solution and the perturbation at the boundaries of the region of excitation are not known. Numerical simulation, however, showed that the gap junction model has similar stability results to the Amari model.

An Evans function analysis has been previously used to find the stability of travelling fronts in an Amari-type model with finite propagation velocity [16]. The technique relies upon writing the model as a double integral. We used a Green's function to write the partial integro-differential equation model as an integral equation model. For the Amari model, no travelling fronts were found for the model with lateral inhibition at the specific parameter values we have used throughout the thesis. For the decaying oscillatory coupling function, travelling fronts were found over a wide range of parameters. Evans function analysis showed that the travelling fronts are stable. The results were confirmed by numerical simulation. We could not extend the Evans function analysis to the gap junction model as we were unable to reduce the eventual integral model from a triple integral to a double integral. Evans function analysis was used in Chapter 5 where stable stationary fronts (heteroclinic orbits) were found in the Amari model with decaying oscillatory coupling function.

We presented a method of eigenvalue analysis we developed for both the models with a smooth firing rate function. An eigenvalue equation was solved for a steady state for particular system parameters. The translational invariance of the models means a zero eigenvalue was always found. If the eigenvalues all had a nonpositive real part, then the steady state was stable, otherwise the steady state was unstable. We used eigenvalue analysis to determine the stability of the solutions found with continuation methods in Chapter 3. Finally, we discussed numerical integration as a way to determine solution stability. This method can be used with any coupling and firing rate function combination. The method numerically integrates with a perturbed steady state as the initial condition. If the solution tends to the steady state as time increases then it is a stable steady state.

Chapter 8

Turing structures

8.1 Introduction

We now investigate spatio-temporal pattern formation out of equilibrium in the neural field models. We refer to the spatio-temporal patterns as Turing structures in recognition of Alan Turing's work in 1952 [97]. Turing proposed that pattern formation in biological systems is caused by chemical morphogenesis. It is well known that spatio-temporal patterns can form as a result of spatially uniform equilibrium states losing stability to a spatially heterogeneous perturbation. Both Turing (stationary) and wave (oscillatory Turing) bifurcations lead to a large variety of spatio-temporal patterns. A Turing bifurcation breaks spatial symmetry, generating a pattern that is stationary in time but oscillatory in space. A wave bifurcation breaks both spatial and temporal symmetries, forming patterns that are oscillatory in both time and space [109]. Examples are found in fluid dynamics, solid-state physics, nonlinear optics, reaction-diffusion systems, chemistry and biology [20, 75]. An example is the Turing structures observed in the Belousov-Zhabotinsky (BZ) reaction [100]. Rotating spirals and target waves have been observed in a variety of two-dimensional physical, chemical and biological reaction-diffusion systems [99]. Once initiated, rotating spiral waves are self-sustaining.

We now briefly discuss several relevant papers in the literature. Hutt *et al.* [53] applied an analytical stability method to a one-dimensional neural field model with lateral inhibition and axonal delay to find instabilities where spatio-temporal patterns can form. These are referred to as Turing instabilities. The method uses a linearised stability analysis to identify the unstable wavenumbers in a spatial perturbation that can cause a periodic pattern to form. A Turing instability was identified, as seen in activator-inhibitor systems [97]. Hutt *et al.* observed oscillatory or wave bifurcations in their neural field

model with local inhibition and lateral excitation when the delay exceeded a threshold. The Turing instabilities were independent of delay effects. Recently, Turing structures have also been analysed in several two-dimensional models. Steyn-Ross *et al.* [94] studied a continuum model of a noise-driven cortex with gap junction connections between inhibitory neurons. Using a linear stability analysis and numerical simulation, they found that Turing structures form when the diffusive coupling between gap junctions is large. Coombes *et al.* [18] studied another continuum model with space-dependent axonal delays. In this chapter we apply the linear stability analysis of [53] to both the Amari model and the gap junction model. Instead of lateral inhibition, we use the decaying oscillatory coupling function and smooth firing rate function introduced in Chapter 3. We look for Turing structures in both one and two spatial dimensions.

The plan of the chapter is as follows. Section 8.2 looks at the Amari model and the gap junction model in one spatial dimension. For the Amari model, spatially uniform steady states of the system are found as a function of system parameters. Regions of parameter space where Turing instabilities can occur are found using a linear stability analysis. Numerical simulations are undertaken to find Turing structures for particular parameter values. This involves numerically integrating with an initial condition of a spatially uniform steady state plus a very small random spatial perturbation. To explain the results, spatially periodic patterns are represented by Fourier series. Bifurcation analysis finds regions of parameter space where both stable and unstable periodic patterns exist. We see that the transiency of some solutions is related to a type-I intermittency. The same method is then applied to the gap junction model and numerical simulations are presented. In Section 8.3, the analysis is extended to two spatial dimensions for the Amari model only. Numerical simulations are presented.

8.2 One spatial dimension

Amari model

We are interested in Turing structures in the Amari model

$$\frac{\partial u(x,t)}{\partial t} = -u(x,t) + \int_\Omega w(x-y) f(u(y,t))\, dy \tag{8.1}$$

with decaying oscillatory coupling function

$$w(x) = e^{-b|x|}(b\sin(|x|) + \cos(x)) \tag{8.2}$$

and smooth firing rate function

$$f(u) = 2e^{-r/(u-\theta)^2}\Theta(u-\theta), \tag{8.3}$$

with parameters $b, r, \theta \in \mathbb{R}^+$. Let the domain be Ω: $[-10\pi, 10\pi]$. Let u^* be a spatially uniform steady state of Equations (8.1)–(8.3). One uniform steady state of the model is $u^* = 0$. Nontrivial steady states satisfy

$$u^* = Wf(u^*) \tag{8.4}$$

where

$$W = \int_\Omega w(x-y)\,dy = \frac{4b(1-e^{-10b\pi})}{b^2+1}. \tag{8.5}$$

That is,

$$u^* = \frac{8b(1-e^{-10b\pi})e^{-r/(u^*-\theta)^2}}{b^2+1}. \tag{8.6}$$

Solving Equation (8.6), u^* is found as a function of b and θ (see Figure 8.1). For a particular value of b, there can be one or three uniform steady states, depending upon θ. With respect to spatially uniform perturbations, the zero and upper steady states are always stable and the middle steady state unstable. See Section 2.2 for a linear stability analysis. The two nonzero steady states are destroyed in a saddle-node bifurcation as θ increases.

Method

We now choose u^* to be the upper spatially uniform steady state found in Equation (8.6). Therefore u^* is stable to spatially uniform perturbations. To find a possible Turing bifurcation point, a linear stability analysis is applied. Let

$$u(x,t) = u^* + \sum_{n=-\infty}^{\infty} u_n \exp(ik_n x + \lambda_n t) \tag{8.7}$$

where $k_n = 2\pi n/|\Omega| = n/10$. Linearising about u^* and substituting into Equation (8.1) gives

$$(1+\lambda_n)e^{ik_n x} = \gamma \int_\Omega w(x-y)e^{ik_n y}\,dy \tag{8.8}$$

where $\gamma = f'(u^*)$. So

$$\lambda_n = -1 + \gamma\,\frac{4b(b^2+1)\big[1-(-1)^n e^{-10b\pi}\big]}{(b^2+k_n^2)^2 + 2(b^2-k_n^2)+1}. \tag{8.9}$$

Only real λ_n exist so no oscillatory bifurcations are expected. Bifurcations can occur at $\lambda_n = 0$. The bifurcations are referred to as Turing instabilities or Turing bifurcations.

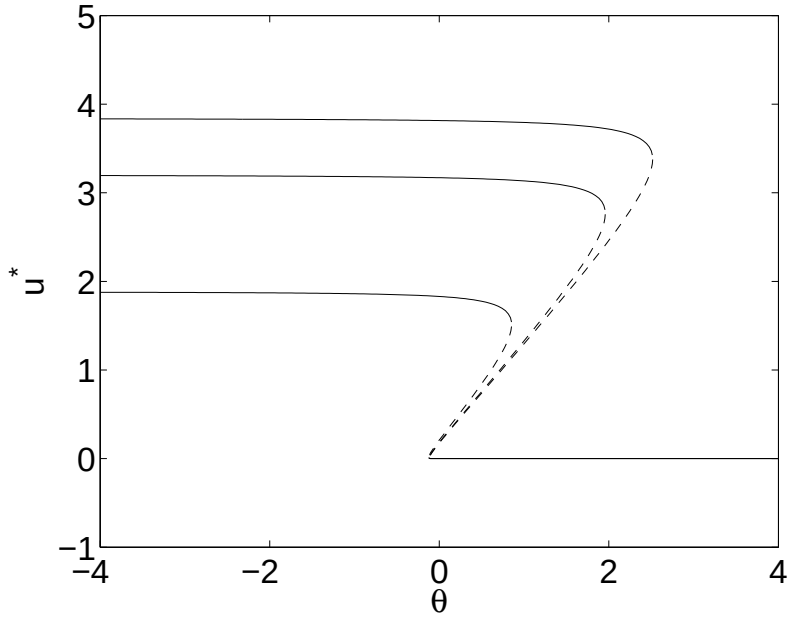

Figure 8.1: Spatially uniform steady states, u^*, of Equations (8.1)–(8.3) as a function of θ, as given by Equation (8.4). Curves from bottom to top are for $b = 0.25, 0.50, 0.75$ respectively. Solid line: stable; dashed line: unstable. $r = 0.095$.

The first instability occurs when there is a value of k_n for which λ_n is non-negative. As θ is varied, the onset of instability is given by $\lambda_n = 0$. We define Ψ as

$$\Psi = \gamma|_{\lambda_n=0} = \frac{(b^2 + k_n^2)^2 + 2(b^2 - k_n^2) + 1}{4b(b^2+1)\left[1 - (-1)^n e^{-10b\pi}\right]}. \tag{8.10}$$

When $\gamma < \Psi$, $\lambda_n < 0$ for all n. Given b, it may be possible to vary the system parameter θ and find u^* such that $\gamma = f'(u^*) = \Psi$. From the definition of Ψ in Equation (8.10), $\lambda_n = 0$. Therefore the onset of instability occurs where γ meets Ψ for the first time from below. The dominant unstable wavenumber is the wavenumber with the smallest value of Ψ. Figure 8.2 shows Ψ as a function of k_n for $b = 0.25, 0.50, 0.75$. The wavenumbers $k_n = n/10$ are indicated by circles, asterisks and diamonds for $b = 0.25, 0.50, 0.75$, respectively. For $b = 0.25$, the horizontal line shows $\gamma = \Psi$ and indicates the onset of instability. We see that the unstable wavenumber is $k_n = 1.0$. As θ is varied further, γ increases through Ψ and u^* loses stability to a spatial perturbation. From Figure 8.2 we also see that the dominant unstable wavenumber for $b = 0.50$ is $k_n = 0.9$.

The minimum of Ψ is found by treating k_n as a continuous variable and solving $d\Psi/\,dk_n = 0$ for k_n. When $0 < b < 1$, the minimum of Ψ is given by

$$k_n = \sqrt{1 - b^2}. \tag{8.11}$$

See Figure 8.3 for the plot of Equation (8.11). We see that as b increases, the dominant

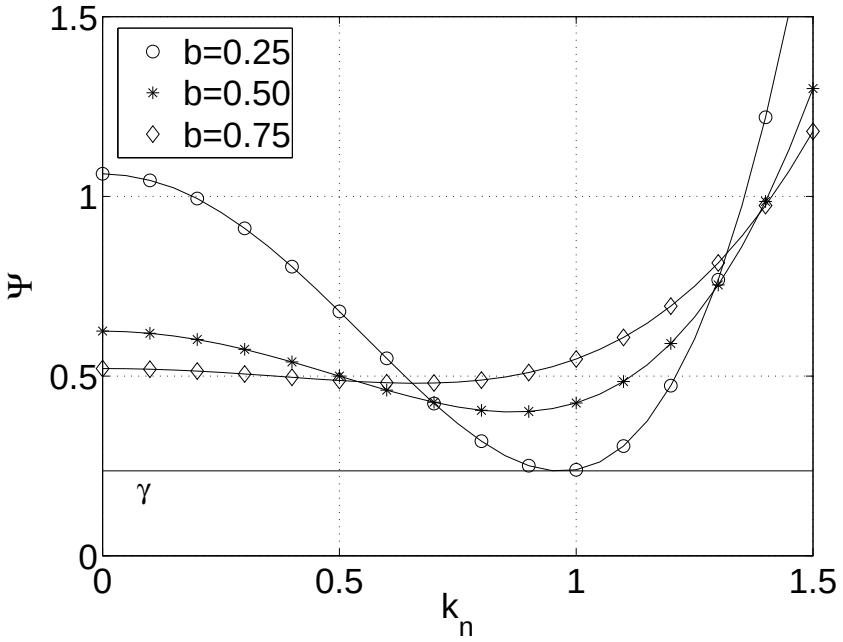

Figure 8.2: Ψ as a function of k_n for $b = 0.25, 0.50, 0.75$. The wavenumbers $k_n = n/10$ are indicated by circles, asterisks and diamonds for $b = 0.25, 0.50, 0.75$, respectively. For $b = 0.25$, the horizontal line of γ indicates the onset of instability and a dominant unstable wavenumber of $k_n = 1.0$.

unstable wavenumber becomes smaller. When $b > 1$, $\dfrac{d\Psi}{dk_n} > 0$, so if u^* is spatially perturbed the system returns either to u^* or the uniform zero steady state.

Results

We tune the system to find Turing instabilities for certain parameter values. We use a uniform grid of 301 points over Ω with periodic boundaries. A random spatial perturbation with absolute value less than 10^{-5} is created using the *rand* function in Matlab [74]. The same random perturbation is used for all numerical simulations in this section. For all numerical work in the chapter, we set $r = 0.095$ in Equation (8.3). Using Equation (8.10) with a particular value of b, if possible, we find Ψ where a Turing instability can occur. We find θ and u^* such that $f'(u^*)$ is just past the onset of instability, that is, $f'(u^*) > \Psi$. An initial condition is set, $u(x, 0)$, of the uniform steady state u^* plus the random spatial perturbation. Euler steps in time are taken until a steady state is reached.

For $b = 0.25$ and $\theta = 0.63$, a stable 10-bump pattern occurs as the dominant wavenumber is $k = 1.0$ (see Figure 8.4). For $b = 0.50$ and $\theta = 1.94$, a transient Turing structure emerges as the system moves eventually to the spatially uniform zero steady state (see Figure 8.5). Here, the transient pattern has $n = 9$, as expected from the analysis above.

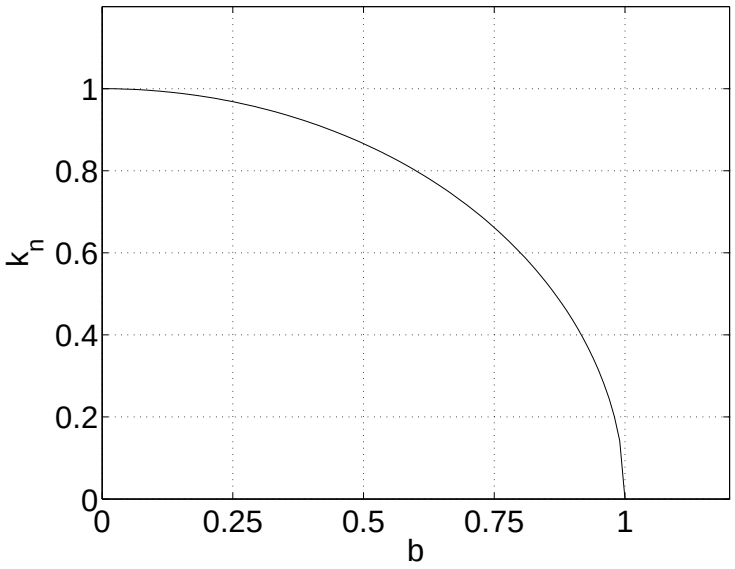

Figure 8.3: Wavenumber k_n as a function of b for the minimum of Ψ.

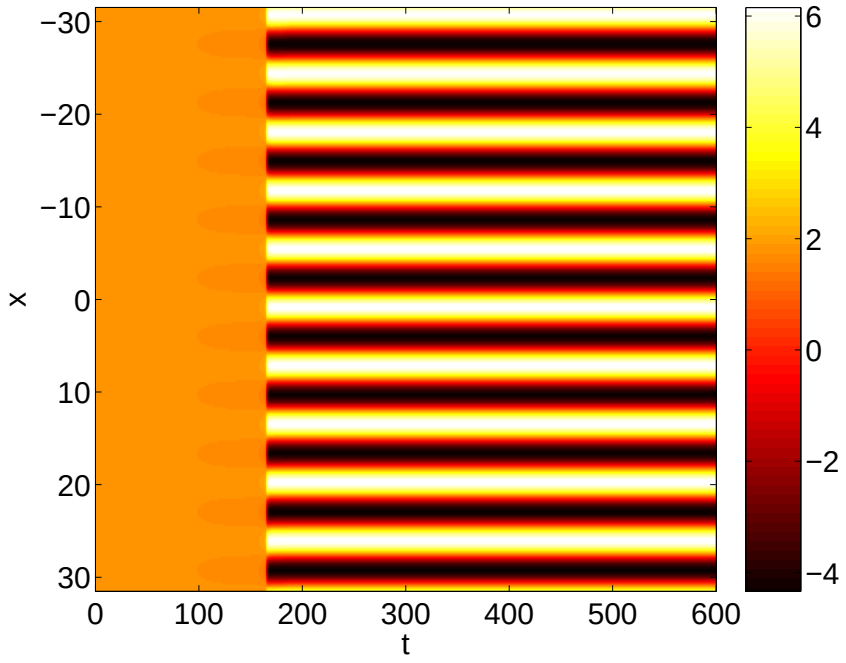

Figure 8.4: A stable Turing structure with $n = 10$ for $b = 0.25$ and $\theta = 0.63$.

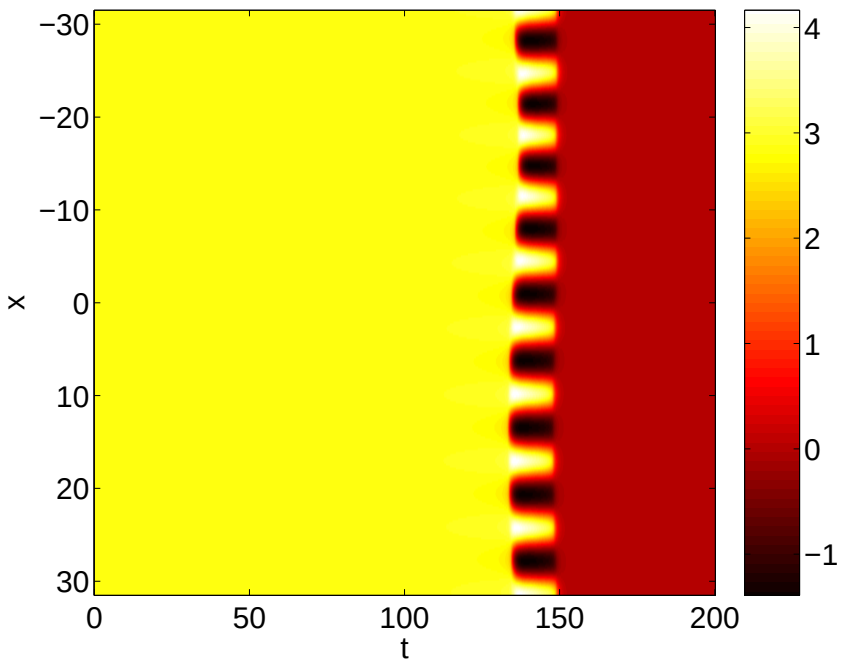

Figure 8.5: A transient Turing structure with $n = 9$ for $b = 0.50$ and $\theta = 1.94$. Compare with Figure 8.4.

For $0.25 < b < 0.50$, it is possible to find further transient patterns. For $b = 0.4825$, both stable and transient Turing structures are found (see Figure 8.6). When $\theta = 1.87$, a stable structure is found (top plot). When θ is increased to 1.88, a transient structure is seen (bottom plot). Our conjecture is that for small b a stable periodic pattern exists and the system is attracted to this pattern when a Turing bifurcation occurs. For larger b, we conjecture that a stable pattern does not exist and therefore only a transient pattern can be seen.

Bifurcation analysis

We test our conjecture using bifurcation analysis. In this section we follow periodic patterns in parameter space to determine the regions for which stable periodic patterns exist. These spatially-periodic patterns can be represented using Fourier series:

$$u(x) = \frac{a_0}{2} + \sum_{m=1}^{\infty} \left[a_m \cos(mk_n x) + b_m \sin(mk_n x) \right]. \tag{8.12}$$

As $k_n = n/10$, this is

$$u(x) = \frac{a_0}{2} + \sum_{m=1}^{\infty} \left[a_m \cos(mnx/10) + b_m \sin(mnx/10) \right]. \tag{8.13}$$

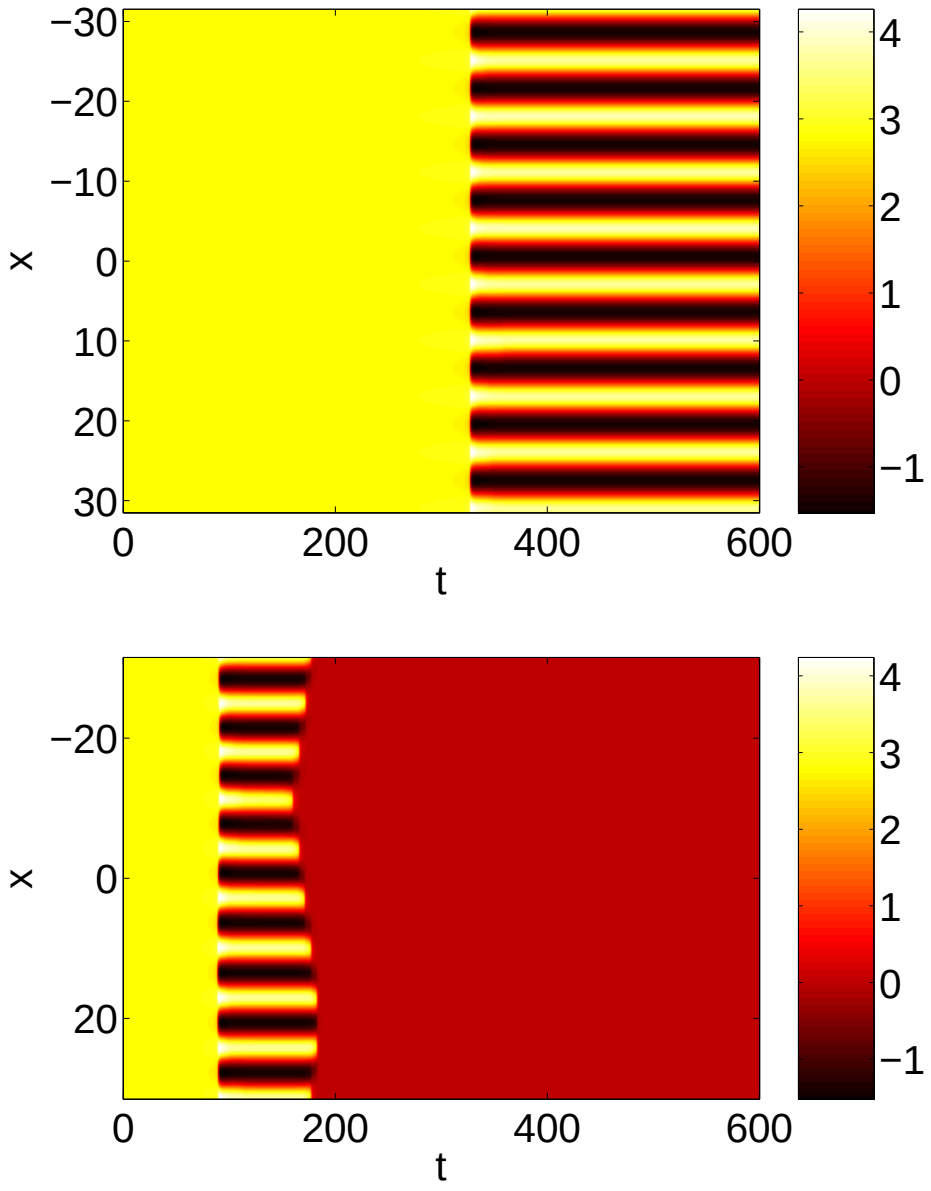

Figure 8.6: Turing structures with $n = 9$ for $b = 0.4825$. Top: A stable pattern with $\theta = 1.87$. Bottom: A transient pattern with $\theta = 1.88$. Compare with Figures 8.4 and 8.5.

Since we are using a domain $\Omega\colon [-10\pi, 10\pi]$, we take $w(x)$ in Equation (8.2) as periodic with period 20π. Therefore

$$w(x) = \frac{\alpha_0}{2} + \sum_{p=1}^{\infty} \alpha_p \cos(px/10) \tag{8.14}$$

where

$$\alpha_0 = \frac{2}{20\pi} \int_\Omega w(x)\, dx = \frac{2b(1 - e^{-10b\pi})}{5\pi(b^2 + 1)} \tag{8.15}$$

and

$$\alpha_p = \frac{2}{20\pi} \int_\Omega \cos(px/10) w(x)\, dx = \frac{2b(b^2+1)(1 - e^{-10b\pi})}{5\pi\{[b^2 + (p/10)^2]^2 + 2[b^2 - (p/10)^2] + 1\}}. \tag{8.16}$$

Setting $\partial u/\partial t = 0$ in Equation (8.1) and using the trigonometric identity

$$\cos(x - y) = \cos(x)\cos(y) + \sin(x)\sin(y),$$

we have

$$\frac{a_0}{2} + \sum_{m=1}^{\infty} [a_m \cos(mnx/10) + b_m \sin(mnx/10)] = \frac{\alpha_0}{2} \int_\Omega f[u(y)]\, dy \tag{8.17}$$

$$+ \sum_{p=1}^{\infty} \alpha_p \left[\cos(px/10) \int_\Omega \cos(py/10) f[u(y)]\, dy + \sin(px/10) \int_\Omega \sin(py/10) f[u(y)]\, dy \right]. \tag{8.18}$$

Thus

$$a_0 = \alpha_0 \int_\Omega f[u(x)] dx \tag{8.19}$$

$$a_m = \alpha_{mn} \int_\Omega \cos(mnx/10) f[u(x)] dx \tag{8.20}$$

and

$$b_m = \alpha_{mn} \int_\Omega \sin(mnx/10) f[u(x)] dx. \tag{8.21}$$

Since $u(x)$ is periodic with period $20\pi/n$ we have the following nonlinear coupled equations

$$a_0 = n\alpha_0 \int_0^{20\pi/n} f[u(x)] dx \tag{8.22}$$

$$a_m = n\alpha_{mn} \int_0^{20\pi/n} \cos(mnx/10) f[u(x)] dx \tag{8.23}$$

$$b_m = n\alpha_{mn} \int_0^{20\pi/n} \sin(mnx/10) f[u(x)] dx. \tag{8.24}$$

where $u(x)$ is a function of a_m, b_m as in Equation (8.13). Given the translational invariance of the system, these equations specify an infinite family of solutions. By imposing a condition, we choose one solution only. We set the condition $a_1 = 0$. Continuation methods can now be used to find the solution curves of n-bump periodic patterns.

Let $b = 0.25$. By solving Equations (8.22)–(8.24) for $n = 8, 9, 10$, we can find 8-, 9- and 10-bump solutions. The solutions can be used as starting solutions with continuation methods. Through continuation in θ, we find the solution curves for $n = 10, 9, 8$ (right to left) in Figure 8.7. Stable solutions are indicated by solid lines and unstable solutions by dashed lines. As θ is increased, 10-bump solutions are the last to be destroyed in a saddle-node bifurcation. Vertical lines indicate the value of θ for which a Turing instability occurs where $n = 10, 9, 8$ (solid, dashed, dashed-dot, respectively). The smallest value of θ for which a Turing instability can occur is for Turing instabilities with the wavenumber $k_n = 1.0$, that is, $n = 10$. Thus a 10-bump periodic solution will always arise in a Turing instability for these parameter values. The saddle-node bifurcation of the upper and middle spatially uniform steady states is given by the circles joined by solid lines. A spatially uniform steady state cannot exist for θ to the right of this line. So for θ to the left of the solid vertical line, a stable uniform steady state will be unaffected by perturbation. For θ between the solid vertical line and the saddle-node bifurcation vertical line, a Turing instability can occur and a stable 10-bump solution forms. For θ to the right of the saddle-node bifurcation line, Turing instabilities cannot occur. A 10-bump solution can still exist, as shown by the solution curve, however, it will not arise through a Turing instability.

When $b = 0.4825$, the system can show both stable and unstable 9-bump Turing structures, depending upon θ (see Figure 8.6). The behaviour is possible as the Turing instability with $n = 9$ occurs for a value of θ only slightly less than the value of θ where the saddle-node bifurcation of 9-bump solutions occurs. So for a small range of θ, a Turing instability can arise and a stable 9-bump solution is the result. As θ increases past the saddle-node bifurcation of the solution curve, only transient Turing structures can occur. Eventually θ increases to where a nonzero spatially uniform steady state can no longer exist and so no Turing instabilities can arise. Numerical analysis in the previous section showed only transient Turing structures for $b = 0.50$ (see Figure 8.5). Turing instabilities can only occur for values of θ greater than where the saddle-node bifurcation of the 9-bump solution curve occurs. Therefore there are no stable 9-bump solutions to be attracted to and only transient structures will occur.

We now summarise these results in the (θ, b) plane for $0.44 \leq b \leq 0.50$ and $1.78 \leq \theta \leq 1.9$. In Figure 8.8, we plot the curves of the n-bump saddle-node bifurcations for $n = 8, 9, 10$ (bold dashed-dot, bold solid and bold dashed, respectively) and the curves of Turing instabilities for $n = 8, 9, 10$ (dashed-dot, solid and dashed, respectively). Given

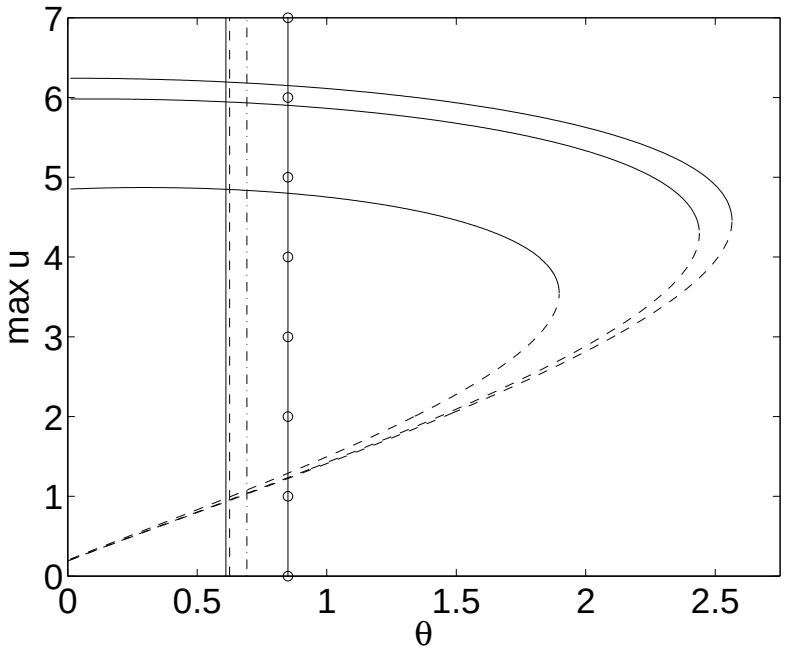

Figure 8.7: Solution curves for $n = 10, 9, 8$ (right to left) n-bump periodic patterns for $b = 0.25$. Solid line for stable solution and dashed line for unstable solution. The vertical lines give the Turing instability for $n = 10, 9, 8$ (solid, dashed, dashed-dot, respectively). The saddle-node bifurcation of the upper and middle spatially uniform steady states is given by the circles joined by solid lines. Turing instabilities give rise to periodic patterns with $n = 10$. Turing instabilities can occur between the solid line for $n = 10$ and the saddle-node bifurcation line.

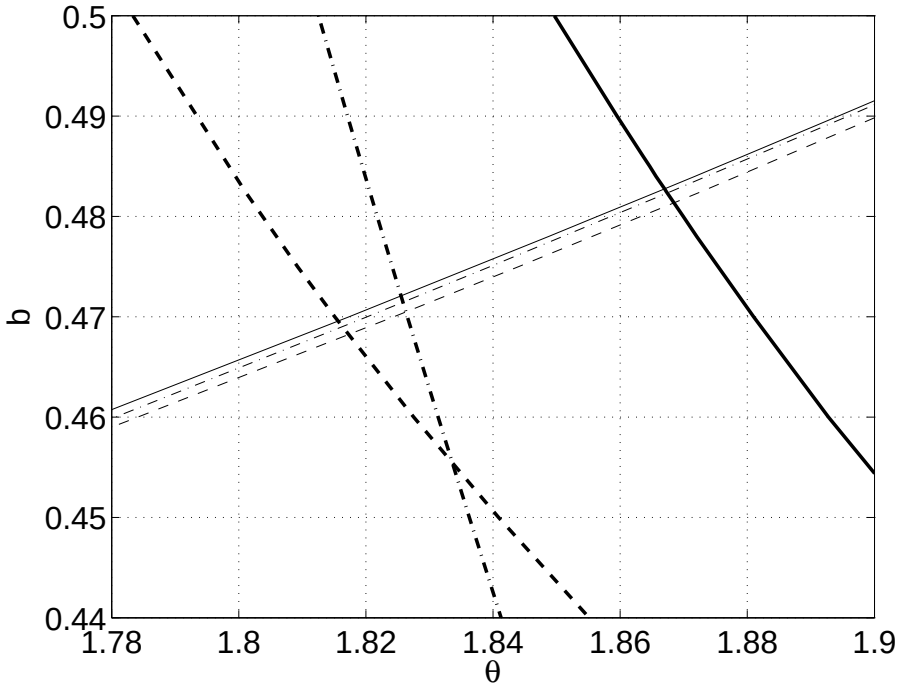

Figure 8.8: Curves of saddle-node bifurcations of n-bump periodic patterns (bold lines) and curves of Turing instabilities for $n = 8, 9, 10$ (dashed-dot, solid and dashed, respectively).

a particular value of b, the Turing instability curve that occurs at the lowest value of θ is the curve for $n = 9$. Therefore, $k = 0.9$ is the dominant unstable wavenumber and only 9-bump Turing structures will appear in this region of parameter space. For any particular value of b, 9-bump Turing structures exist for θ to the right of the 9-bump Turing instability curve (solid line). If the Turing instability curve is to the right of the saddle-node curve (bold solid line), only transient Turing structures can occur as there is no stable 9-bump pattern to be attracted to. If the Turing instability curve is to the left of the saddle-node curve, stable Turing structures exist for θ between the two curves and transient Turing structures for θ to the right of the saddle-node curve.

In Figure 8.9, we plot the curves of Turing instabilities and the curve of saddle-node bifurcations of the upper and middle spatially uniform steady states in the (θ, b) plane. The top plot shows $0.46 \leq b \leq 0.50$. The bottom plot shows $0.25 \leq b \leq 0.30$. In each case, the curves of Turing instabilities for $n = 8, 9, 10$ (dashed-dot, solid and dashed, respectively) are shown. The curve of saddle-node bifurcations of the upper and middle fixed points is given by the circles joined by solid lines. No Turing structures can exist for (θ, b) to the right of the saddle-node bifurcation curve as no nonzero spatially-uniform steady state exists. In the top plot, the Turing instability curve for $n = 9$ is always leftmost, so only 9-bump periodic patterns will occur for $0.46 \leq b \leq 0.50$. In the bottom plot, the Turing

instability curve for $n = 10$ is always leftmost, so only 10-bump periodic patterns will occur for $0.25 \leq b \leq 0.30$. The results are confirmed by the numerical simulations in Figures 8.4–8.6.

Intermittency

The transient behaviour seen in the solutions for $b = 0.4825$ and $b = 0.50$ is caused by the system passing close to a region of phase space where stable periodic patterns exist. A "ghost" of the stable periodic pattern is seen as a transient pattern as the system is attracted to another stable spatially-uniform steady state. A "ghost" effect is known in relation to type-I intermittency and has been described in chemical systems [26, 46, 56, 71].

If a periodic pattern has a wavenumber of k, then it is an n-bump solution where $n = 10k$, $(n = 0, 1, 2, \ldots)$. An n-bump periodic pattern is destroyed in a saddle-node bifurcation as θ increases through θ^*, say. Transient patterns may appear for $\theta > \theta^*$. Theory says that the length of time a transient pattern appears scales as $(\theta - \theta^*)^{-1/2}$ [46]. By observing the length of time, T, a transient periodic pattern exists for varying values of θ close to θ^*, the scaling relationship can be verified. If this type of intermittency occurs then

$$T = \frac{A}{\sqrt{(\theta - \theta^*)}} \tag{8.25}$$

for some $A \in \mathbb{R}$. Therefore, a plot of $\log(T)$ as a function of $\log(\theta - \theta^*)$ would have a slope of -0.5. Both stable and transient 9-bump periodic patterns were seen for $b = 0.4825$. We found a saddle-node bifurcation at $\theta^* = 1.8673$ for 9-bump solutions. Turing structures are stable for $\theta < \theta^*$ and unstable for $\theta > \theta^*$. In numerical simulations we vary θ close to θ^* and find T, the length of time the transient pattern is seen. Figure 8.10 shows a plot of $\log(T)$ as a function of $\log(\theta - \theta^*)$ for $b = 0.4825$. As $\theta - \theta^* \to 0^+$, the length of time the transient structure is seen increases. A least-squares fitted straight line through the data points has a slope of -0.50071. The result confirms the transient patterns are a type-I intermittency. Numerically, it was found that both the spatial and temporal discretisations in the numerical integration scheme are very important as $\theta - \theta^*$ becomes smaller. If the time step is too large, the length of the time the transient Turing structure exists may be inaccurate. If the spatial step is too large, the true transiency of the Turing structure may not be displayed.

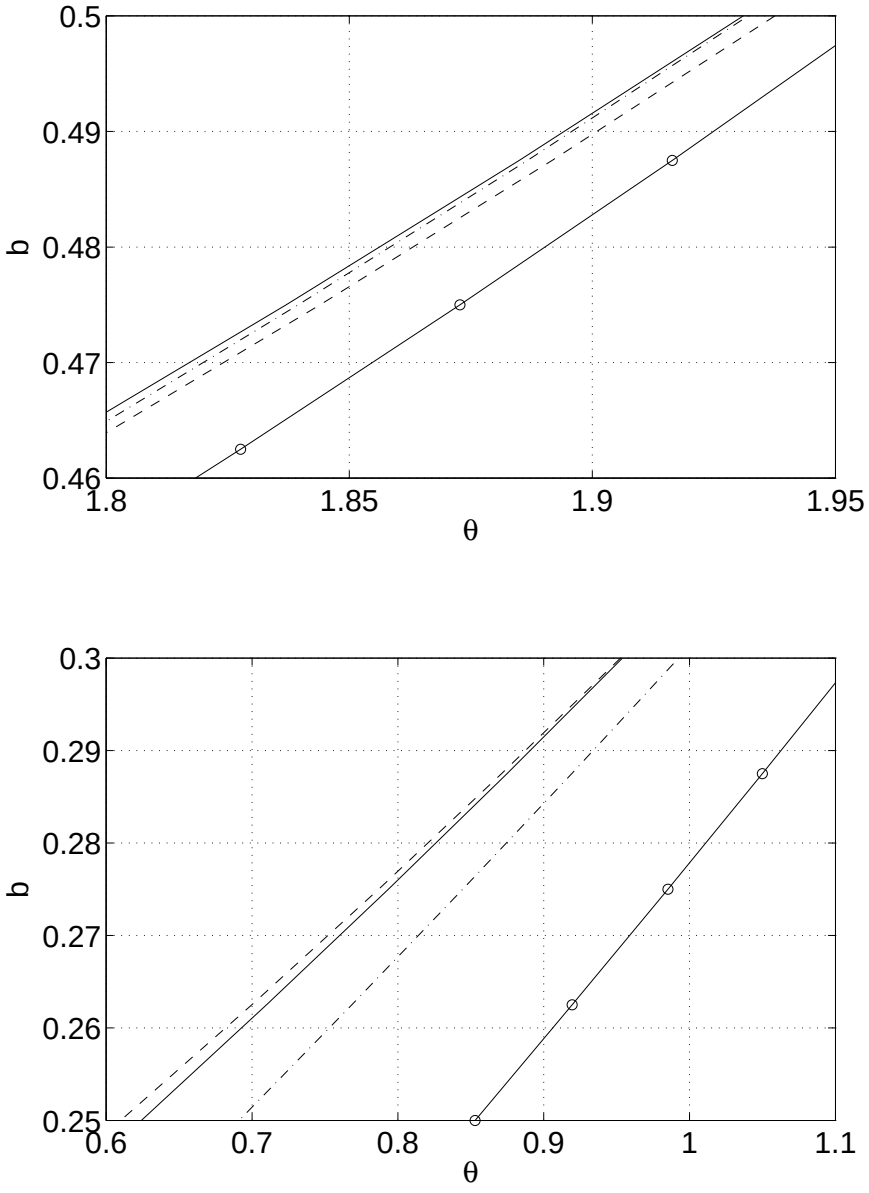

Figure 8.9: Curves of saddle-node bifurcations of n-bump periodic patterns (circles joined by solid lines) and curves of Turing instabilities for $n = 8, 9, 10$ (dashed-dot, solid and dashed, respectively).

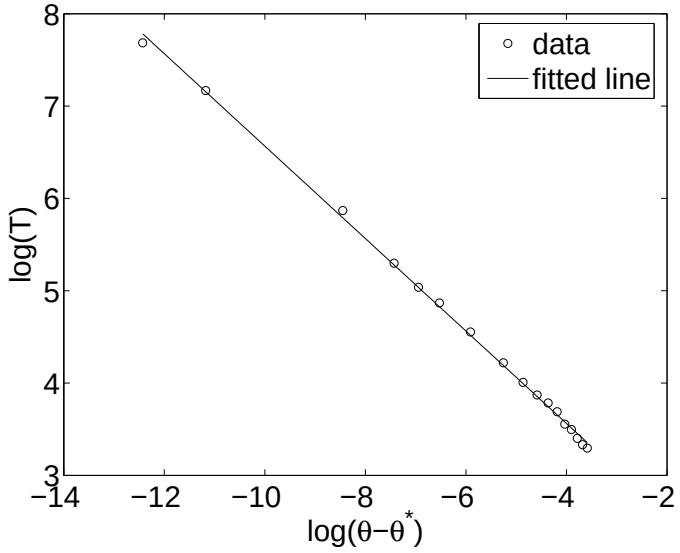

Figure 8.10: Plot of $\log(T)$ as a function of $\log(\theta - \theta^*)$ where T is the length of time the transient 9-bump Turing structure is present for $b = 0.4825$ and θ. The saddle-node bifurcation of 9-bump periodic patterns occurs at θ^*. The fitted line has a slope of -0.50071 and confirms intermittency.

Gap junction model

We now look for Turing instabilities in the gap junction model

$$\frac{\partial u(x,t)}{\partial t} = \kappa^2 \frac{\partial^2 u}{\partial x^2} - u(x,t) + \int_{-\infty}^{\infty} w(x-y) f(u(y,t))\, dy \tag{8.26}$$

where $w(x)$ is as in Equation (8.2), $f(u)$ is as in Equation (8.3) and $\kappa^2 > 0$.

Method

To find Turing bifurcation points, the same linear stability analysis is followed as for the Amari model. Due to the presence of the second spatial derivative, Equation (8.9) becomes

$$\lambda_n = -1 - k_n^2 \kappa^2 + \gamma \, \frac{4b(b^2+1)\left[1 - (-1)^n e^{-10b\pi}\right]}{(b^2 + k_n^2)^2 + 2(b^2 - k_n^2) + 1} \tag{8.27}$$

where $\gamma = f'(u^*)$. Again, only real solutions exist for λ_n so no oscillatory bifurcations are expected. Again, we define Ψ as follows

$$\Psi = \gamma|_{\lambda_n = 0} = (1 + k_n^2 \kappa^2) \frac{(b^2 + k_n^2)^2 + 2(b^2 - k_n^2) + 1}{4b(b^2+1)\left[1 - (-1)^n e^{-10b\pi}\right]}. \tag{8.28}$$

When $\kappa^2 > 0$, a Turing bifurcation point for the gap junction model occurs at a higher value of $f'(u^*)$ than when $\kappa^2 = 0$ as in the Amari model in Equation (8.10).

Results

The general results are the same as for the Amari model in that stable Turing structures exist for small b and unstable Turing structures exist for larger b. The diffusive effect of

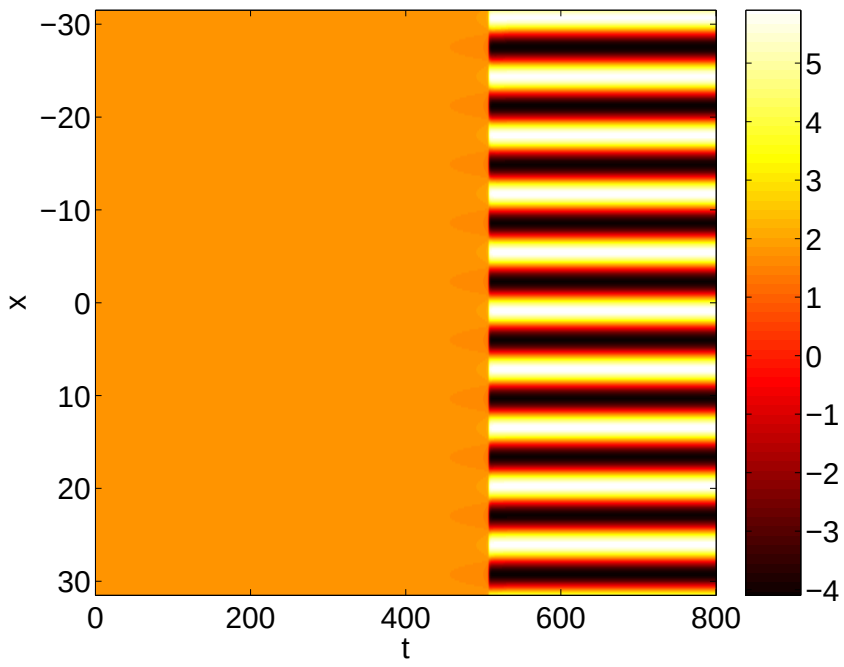

Figure 8.11: A stable Turing structure with $n = 10$ for $\kappa^2 = 0.05$, $b = 0.25$ and $\theta = 0.63$.

the gap junction term causes the Turing instability to take longer to appear. The effect can be seen in Equation (8.27) where λ_n is smaller for $\kappa^2 > 0$ than for $\kappa^2 = 0$. We first set $\kappa^2 = 0.05$. For $b = 0.25, 0.50$, the Turing instability appears later than when $\kappa^2 = 0$. Compare Figures 8.11–8.12 to Figures 8.4–8.5. For $b = 0.25$ and $\theta = 0.63$, a stable 10-bump Turing structure occurs (see Figure 8.11). When $b = 0.50$, there is a Turing instability at $\theta = 1.94$ (see Figure 8.12). For $\kappa^2 = 0.05$ (top), a transient Turing structure occurs much earlier than when $\kappa^2 = 0.10$ (bottom). In general, increasing κ^2 causes a Turing structure to take longer to appear as the diffusive effect dampens the exponential growth of the unstable wavenumber. Eventually, κ^2 increases to a level where a Turing instability cannot occur.

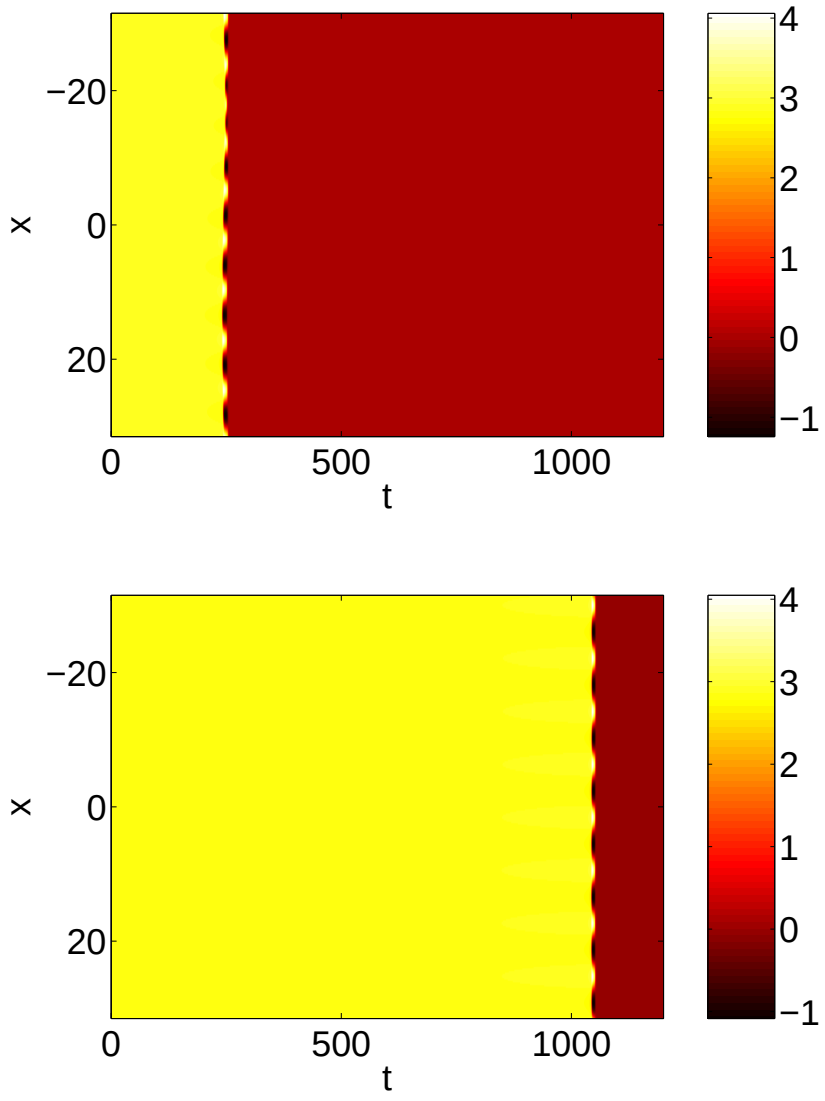

Figure 8.12: Transient Turing structures with $n = 9$ and $\kappa^2 > 0$ for $b = 0.50$ and $\theta = 1.94$. When $\kappa^2 = 0.05$ (top plot), the pattern appears earlier than when $\kappa^2 = 0.10$ (bottom plot).

8.3 Two spatial dimensions

We now extend the Turing instability analysis of the Amari model to two spatial dimensions. In Section 8.2, we studied the one-dimensional Amari model of

$$\frac{\partial u(x,t)}{\partial t} = -u(x,t) + \int_{\Omega} w(x-y) f(u(y,t))\, dy \tag{8.29}$$

where $w(x)$ and $f(u)$ are as in Equations (8.2) and (8.3) respectively. By taking Fourier transforms we obtain

$$\left(\frac{\partial^4}{\partial x^4} + 2(1-b^2)\frac{\partial^2}{\partial x^2} + (b^2+1)^2\right)\left(\frac{\partial u(x,t)}{\partial t} + u(x,t)\right) = 4b(b^2+1) f\big(u(x,t)\big). \tag{8.30}$$

The two-dimensional analogue is

$$\left(\nabla^4 + 2(1-b^2)\nabla^2 + (b^2+1)^2\right)\left(\frac{\partial u(\mathbf{x},t)}{\partial t} + u(\mathbf{x},t)\right) = 4b(b^2+1) f\big(u(\mathbf{x},t)\big) \tag{8.31}$$

where $\mathbf{x} \in \mathbb{R}^2$. Here, ∇^2 is the two-dimensional Laplacian $\nabla^2 u = u_{xx} + u_{yy}$ and ∇^4 is the biharmonic operator $\nabla^4 u = u_{xxxx} + 2u_{xxyy} + u_{yyyy}$. By using the form of the model in Equation (8.31), we avoid the numerical computation of a convolution. In two dimensions, numerically evaluating finite difference approximations is much less computationally expensive than the evaluation of a convolution.

Method

We assume an infinite domain in the analysis. Spatially uniform steady states of Equation (8.31) are denoted by u^*. One is $u^* = 0$. Nontrivial solutions satisfy

$$(b^2+1)^2 u^* = 4b(b^2+1) f(u^*) \tag{8.32}$$

where $u^* > \theta$, as before. Hence $u^* = 4bf(u^*)/(b^2+1)$. We can see that steady states are the same as those for the one-dimensional Amari model in Section 8.2. Let

$$u(\mathbf{x},t) = u^* + \int_{\mathbb{R}^2} u_{\mathbf{k}} e^{i\mathbf{k}\cdot\mathbf{x} + \lambda t}\, d\mathbf{k}. \tag{8.33}$$

Linearising about u^* and substituting into Equation (8.31), we obtain

$$\big(|\mathbf{k}|^4 - 2(1-b^2)|\mathbf{k}|^2 + (b^2+1)^2\big)(1+\lambda) = 4b(b^2+1)\gamma \tag{8.34}$$

where $\gamma = f'(u^*)$. So

$$\lambda = -1 + \gamma \frac{4b(b^2+1)}{(b^2+|\mathbf{k}|^2)^2 + 2(b^2-|\mathbf{k}|^2) + 1}. \tag{8.35}$$

The expression for λ is the same as for the one-dimensional model except for a correction term due to the finite domain. The finite size of the domain is expected to have a small effect. The analysis proceeds as for the one-dimensional case but over a two-dimensional domain.

Results

Let Ω be $[-10\pi, 10\pi]$. The system in Equation (8.31) is numerically simulated over the two-dimensional square domain $\Omega \times \Omega$. The domain is discretised by a uniform 100×100 grid with periodic boundaries. Both ∇^2 and ∇^4 are approximated using finite differences. A random two-dimensional spatial perturbation with absolute value less than 10^{-5} is created using Matlab [74], as in the one-dimensional study. The same perturbation is used for all two-dimensional numerical simulations in this section. With the initial condition, $u(\mathbf{x}, 0)$, of a spatially perturbed uniform steady state, Euler steps in time are taken. For $b = 0.25$ and $\theta = 0.67$, a Turing structure occurs. As time increases, the structure remains relatively constant. Figure 8.13 shows the development of the Turing structure as time increases (top to bottom). When $t = 120$ (top plot), some hexagonal Turing structures have appeared. At $t = 300$ (middle plot), a Turing structure is seen. At $t = 1000$ (bottom plot), the Turing structure has changed very little.

For $b = 0.5$ and $\theta = 1.96$, a transient Turing structure is observed. Figure 8.14 shows $u(\mathbf{x}, t)$ at three different times in the numerical integration. When $t = 30$ (top plot), a pattern is beginning to appear. At $t = 36$ (middle plot), a Turing structure is clearly seen. At $t = 41$ (bottom plot), the Turing structure is disappearing as the system moves to the stable spatially uniform zero steady state.

So for the two-dimensional Amari model, Turing structures are seen for small b that appear to be quite stable and transient Turing structures are seen for large b. The general behaviour is the same as in one spatial dimension. In one spatial dimension, the effect of increasing κ^2 in the gap junction model caused Turing instabilities to take longer to appear. We expect the two-dimensional gap junction model to show similar behaviour.

8.4 Conclusion

In this chapter we studied pattern formation arising out of Turing bifurcations. We have analytically and numerically demonstrated the existence of Turing structures in the Amari model and in the gap junction model in one spatial dimension. Analysis and numerical simulations were also carried out for the Amari model in two spatial dimensions. In one spatial dimension, we investigated the dependence of Turing structures upon the parameters of the system using a linear stability analysis. The analysis permitted us to determine regions of parameter space where Turing bifurcations (Turing instabilities) occur. The analysis also found the dominant wavenumber of the periodic patterns arising

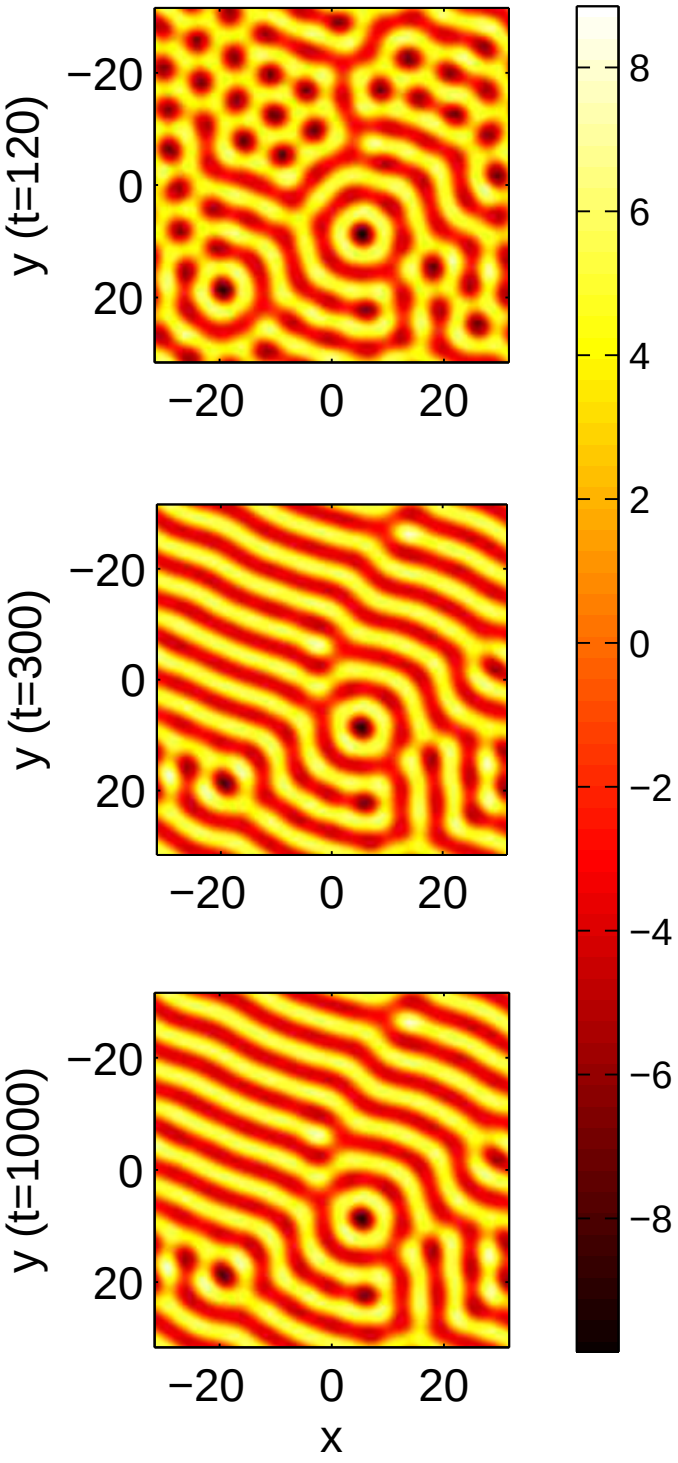

Figure 8.13: A stable Turing structure for $b = 0.25$ and $\theta = 0.67$ in two spatial dimensions for three different time lengths, t, of numerical integration. As t increases (top to bottom), some hexagonal Turing structures appear and a Turing structure emerges.

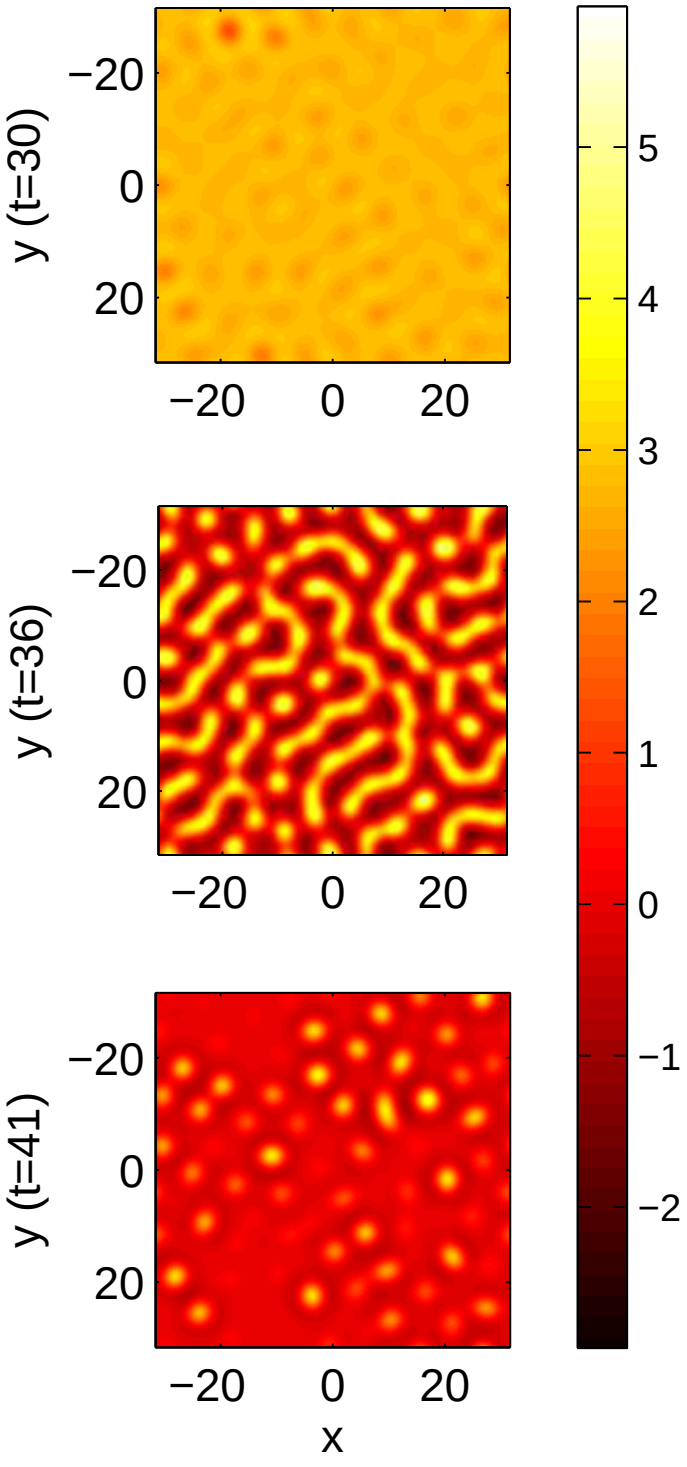

Figure 8.14: A transient Turing structure for $b = 0.50$ and $\theta = 1.96$ in two spatial dimensions for three different time lengths, t, of numerical integration. As t increases (top to bottom), a transient Turing structure appears and then disappears, eventually moving to the spatially uniform zero steady state.

out of a Turing instability.

Numerically, both stable and unstable Turing structures are found. In general, stable Turing structures are found for small b. As b increases, a Turing structure appears through a Turing instability but it is only seen transiently. Using bifurcation analysis, we determined the parameter ranges of both stable and unstable periodic patterns. For small b, it was found that stable periodic patterns exist in the regions of parameter space where Turing instabilities can occur. As b increases, no stable periodic patterns exist in the regions of parameter space where Turing instabilities can arise. In these regions, if a Turing instability occurs, a Turing structure exists only briefly as the system moves to another stable attractor. The transient behaviour is caused by the system passing close to a region of phase space where stable periodic patterns exist. We have shown the transient behaviour is a type-I intermittency as seen previously in the literature in chemical systems.

As the strength of the term modelling gap junctions is increased, a Turing instability takes longer to appear. The cause is the diffusive effect of the gap junction term dampening the exponential growth of the perturbation. In general, however, the gap junction model displays similar behaviour to the Amari model in that stable Turing structures are seen for small b and transient patterns for larger b.

Analysis was extended to the Amari model in two spatial dimensions. To reduce computational demands, the model was written in PDE form rather than the partial integro-differential equation in one dimension. Numerical simulation showed the two-dimensional model has similar behaviour to the one-dimension model. For small b, Turing structures appear that seem to be stable. For large b, transient Turing structures appear. We expect the two-dimensional gap junction model to display similar behaviour to the one-dimensional gap junction model. We note the extension of the analysis and numerical work to two dimensions for the gap junction model as a suitable project for future study.

Appendix

A1. Numerical integration schemes

In Chapter 3, we use numerical integration with suitable initial conditions to find stable steady states of the neural field model

$$\frac{\partial u(x,t)}{\partial t} = \kappa^2 \frac{\partial^2 u}{\partial x^2} - u(x,t) + \int_{-\infty}^{\infty} w(x-y) f(u(y,t))\, dy \tag{8.36}$$

where $\kappa^2 > 0$, $f(u)$ is the smooth firing rate function

$$f(u) = 2e^{-r/(u-\theta)^2}\Theta(u-\theta), \tag{8.37}$$

Θ is the Heaviside function and w is the decaying oscillatory coupling function

$$w(x) = e^{-b|x|}\left(b\sin(|x|) + \cos(x)\right). \tag{8.38}$$

The model is defined over an infinite domain, however, computational methods require a finite domain. We approximate an infinite domain by choosing a finite domain sufficiently large that there is no activity near the boundaries. That is, $u \to 0$ as $x \to \pm\infty$. For numerical integration in the thesis we assume a finite domain of Ω: $[-10\pi, 10\pi]$. Periodic boundary conditions are used when "bump" solutions are being sought. For the numerical simulation of travelling fronts, the derivatives of u are zero at the boundaries. When κ^2 is very small or zero, an explicit method of numerical integration can be used. For larger κ^2, an explicit method becomes very slow and eventually numerically unstable and we instead use a "hybrid" method based upon the Crank-Nicolson method.

We discretise over space by dividing the domain Ω into n equal intervals of size h such that

$$h = \frac{20\pi}{n} \tag{8.39}$$

and write $x_i = ih$ for $i = 0, 1, \ldots, n$. To find $u(x,T)$ where $T > 0$, we discretise time T into m equal steps of size k such that

$$k = \frac{T}{m} \tag{8.40}$$

and write $t_j = jk$ for $j = 0, 1, \ldots, m$. We construct a grid of $(n+1)$ spatial points by $(m+1)$ time points and let $v_{i,j}$ be the approximate value of u at (x_i, t_j) in Equation (8.36). We have an initial condition $u(x, 0) = g(x)$ where $g\colon \mathbb{R}^n \to \mathbb{R}^n$. Assume boundary conditions of $u(-10\pi, t) = u(10\pi, t) = 0$. The initial and boundary conditions mean that $v_{i,0}$, $v_{0,j}$ and $v_{n,j}$ are known for all i, j. This method of discretisation produces a problem containing a finite number of function points to evaluate which allows us to approximate spatial and time derivatives with finite difference quotients and solve for $v_{i,m}$.

A forward difference scheme, backward difference scheme, or average of the two, each with different stability criteria and/or truncation errors [19, 60, 86], can be used to approximate the spatial and time derivatives. Next, we give a brief overview of both the explicit and hybrid methods. We refer the interested reader to [25] for more detail on numerical integration schemes.

Explicit method

We replace the derivatives in Equation (8.36) by the forward difference approximation

$$u_t = \frac{v_{i,j+1} - v_{i,j}}{k} + \mathcal{O}(k) \tag{8.41}$$

and the centred difference approximation

$$u_{xx} = \frac{v_{i+1,j} - 2v_{i,j} + v_{i-1,j}}{h^2} + \mathcal{O}(h^2) \tag{8.42}$$

where $v_{i,j}$ is the approximation to $u(x_i, t_j) = u(ih, jk)$. The centred difference approximation of the second spatial derivative has second order accuracy. To find the stability of the method, the nonlinear term formed by the integral

$$\int_{-\infty}^{\infty} w(x - y) f(u(y, t))\, dy \tag{8.43}$$

is ignored. We have the scheme

$$v_{i,j+1} = (1 - k - 2s\kappa^2)v_{ij} + s\kappa^2(v_{i+1,j} + v_{i-1,j}) \tag{8.44}$$

where $s = k/h^2$, $0 \leq i \leq n + 1$ and $j \geq 0$. This method is unstable unless the coefficient of $v_{i,j}$ is nonnegative. This gives the matrix equation $V_{j+1} = \mathbf{A}V_j$ where $V_j = [v_{1,j}, v_{2,j}, \cdots, v_{n-1,j}]^T$ and T denotes the transpose of the vector. We have the

matrix $\mathbf{A} = (1-k)\mathbf{Id} - s\kappa^2\mathbf{B}$, where $\mathbf{B}$ is the positive definite second difference matrix

$$\mathbf{B} = \begin{pmatrix} 2 & -1 & 0 & \dots & 0 \\ -1 & 2 & -1 & \dots & 0 \\ 0 & -1 & 2 & \dots & 0 \\ \vdots & \vdots & \vdots & \ddots & \vdots \\ 0 & 0 & 0 & \dots & 2 \end{pmatrix}. \tag{8.45}$$

The matrix $\mathbf{Id}$ is the identity matrix. The method is stable if $1 - k - 2s\kappa^2 \geq 0$, therefore the condition for stability (ignoring the nonlinear term) is

$$k \leq \frac{h^2}{h^2 + 2\kappa^2} \tag{8.46}$$

with truncation error of $\mathcal{O}(k) + \mathcal{O}(h^2)$. The stability condition demonstrates the inverse relationship between the size of the time step, k, and the coefficient of the second spatial derivative, κ^2. As κ^2 increases, the size of the time step, k, must decrease to maintain stability.

To solve Equation (8.36) numerically, the nonlinear term is evaluated at step j (the previous time step) using the trapezoid rule as this is very efficient and increasingly accurate as the spatial step, h, becomes smaller. We use W_j to denote the evaluation of the nonlinear term at time step j. Then the explicit method is the numerical scheme

$$V_{j+1} = \mathbf{A}V_j + W_j. \tag{8.47}$$

Hybrid method

We use the Crank-Nicolson method and replace the second spatial derivative with the mean of the forward difference and centred difference approximations

$$u_{xx} = \frac{v_{i+1,j+1} - 2v_{i,j+1} + v_{i-1,j+1} + v_{i+1,j} - 2v_{i,j} + v_{i-1,j}}{2h^2} + \mathcal{O}(h^2). \tag{8.48}$$

To apply to Equation (8.36), ignoring the nonlinear term, we obtain the Crank-Nicolson finite difference scheme of

$$\begin{aligned}(2 + k + 2s\kappa^2)v_{i,j+1} - s\kappa^2(v_{i+1,j+1} + v_{i-1,j+1}) \\ = (2 - k - 2s\kappa^2)v_{i,j} + s\kappa^2(v_{i+1,j} + v_{i-1,j}).\end{aligned} \tag{8.49}$$

for $0 \leq i \leq n+1$ and $j \geq 0$. This numerical scheme is stable for all $s > 0$. If the nonlinear term is taken also as the mean of the j^{th} and $(j+1)^{th}$ time levels, then the matrix form of the numerical scheme is

$$\mathbf{A}V_{j+1} + kW_{j+1} = \mathbf{C}V_j + kW_j \tag{8.50}$$

where $\mathbf{B}$ is the matrix in Equation (8.45), $\mathbf{A} = (2+k)\mathbf{Id} + s\kappa^2\mathbf{B}$ and $\mathbf{C} = (2-k)\mathbf{Id} - s\kappa^2\mathbf{B}$. Newton's method must now be used to solve Equation (8.50), as evaluation of the nonlinear term at both the j^{th} and $(j+1)^{th}$ time levels creates a set of nonlinear equations. The need to use Newton's method makes the Crank-Nicolson method much slower than the explicit method. To speed up the Crank-Nicolson method, we take the nonlinear term at the j^{th} time level only, creating the linear system of equations

$$\mathbf{A}V_{j+1} = \mathbf{C}V_j + 2kW_j. \tag{8.51}$$

We call this numerical scheme the "hybrid" method. Newton's method is no longer required and Equation (8.51) can be solved effectively using LU decomposition to evaluate $A^{-1}C$ in

$$V_{j+1} = \mathbf{A}^{-1}\left[\mathbf{C}V_j + 2kW_j\right]. \tag{8.52}$$

LU decomposition makes this method very fast. The hybrid method has speed comparable to the explicit method with stability and truncation error similar to the Crank-Nicolson method. Thus the hybrid method is stable for all $s > 0$ and has truncation error of $\mathcal{O}(k) + \mathcal{O}(h^2)$.

A2. Continuation methods

Numerical continuation is a method for computing solutions of a system of parameterised nonlinear equations

$$G(\mathbf{y}, \lambda) = 0 \tag{8.53}$$

where $\mathbf{y}$ is an n-dimensional vector and λ is a real scalar parameter. An initial solution $(\mathbf{y}_0, \lambda_0)$ satisfying $G(\mathbf{y}_0, \lambda_0) = 0$ must be known. By varying the parameter λ, it may be possible to compute the branch of solutions of $G(\mathbf{y}, \lambda) = 0$ upon which $(\mathbf{y}_0, \lambda_0)$ lies.

Pseudo-arclength method

A continuation program was developed in MATLAB [74] for bifurcation analysis, using the pseudo-arclength continuation method [22]. This method is particularly suited to the complex neural model investigated in the thesis, given its ability to compute folds on the bifurcation curve. The pseudo-arclength method was proposed by H.B. Keller in the late 1970's and is based upon the idea that the "ideal" parameterisation of a curve is arclength. Pseudo-arclength is an approximation of the arclength in the tangent space and a step is

made in arclength rather than in the parameter. A brief overview of the method is given here.

The pseudo-arclength continuation method attempts to find the solutions for a function

$$G(\mathbf{y}, \lambda) = 0, \qquad G\colon \mathbb{R}^n \times \mathbb{R} \to \mathbb{R}^n,\ \mathbf{y} \in \mathbb{R}^n,\ \lambda \in \mathbb{R} \tag{8.54}$$

where $\mathbf{y}$ is a vector of length n and λ is a real, scalar parameter. The parameter λ is known as the continuation parameter. Geometrically speaking, the method finds a solution $(\mathbf{y}_1, \lambda_1)$ of the equation $G(\mathbf{y}, \lambda) = 0$ in a hyperplane that is both a distance Δs from the starting point on the curve, $(\mathbf{y}_0, \lambda_0)$, and perpendicular to the direction vector $(\dot{\mathbf{y}}_0, \dot{\lambda}_0)$. Newton's method is then used to find a new solution point on the curve by solving

$$\begin{pmatrix} (G_y^1)^{(v)} & (G_\lambda^1)^{(v)} \\ \dot{\mathbf{y}}_0^T & \dot{\lambda}_0 \end{pmatrix} \begin{pmatrix} \Delta \mathbf{y}_1^{(v)} \\ \Delta \lambda_1^{(v)} \end{pmatrix} = - \begin{pmatrix} G(\mathbf{y}_1^{(v)}, \lambda_1^{(v)}) \\ (\mathbf{y}_1^{(v)} - \mathbf{y}_0)^T \dot{\mathbf{y}}_0 + (\lambda_1^{(v)} - \lambda_0)\dot{\lambda}_0 - \Delta s \end{pmatrix} \tag{8.55}$$

To explain the notation:

1. The symbol T indicates the transpose of a vector;
2. $\mathbf{y}$ is the $n \times 1$ vector $[y_1; y_2; \ldots; y_n]$;
3. $(\mathbf{y}_1, \lambda_1)$ is the point found by stepping out the distance Δs from $(\mathbf{y}_0, \lambda_0)$ in the direction of the vector $(\dot{\mathbf{y}}_0, \dot{\lambda}_0)$;
4. $(\mathbf{y}_1^{(v)}, \lambda_1^{(v)})$ is the v^{th} iteration of the point $(\mathbf{y}_1, \lambda_1)$;
5. The function G is the $n \times 1$ vector
$$\begin{pmatrix} G_1(\mathbf{y}, \lambda) \\ G_2(\mathbf{y}, \lambda) \\ \vdots \\ G_n(\mathbf{y}, \lambda) \end{pmatrix}; \tag{8.56}$$
6. $G(\mathbf{y}_1^{(v)}, \lambda_1^{(v)})$ is the value of the function G valued at $(\mathbf{y}, \lambda) = (\mathbf{y}_1^{(v)}, \lambda_1^{(v)})$;
7. $(G_y^1)^{(v)}$ is the $n \times n$ Jacobian of G with respect to $\mathbf{y}$, that is,
$$\begin{pmatrix} \frac{\partial G_1}{\partial y_1} & \frac{\partial G_1}{\partial y_2} & \cdots & \frac{\partial G_1}{\partial y_n} \\ \frac{\partial G_2}{\partial y_1} & \frac{\partial G_2}{\partial y_2} & \cdots & \frac{\partial G_2}{\partial y_n} \\ \vdots & \vdots & \ddots & \vdots \\ \frac{\partial G_n}{\partial y_1} & \frac{\partial G_n}{\partial y_2} & \cdots & \frac{\partial G_n}{\partial y_n} \end{pmatrix}, \tag{8.57}$$

evaluated at $(\mathbf{y}, \lambda) = (\mathbf{y}_1^{(v)}, \lambda_1^{(v)})$;

8. $(G_\lambda^1)^{(v)}$ is the $n \times 1$ vector of the derivative of G with respect to λ,

$$\begin{pmatrix} \frac{\partial G_1}{\partial \lambda} \\ \frac{\partial G_2}{\partial \lambda} \\ \vdots \\ \frac{\partial G_n}{\partial \lambda} \end{pmatrix} \tag{8.58}$$

evaluated at $(\mathbf{y}, \lambda) = (\mathbf{y}_1^{(v)}, \lambda_1^{(v)})$;

9. $\begin{pmatrix} \dot{\mathbf{y}}_0^T & \dot{\lambda}_0 \end{pmatrix}$ is the direction vector of length $(n+1)$ evaluated at $(\mathbf{y}_0, \lambda_0)$;

10. $(\mathbf{y}_1^{(v+1)}, \lambda_1^{(v+1)}) = (\mathbf{y}_1^{(v)}, \lambda_1^{(v)}) + (\Delta\mathbf{y}_1^{(v)}, \Delta\lambda_1^{(v)})$ where $\Delta\mathbf{y}_1^{(v)}$ and $\Delta\lambda_1^{(v)}$ are found by solving the system in Equation (8.55).

The direction vector for the next iteration is defined as

$$G_y^1 \dot{\mathbf{y}}_1 + G_\lambda^1 \dot{\lambda}_1 = 0$$

with normalisation of

$$(\dot{\mathbf{y}}_\mathbf{0})^T \dot{\mathbf{y}}_1 + \dot{\lambda}_0 \dot{\lambda}_1 = 1.$$

The direction vector $(\dot{\mathbf{y}}_1, \dot{\lambda}_1)$ is solved by one extra back substitution at the end of the iterations. In order to start the continuation, the initial direction vector $(\dot{\mathbf{y}}_0, \dot{\lambda}_0)$ is found by calculating the null vector of the $n \times (n+1)$ Jacobian

$$\begin{pmatrix} (G_y^1) & (G_\lambda^1) \end{pmatrix} \tag{8.59}$$

evaluated at $(\mathbf{y}_0, \lambda_0)$.

AUTO 2000

Throughout the thesis, we also use AUTO 2000 for bifurcation analysis. AUTO 2000 [23] is a software package for continuation and bifurcation problems in ordinary differential equations of the form

$$\mathbf{x}'(t) = H(\mathbf{x}(t), p), \qquad H\colon \mathbb{R}^n \times \mathbb{R} \to \mathbb{R}^n,\ \mathbf{x} \in \mathbb{R}^n \tag{8.60}$$

where p denotes one or more free parameters. AUTO can also perform limited bifurcation analysis of algebraic systems

$$H(\mathbf{x}, p) = 0, \qquad \mathbf{x}, H \in \mathbb{R}^n. \tag{8.61}$$

The package HomCont is included. HomCont contains the algorithms for the bifurcation analysis of homoclinic orbits. We use HomCont to follow curves of homoclinic orbits of our neural field models.

Bibliography

[1] S. Amari. Dynamics of pattern formation in lateral-inhibition type neural fields. *Biological Cybernetics*, 27:77–87, 1977.

[2] F.M. Atay and A. Hutt. Neural fields with distributed transmission speeds and long-range feedback delays. *SIAM Journal of Dynamical Systems*, 5(4):670–698, 2006.

[3] A.D. Baddeley. *Working memory.* Oxford University Press, New York, 1986.

[4] S. Baigent, J. Stark, and A. Warner. Modelling the effect of gap junction nonlinearities in systems of coupled cells. *Journal of theoretical biology*, 186:223–239, 1997.

[5] M. V. L. Bennett. Gap junctions as electrical synapses. *Journal of Neurocytology*, 26:349–366, 1997.

[6] M. V. L. Bennett and R. S. Zukin. Electrical coupling and neuronal synchronization in the mammalian brain. *Neuron*, 41:495–511, 2004.

[7] P. Blomquist, J. Wyller, and G.T. Einevoll. Localized activity patterns in two-population neuronal networks. *Physica D*, 206:180–212, 2005.

[8] P.C. Bressloff. New mechanism for neural pattern formation. *Physical Review Letters*, 76:4644–4647, 1996.

[9] P.C. Bressloff. Spatially periodic modulation of cortical patterns by long-range horizontal connections. *Physica D*, 185:131–157, 2003.

[10] P.C. Bressloff, J.D. Cowan, M. Golubitsky, P.J. Thomas, and M. Wiener. Geometric visual hallucinations, Euclidean symmetry and the functional architecture of striate cortex. *Philosophical Transactions of the Royal Society London B*, 40:299–330, 2001.

[11] P.C. Bressloff and S.E. Folias. Front-bifurcations in an excitatory neural network. *Physical Review E*, 70:052902, 2004.

[12] A.R. Champneys. Homoclinic orbits in reversible systems and their applications in mechanics, fluids and optics. *Physica D*, 112:158–186, 1998.

[13] A.R. Champneys and A. Spence. Hunting for homoclinic orbits in reversible systems: A shooting technique. *Advances in Computational Mathematics*, 1:81–108, 1993.

[14] S. Coombes. Waves, bumps, and patterns in neural field theories. *Biological Cybernetics*, 93:91–108, 2005.

[15] S. Coombes, G.J. Lord, and M.R. Owen. Waves and bumps in neuronal networks with axo–dendritic synaptic interactions. *Physica D–Nonlinear Phenomena*, 178:219–241, 2004.

[16] S. Coombes and M.R. Owen. Evans functions for integral neural field equations with Heaviside firing rate function. *SIAM Journal on Applied Dynamical Systems*, 3(4):574–600, 2004.

[17] S. Coombes and M.R. Owen. Bumps, breathers, and waves in a neural network with spike frequency adaptation. *Physical Review Letters*, 94, 2005.

[18] S. Coombes, N.A. Venkov, L. Shiau, I. Bojak, D.T.J. Liley, and C.R. Laing. Modeling electrocortical activity through improved local approximations of integral neural field equations. *Physical Review E*, 76:051901, 2007.

[19] J.M. Cooper. *Introduction to Partial Differential Equations with MATLAB.* Birkhauser, 1998.

[20] M.C. Cross and P.C. Hohenberg. Pattern formation out of equilibrium. *Reviews of Modern Physics*, 65:851–1114, 1993.

[21] R. Curtu and G.B. Ermentrout. Pattern formation in a network of excitatory and inhibitory cells with adaptation. *SIAM Journal on Applied Dynamical Systems*, 3:191–231, 2004.

[22] E. Doedel, H.B. Keller, and J.P. Kernévez. Numerical analysis and control of bifurcation problems (I): Bifurcation in finite dimensions. *International Journal of Bifurcation and Chaos*, 1(3):493–520, 1991.

[23] E.J. Doedel, R.C. Paffenroth, A.R. Champneys, T.F. Fairgrieve, Y.A. Kuznetsov, B.E. Oldeman, B. Sandstede, and X. Wang. AUTO 2000: Continuation and bifurcation software for ordinary differential equations (with HomCont), 2000.

[24] D. Durstewitz, J.K. Seamans, and T.J. Sejnowski. Neurocomputational models of working memory. *Nature Neuroscience Supplement*, 3, 2000.

[25] A. Elvin and C. Laing. Evaluation of numerical integration schemes for a partial integro-differential equation. *Research Letters in the Information and Mathematical Sciences – ISSN 1175-2777*, 7:171–186, 2005.

[26] I.R. Epstein and J.A. Pojman. *An introduction to nonlinear chemical dynamics.* Oxford University Press, 1998.

[27] G.B. Ermentrout. Neural networks as spatio–temporal pattern–forming systems. *Reports on Progress in Physics*, 61:353–430, 1998.

[28] G.B. Ermentrout. Gap junctions destroy persistent states in excitatory networks. *Physical Review E*, 74, 2006.

[29] G.B. Ermentrout and J.D. Cowan. A mathematical theory of visual hallucination patterns. *Biological Cybernetics*, 34:137–150, 1979.

[30] J.W. Evans. Nerve axon equations: IV The stable and the unstable impulse. *Indiana University Mathematics Journal*, 24(12), 1975.

[31] S.E. Folias and P.C. Bressloff. Breathing pulses in an excitatory neural network. *SIAM Journal of Applied Dynamical Systems*, 3(3):378–407, 2004.

[32] S.E. Folias and P.C. Bressloff. Breathers in two-dimensional neural media. *Physical Review Letters*, 95(20), 2005.

[33] C.G. Fonseca, C.R. Green, and L.F.B. Nicholson. Upregulation in astrocytic connexin 43 gap junction levels may exacerbate generalised seizures in mesial temporal lobe epilepsy. *Brain Research*, 929:105–116, 2002.

[34] G. Francisco and A. Fonseca. Homoclinic bifurcations in reversible Hamiltonian systems. *Applied Mathematics and Computation*, 176:654–661, 2006.

[35] D.A. French. Identification of a free energy functional in an integro-differential equation model for neuronal network activity. *Applied Mathematics Letters*, 17:1047–1051, 2004.

[36] T. Fukuda, T. Kosaka, W. Singer, and R.A.W. Galuske. Gap junctions among dendrites of cortical GABAergic neurons establish a dense and widespread intercolumnar network. *Journal of Neuroscience*, 26(13):3434–3443, 2006.

[37] S. Funahashi, C.J. Bruce, and P.S. Goldman-Rakic. Mnemonic coding of visual space in the monkey's dorsolateral prefrontal cortex. *Journal of Neurophysiology*, 61(2), 1989.

[38] M. Galarreta and S. Hestrin. A network of fast-spiking cells in the neocortex connected by electrical synapses. *Nature*, 402:72–75, 1999.

[39] W. Gerstner and W. Kistler. *Spiking Neuron Models: Single Neurons, Populations, Plasticity*. Cambridge University Press, second edition, 2005.

[40] J.R. Gibson, M. Belerlein, and B.W. Connors. Two networks of electrically coupled inhibitory neurons in neocortex. *Nature*, 402:75–79, 1999.

[41] M.A. Giese, G. Schöner, and H.S. Hock. Neural field dynamics for motion perception. *Lecture Notes in Computer Science*, 1112:335–340, 1996.

[42] P. Glendinning. *Stability, instability and chaos: an introduction to the theory of nonlinear differential equations*. Cambridge University Press, 1994.

[43] P. Glendinning and C. Sparrow. *T*-points: A codimension two heteroclinic bifurcation. *Journal of Statistical Physics*, 43(3–4), 1986.

[44] P.S. Goldman-Rakic. Cellular basis of working memory. *Neuron*, 14:477–485, 1995.

[45] D. Golomb and Y. Amitai. Propagating neuronal discharges in neocortical slices: computational and experimental study. *Journal of Neurophysiology*, 78:1199–1997, 1997.

[46] J. Guckenheimer and P. Holmes. *Nonlinear oscillations, dynamical systems, and bifurcations of vector fields*. Springer-Verlag New York, Inc., 1983.

[47] Y. Guo. *Existence and stability of standing pulses in neural networks*. PhD dissertation, Department of Mathematics, University of Pittsburgh, 2003.

[48] Y. Guo and C.C. Chow. Existence and stability of standing pulses in neural networks: I. Existence. *SIAM Journal on Applied Dynamical Systems*, 4(2):217–248, 2005.

[49] Y. Guo and C.C. Chow. Existence and stability of standing pulses in neural networks: II. Stability. *SIAM Journal on Applied Dynamical Systems*, 4(2):249–281, 2005.

[50] B.S. Gutkin, G.B. Ermentrout, and J. O'Sullivan. Layer 3 patchy recurrent excitatory connections may determine the spatial organization of sustained activity in the primate prefrontal cortex. *Neurocomputing*, 32–33:391–400, 2000.

[51] X. Huang, W.C. Troy, Q. Yang, H. Ma, C.R. Laing, S.J. Schiff, and J. Wu. Spiral waves in disinhibited mammalian neocortex. *The Journal of Neuroscience*, 24(44), 2004.

[52] G.W. Hunt, M.A. Peletier, A.R. Champneys, P.D. Woods, M. Ahmer Wadee, C.J. Budd, and G.J. Lord. Cellular buckling in long structures. *Nonlinear Dynamics*, 21:3–29, 2000.

[53] A. Hutt, M. Bestehorn, and T. Wennekers. Pattern formation in intracortical neuronal fields. *Network: Computational Neural Systems*, 14, 2003.

[54] V.K. Jirsa and H. Haken. Field theory of electromagnetic brain activity. *Physical Review Letters*, 77:960–963, 1996.

[55] V.K. Jirsa and J.A.S Kelso. Spatiotemporal pattern formation in neural systems with heterogeneous connection topologies. *Physical Review E*, 62:8462–8465, 2000.

[56] S. Kádár, I. Lengyel, and I.R. Epstein. Modeling of transient Turing-type patterns in the closed chlorine dioxide – iodine–malonic acid–starch reaction system. *Journal of Physical Chemistry*, 99:4054–4058, 1995.

[57] E.R. Kandel, J.H. Schwartz, and T.M. Jessell. *Principles of neural science*. McGraw-Hill, New York, third edition, 2000.

[58] T. Kapitula, N. Kutz, and B. Sandstede. The Evans function for nonlocal equations. *Indiana University Mathematics Journal*, 53(4):1095–1126, 2004.

[59] J. Keener and J. Sneyd. *Mathematical Physiology*. Springer-Verlag, New York, 1998.

[60] D. Kincaid and W. Cheney. *Numerical Analysis: Mathematics of Scientific Computing*. Brooks/Cole, third edition, 2002.

[61] K. Kishimoto and S. Amari. Existence and stability of local excitations in homogeneous neural fields. *Journal of Mathematical Biology*, 7:303–318, 1979.

[62] W. M. Kistler, R. Seitz, and J. L. van Hemmen. Modelling collective excitations in cortical tissue. *Physica D*, 114:273–295, 1998.

[63] E. Knobloch. Spatially localized structures in dissipative systems: open problems. *Nonlinearity*, 21:T45–T60, 2008.

[64] N. Kopell and G.B. Ermentrout. Chemical and electrical synapses perform complementary roles in the synchronization of interneuronal networks. *Proceedings of the National Academy of Science of the United States of America*, 101(43):15482–15487, 2004.

[65] C.R. Laing. Spiral waves in nonlocal equations. *SIAM Journal of Applied Dynamical Systems*, 4(3):588–606, 2005.

[66] C.R. Laing and S. Coombes. The importance of different timings of excitatory and inhibitory pathways in neural field models. *Network: Computation in Neural Systems*, 17:151–172, 2006.

[67] C.R. Laing and P. Glendinning. Bifocal homoclinic bifurcations. *Physica D*, 102:1 –14, 1997.

[68] C.R. Laing and W.C. Troy. PDE methods for non-local models. *SIAM Journal of Applied Dynamical Systems*, 2(3), 2003.

[69] C.R. Laing and W.C. Troy. Two-bump solutions of Amari-type models of neuronal pattern formation. *Physica D*, 178:190–218, 2003.

[70] C.R. Laing, W.C. Troy, B. Gutkin, and G.B. Ermentrout. Multiple bumps in a neuronal model of working memory. *SIAM Journal of Applied Mathematics*, 63(1):62–97, 2002.

[71] I. Lengyel, S. Kádár, and I.R. Epstein. Transient Turing structures in a gradient-free closed system. *Science*, 259(5094):493–495, 1993.

[72] T.J. Lewis and J. Rinzel. Self-organized synchronous oscillations in a network of excitable cells coupled by gap junctions. *Network: Computational Neural Systems*, 11:299–320, 2000.

[73] D.V. Madison and R.A. Nicoll. Control of the repetitive discharge of rat CA1 pyramidal neurones *in vitro*. *Journal of Physiology*, 354:319–331, 1984.

[74] MATLAB ®. *http://www.mathworks.com*, The MathWorks, Inc, 1984–2004.

[75] J.D. Murray. *Mathematical Biology II: Spatial models and biomedical applications*. Springer-Verlag, Berlin, third edition, 2003.

[76] J.G. Nicholls, A. R. Martin, B.G. Wallace, and P. A. Fuchs. *From neuron to brain*. Sinauer Associates Inc., fourth edition, 2001.

[77] K.E. Nilsen, A.R.C. Kelso, and H.R. Cock. Antiepileptic effect of gap–junction blockers in a rat model of refractory focal cortical epilepsy. *Epilepsia*, 47(7):1169–1175, 2006.

[78] NINDS. Seizures and Epilepsy: Hope through research. *NIH Publication*, No. 04-156, 2004, May.

[79] M.R. Owen, C.R. Laing, and S. Coombes. Bumps and rings in a two-dimensional neural field: splitting and rotational instabilities. *New Journal of Physics*, 9, 2007.

[80] L.A. Peletier and W.C. Troy. *Spatial patterns : higher order models in physics and mechanics*. Birkhauser, Boston, 2001.

[81] D.J. Pinto and G.B. Ermentrout. Spatially structured activity in synaptically coupled neuronal networks: I. Travelling fronts and pulses. *SIAM Journal of Applied Mathematics*, 62(1):206–225, 2001.

[82] D.J. Pinto and G.B. Ermentrout. Spatially structured activity in synaptically coupled neuronal networks: II. Lateral inhibition and standing pulses. *SIAM Journal of Applied Mathematics*, 62(1):226–243, 2001.

[83] D.J. Pinto, R.K. Jackson, and C.E. Wayne. Existence and stability of traveling pulses in a continuous neuronal network. *SIAM Journal on Applied Dynamical Systems*, 4(4):954–984, 2005.

[84] A. Prat, Y. Li, and P. Bressloff. Inhomogeneity-induced bifurcation of stationary and oscillatory pulses. *Physica D*, 202:177–199, 2005.

[85] C.B. Price. Traveling Turing patterns in nonlinear neural fields. *Physical Review E*, 55:6698–6706, 1997.

[86] L. Rade and B. Westergren. *Mathematics Handbook for Science and Engineering*. Springer-Verlag Berlin Heidelberg New York, fifth edition, 2004.

[87] K.A. Richardson, S.J. Schiff, and B.J. Gluckman. Control of traveling waves in the mammalian cortex. *Physical Review Letters*, 94, 2005.

[88] B. Sandstede. Evans functions and nonlinear stability of travelling waves in neuronal network models. *International Journal of Bifurcation and Chaos*, 2007.

[89] F.K. Skinner, L. Zhang, J.L. Perez Velazquez, and P.L. Carlen. Bursting in inhibitory interneuronal networks: a role for gap-junctional coupling. *Journal of Neurophysiology*, 81:1274–1283, 1999.

[90] I. Stakgold. *Green's functions and boundary value problems.* Wiley-Interscience, second edition, 1997.

[91] M.L. Steyn-Ross, D.A. Steyn-Ross, and J.W. Sleigh. Modelling general anaesthesia as a first-order phase transition in the cortex. *Special issue: Progress in Biophysics and Molecular Biology*, 85(3–4):369–385, 2004.

[92] M.L. Steyn-Ross, D.A. Steyn-Ross, J.W. Sleigh, and D.T.J. Liley. Theoretical electroencephalogram stationary spectrum for a white-noise driven cortex: Evidence for a general anesthetic-induced phase transition. *Physical Review E*, 60(6):7299–7311, 1999.

[93] M.L. Steyn-Ross, D.A. Steyn-Ross, J.W. Sleigh, and D.R. Whiting. Theoretical predictions for spatial covariance of the electroencephalographic signal during the anesthetic-induced phase transition: Increased correlation length and emergence of spatial self-organization. *Physical Review E*, 68:021902, 2003.

[94] M.L. Steyn-Ross, D.A. Steyn-Ross, M.T. Wilson, and J.W. Sleigh. Gap junctions mediate large-scale Turing structures in a mean-field cortex driven by subcortical noise. *Physical Review E*, 76, 2007.

[95] R.D. Traub, N. Kopell, A. Bibbig, E.H. Buhl, F.E.N. LeBeau, and M.A. Whittington. Gap junctions between interneuron dendrites can enhance synchrony of gamma oscillations in distributed networks. *The Journal of Neuroscience*, 21(23):9478–9486, 2001.

[96] R.D. Traub, M.A. Whittington, E.H. Buhl, F.E.N. LeBeau, A. Bibbig, S. Boyd, H. Cross, and T. Baldeweg. A possible role for gap junctions in generation of very fast EEG oscillations preceding the onset of, and perhaps, initiating, seizures. *Epilepsia*, 42(2):153–170, 2001.

[97] A.M. Turing. The chemical basis of morphogenesis. *Philosophical Transactions of the Royal Society of London Series B – Biological Sciences*, 237(641):37–72, 1952.

[98] G. J. B. van den Berg. *Dynamics and equilibria of fourth order differential equations*. PhD thesis, Leiden University, The Netherlands, 2000.

[99] V.K. Vanag and I.R Epstein. Inwardly rotating spiral waves in a reaction-diffusion system. *Science*, 294, 2001.

[100] V.K. Vanag and I.R Epstein. Pattern formation in a tunable medium: The Belousov-Zhabotinsky reaction in an aerosol OT microemulsion. *Physical Review Letters*, 87, 2001.

[101] J.L.P. Velazquez and P.L. Carlen. Gap junctions, synchrony and seizures. *Trends in Neurosciences*, 23:68–74, 2000.

[102] N.A. Venkov, S. Coombes, and P.C. Matthews. Dynamic instabilities in scalar neural field equations with space-dependent delays. *Physica D*, 232:1–15, 2007.

[103] R. Walsh. Epilepsy focus has wider implications. *The New Zealand Herald (25 May)*, 2003.

[104] X. Wang. Discovering spatial working memory fields in prefrontal cortex. *Journal of Neurophysiology*, 93:3027–3028, 2005.

[105] H.R. Wilson and J.D. Cowan. A mathematical theory of the functional dynamics of cortical and thalamic nervous tissue. *Kybernetik*, 13:55–80, 1973.

[106] J. Wu, L. Guan, and Y. Teau. Propagating activation during oscillations and evoked responses in neocortical slices. *Journal of Neuroscience*, 19(12):5005–5015, 1999.

[107] J. Wyller, P. Blomquist, and G.T. Einevoll. Turing instability and pattern formation in a two-population neuronal network model. *Physica D*, 225:75–93, 2007.

[108] X. Xie and M.A. Giese. Nonlinear dynamics of direction-selective recurrent neural media. *Physical Review E*, 65, 2002.

[109] L. Yang, M. Dolnik, A.M. Zhabotinsky, and I.R. Epstein. Pattern formation arising from interactions between Turing and wave instabilities. *Journal of Chemical Physics*, 117(15), 2002.

[110] L. Zhang. On stability of traveling wave solutions in synaptically coupled neuronal networks. *Differential and Integral Equations*, 16:513–536, 2003.